ROBUST OPTIMISATION OF ULTRASONIC FLOW METERS BY COMPUTATIONAL FLUID DYNAMICS AND ENHANCED TURBULENCE MODELLING

Mario Javier Rincón

Ph.D. Thesis

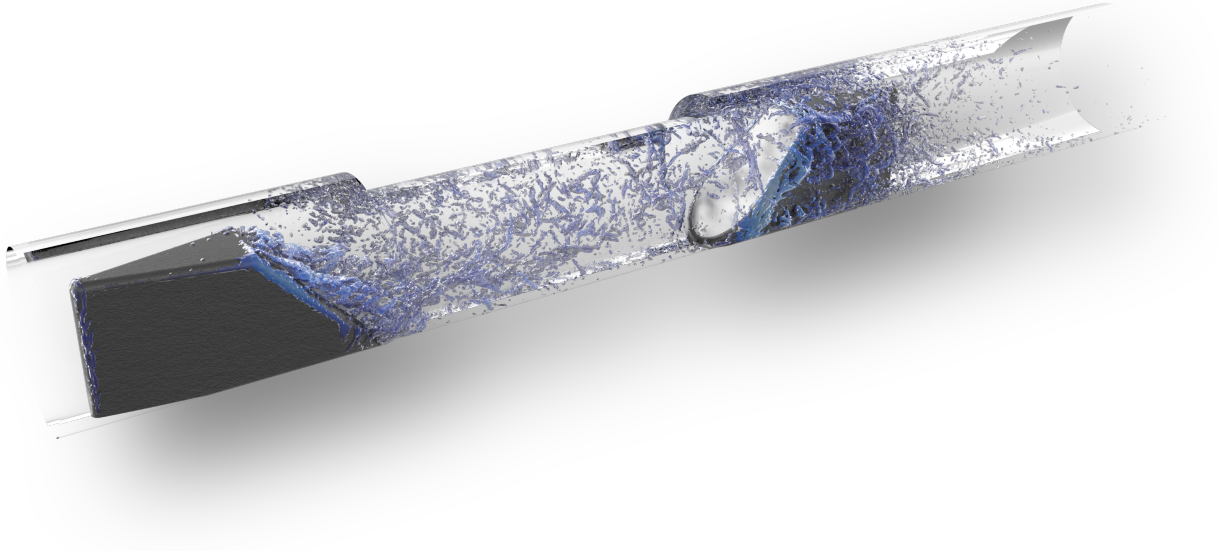

AARHUS UNIVERSITY

kamstrup

Mario Javier Rincón
Robust Optimisation of Ultrasonic Flow Meters by Computational Fluid Dynamics and Enhanced Turbulence Modelling
Fluid Mechanics & Turbulence Research Group
Ph.D. Thesis
October 2023

Aarhus University
Department of Mechanical and Production Engineering
Katrinebjergvej 89 G-F
8200 Aarhus N, Denmark
https://www.mpe.au.dk

Cover page image
Large-eddy simulation performed in a very fine grid (quasi-DNS) of a typical two-stand ultrasonic flow meter. Results show instantaneous 3-dimensional $\lambda_2 = 2 \cdot 10^6$ criterion iso-contours. Simulation performed with the wall-adapting local eddy-viscosity subgrid-scale model at an inflow Reynolds number of $2.82 \cdot 10^4$. Flow direction from left to right.
Data rendered during postprocess
DOI: 10.7146/aul.508
ISBN: 978-87-7507-554-6

To everything that makes life beautiful.
Family, friendship, croquetas, and vinitos included...

Abstract

The accurate measurement of fluid flow is essential in a wide range of industrial applications. In this regard, ultrasonic flow meters present an accurate and cost-effective solution; however, these systems introduce challenges due to their complex geometry and interaction with fluid flow. Hence, understanding their flow dynamics is paramount in the improvement of their design and operation. Simultaneously, data-driven turbulence modelling techniques have emerged as promising tools to improve the precision of fluid flow simulations. This doctoral thesis focuses on bridging these two domains by predicting complex flows in ultrasonic flow meters, developing a robust methodology for geometrical optimisation, and enhancing existing Reynolds-averaged Navier-Stokes (RANS) turbulence models with progressive and generalisable data-driven methods.

A methodology based on computational fluid dynamics (CFD) is developed to predict the flow dynamics throughout ultrasonic flow meters by the use of RANS $k-\omega$ SST. The method is experimentally validated with laser Doppler velocimetry and pressure drop experiments for the whole dynamic range of operation of these systems. Subsequently, a series of flow simulations are driven by surrogate and Bayesian multi-objective optimisation methods to provide improved geometrical designs. These improved geometries are further optimised by an adjoint-based shape optimisation method that enables the 3-dimensional morphing of the geometry, allowing higher improvement gains which cannot be achieved by traditional engineering ingenuity.

In the realm of data-driven turbulence modelling, two critical aspects take centre stage: generalisability and the consistency of *a posteriori* results. This thesis addresses these challenges through a systematic approach that combines the CFD-driven optimisation techniques developed for flow meter improvement with a progressive augmentation strategy in the $k-\omega$ SST turbulence model. The goal is to improve the prediction of turbulence anisotropy-based secondary flows, and flow separation — two common stumbling blocks in fluid flow simulations — without altering the successful law of the wall prediction by the original model. Two correction terms are carefully defined and introduced in the momentum and specific dissipation rate (ω) transport equations. After extensive numerical verification, the enhanced models exhibit significant improvements in the prediction of secondary flows, boundary-layer detachment and reattachment, and friction coefficients in both training and testing cases, reaffirming their *a posteriori* reliability and generalisability.

In conclusion, this doctoral thesis presents a robust and cost-efficient methodology to systematically improve the performance of complex engineering systems based on CFD simulations. Additionally, two generalisable methods are developed to enhance turbulence modelling based on data-driven progressive approaches. By addressing challenges related to flow separation and secondary flow predictions in complex geometries together with design and shape optimisation techniques, this research contributes to more accurate fluid flow predictions and simulation-based optimisation; benefiting industries dependent on precise flow measurements and simulations. The synergy between data-driven modelling and complex system optimisation demonstrates the potential for innovative solutions in both turbulence modelling and flow measurement technologies, with broad implications across academic and industrial engineering sectors.

Resumé

En nøjagtig måling af fluidstrømninger er essentiel indenfor en bred vifte af industrielle applikationer. I dette henseende præsenterer ultralyd-flowmålere en nøjagtig og omkostningseffektiv løsning; disse systemer introducerer dog udfordringer grundet deres komplekse geometri og interaktion med fluidstrømningerne. Derfor er forståelsen af deres dynamiske rolle afgørende for forbedring af deres design og drift. Samtidig har datadrevne metoder til turbulensmodellering vist sig som et lovende værktøj til at forbedre præcisionen i simuleringer af fluidstrømninger. Denne ph.d.-afhandling fokuserer på at bygge bro mellem disse to områder ved at forudsige komplekse fluidstrømninger i ultralyd-flowmålere, udvikle en robust metode til deres geometriske optimering, og forbedre eksisterende Reynolds-averaged Navier-Stokes (RANS) turbulensmodeller med progressive og generaliserbare datadrevne metoder.

Der er udviklet en metode baseret på computational fluid dynamics (CFD) til at forudsige fluidstrømningerne i ultralyd-flowmålere ved hjælp af RANS $k-\omega$ SST. Metoden er eksperimentelt valideret med laser Doppler velocimetri og tryktabseksperimenter for hele driftsområdet af disse systemer. Derefter styres en række simuleringer af surrogate og Bayesianske multi-objektive optimeringsmetoder for at levere forbedrede geometriske designs. Disse forbedrede geometrier optimeres yderligere ved hjælp af en adjoint-baseret formoptimeringsmetode, der muliggør tredimensionel formændring af geometrien, hvilket muliggør større forbedringer, der ikke kan opnås ved traditionelle ingeniørmetoder.

Inden for datadreven turbulensmodellering findes to centrale kritiske aspekter: generalisering og konsistensen af *a posteriori* resultater. Denne afhandling adresserer disse udfordringer gennem en systematisk tilgang, der kombinerer de CFD-drevne optimeringsteknikker, der er udviklet til forbedring af flowmåleren, med en progressiv strategi for augmentering af $k-\omega$ SST turbulensmodellen. Målet er at forbedre forudsigelsen af turbulensbaserede sekundære strømninger og flowseparation (to almindelige udfordringer i fluidstrømningssimuleringer) uden at ændre den oprindelige models vellykkede forudsigelse af den logaritmiske lov. To korrektionstermer er omhyggeligt defineret og indført i henholdsvis bevægelsesligningerne og transportligningerne for den specifikke dissipationshastighed (ω). Efter omfattende numerisk verifikation, viser de augmenterede modeller betydelige forbedringer i forudsigelsen af sekundære strømninger, løsrivelse og gentilknytning i grænselag, samt friktionskoefficienter i både trænings- og testsenarier, hvilket bekræfter deres *a posteriori* pålidelighed og generalisering.

Afslutningsvis præsenterer denne ph.d.-afhandling en robust og omkostningseffektiv metode til systematiske forbedringer af præstationen for komplekse ingeniørsystemer baseret på CFD-simuleringer. Derudover er der udviklet to generaliserbare metoder til at forbedre turbulensmodellering baseret på datadrevne progressive tilgange. Ved at adressere udfordringer i forbindelse med flowseparation og forudsigelse af sekundære strømninger i komplekse geometrier, sammen med design- og formoptimeringsteknikker, bidrager denne forskning til mere nøjagtige forudsigelser af fluidstrømninger og simuleringsbaseret optimering, hvilket gavner industrier som er afhængige af præcise flowmålinger og simuleringer. Samspillet mellem datadreven modellering og kompleks systemoptimering demonstrerer potentiale for innovative løsninger inden for både turbulensmodellering og flowmåleteknologier med brede implikationer inden for akademiske og industrielle ingeniørsektorer.

Resumen

La precisa medición del flujo de fluidos es esencial en una amplia gama de aplicaciones industriales. En este sentido, los caudalímetros ultrasónicos presentan una solución precisa y rentable; sin embargo, predecir el flujo en estos sistemas plantea desafíos debido al diseño de su intricada geometría. Es así que comprender su fluidodinámica es fundamental para mejorar su diseño y funcionamiento. A su vez, las técnicas de modelado de turbulencia basadas en datos han surgido como herramientas prometedoras para mejorar la precisión de las simulaciones de flujo de fluidos. Esta tesis doctoral se centra en unir estos dos campos al predecir flujos complejos en caudalímetros ultrasónicos, desarrollar una metodología sólida de optimización geométrica y mejorar los modelos de turbulencia de Reynolds-averaged Navier-Stokes (RANS) existentes con métodos progresivos y generalizables basados en datos.

Esta tesis desarrolla una metodología basada en la dinámica de Fluidos Computacional (CFD) para predecir la dinámica del flujo a lo largo de los caudalímetros ultrasónicos utilizando RANS $k-\omega$ SST. El método es validado experimentalmente con velocimetría láser Doppler y experimentos de pérdida de carga para todo el rango dinámico de funcionamiento de estos sistemas. A continuación, se realizado una serie de simulaciones de flujo mediante métodos de optimización multiobjetivo bayesianos y basados en modelos de sustitución para proporcionar diseños geométricos mejorados. Estas geometrías mejoradas se optimizan aún más mediante un método de optimización morfológica basado en métodos adjuntos que permite obtener mejoras dificilmente alcanzables mediante la ingeniería tradicional.

En el ámbito del modelado de turbulencia basado en datos, dos aspectos críticos cobran protagonismo: la generalización y la consistencia de los resultados *a posteriori*. Esta tesis aborda estos desafíos a través de un enfoque sistemático que combina las técnicas de optimización impulsadas por CFD desarrolladas para la mejora de los caudalímetros con una estrategia de ampliación progresiva en el modelo de turbulencia $k-\omega$ SST. El objetivo es mejorar la predicción de flujos secundarios basados en anisotropía de turbulencia y la separación de flujos, dos obstáculos comunes en las simulaciones de flujo de fluidos, sin alterar la exitosa predicción de la ley de la pared del modelo original. Se definen y se introducen cuidadosamente dos términos de corrección en las ecuaciones de transporte del momento y la tasa de disipación específica (ω). Después de una amplia verificación numérica, los modelos mejorados muestran mejoras significativas en la predicción de flujos secundarios, el desprendimiento y unión de capas límite y los coeficientes de fricción para casos de entrenamiento y pruebas; reafirmando la fiabilidad y generalización *a posteriori* del método.

En conclusión, esta tesis doctoral presenta una metodología sólida y rentable para mejorar sistemáticamente el rendimiento de sistemas de ingeniería complejos basados en simulaciones de CFD. A su vez, se han desarrollado dos métodos para mejorar el modelado de turbulencia basado en enfoques progresivos e impulsados por datos. Al abordar desafíos relacionados con el desprendimiento de la capa límite y predicciones de flujos secundarios en geometrías complejas junto con técnicas de diseño y optimización morfológica, esta investigación contribuye a predicciones de flujo de fluidos más precisas y optimización basada en simulaciones. La sinergia entre el modelado basado en datos y la optimización de sistemas complejos demuestra el potencial de éstas soluciones innovadoras; resultando en amplias implicaciones en los sectores de la ingeniería académica e industrial.

Acknowledgments

This modest page is a dedication to 30 years of all the little pieces that have comprised my life until now; giving me a touch of three beautiful things: friendship, discovery, and love.

Growing up in beautiful Spain and living abroad allowed me to meet wonderful people from different backgrounds, developing both professionally and personally in ways that I could have never imagined. Hence, this thesis is not just a personal goal, but the consequence of meeting each and every person that has shared their precious time with me.

First and foremost, I would like to thank my main supervisors Mahdi Abkar and Martino Reclari. Their time and effort to always point me in the right direction, their ability to encourage me when I most needed it, and their patience to deal with my mistakes and somewhat, eccentric personality, have been invaluable. Thanks to my colleagues from the Quality & Sustainability Department at Kamstrup and my fellow Ph.D. students and friends at Aarhus University and Penn State University; who have always welcomed and shared with me this journey with kindness, patience, and great insights. Thanks as well to the rest of the flow group and technicians at Kamstrup, who have always been open to building all my crazy ideas for my experiments and allowed my mess in the laboratory.

Exceptional gratitude goes to my good friends Daniel Fiuza and Dominique Alonso who, apart from sharing their time, ups, downs, holidays, and this doctoral path with me; made me a better person and always motivated me to achieve higher goals — although we all know that the path to reach those goals has not always been easy.

With a special mention to my friends; the ones in Denmark, who became a family to me and kept me sane all these years (if I have ever been at all); and thank you to my friends abroad, since it does not matter the distance that separates us, you have always prioritised our friendship and never said no to a fantastic time with a beer (or two) on a beautiful terrace. I am fortunate enough to not have enough space on this page to name all the especially wonderful people who are part of my life, although, at the same time, I feel that there is no need, because you my dear friends, already know how grateful I am to have you. That is why these words are for all of you, friends: we are so lucky; we have shared so many stories, so many travels, so many parties, so many adventures, and we still have each other after all this time. Let us not forget the most important thing, we have so many more experiences to undergo together.

Last but not least, I would like to thank my family, for their continuous support and encouragement in the pursuit of my dreams, even if those dreams placed me far away from them. Home is where the heart is, and our beautiful town Segovia has never left my heart because you are there.

I am who I am because of all of you, and this thesis would not have been possible without any of you. Thank you.

Mario Javier Rincón

Preface

This Ph.D. thesis represents the work conducted in three years of research efforts from November 2020 to November 2023 during the industrial Ph.D. program at the Graduate School of Technical Sciences (GSTS) at Aarhus University and Kamstrup A/S in Denmark. At Aarhus University as the main academic institution of this project, most of the research work was carried out at the Department of Mechanical and Production Engineering within the section of Fluids and Energy inside the Fluid Mechanics & Turbulence research group and under the supervision of Associate Professor Mahdi Abkar. From Kasmtrup A/S as the industrial institution, the research work was carried out at the Department of Quality & Sustainability within the Metrology and Flow Laboratory group and under the supervision of Dr. Martino Reclari, and co-supervision by Dr. Jens Lykke Sørensen. Additional collaborations were also established with Associate Professor Xiang I. A. Yang from the Department of Mechanical Engineering at Pennsylvania State University.

This Ph.D. thesis elaborates on the development of a methodology to enhance current turbulence models by data-driven methods and accurately predict the flow of ultrasonic flow meters while optimising their design and operation. The outcomes of the project have yielded 4 scientific publications in the area of fluid mechanics with their application to ultrasonic flow metering. Additionally, several contributions to the area of data-driven turbulence modelling have been made with 2 scientific publications. In all these publications, this thesis' author is the main contributor.

The thesis is written as a cohesive monograph constituted by: a combination of an extended introduction to the research topics and state-of-the-art, a description of the proposed research questions, the most relevant published manuscripts during the Ph.D. project, conclusions, future perspectives in the researched area, and some final reflections by the author.

Recognition of funding and grants

This thesis is supported by Innovation Fund Denmark (IFD) under Grant No. 0153-00051B and Kamstrup A/S. The author would also like to acknowledge the EuroHPC Joint Undertaking for awarding this project access to the EuroHPC supercomputer LUMI, hosted by CSC (Finland) and the LUMI consortium through a EuroHPC Regular Access call. This work was also partially supported by the Danish e-Infrastructure Cooperation (DeiC) National HPC under grant number DeiC-AU-N2-2023006.

Reading guide

The contents of the individual chapters in this dissertation with published manuscripts are introduced with an abstract summarising the contents of the chapter and a reference to the original published work. References throughout the dissertation are listed at the end of the main document. The standard numbered style denounces the references, hence a citation is referred to by [Number]. Bibliographical citations appear at the end of the document where journal and proceedings papers are referred by author, article title between quotes, and journal names in *italics*. Books are referred by author, title in *italics*, publisher, edition,

and year; while websites are referred by author, title, year, URL, and time of last visit. Figures, tables and equations are numbered according to the particular chapter they are placed in where uppercase Roman numerals number chapters. Therefore, the first figure in chapter three is assigned with figure number III.1 and the second III.2 etc. Descriptive captions for tables are found above relevant tables and captions for figures are found under relevant figures. Additional explanatory concepts are added with footnotes, labelled with $*$, †, ‡ and so forth.

The thesis is divided into 9 chapters. The first one introduces the general topic and motivates the importance of ongoing research activities in the field. The bulk of the dissertation is a compilation of several manuscripts that include both published peer-reviewed documents and submitted manuscripts that are under review and awaiting final publication at the time of submission of this thesis. The manuscripts are identical to their published versions with the exception of minor typo corrections, and minor adjustments in the figures to increase their quality and adjust them to this thesis' format. The final two chapters disclose the main conclusions of the research outcomes, identify future work in the research field to be done, and closing this thesis with some words from the author. A common denominator of all chapters is that they contribute to an enveloping class of research on fluid mechanics, experimental validation of methods, complex optimisation techniques, and data-driven turbulence modelling.

Dissemination activities

As a Ph.D. candidate, one has the pleasure of disseminating parts of their research outcomes on several occasions. In addition to several internal presentations within associated research and industrial groups, part of lectures and supervision for master's level students, and co-supervision of interns; the following list includes memorable dissemination in terms of presenting this work at diverse scientific conferences and events:

- Danish Society for Industrial Fluid Dynamics (DANSIS) Symposium on Workflows – Parametrisation, Integration and Automation. October 2021. Copenhagen, Denmark.
- 74$^{\text{th}}$ Annual Meeting of American Physical Society (APS), Division of Fluid Dynamics (DFD). November 2021. Phoenix, Arizona, USA.
- 18$^{\text{th}}$ Internal Symposium of the Danish Center for Applied Mathematics and Mechanics (DCAMM). March 2022. Sønderborg, Denmark
- 8$^{\text{th}}$ European Congress on Computational Methods in Applied Sciences and Engineering (ECCOMAS). June 2022. Oslo, Norway
- 7$^{\text{th}}$ Congreso Nacional de Metrología. September 2022. Ávila, Spain.
- 75$^{\text{th}}$ Annual Meeting of American Physical Society (APS), Division of Fluid Dynamics (DFD). November 2022. Indianapolis, Indiana, USA.
- 22$^{\text{nd}}$ IACM Computational Fluids Conference (CFC 2023). April 2023. Cannes, France.
- Danish Society for Industrial Fluid Dynamics (DANSIS) Symposium on Turbulence: New Views on an Old Challenge. May 2023. Copenhagen, Denmark.
- 14$^{\text{th}}$ Ercoftac Symposium on Engineering, Turbulence, Modelling and Measurements (ETMM14). September 2023. Barcelona, Spain.

Including co-supervision of the following M.Sc. theses:

- M.Sc. Thesis supervision: *Shape Optimization of Obstacles in Channel Flows* by Johan Lobner. February 2021 - June 2021.
- M.Sc. Thesis supervision: *Stratified flow in hot-water pipes* by Mathias Brønderup Christiansen. February 2022 - June 2022.
- M.Sc. Thesis supervision: *Numerical and experimental investigation of complex internal flows: Validation of the dynamic range and analysis of physical installation effects on ultrasonic flow meters* by Anders Caspersen and Nicolai Thorenfeldt Ingwersen. February 2023 - June 2023.

List of publications

The following scientific manuscripts included in this thesis (in chronological order of submission) have been published during the Ph.D. period or are under review by the time of submission of this thesis:

- **M. J. Rincón**, M. Reclari, and M. Abkar (2022). "Turbulent flow in small-diameter ultrasonic flow meters: A numerical and experimental study," *Flow Measurement and Instrumentation*, 87, 102227.
- **M. J. Rincón**, M. Reclari, X. I. A. Yang, and M. Abkar (2023). "Validating the design optimisation of ultrasonic flow meters using computational fluid dynamics and surrogate modelling," *International Journal of Heat and Fluid Flow*, 100, 109112.
- **M. J. Rincón**, M. Reclari, X. I. A. Yang, and M. Abkar (2023). "CFD-aided morphing and design optimisation of ultrasonic flow meters," The *14^{th} ERCOFTAC Symposium on Engineering Turbulence Modelling and Measurements*, 109-114.
- **M. J. Rincón**, A. Amarloo, M. Reclari, X. I. A. Yang, and M. Abkar (2023). "Progressive augmentation of Reynolds stress tensor models for secondary flow prediction by computational fluid dynamics driven surrogate optimisation," *International Journal of Heat and Fluid Flow*, 104, 109242.
- A. Amarloo, **M. J. Rincón**, M. Reclari, and M. Abkar (2023). "Progressive augmentation of turbulence models for flow separation by multi-case computational fluid dynamics driven surrogate optimization," *Physics of Fluids*, vol.35, p. 125154, 12 2023
- **M. J. Rincón**, A. Caspersen, N. T. Ingwersen, M. Reclari, and M. Abkar (2024). "Flow investigation of two stand ultrasonic flow meters in a wide dynamic range by numerical and experimental methods," *Flow Measurement and Instrumentation*, vol. 96, p. 102543, 2024.

AARHUS UNIVERSITY
DEPARTMENT OF MECHANICAL AND PRODUCTION ENGINEERING

Aarhus University
Department of Mechanical and Production Engineering
Katrinebjergvej 89 G-F
8200 Aarhus N, Denmark
https://www.mpe.au.dk

Thesis submitted:

October 31st, 2023

Author:

Mario Javier Rincón
mjrp@mpe.au.dk
mjrp@kamstrup.com

Pages: 146
Appendices: None

Supervisors:

Mahdi Abkar
Associate Professor
Head of Section of Fluids & Energy
Department of Mechanical and Production Engineering
Aarhus University
abkar@mpe.au.dk

Martino Reclari
Head of Metrology & Accreditation
Department of Quality & Sustainability
Kamstrup A/S
marr@kamstrup.com

Project colaborators:

AARHUS UNIVERSITY
kamstrup
PennState
EuroHPC Joint Undertaking
DeiC
Innovation Fund Denmark

Contents

List of Figures

List of Tables

Nomenclature

$\alpha^{(n)}$	Data-driven enhancement function
$\alpha_{s,c}$	Geometrical angles for step and constriction
β	Deterministic model
Δp	Pressure drop
δ_{ij}	Kronecker delta
$\dot{Q}$	Volumetric flow rate
ϵ	Associated uncertainty
$\hat{e}$	Unitary vector in the sound wave propagation direction
$\hat{n}$	Surface normal displacement
$\hat{y}$	Objective function from surrogate prediction
λ	Wavelength
λ_2	Vortical structures visualisation criterion
λ_i	Power activation function parameter
$\mathcal{B}_i$	Normalised candidate function
$\mathcal{D}$	Desing optimisation space
$\mathcal{D}_i$	Absolute candidate function
$\mathcal{F}_2$	Modified version of flow meter uncertainties
$\mathcal{K}$	Number of optimisation design variables
$\mathcal{X}$	Separation model activation function
μ	Mean
ν	Kinematic viscosity
ν_t	Turbulence viscosity
Ω	Reflected sound-path volume
ω	Specific turbulence dissiparion rate
Ω_{ij}	Rotation rate tensor
ω_i	Vorticity

Φ	Cumulative distribution function
ϕ	Probability distribution function
σ	Standard deviation
Re	Reynolds number
θ_i	Absolute data-driven optimisation constant
θ_l	Surrogate correlation scalar
ε	Turbulence dissipation rate
φ_j	Principal component
A_{ij}	Anisotropic part of the Reynolds stress tensor
b_n	Design variable set
C_μ	$k-\omega$ SST model specific constant
C_i	Normalised data-driven optimisation constant
D	Diameter
$E[I]$	Expected improvement function
E_k	Kinetic energy
F_2	$k-\omega$ SST model blending function
F_{sep}	Separation factor
H	Characteristic height
h	Height
I	Turbulence intensity
I_i	Flow invariant
J	Global objective function
j_i	Objective function
k	Turbulence kinetic energy
k^+	Dimensionless turbulence kinetic energy of the grid cells to wall
L	Length
n	Number of test observations
P	Modified kinematic pressure
p	Kinematic pressure
P_k	Turbulence kinetic energy production

R	Spatial correlation function
r^2	Pearson's linear correlation coefficient squared
R_{ij}	Reynolds stress tensor
S	Cross-sectional surface
S_{ij}	Strain rate tensor
T	Temperature
t	Time
T_{ij}^n	Flow basis tensor
u	x-component of velocity
u^+	Dimensionless velocity of the grid cells to wall
u_τ	Friction velocity
u_c	Characteristic velocity
u_i	Velocity vector
V	Volume
v	y-component of velocity
w	z-component of velocity
y^+	Dimensionless distance of the grid cells to wall
Z	Stochastic realisation process

I

Introduction & Motivation

In the world of today, where sustainability and conservation are of paramount importance, the responsible use of our planet's resources has become an urgent matter. Water and energy, in particular, are precious commodities that require careful management to ensure their availability for future generations. Specifically, an increasingly large portion of the world's population is experiencing water scarcity due to direct human impact on the environment, resulting in extreme weather conditions, and increasing demand due to the accelerated population growth [1, 2]. Recognising this critical need and in order to avert a global crisis, the water supply chain must adapt to this landscape by embracing and accommodating the newest advancements in technology and engineering [3].

The water supply chain involves a significant amount of stakeholders from retrieval, treatment, and distribution; and while all stakeholders should incorporate changes, some of them show a significantly higher influence on the overall supply chain efficiency than others. One of the key stakeholders is the water distribution network, where a global average of 30% of the water in the network does not reach its destination. All unregistered water loss not accounting in the system input volume is known as Non-Revenue Water (NRW) [6]. Specifically, in the countries of the European Union (EU), 25% of the water distribution is NRW, where leakages are the cause of 71% of this water loss (Fig. I.1) [4, 5]. The main factor in the appearance of leakages is the ageing and deterioration of the network, which is solved by replacing pipe segments. Particularly, in Europe, the water infrastructure is suffering from low replacement rates, hence, effectively and accurately localising and preventing leakages is a major task to reduce NRW and make a paramount impact on the supply chain as a whole [7].

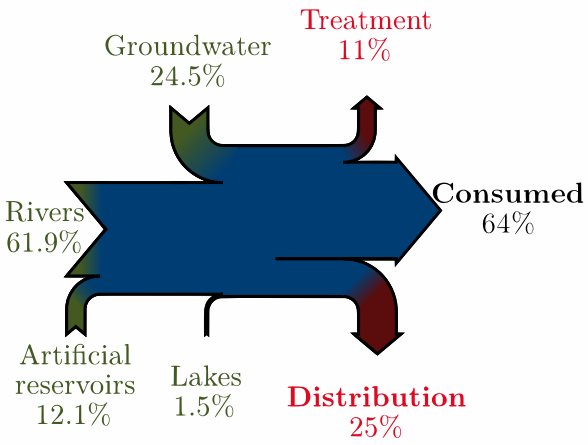

Figure I.1: Water supply chain sources (green) and losses (red) of the EU in 2023 [4, 5].

Currently, water scarcity and the rising demand for energy have spurred the development of innovative technologies to monitor and control resource consumption. In this regard, there is a leading solution to minimise NRW through continuous network monitoring and data analytics: installing flow meters at designated locations in the network (Fig. I.2).

Ultrasonic flow meters have emerged as a promising solution due to their non-invasive nature, high accuracy, and versatility. While metering has been proven to be an effective approach to identifying leakages, a great number of devices are required to precisely pinpoint leakage locations, comprehend consumption patterns, identify anomalies, and ultimately, formulate strategies for consumption reduction. In the past, the only available cost-efficient

solution has been the installation of flow meters at important locations (e.g. representative junctions) due to the high cost and impact of flow meters on the network. Nevertheless, in recent years, compact versions of traditional flow meters for water measurements have been democratised (making the technology cost-efficient) and widely installed even at an individual residence level. However, the high number of installed devices accounts for a significant pressure loss and influence in the network that cannot be disregarded [8]. It is then clear that leveraging the potential of ultrasonic flow meters to optimise water and energy usage is of paramount importance.

Figure I.2: Example of metering on a distribution network. Each coloured point is a flow meter displaying the network data where red points show there is an issue in the network. Figure adapted from [9].

Efficient water and energy management goes beyond mere deployment and measurement. Understanding the causes of patterns and anomalies in the network is recognised to be vital to mitigating losses. Hence, understanding the flow physics within ultrasonic flow meters is likewise essential for improving the design and operation of not only these systems but the water grid as a whole. By investigating the intricacies of fluid behaviour within these devices, it is possible to uncover insights that lead to enhanced accuracy, increased reliability, and optimised performance. However, in order to push the boundaries of flow meter technology, a multidisciplinary approach is required by the combined efforts of engineering principles, computational modelling, and data analysis.

The insights gained from investigating flow physics within ultrasonic flow meters by the combined efforts of academia and industry unlock new possibilities for conservation and inspire further advancements in resource management practices. Therefore, this thesis aspires to contribute to a more sustainable future by unveiling the flow complexities of ultrasonic flow metering, providing the knowhow to improve these systems, and as a consequence, reducing water and energy consumption, alleviating the strain on resources, and minimising the significant environmental footprint associated with their losses.

I.1 State-of-the-art

To fulfil these objectives, several fields of knowledge must be reviewed and applied synergetically. To this end, understanding *ultrasonic flow metering* technology allows the accurate simulation modelling of these systems and evaluation of their key parameters; the application of *computational fluid dynamics* allows the prediction of flows in complex environments, providing quantifiable metrics; *turbulence modelling* accelerates the computational time required to obtain numerical results in turbulence flows while maintaining accuracy; and *optimisation* techniques allow the use of the obtained results to improve the design and operation of ultrasonic flow meters. Therefore, these fields of knowledge are hereby reviewed, providing a comprehensive summary of the latest research.

I.1.1 Ultrasonic flow meters

Several water meter types are available in the market, however, in terms of cost, low-pressure drop, and easy operation; transient-time ultrasonic flow meters are currently a state-of-the-art, versatile, and efficient choice. Since 1955 (when there was arguably a single manufacturer in the world trying to democratise ultrasonic metering), more than fifty manufacturers mass-producing *all* types of ultrasonic flow meters joined the market [10]. The functioning principle of these devices relies on the propagation of ultrasounds to measure the flow rate of water moving through a pipe. The most widespread working principle for ultrasonic flow meters is the transient time method, where two ultrasound waves are sent and received by transducers. The speed of the sound wave varies due to its interaction with the fluid medium and that time differential makes it possible to predict the volumetric flow [11]. Traditionally in large-diameter pipes, the meter configuration allows the sound to travel in a straight line throughout the pipe diameter and the time of flight calculation is straightforward [12]. Nevertheless, as this technology advances and adapts, more complex and accurate techniques such as multi-path and off-diameter sound paths are more commonly used.

The most widespread residential ultrasonic flow meter for small-diameter pipes is precisely a multi-path and off-diameter sound path flow meter, leading to the implementation of intrusive geometries (two-stand configuration) which interact with the flow. Most meters adopt this configuration if the size of the transducers is of the same order of magnitude as the pipe diameter (below DN40: $40\ \mathrm{mm}$ of internal diameter). Each of these stands is located up and downstream of a constriction where the measurement is taken and the sound wave travels. Here, the wave bounces at two reflectors placed on the stands and is directed towards the transducers. The main objective of this practice is to allow the sound wave to travel through the highest volume of the fluid possible and, therefore, obtain a more accurate measurement. However, the introduction of two stands in the pipe yields a highly complex flow behaviour inside the flow meter.

I.1.2 Applied computational fluid dynamics

Computational fluid dynamics (CFD) is the general term for various methods that aim at simulating the behaviour of fluids through calculation. Fluid motion generally displays chaotic and complex behaviour in terms of turbulence. The correct prediction of turbulence has been shown as one of the most complicated problems to solve in the field of physics and engineering for more than a century [13, 14]. In particular, the wide range of spatial and temporal scales of turbulence to solve involves very costly calculations. High-fidelity scale-resolving techniques such as large-eddy simulation (LES) and direct numerical simulation (DNS) involve substantial computational expenses, which makes their feasibility and application in industrial flows difficult to democratise nowadays [15]. Hence, CFD simulations mainly use turbulence modelling techniques such as Reynolds-averaged Navier-Stokes (RANS) to reduce computational costs. Consequently, several investigations utilise RANS to explore the impacts on flow meters caused by distinct inlet conditions and various configurations of bent pipes [16–19]. This approach even encompasses the evaluation of a portion of the operational dynamic range of single-path ultrasonic flow meters [20]. Studies on the effectiveness of CFD as a tool to analyse transducer location in multi-path ultrasonic flow meters without intrusive geometries have been reported in Ref. [21]. CFD has also been employed to study the effect of the header [22, 23] and flow conditioners in the steadiness of the flow for gas multi-path ultrasonic flow meters [24, 25]. Commonly, the literature compares numerical results against experimental data [26, 27], which is generally based on particle image velocimetry (PIV) to study possible design improvements and inflow configurations [28]. However, previous

publications only consider the interaction of diverse inflow conditions with a large-diameter ultrasonic flow meter without invasive geometries in the flow.

To date, the main assumption is to model the flow meter as a straight section of pipe. Hence, there has been a lack of reliable studies that numerically predict the interaction of the flow with an intrusive two-stand configuration ultrasonic flow meter in an accurate manner. In addition, previous research only focused on RANS turbulence modelling without exploring the eddy-resolving CFD methods.

I.1.3 Turbulence modelling

Accurately predicting turbulent flows within intricate environments remains a challenging task within RANS models [29], where their progress has exhibited a state of relative stagnation through several decades [30]. While recent advances in data-driven methodologies have initiated a surge of investigation aimed at refining the efficacy of these models [31], limitations in terms of generalisability constrain the applicability of data-driven models to more general contexts. A predominant thrust of these investigations involves harnessing high-fidelity Reynolds stress tensor (RST) data to train and correct models with the aim of augmenting outcomes derived from empirical models [32–37]. A distinct approach lies in CFD-driven models [38, 39], which have demonstrated promise in the pursuit of dependable RANS turbulence models due to their capacity to ensure coherence and robustness in their results. Unlike other data-driven models, CFD-driven models undergo optimisation within RANS simulations, thereby assuring the robustness of results by novel models. Meanwhile, models developed via model-consistent training strategies [40] have yielded promising outcomes for reliable RANS turbulence models. In these methodologies, model performance (i.e. *a posteriori* outcomes) is integrated into the training process, ensuring the capability of the final models' consistency and robustness. The incorporation of optimisation algorithms within CFD-driven techniques [38, 39] has demonstrated very promising performance in the discovery of new generalisable RANS models. Hence, the enhancement of common RANS models with robust optimisation and data-driven techniques seems to narrow the gap between the fast and accurate prediction of complex flows (such as the flow through ultrasonic flow meters) for further analysis and optimisation.

I.1.4 Optimisation

Coupling of CFD and optimisation techniques have been used extensively in the last 20 years as a powerful tool to find the best possible parameters (shape, operating condition, model variables, etc.) in industrial and academic applications alike [41]. Regarding optimisation, algorithms to find the minimum (or maximum) of one or more given functions in a multidimensional parameter space include slope followers, simplex methods [42], multi-objective evolutionary [43], and particle swarm algorithms [44] among others. An early recognised problem is that these methods require the evaluation of an objective function (i.e. performing a CFD computation) in a large number of test configurations, which require considerable computational resources. This leads to two distinct developments: the first one uses a relatively smaller set of CFD simulations (whose parameters are selected using specific methods [45, 46]) to create computationally cost-efficient models, known as surrogates or response surfaces [47], that are then fastly optimised. The second innovation is the adjoint method, where the adjoint equations are solved numerically to locally assess the effect of a change of parameters on the quality (in the specific sense of optimisation) of the solution [48, 49]. Optimised solutions are therefore obtained with fewer computations at the cost of increased

mathematical complexity. However, although the adjoint method has shown its maturity in the field of solid mechanics, its robust application to fluid and turbulent flow is still in its infancy [48]; by studies still using the frozen turbulence assumptions [50] or inexact meshes [51].

Nevertheless, the adjoint method in turbulent flow has gained popularity in external aerodynamics optimisation in aircraft [52–54], automotive applications [55, 56], and conjugate heat transfer [57] among others. In numerous research studies, design and shape optimisation techniques have been employed to enhance the forms of various engineering applications. These investigations are primarily conducted in scenarios where structured grids are conventionally utilised, as seen in canonical flow cases and simplified external aerodynamics [58]. This choice of applications facilitates adaptable and accessible mesh manipulation. However, within the literature, there exists a notable gap in comprehensive studies concerning internal flow and intricately constrained problems that involve the utilisation of unstructured grids, such as the case of ultrasonic flow meters. Furthermore, a thorough examination of outcomes achieved through these methodologies is lacking. Therefore, no concerted and sustained effort has been made to develop a multi-objective optimisation strategy based on verified and validated numerical CFD predictions, taking into account the main factors defining system performance, and being able to provide solutions for diverse optimisation methodologies.

I.2 Research questions

This thesis, therefore, aims to develop the methodologies to accurately evaluate and validate the flow through two-stand ultrasonic flow meters and to optimise current ultrasonic flow meters by means of fluid mechanics alone. To this end, the following research questions are to be answered:

1. Is it possible to accurately predict the flow in ultrasonic flow meters by numerical methods?

2. Is it possible to optimise ultrasonic flow meters with a fast and robust numerical methodology based on fluid mechanics?

3. Can RANS models be enhanced by data-driven approaches in a generalisable manner?

I.3 Project structure

To answer the research questions, this thesis is structured as a cohesive compilation of different scientific publications dealing with unique objectives. The first chapter introduces the research and lays the foundation for its motivation. The second chapter of this thesis studies the development of a numerical methodology based on CFD to accurately predict turbulent flows in flow meters. The third chapter expands on the validation of previous methods to ensure an accurate flow prediction for the whole dynamic range of operation of the system. The fourth chapter develops a design optimisation methodology to improve the original flow meter based on key geometrical parameters whereas the fifth chapter applies adjoint optimisation methods and mesh morphing to further improve the flow meter designs obtained in chapter four. The sixth and seventh chapters develop and apply a methodology based on the previous optimisation strategies, to enhance turbulence modelling; chapter six focuses on the prediction of secondary flows while chapter seven focuses on the accurate prediction of separated flows. The eighth chapter summarises the findings, answers the

proposed research questions, and provides insights into the future research prospects in the field. Lastly, the ninth and final chapter concludes this thesis with some words and reflections from the author.

II

Turbulent Flow in Ultrasonic Flow Meters

Turbulent flow in small-diameter ultrasonic flow meters: A numerical and experimental study

ABSTRACT Small-diameter ultrasonic flow meters present an interesting industrial internal-flow problem due to their unique geometry and complex interaction with fluid flow. In order to efficiently evaluate and optimise these flow meters, their flow physics must be accurately understood and predicted. In this study, computational fluid dynamics is used to predict the turbulent flow inside a residential ultrasonic flow meter with an intrusive two-stand configuration. Reynolds-averaged Navier-Stokes (RANS), with $k-\varepsilon$ and $k-\omega$ SST turbulence models, are evaluated in a wall-modelled and a wall-resolved grid. The simulation results are compared against laser Doppler velocimetry, pressure drop, and vortices visualisation experiments in both qualitative and quantitative manners. Numerical results qualitatively agree with experimental data although some discrepancies are predicted by the $k-\varepsilon$ model. Overall, the results that best predict the flow structures, axial velocity, and pressure drop are achieved by wall-resolved RANS $k-\omega$ SST model. While minor differences are predicted by the wall-modelled $k-\omega$ SST, it is concluded that this approach is a good candidate for performing time-efficient studies due to the reduced computational cost.

REFERENCE [59]: M. J. Rincón, M. Reclari, and M. Abkar (2022). "Turbulent flow in small-diameter ultrasonic flow meters: A numerical and experimental study," *Flow Measurement and Instrumentation*, 87, 102227.

II.1 Introduction

Ultrasonic flow meters are highly accurate instruments that rely on the propagation of ultrasounds to measure the flow rate of moving fluid through a conduit [11]. Compared to non-ultrasonic technology, ultrasonic flow meters have several advantages: the equipment is easy to handle and install; the flow regime can be laminar, transitional, or turbulent; pressure drop is reduced; measurement accuracy, under favourable conditions, can be as low as 0.5%; purchase, operating, and maintenance costs are very reasonable, and the fluid can be single or multi-phase [60].

One of the most widely used instruments of this family is residential ultrasonic meters for water measurement. These flow meters work following the transient time method where two ultrasound waves are sent and received by transducers. The speed of the sound wave varies due to its interaction with the medium, making it possible to predict the volumetric flow based on the time differential. Traditionally, in ultrasonic flow meters, the sound can be assumed to travel in a straight line where the velocity profile along the sound path line is integrated, providing a difference in time of flight which is used to estimate the flow rate [12].

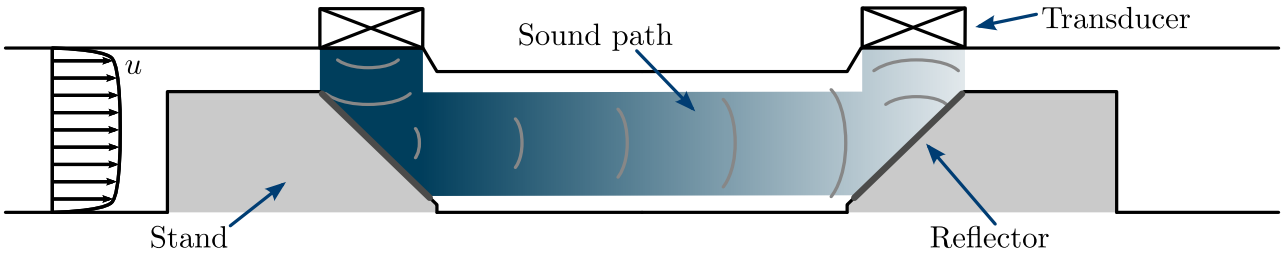

Figure II.1: Schematic of a reflected sound-path two-stand ultrasonic flow meter.

Nevertheless, as the technology advances, more advanced techniques such as multi-path and reflected sound-path (where the sound is redirected by reflectors inside the pipe between transducers) are more commonly used to obtain a more accurate measurement [61].

In terms of fluid mechanics, an ultrasonic flow meter with these characteristics presents an interesting wall-bounded flow problem. Understanding and evaluating how these devices work from a fluid mechanics perspective allows for confidently evaluating and optimising residential flow meters for diverse inlet flow conditions and minimising the load on the network. To obtain so, numerical methods with computational fluid dynamics (CFD) are an efficient candidate to predict the fluid flow in these devices.

Among previous studies in this area, CFD simulations are commonly used to study the inlet effects for various bent pipe configurations [16]. Studies on the effectiveness of CFD as a tool to analyse transducer location in reflected sound-path ultrasonic flow meters without intrusive geometries have been reported in [21]. CFD has also been employed to study the effect of a header [22, 23] and flow conditioners in the steadiness of the flow for gas reflected sound-path ultrasonic flow meters [24, 25]. Commonly, the literature compares numerical results against experimental data [26, 27], which is generally based on particle image velocimetry (PIV) to study possible design improvements and inflow configurations [28]. However, previous publications only consider the interaction of diverse inflow conditions with a large-diameter ultrasonic flow meter without invasive geometries in the flow. Up to date, the main assumption is to model the flow meter as a straight section of pipe, hence, there has not been any reliable study that numerically predicts the interaction of the flow with an intrusive two-stand configuration ultrasonic flow meter.

In this study, CFD tools with different Reynolds-averaged Navier-Stokes (RANS) turbulence modelling are analysed together with experimental methods to verify and validate the flow prediction throughout the flow meter. Unsteady RANS and other high-fidelity methods such as large-eddy simulation (LES) are not considered due to their high computational costs. Laser Doppler velocimetry (LDV), pressure drop, and vortical flow structure visualisation experiments are chosen to perform this validation. Section II.2 presents the numerical and experimental methods and their theoretical background used to predict the flow. Section II.3 shows and discusses the results obtained together with a quantitative and qualitative verification of the methods. Finally, a summary and discussion of the findings are presented in Section II.4.

II.2 Methodology

The governing equations used in this study are the incompressible form of Navier-Stokes equations, excluding heat transfer. These are written following Einstein's summation convec-

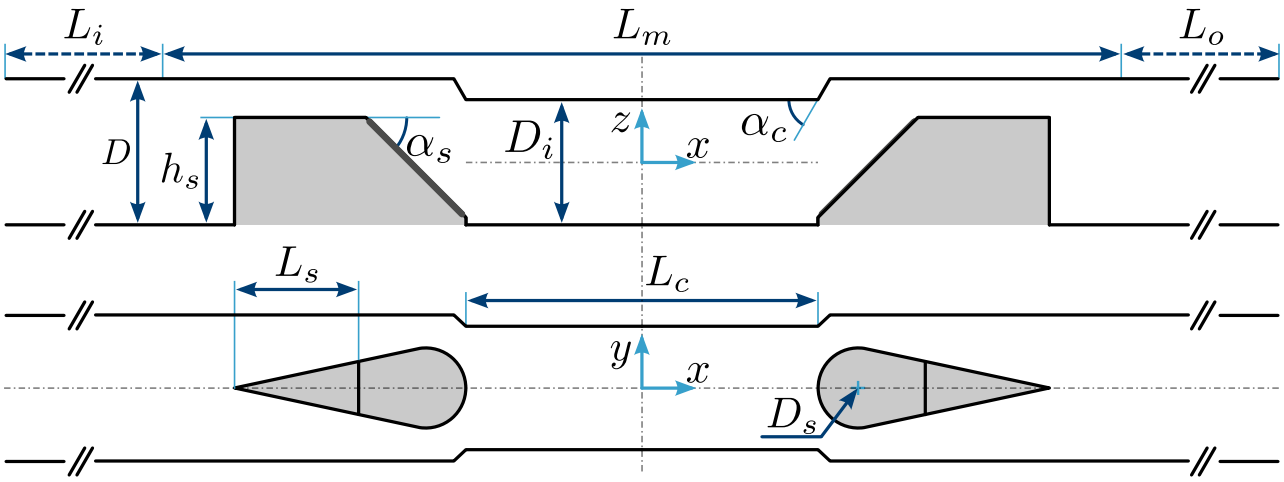

Figure II.2: Parametric description of chosen flow meter geometry for y-normal (top), and z-normal (bottom) planes. Note that sharp edges at the stands are filleted with a constant radius of $1\ \mathrm{mm}$ in order to ease the extrusion layer generation of the grid. Furthermore, note that the origin of coordinates is located at the mid-point of the constriction section.

tion in their convective form [62] as

$$\frac{\partial u_i}{\partial x_i} = 0, \tag{II.1a}$$

$$\frac{\partial u_i}{\partial t} + u_j \frac{\partial u_i}{\partial x_j} = -\frac{\partial p}{\partial x_i} + \nu \frac{\partial^2 u_i}{\partial x_j \partial x_j}, \tag{II.1b}$$

where x_i is the i^{th} axis in Cartesian coordinates with $i = 1, 2, 3$ corresponding to the streamwise (x), lateral (y), and vertical (z) directions, respectively. $(u_1, u_2, u_3) = (u, v, w)$ are the components of the velocity field. t is time. p is the kinematic pressure, and ν is the molecular kinematic viscosity. These equations are further developed to the RANS methods used in this study.

The RANS equations are developed by applying the Reynolds decomposition $u_i = \langle u_i \rangle + u_i'$ to Equations (II.1a) and (II.1b), where the angle $\langle \cdot \rangle$ operators represent the mean value in time and the prime superscript $\cdot'$ represents its fluctuating part. The RANS equations are, therefore, written as

$$\frac{\partial \langle u_i \rangle}{\partial x_i} = 0, \tag{II.2a}$$

$$\frac{\partial \langle u_i \rangle}{\partial t} + \langle u_j \rangle \frac{\partial \langle u_i \rangle}{\partial x_j} = -\frac{\partial \langle p \rangle}{\partial x_i} + \nu \frac{\partial^2 \langle u_i \rangle}{\partial x_j \partial x_j} - \frac{\partial \langle u_i' u_j' \rangle}{\partial x_j}, \tag{II.2b}$$

The Reynolds stress tensor $R_{ij} = \langle u_i' u_j' \rangle$ can be approximated by the Boussinesq hypothesis and obtain closure by the two RANS turbulence models applied in this study: $k - \varepsilon$ [63] and $k - \omega$ SST [64]. In this study, the equations of fluid motion are solved numerically by the general-purpose software OpenFOAM [65].

II.2.1 Computational domain and grids

A simplified version of a two-stand ultrasonic flow meter based on *flowIQ 2200* of the manufacturer Kamstrup A/S, is parametrised and generated with Computer-Aided Design (CAD). These ultrasonic flow meters estimate the volumetric flow rate with a correction curve determined by calibration instead of a processing equation. In addition, these meters take a flow measurement every 4 seconds and update their display every 30 seconds by integrating the previous measurements into a mean value. The simplified geometry is designed taking into consideration the difficulties of manufacturing and the areas that could lead to low-quality numerical grid generation. Hence, the geometry chosen in Figure II.2 exhibits a compromise between real flow meter fidelity, numerical, and experimental applications. The geometry is parametrised as shown in Table II.1 with a pipe diameter of $D = 20$ mm, consistent with the pipe diameter of the reference flow meter: Kamstrup *flowIQ 2200*.

Table II.1: Geometry parameters values and relationships. Note that the i, o, m, s, and c subscripts stand for inlet, outlet, meter, stand, and constriction respectively.

Parameter	Value
D	20 mm
D_i	$0.865D$
L_i	$5D$
L_o	$5D$
L_m	$9.5D$
L_c	$2.25D$
L_s	$1.25D$
D_s	$0.6125D$
h_s	$0.7785D$
α_s (rad)	π / 4
α_c (rad)	π / 3

Two types of hexahedral-based grids are used in this study: a wall-resolved and a wall-modelled grid. Both grids are compared in order to validate the methods and to select the best approach toward time-efficient numerical studies. Walls are considered perfectly smooth and the wall model used is based on the prediction of ν_t based on the turbulent kinetic energy (named *nutkWallFunction* in OpenFOAM). Moreover, a grid independence study based on RANS $k-\omega$ SST model is performed (see II.A) and symmetry boundary conditions are applied at the $x-z$ plane, hence, results are mirrored while post-processing the data to display the full pipe.

II.2.2 Initial and boundary conditions

A standard simulation for the nominal flow of the flow meter according to the industry standards is defined. Therefore, all numerical simulations performed in this study follow the same conditions:

a) Pure water as fluid medium.

b) Inlet volumetric flow of $\dot{Q} = 1.6\ \mathrm{m^3\,h^{-1}}$, equalling a uniform $u_{inlet} = 1.41\ \mathrm{m\,s^{-1}}$.

c) Inlet temperature of $T = 20\ ^\circ\mathrm{C}$, equivalent to $\nu = 1.00381 \cdot 10^{-6}\ \mathrm{m^2\,s^{-1}}$.

d) Linear limited divergence scheme with correction of the velocity gradient in interpolation weights ($\mathcal{O}^2$, conditionally bounded). This scheme is implicit, bounded, and second-order accurate to avoid stability restrictions [66, 67].

II.2.3 Inflow turbulent conditions

Following the best practices in CFD for internal-flow problems in circular pipes [68, 69], RANS initial turbulence conditions are calculated as follows,

Figure II.3: Rendered image of the test pipe and stands used in the experiments.

$$I = 0.16\mathrm{Re}^{\frac{-1}{8}}, \tag{II.3a}$$

$$k = \frac{3}{2}\left(u_{inlet}I\right)^2, \tag{II.3b}$$

$$\varepsilon = C_\mu \frac{k^{\frac{3}{2}}}{l}, \tag{II.3c}$$

$$\omega = \frac{\varepsilon}{C_\mu k}, \tag{II.3d}$$

where Re is the Reynolds number, l is the turbulent length scale ($l = 0.038D$ for internal-flows in circular pipes), and $C_\mu = 0.09$ is the turbulence model constant coefficient. Furthermore, in order to ensure fully developed flow conditions before the flow starts conditioning due to the upstream stand, the solution field is mapped at the inlet at a distance of $4D$.

II.2.4 Experimental methods

Current non-intrusive experimental methods such as PIV and LDV are capable of yielding qualitative and quantitative data with minimum influence on the flow. However, the experimental setup and flow conditions must be properly adapted to the methods to generate high-quality data. In this regard, a 1:1 pipe and stand set are manufactured. On the one hand, the pipe is manufactured by drilling a well-polished polymethyl methacrylate (PMMA) block in three operations; whereas additive manufacturing is chosen to fabricate the stand set. PMMA is chosen as a material in order to minimise the light diffraction between water and the material since both compounds have a similar refractive index ($n_{\text{water}} = 1.333$ and $n_{\text{PMMA}} = 1.4906$). On the other hand, the stands are fabricated with black Acrylonitrile Butadiene Styrene (ABS) powder. Finally, two passing holes are drilled in the pipe together with a thread in the stands to accurately fix them in place with screws (Figure II.3).

The pipe and stands are placed on a test bench with accurate control of volumetric flow and temperature of the flow, maintaining constant conditions throughout the tests. In order to perform the experiments, silver-coated glass-hollow neutrally-buoyant reflective particles of $15\ \mu\mathrm{m}$ in diameter are introduced in the string. Experiments yielding velocity data at x-normal planes are taken by means of LDV.

Regarding LDV, a 100 mW Nd:YAG (neodymium-doped yttrium aluminium garnet) laser of a wavelength of $\lambda = 532\ \mathrm{nm}$ is used to obtain the measurements, taking a minimum of 500 valid bursts per point. A 2D traverse unit (motorised and programmable in the y and z axis where the change in x direction is done manually) is likewise used to take with control

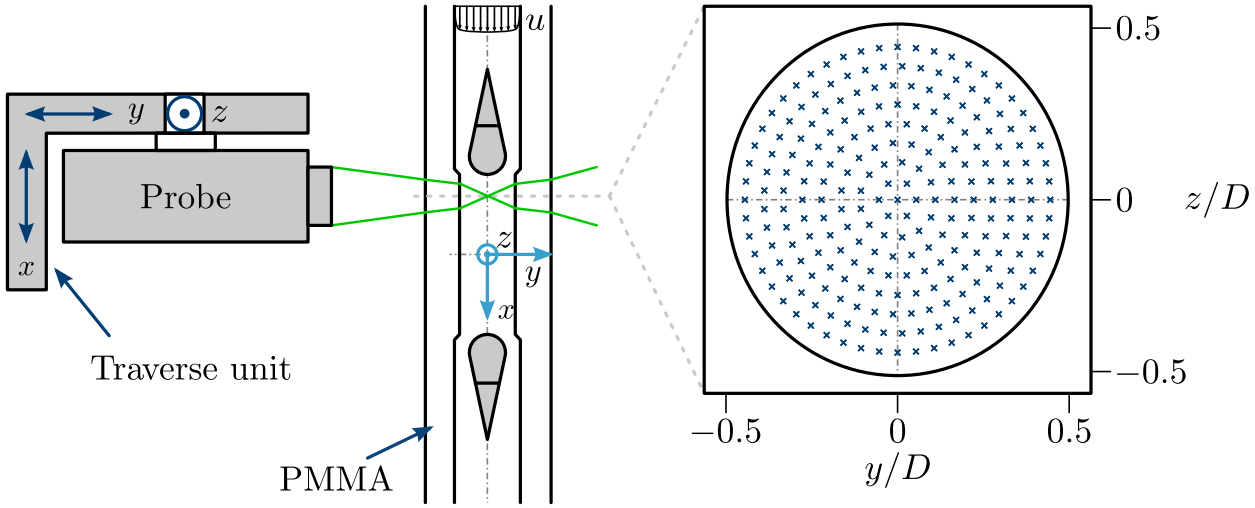

Figure II.4: LDV experimental setup schematic and cross-sectional data acquisition grid.

(a) Schematic.

(b) Laboratory setup.

Figure II.5: Vortices visualisation experimental setup.

the measurements at different points. A uniformly spaced grid of 232 points to evaluate the cross-sectional (x-normal planes) axial velocity is created (Figure II.4). To account for the light diffraction, raytracing methods are employed taking into consideration the media between the measurement points and the laser probe.

Moreover, pressure drop data is taken by two OMEGA PX429-100GI high accuracy pressure transducers with a measuring uncertainty of $\pm 0.08\%$ placed right up and downstream of the measurement pipe.

Finally, a valve is introduced into the test bench that allows the inclusion of controlled air bubbles in the flow. As depicted in Figure II.5, a manual ball valve controls the gas fraction into the water, allowing to visualise vortical structures at different levels of intensity. A flow conditioner is likewise placed downstream of the air insertion location in order to radially distribute the bubbles uniformly. Since the air bubbles coalesce at the low-pressure regions in the flow, a record of this phenomenon with a high-speed camera at 9000 fps is used to qualitatively analyse the problem and make a comparative study of the flow behaviour and vortical structures.

II.3 Results and discussion

Numerical and experimental results are hereafter depicted. Concerning numerical methods, the studied cases are divided by grid and turbulence model: RANS $k-\varepsilon$ and $k-\omega$ SST; wall-resolved and wall-modelled grids. Moreover, the pipe and stand walls are considered perfectly smooth in all cases regarding wall functions. The main objective of this study is to validate numerical results by discussing a series of depictions between methods. However,

since the studied case is non-canonical in the fluid mechanics field, it is necessary to describe and analyse the physics and flow structures involved beforehand. Therefore, a thorough comparative analysis is performed. The analysis is composed of, firstly, the description of the flow behaviour and structures in the system. Secondly, a pressure drop comparison of the flow for both numerical and experimental methods. Thirdly, a more detailed study is performed where a general qualitative study with velocity contours of the flow, is shown. Finally, a quantitative comparison of velocity profiles at regions of interest in the flow is presented. All results are similarly discussed and described followed by their corresponding figures.

II.3.1 Flow behaviour

The ultrasonic flow meter analysed is composed of a symmetrical 3D geometry along the $x-z$ plane. The two stands are identical and located immediately upstream and downstream of the constriction. This geometrical configuration is used in residential ultrasonic flow meters to obtain a consistent flow profile throughout the flow meter measurement volume, minimising inflow dependence without compromising pressure drop. In terms of flow mechanisms, three regions of the flow can be discerned:

- The upstream pipe.
- The upstream stand and constriction.
- The downstream stand and pipe.

In numerical solutions, sufficiently high and local pressure gradients in the flow yield vortical structures which can be predicted by vortex visualisation methods like the λ_2 criterion [70], whereas experimentally, the inclusion of air in the flow of water and its uniform distribution allows the visualisation of coalesced bubbles in the low-pressure regions where vortices are formed. The geometry of the system can be seen in Figure II.6, showing a depiction of the instantaneous and averaged images of the vortex visualisation experiments at different intensities as well as numerical λ_2 iso-surfaces.

Throughout the upstream pipe region, the fully developed turbulent flow evolves to an adjusted and slightly skewed profile towards the upper section of the pipe. This is the result of the constriction created by the presence of the upstream stand. The upstream stand region is composed of gradual and steep cross-sectional area changes due to the stand and reflector placement. Since cross-sectional gradients are not axially uniform throughout the stand, the flow is accelerated unevenly and high-velocity gradients in z-direction occur, yielding two symmetrical coherent structures in the form of vortices immediately downstream of the stand. These vortices propagate throughout the constriction yielding high vorticity regions. Subsequently, the flow interacts with the downstream stand. This region is greatly defined by the presence of an adverse pressure gradient. The geometry of the downstream stand disrupts the flow with a sudden section change followed by an elongated tail section. This causes boundary-layer detachment, high vorticity, and high shear; yielding complex flow conditions.

Regarding the experimental results, the instantaneous frame in Figure II.6 shows the uniform distribution of air bubbles and their size compared to the experimental setup. Some coherent structures can be visualised by the experiment. The low gas fraction case yields the visualisation of a higher vortex intensity and vice-versa. Both cases display the initial formation of vortices from the upper section of the upstream stand. In addition, the high gas fraction case likewise displays the roll-up of another vortex from the bottom sides of the

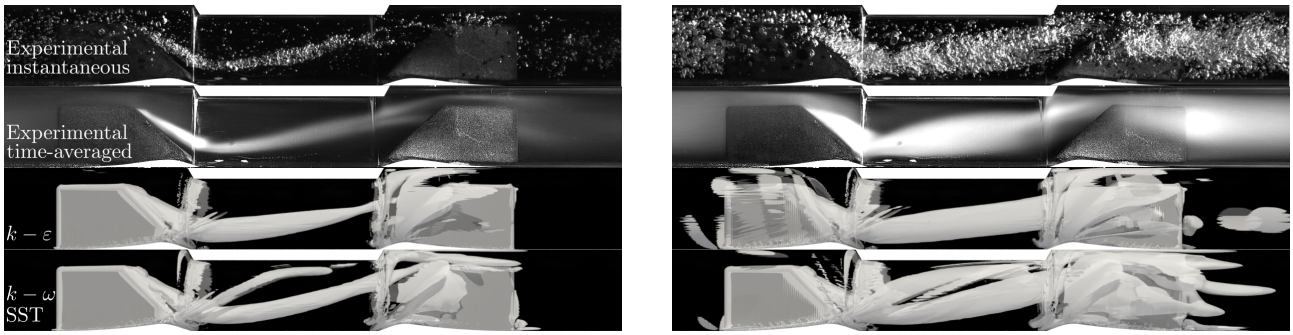

(a) (b)

Figure II.6: Vortices visualisation experiment with two different gas fractions (a and b). From top to bottom: instantaneous frame from the experiment, time-averaged image of the experiment, wall-resolved $k-\varepsilon$, and wall-resolved $k-\omega$ SST results respectively. The difference of gas fraction in the experiments is achieved by varying the amount of air in the pipe, where high-intensity (II.6a) and low-intensity (II.6b) vortices are visualised. Vortices intensity in the CFD simulations is defined by iso-surfaces of $\lambda_2 = 4 \cdot 10^4$ and $\lambda_2 = 10^5$ (II.6a); and $\lambda_2 = 10^4$ and $\lambda_2 = 3 \cdot 10^4$ (II.6b) for $k-\varepsilon$ and $k-\omega$ SST, respectively. Furthermore, the positive axial flow direction follows left to right.

upstream stand. These vortices evolve and diffuse upwards through the constriction to finally break and diffuse on the upper section of the downstream stand. Concerning the numerical λ_2 contours, both cases display a high degree of agreement with the experiments, where the location and shape of the vortices predominantly match. Nevertheless, $k-\varepsilon$ predicts a higher diffusivity of the vortices which deviates from the experiment.

The most characteristic flow structure in the system is the vortices throughout the constriction. Due to the importance of the constriction for the flow measurement in ultrasonic flow meters, performing a qualitative study of this pipe section is certainly important to ensure the validation of the numerical methods.

II.3.2 Pressure drop

The momentum loss as a consequence of shear stresses and pressure gradients due to fluid-solid interaction is characterised by the pressure drop (Δp). This parameter is a common quality metric for wall-bounded flows due to the importance of energy losses in internal-flow systems, metrology, and large pipe networks [71].

Diverse pressure drop experiments are performed where the radial position of the pressure transducers is changed ensuring results repeatability. One final experiment is performed after repeatability is ensured where 5 pressure measurements are taken each second during a long acquisition time of 75 minutes. Experimental and numerical results of Δp are shown in Figure II.7 where all results predict the pressure drop inside the standard deviation of the experiments. Whereas, $k-\varepsilon$ tends to over-predict Δp with values of 105.4% and 115.1% of the experimental mean for its wall-modelled and wall-resolved grids, respectively; $k-\omega$ SST shows better agreement with a prediction of 98.2% and 104.9% of the mean experimental value for its wall-modelled and wall-resolved grids, respectively.

Both numerical models and grids accurately predict pressure drop throughout the flow meter. RANS $k-\omega$ SST shows a better agreement, while RANS $k-\varepsilon$ tends to slightly over-estimate Δp.

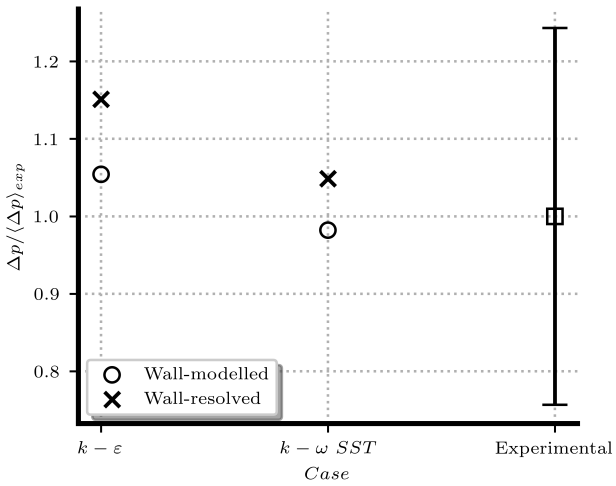

Figure II.7: Pressure drop comparison between RANS and experimental results. Experimental results show the mean value and standard deviation (σ) of the performed experiment. Note that RANS does not display any fluctuation due to the averaging operation of the method.

II.3.3 Velocity distribution

Axial velocity contours are shown in this section to perform a comparative analysis between experimental LDV data, and numerical methods. Figure II.8 shows axial velocity data for both LDV experiments and numerical methods at different cross-sections in the pipe.

Fully-developed turbulent pipe flow is predicted and measured by all methods at $x = -5D$ where minimal differences can be qualitatively seen. The vortices regions throughout the constriction and their propagation can be more clearly seen at $x \in [-1, 1]D$. The formation and propagation of these vortices drive the flow to accelerate towards the centre region of the pipe throughout the whole constriction. The latter effect can be distinctly seen at $x - 1D$. Furthermore, the vortices diffuse from the central bottom region towards the bottom-sides ($x = 0D$) and upper-sides pipe walls ($x = 1D$), elongating and stretching throughout the constriction. Since the constriction is not long enough for the flow to develop to be fully turbulent, the upstream stand influences the incident flow towards the downstream stand as seen at $x = 1D$. At this cross-section, both RANS models predict a similar axial velocity with a region of high velocity at the pipe centre and two symmetrical lower velocity regions towards the upper sides of the pipe, which is consistent with the experimental observation.

According to the results obtained, all numerical methods are capable of accurately predicting the majority of the flow in a qualitative manner. Minimal differences can be seen between the two grids evaluated, with the exception of the predicted vortices size by $k-\omega$ SST at $x = -1D$. Whereas RANS $k-\varepsilon$ predicts high diffusivity affecting the vortices propagation, $k-\omega$ SST predicts the flow more accurately with more defined shear layers in agreement with the LDV data.

II.3.4 Velocity profiles analysis

To deliver a precise and more complete study of the flow, the numerical and experimental axial velocity profiles along y for diverse x-normal planes are evaluated and compared as shown in Figure II.10. The profiles evaluated are depicted in Figure II.9 by the dashed lines at $z = [-0.2125, -0.125, 0.125]D$ respectively to $x = [-1, 0, 1]D$. The results of $WR\,k-\omega$ SST are chosen to define these locations since 1D LDV cannot reproduce sufficient data to locate the

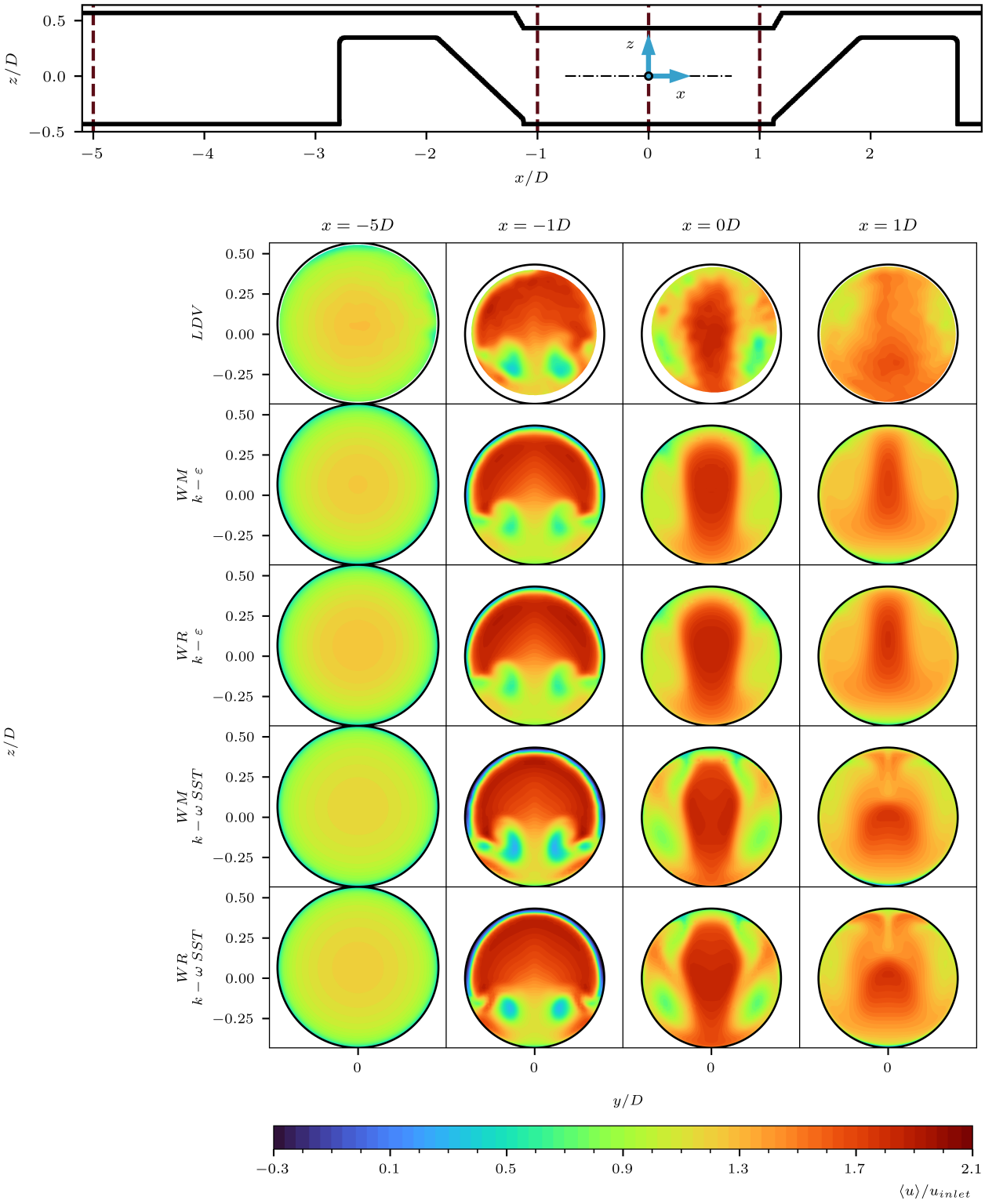

Figure II.8: LDV experimental results and CFD axial velocity contours at planes $x \in [-5, -1, 0, 1]D$. The abbreviations WM and WR stand for wall-modelled and wall-resolved grids respectively. Note the reference frame location at the constriction and the cross-sectional changes due to the system geometry throughout the streamwise direction.

vortices centres. These specific locations are chosen to compare the location and magnitude of the vortex regions, which are the most representative locations of the flow.

Minor asymmetries of LDV data can be seen in Figure II.10. Due to the low value of

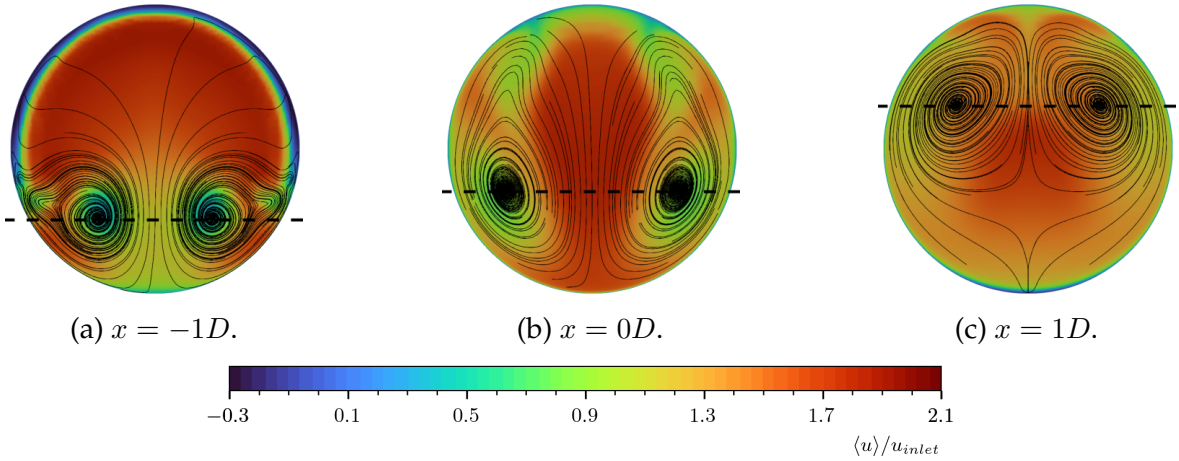

(a) $x = -1D$. (b) $x = 0D$. (c) $x = 1D$.

Figure II.9: Wall-resolved RANS $k-\omega$ SST surface streamlines and axial velocity profiles. Here the vortices locations at $z = [-0.2125, -0.125, 0.125]D$ are more obvious for $x = [-1, 0, 1]D$ respectively.

the pipe diameter ($D = 20$ mm), slight deviations in the experimental setup in terms of manufacturing and stand placement can affect the perfect symmetry of experimental results. Despite these experimental inaccuracies, experiments are ensured to be repeatable and accurate. At $x = -1D$ (Figure II.10a), five extrema are seen. Experimental results show a clear deficit of velocity as two minima at the vortices location, where three maxima are seen at the pipe centre and close to the walls. Both RANS methods and grids predict the velocity deficit in agreement with the experiments. However, only $k-\omega$ SST matches the magnitude of the experiments where $k-\varepsilon$ underestimates the velocity deficit. Regarding the three maxima, both numerical methods and grids agree with LDV data at the pipe centre, although only WR $k-\omega$ SST agrees with LDV data near the wall.

Experimental data at $x = 0D$ (Figure II.10b) shows a velocity maximum at the centre of the pipe and two minima consistent with the vortices locations at the near-wall regions. In this profile, both grids of $k-\omega$ SST agree at all locations with LDV data. However, although $k-\varepsilon$ likewise agrees with experimental data at the pipe centre, it overestimates the velocity at the near-wall regions where vortices are located. Furthermore, negligible differences in the velocity profiles between grids can be seen at this location.

At $x = 1D$ (Figure II.10c), LDV data shows a profile characterised by the presence of inflexion points, with a global maximum at the pipe centre. Experimental data at this location shows slightly higher asymmetry due to spurious reflections made by manufacturing constraints. Similarly to Figure II.10b, $k-\omega$ SST generally agrees with the experiments, where the wall-resolved grid shows the highest agreement. On the other hand, $k-\varepsilon$ overestimates the velocity overall and does not agree in terms of gradients with the experimental data for any of the grids analysed.

The velocity profiles at other locations are also analysed displaying results consistent with Figure II.10. Hence, for the sake of simplicity and space limitation, these are not shown. In summary, the RANS methods evaluated are able to predict the flow structures inside the flow meter constriction. In terms of axial velocity gradients and magnitude, however, $k-\omega$ SST agrees with experimental data more than $k-\varepsilon$. Overall, RANS $k-\omega$ SST is capable to predict much more accurately the vortices' locations and the axial velocity than $k-\varepsilon$, where wall-resolved $k-\omega$ SST does predict the flow inside 2σ experimental levels of uncertainty.

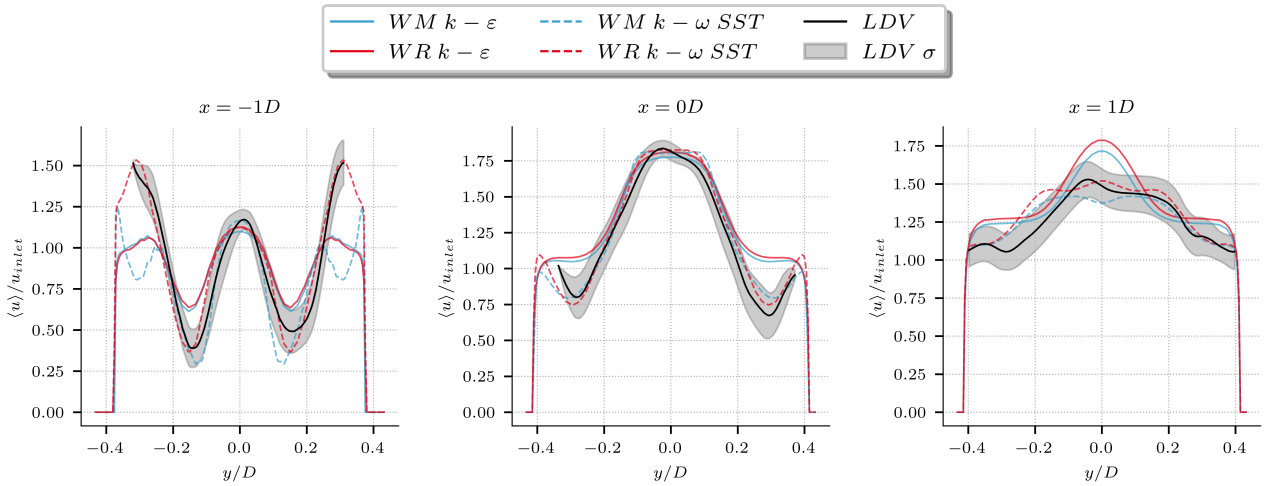

(a) (b) (c)

Figure II.10: Quantitative analysis of the velocity profiles at different locations in the flow meter. The dashed lines in Figure II.9 represent the evaluated locations of the different figures. Blue and red lines represent the methods using the wall-resolved or the wall-modelled grid, respectively.

II.4 Conclusions

This study showed the applicability of current CFD methods with diverse fidelity levels and their accuracy when tested in a simplified version of a reflected sound-path residential ultrasonic flow meter. The geometry analysed yields a complex internal-flow problem at a moderate Reynolds number of the order of 10^4. CFD with RANS $k-\varepsilon$ and $k-\omega$ SST turbulence models were evaluated. In addition, LDV together with pressure drop and vortices visualisation experiments were performed to verify and validate the numerical results both in qualitative and quantitative manners.

Both numerical models and grids studied were accurately capable of predicting the majority of the flow throughout the measurement region of the system although RANS $k-\omega$ SST showed an overall higher agreement with the experiments than RANS $k-\varepsilon$. Coherent structures in the form of vortices were predicted by all models, nevertheless, RANS $k-\varepsilon$ was not capable of correctly predicting the magnitude and propagation of lower-intensity vortices. Pressure drop was predicted by both models inside 2σ uncertainty margins where RANS $k-\omega$ SST yielded the highest agreement. Hence, the measurement region of the flow meter was consistently accurately predicted by $k-\omega$ SST.

Negligible differences in the predicted axial velocity were seen between the wall-resolved and wall-modelled grids for all methods, where the results on the wall-modelled grid were obtained with a factor of 25 times less computational time required than for the wall-resolved grid.

A summary of the findings is shown in Table II.2.

Finally, the work done in this study showed the robustness and accuracy of CFD methods against experimental data to predict complex wall-bounded flows. Future studies aim to optimise the internal geometry of the flow meter based on CFD by using wall-modelled $k-\omega$ SST as the most time-efficient and accurate method.

Table II.2: A summary of the comparison between different numerical methods and experimental data.

Grid	Turbulence model	$\Delta p/\langle\Delta p\rangle_{exp}$	Vortices propagation	Vortices magnitude	Velocity profiles
Wall-modelled	$k-\varepsilon$	1.054	Inaccurate	Underestimated	Relatively inaccurate
	$k-\omega$ SST	0.982	Relatively accurate	Relatively accurate	Relatively accurate
Wall-resolved	$k-\varepsilon$	1.151	Inaccurate	Underestimated	Relatively inaccurate
	$k-\omega$ SST	1.049	Accurate	Accurate	Accurate

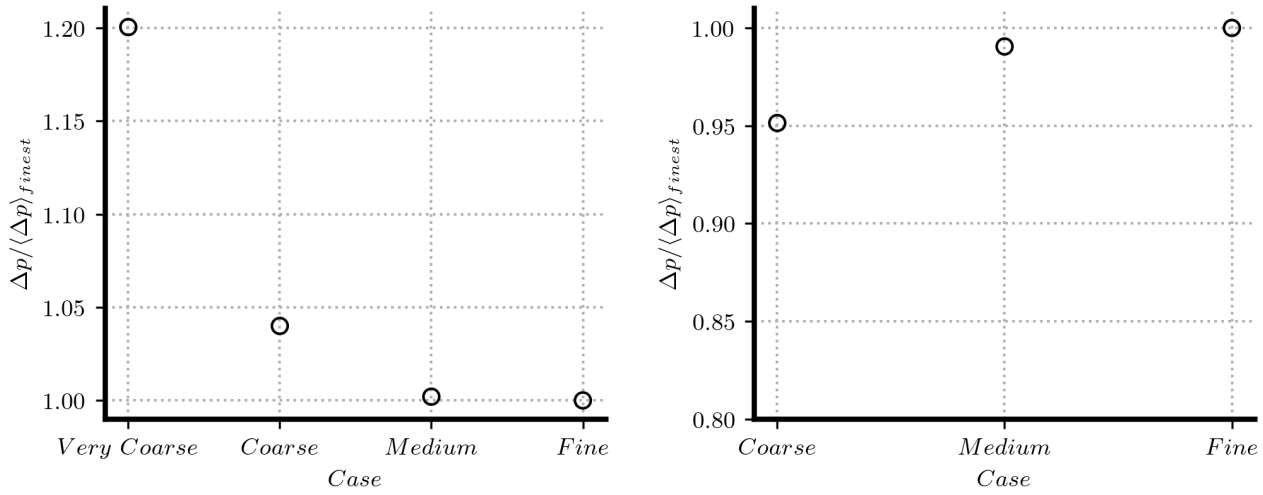

(a) Wall-modelled.

(b) Wall-resolved.

Figure II.11: Grid independence study represented as pressure drop in function of grid quality for RANS $k-\omega$ SST.

II.A Appendix — Grid independence

A grid independence study is performed with the criterion of obtaining pressure drop mesh independence for RANS $k-\omega$ SST turbulence model. The converged grid is likewise used for all RANS models to obtain an identical resolution comparison.

On the one hand, regarding wall-modelled simulations, a fixed 5-layer extrusion-mesh is defined with the first wall-adjacent cell thickness of $40\mu m$ and an expansion ratio of 1.25. The coarse grid is defined by 20 cells along the pipe diameter. Subsequently, refined grids are doubled in the number of cells. Figure II.11a shows the convergence of pressure drop through refinement cases. The *fine* mesh shows convergence with 2.07 million cells.

On the other hand, for the wall-resolved cases, a fixed 15-layer extrusion-mesh is defined with the first wall-adjacent cell thickness of $2.5\ \mu m$ and an expansion ratio of 1.1. To ensure an adequate cell-volume gradient between the bulk mesh and the extrusion layers, two oct-tree refinement levels of 3-cells wide are specified near the walls: refinement level 2 at $1\ mm$, and refinement level 3 at $0.5\ mm$ from all wall-type patches. Hence, refinement level 1 corresponds to the bulk mesh. The *coarse* grid is defined by 40 cells along the pipe diameter. Subsequently, refined grids are doubled in the number of cells.

Figure II.11b shows the convergence of pressure drop through refinement cases. The *fine* mesh shows convergence with 23.7 million cells.

III

Dynamic Range Validation

Flow investigation of two-stand ultrasonic flow meters in a wide dynamic range by numerical and experimental methods

ABSTRACT The enhancement of two-stand ultrasonic flow meters relies upon obtaining a precise understanding and prediction of their complex flow physics throughout their entire dynamic range of operation. This study provides a comprehensive numerical and experimental investigation of the flow physics of a typical two-stand ultrasonic flow meter by industry standards. Predictions based on computational fluid dynamics simulations are employed to obtain numerical results, which are validated through experiments based on laser Doppler velocimetry and static pressure drop. Results indicate that no qualitative changes occur beyond an inflow Reynolds number of 10^4 in terms of coherent structures and flow dynamics. Analysis of the static pressure distribution across cross-sections reveals that the stands are the most influential areas contributing to pressure drop. In cases with turbulent inflow, there is a noticeable recovery of static pressure following significant pressure gradients across the stands, while such recovery is absent in scenarios with laminar inflow. Both numerical and experimental approaches yield excellent agreement in outcomes, accurately estimating the axial velocity within the flow meter's measurement volume and the pressure drop across it, with deviations within experimental uncertainty ranges of 2 standard deviations. The developed numerical methodology demonstrates its potential to accurately evaluate complex internal-flow systems with similar flow features and Reynolds number ranges. The flow dynamics for a wide dynamic range of operation in two-stand ultrasonic flow meters are shown in detail in both laminar and turbulent flow regimes, displaying rolling vortices, detached flow, and recirculation zones.

REFERENCE [72]: M. J. Rincón, A. Caspersen, N. T. Ingwersen, M. Reclari, and M. Abkar (2024). "Flow investigation of two-stand ultrasonic flow meters in a wide dynamic range by numerical and experimental methods," *Flow Measurement and Instrumentation*, vol. 96, p. 102543.

III.1 Introduction

Efficient management of water supply heavily relies on accurate flow measurements since obtaining accurate network data plays a crucial role in identifying and preventing issues such as excessive water consumption, leaks, and water theft. To achieve this, an efficient method is establishing a comprehensive flow meter network in the water grid. In this regard, installing intelligent ultrasonic flow meters offers one of the best solutions by enabling accurate and remote data acquisition of the water networks. Hence, by leveraging such technologies, securing a clean water supply on a global scale becomes achievable [73].

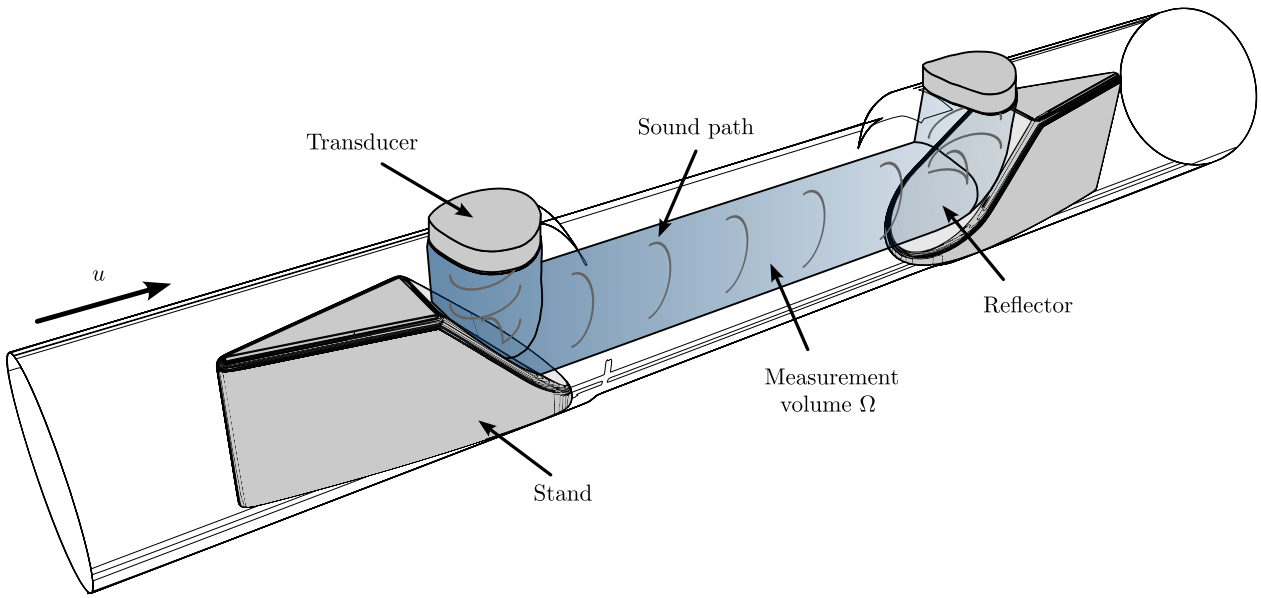

Figure III.1: Schematic of a simplified two-stand ultrasonic flow meter with its main functioning components.

Ultrasonic flow meters operate by measuring the time difference of sound waves transmitted by piezoelectric transducers in both directions relative to the flow. The interaction between the waves and the flowing medium causes acceleration and deceleration of the waves, resulting in a time disparity between the up and downstream measurements. This time disparity accurately estimates the volumetric flow passing through the flow meter [60, 61, 74]. In low-diameter pipes (below an internal diameter of $20\ \mathrm{mm}$), ultrasonic flow meters commonly display a two-stand configuration. This enables improved measurement accuracy and robustness by reflecting the soundwaves in the bulk of the flow, yielding a larger measurement volume, and reducing possible inlet sensitivities (Fig. III.1). However, the high blockage ratio of the stands introduces complex flow dynamics, making these systems an intriguing and challenging subject for investigating fluid motion in wall-bounded flows.

The accurate prediction of the flow dynamics throughout the dynamic range of flow meters aids in the identification of possible sources of uncertainties, ultimately leading to the improvement of measurement robustness and the development of more advanced systems [75]. It is then paramount for water distribution networks to rely on robust and reliable metering devices under a wide range of flow conditions.

Previous research in this field has commonly employed computational fluid dynamics (CFD) simulations based on Reynolds-averaged Navier-Stokes (RANS). Further high-fidelity and eddy-resolving methods such as large-eddy simulation (LES) are yet to be studied for these complex and industrial systems, where the high computational cost of these methods is on the verge of their applicability in industrial flows [15]. Hence, numerous studies use RANS to examine the effects in flow meters of different inlet conditions and different bent pipe configurations [16–19], even assessing part of the dynamic range of operation of single-path ultrasonic flow meters [20]. Additionally, some studies have investigated the use of CFD for analysing the positioning of transducers in non-intrusive reflected sound-path ultrasonic flow meters [21]. Furthermore, CFD has been utilised to explore the impact of headers [22, 23] and flow conditioners on flow stability in gas-based reflected sound-path ultrasonic flow meters [24, 25]. Some of these investigations compare numerical findings with experimental data, often obtained through particle image velocimetry (PIV), to investigate and validate potential

design improvements and optimal inflow configurations [26–28]. However, previous studies have predominantly focused on examining the interaction between diverse inflow conditions and large-diameter ultrasonic flow meters without intrusive geometries in the flow. Only recent studies have been focused on the more complex two-stand configuration, where diverse CFD turbulence models have been validated against laser Doppler velocimetry (LDV) [59], and where the geometry has been improved by design optimisation studies for the nominal flow rate of the system [76].

The previous studies regarding two-stand ultrasonic flow meters have only focused on a single nominal inlet flow in the turbulent regime, resulting in a gap in the literature when assessing the robustness and accuracy of common RANS models in their prediction of the dynamic range of complex internal flows. This study thus presents a comprehensive numerical and experimental investigation of the dynamic range of operation of a typical two-stand ultrasonic flow meter by industry standards. By using numerical methods, we aim to understand, accurately predict, and investigate the flow dynamics within the device and evaluate its performance under varying flow rates within its dynamic range. Furthermore, with a well-documented and grounded numerical foundation of the flow physics of the dynamic range in these systems, we aim to provide the knowledge to analyse the performance of ultrasonic flow meters and improve their performance based on numerical data.

In this study, Section 2 provides an overview of the numerical and experimental methods used, along with the underlying assumptions. The results obtained and their discussions, including experimental validation of the numerical methods, are presented in Section 3. Finally, Section 4 offers a summary and a comprehensive discussion of the findings.

III.2 Methodology

To approach the numerical methodology, the incompressible form of the Navier-Stokes equation is solved. Continuity and momentum equations are therefore defined as

$$\frac{\partial u_i}{\partial x_i} = 0, \tag{III.1a}$$

$$\frac{\partial u_i}{\partial t} + \frac{\partial u_j u_i}{\partial x_j} = -\frac{\partial p}{\partial x_i} + \nu \frac{\partial^2 u_i}{\partial x_j \partial x_j}, \tag{III.1b}$$

with $i = 1, 2, 3$, x_i corresponding to the x, y and z directions in the cartesian corrdinate system, respectively. The variable u_i respectively represents the components of the velocity field u, v, w; t is the time, p is the static kinematic pressure, and ν is the kinematic viscosity. These are rewritten using the RANS equations to evaluate mean fields and reduce the complexity of the numerical simulations. The Reynolds decomposition, $u_i = \langle u_i \rangle + u_i'$, is applied to Eq. III.1a and III.1b, yielding

$$\frac{\partial \langle u_i \rangle}{\partial x_i} = 0, \tag{III.2a}$$

$$\frac{\partial \langle u_i \rangle}{\partial t} + \langle u_j \rangle \frac{\partial \langle u_i \rangle}{\partial x_j} = -\frac{\partial \langle p \rangle}{\partial x_i} + \nu \frac{\partial^2 \langle u_i \rangle}{\partial x_j \partial x_j} - \frac{\partial \langle u_i' u_j' \rangle}{\partial x_j}, \tag{III.2b}$$

where $\langle \cdot \rangle$ is the Reynolds average and $\cdot'$ represents the fluctuating part of a field. To solve the RANS closure problem and predict the Reynolds stresses ($R_{ij} = \langle u_i' u_j' \rangle$), we use the 2-equation $k - \omega$ SST model [77], where its strengths and pitfalls by utilising the Boussinesq

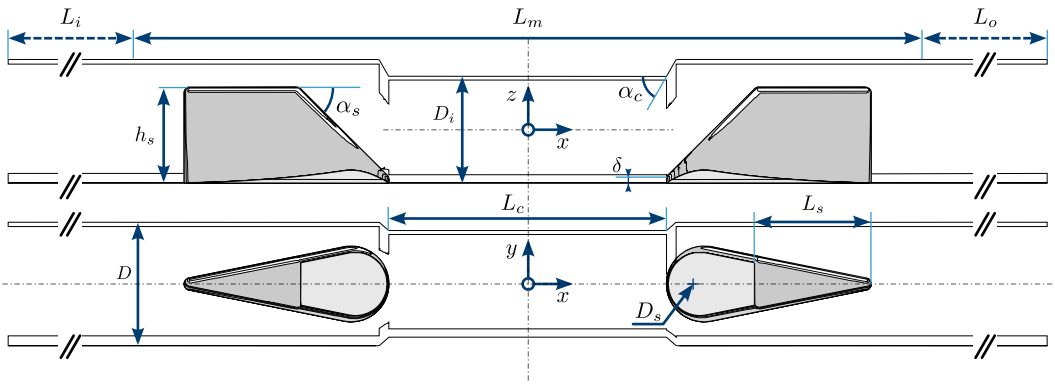

Figure III.2: Parametric description of the ultrasonic flow meter geometry. Top: y-normal plane. Bottom: z-normal plane. It should be noted that both stands have their edges filleted by a radius of $0.05D$ to ease the meshing procedure.

Table III.1: Geometry parameters for the baseline geometry as defined by [59]. Values are noted as a function of the pipe diameter D. Subscripts i, o, m, s, and c stand for inlet, outlet, meter, stand, and constriction respectively.

Parameter	Value
D	$20\ \mathrm{mm}$
D_i	$0.865D$
L_i	$5D$
L_o	$5D$
L_m	$9.5D$
L_c	$2.25D$
L_s	$1.25D$
D_s	$0.6125D$
h_s	$0.7785D$
α_s (rad)	$\pi/4$
α_c (rad)	$\pi/3$

approximation has been thoroughly studied in the literature [78]. The applied methodology in this study is based and improved upon the techniques developed in [59, 76], where a validated CFD method is developed based on wall-modelled RANS $k-\omega$ SST and more information can be found.

III.2.1 Geometry

The methodology is applied to an ultrasonic flow meter based on a simplified version of Kamstrup's *flowIQ 2200* where its geometry parameters are shown in Fig. III.2 with their specific values in Table III.1. Regarding the geometry description, a circular pipe of internal diameter D drives the inlet flow into a constriction of diameter D_i where two identical stands are located up and downstream. Downstream of the constriction, another section of circular pipe of internal diameter D drives the flow out of the system.

III.2.2 Simulation framework

A validated wall-modelled hexahedral-based grid for an inlet $\mathrm{Re} = 2.82 \cdot 10^4$ (equivalent to a volumetric flow of $\dot{Q} = 1.6\ \mathrm{m^3\,h^{-1}}$) is generated, where some improvements to the original grid by [59], are performed. An overall improvement of the extrusion layer generation is done, yielding 5 extrusion layers with an expansion ratio of 1.2 and a maximum volume difference between the bulk mesh and the last extrusion layer of 20%. Furthermore, one oct-tree level of refinement at a normal wall distance of $0.05D$ is applied on the surfaces of stands and mirrors in order to better approximate the prediction of the wall shear stresses in areas where the flow is in a non-equilibrium state. Hence, the generated grid contains $1\,384\,762$ cells of which 96% are hexahedra with a maximum and mean non-orthogonality of 59.9 and 4.6, respectively. These values are inside of what is generally considered a good-quality unstructured grid [79].

The full numerical methodology is applied using the general-purpose code OpenFOAM [65]. The incompressible solver for steady-state turbulent flows by the SIMPLE algorithm

[80], is used.

For the discretisation of gradient and divergence terms in the general transport equation, a second-order central-difference scheme is used for stability measures (*SFCDV* scheme in OpenFOAM). Finally, the pressure drop across the flow meter is calculated by performing a surface average subtraction of the static pressure of the inlet to the outlet patch as follows

$$\Delta p = \frac{1}{\Sigma_i}\int_{\Sigma_i}\langle p\rangle \mathrm{d}S - \frac{1}{\Sigma_o}\int_{\Sigma_o}\langle p\rangle \mathrm{d}S, \quad \text{(III.3)}$$

where Σ is the associated surface patch and i, o as inlet and outlet, respectively; and $\mathrm{d}S$ is the surface derivative. Since the numerical simulations are performed assuming incompressible flow conditions, the static pressure results are divided by the density of water at standard temperature and pressure (STP) conditions (fluid density $\rho = 998.2\ \mathrm{kg\,m^{-3}}$) [81].

In addition, the performance of the flow meter is numerically evaluated in the dynamic range following the work by Rincón *et al.* [76, 82]. This performance function is defined as

$$f_2 = -\left(\frac{u_\Omega - u'_\Omega - \sigma_{u_\Omega}}{u_b}\right), \quad \text{(III.4)}$$

where Ω is the estimated sound propagation volume, u_Ω is the integrated velocity of the fluid in the sound-path volume, u'_Ω is the integrated velocity fluctuations in the sound-path volume, σ_{u_Ω} is the standard deviation of the integrated velocity distribution in the sound-path volume. For more information about the performance function calculation, the reader is referred to [76].

Table III.2: Inlet conditions for the simulation and experimental cases. Flow rate with corresponding mean inlet velocities and Reynolds number.

Case	$\dot{Q}\ (\mathrm{L\,h^{-1}})$	$u_b\ (\mathrm{m\,s^{-1}})$	Re
1	6.0	0.0053	105.7
2	8.6	0.0076	151.5
3	86.3	0.0763	1520.9
4	169	0.1491	2971.4
5	251	0.2219	4421.8
6	333	0.2947	5872.3
7	500	0.4421	8808.4
8	667	0.5895	11744.5
9	833	0.7368	14680.6
10	1000	0.8842	17616.8
11	1167	1.0316	20552.9
12	1333	1.1789	23489.0
13	1500	1.3263	26425.1
14	1600	1.4147	28186.8
15	1833	1.6210	32297.4
16	2000	1.7684	35233.5

III.2.3 Dynamic range

The nominal flow rate in the simulated flow meter is $\dot{Q}_{\mathrm{nom}} = 1.6\ \mathrm{m^3\,h^{-1}}$. Simultaneously, the minimum and maximum flow rates are determined from $\dot{Q}_{\mathrm{nom}}$ as $\dot{Q}_{\mathrm{min}} = \dot{Q}_{\mathrm{nom}}/400$ and $\dot{Q}_{\mathrm{max}} = 1.2\dot{Q}_{\mathrm{nom}}$, respectively. Which is similarly equivalent to a dynamic range of *R400* following the international standards by [83]. This yields an investigated range of inflow Re $\in [106, 3.52 \cdot 10^4]$ as shown in Table III.2 and a nominal inlet bulk velocity $u_{b,norm} = 1.41\ \mathrm{m\,s^{-1}}$.

III.2.4 Experimental methods

LDV and pressure drop experiments are conducted using a polymethyl methacrylate (PMMA) pipe and acrylonitrile butadiene styrene (ABS) powder stand set. The experimental setup is designed to replicate the numerical simulations on a 1:1 scale. PMMA is chosen as the material to minimise light refraction between the water and the material due to their similar

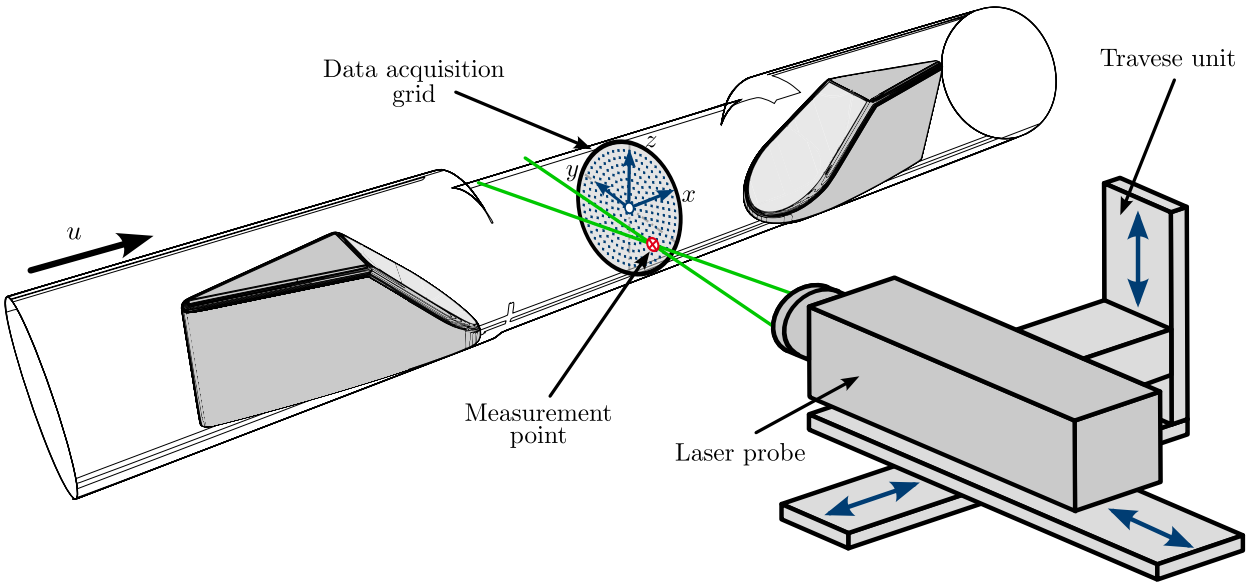

Figure III.3: LDV experimental setup schematic and cross-sectional data acquisition grid.

refractive indices. The experimental setup is placed on a test bench with precise temperature and volumetric flow control, ensuring consistent flow conditions throughout the experiments.

LDV experiments are utilised to obtain qualitative and quantitative velocity data with minimal impact on the flow where silver-coated glass-hollow neutrally-buoyant reflective particles with a diameter of $15\ \mu\mathrm{m}$ and $80\ \mathrm{g}$ are introduced into the test bench. An Nd:YAG laser with a power of $100\ \mathrm{mW}$ and a wavelength of $\lambda = 532\ \mathrm{nm}$ is employed to make the measurements [84]. A data-acquisition grid comprising 233 uniformly spaced points is generated covering 85% of the pipe cross-section to avoid the total reflection of the laser beam at the near-wall regions. The position of the laser probe is adjusted using a 3D traverse unit and ray-tracing methods to account for light diffraction in different media. The traverse unit is motorised and programmable in all axes (see Fig. III.3). The LDV experiments are conducted with a minimum of $60\ \mathrm{s}$ of measurement per point, ensuring statistical convergence of the mean axial velocity. Furthermore, to avoid physical asymmetries in the LDV data, a spatial y-average is performed in the yielded data.

Pressure drop experiments involve the use of two high-precision pressure transducers OMEGA PX429-100GI placed upstream and downstream of the measurement pipe. Both sensors are calibrated, and measurement repeatability is verified prior to conducting the final measurements. The experiments involve sampling pressure data every $5\ \mathrm{ms}$ for a minimum duration of $150\ \mathrm{s}$ and ensuring statistical convergence of first and second-order statistics.

III.3 Results and discussion

Numerical simulations and static pressure drop experiments are performed for all cases shown in Table III.2. Simultaneously, the axial velocity of three x-normal planes in the constriction region at $x = [-1, 0, 1]D$ are evaluated experimentally with LDV for two different flow rates at inflow $\mathrm{Re} = [106, 2.82 \cdot 10^4]$. Results are shown by initially qualitatively comparing the flow characteristics at different inflow Re. Subsequently, a quantitative comparison of the axial velocity obtained by CFD and experiments is shown by displaying the velocity profiles at the measured regions. Finally, a comparison of the numerical and experimental results of the static pressure drop as an important bulk quantity is performed. Experimental

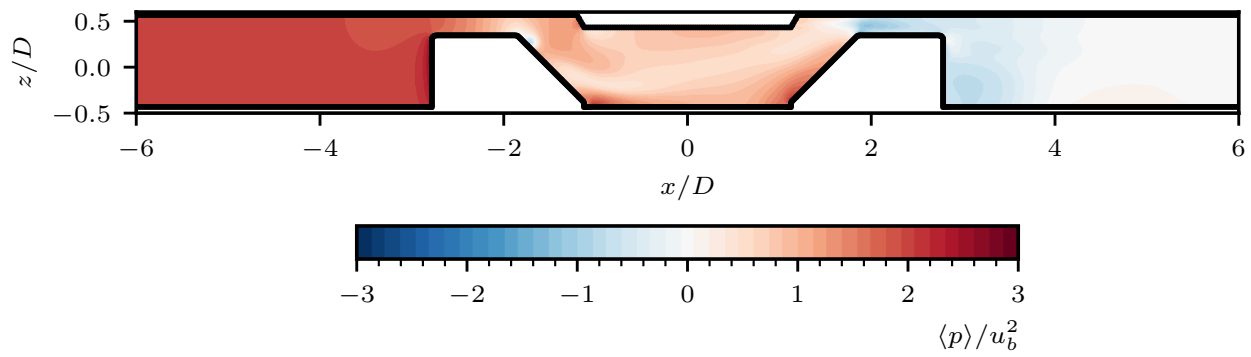

Figure III.4: Normalised kinematic pressure contours predicted at y-normal plane of the baseline case for inflow Re $= 2.82 \cdot 10^4$.

uncertainties follow the convention by ISO/IEC Guide 98-3 Part 3: GUM [85], displaying 2σ ranges. All results are similarly discussed and described followed by their corresponding figures.

III.3.1 Qualitative numerical analysis

It is remarkable to highlight that there is not a single geometrical parameter that holistically governs the flow physics present in this type of ultrasonic flow meter. It is very complex to determine and evaluate in detail the geometrical causes of all the physics present in this case, therefore, the results section of this study focuses on the qualitative and quantitative description of the physics and phenomena. For more information about the parameter influence in this case, the reader is referred to the study by Rincón *et al.* (2023) [76].

The flow behaviour is complex due to the presence of the stands, as well as the converging-diverging section of the flow meter. At nominal flow, this unique geometry induces a combination of non-equilibrium flows by the presence of adverse pressure gradient regions. These conditions hence yield recirculation zones, streamwise vortices generation and breakup, and boundary-layer detachment and reattachment. These flow characteristics are common to all tested cases at inflow Re > 1500, where turbulence transition takes place at diverse regions throughout the flow meter. Figure III.4 displays the static pressure results, revealing the imminent pressure drop across the flow meter and an adverse pressure gradient region across the downstream stand. These results likewise indicate a complex flow throughout the flow meter.

Axial velocity contours for cases 1, 3, 4, 9, and 14 (refer to Table III.2) are chosen as distinctive numerical simulations to evaluate where their axial velocity contours are shown in Fig. III.5. On the one hand, for all turbulent cases, two small recirculation zones are predicted at the reflector of the upstream stand. A larger recirculation zone is present as the boundary layer detaches from the reflector edge of the downstream stand and follows its sides. Furthermore, any marginal variability on these flow characteristics settles at inflow Re $> 10^4$. On the other hand, in the lowest inflow Re regime, the case exhibits a seamless velocity profile throughout where the vortices and recirculation zones are largely reduced in size and magnitude. Laminar flow is generally present throughout the system and boundary-layer detachment is not visible.

As the inflow Re increases, the velocity profile at the inlet becomes more uniform, indicating the development and transition to turbulent flow. In the analysed cases, two main and two secondary vortices are symmetrically formed along the x-axis. The main vortices

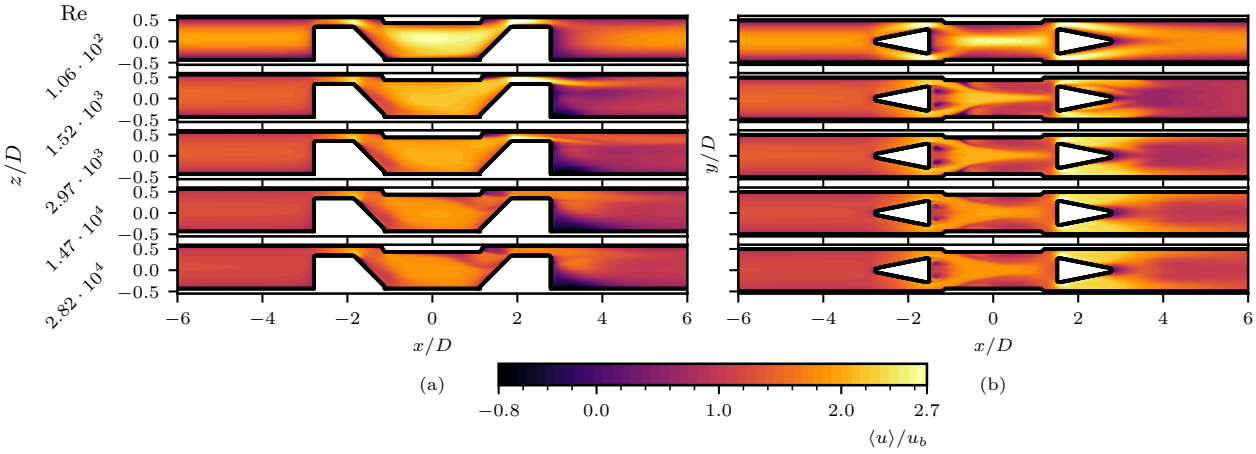

Figure III.5: Normalised streamwise velocity at y and z-normal planes for diverse inflow Re cases of the dynamic range.

originate when the boundary layer detaches from the trailing edge of the upstream stand and high-vorticity regions extend in the streamwise direction of the flow. These vortex pairs display anti-symmetric rotation, where clockwise rotation is predicted by the vortex located in the y-positive section, and counter-clockwise rotation by the vortex at the y-negative section. The breakup of these vortices takes place at the start of the diverging section of the system, with the exception of the laminar-inflow cases, where the vortices break up before the end of the constriction is reached.

The flow behaviour undergoes changes as the inflow Re varies. Specifically, weaker vortices are predicted in cases at low Re. Conversely, for all cases where the inflow Re > 3000, λ_2 values are at least one order of magnitude higher, whereas, for all cases, the primary vortices originate from the top of the upstream stand trailing edges and extend to the top of the downstream stand passing through the bottom and pipe sides of the constriction.

The secondary vortices are generated at the lower trailing edge of the upstream stand and are influenced by the stronger vorticity of the primary vortices. As they develop through the constriction, these secondary vortices eventually coalesce with the primary vortices just downstream of the midpoint of the flow meter ($x \approx 0D$). This phenomenon is shown in the λ_2 isocontours for selected flow rates in Fig. III.6 [70]. The λ_2 values represent a good criterion to identify vortical structures. The criterion is defined as the second biggest eigenvalue (in magnitude) of the matrix $S_{ik}S_{kj} + \Omega_{ik}\Omega_{kj}$, where S_{ij} is the rate-of-strain tensor and Ω_{ij} is the rate-of-rotation tensor, defined as

$$S_{ij} = \frac{1}{2}\left(\frac{\partial u_i}{\partial x_j} + \frac{\partial u_j}{\partial x_i}\right) \tag{III.5a}$$

$$\Omega_{ij} = \frac{1}{2}\left(\frac{\partial u_i}{\partial x_j} - \frac{\partial u_j}{\partial x_i}\right). \tag{III.5b}$$

At lower inflow Re, the primary and secondary vortices are easily distinguishable. However, as the inflow Re increases, the secondary vortices become more chaotic and harder to differentiate from the primary vortices.

As a final qualitative evaluation, the different cross-sections of interest are analysed in Figure III.7, where axial velocity results are displayed showcasing the influence of the inflow Re on the velocity field. Firstly, for all cross-sections, the transition from laminar to turbulent flow regimes is seen in the lower Re cases. Secondly, a progressive change in the velocity

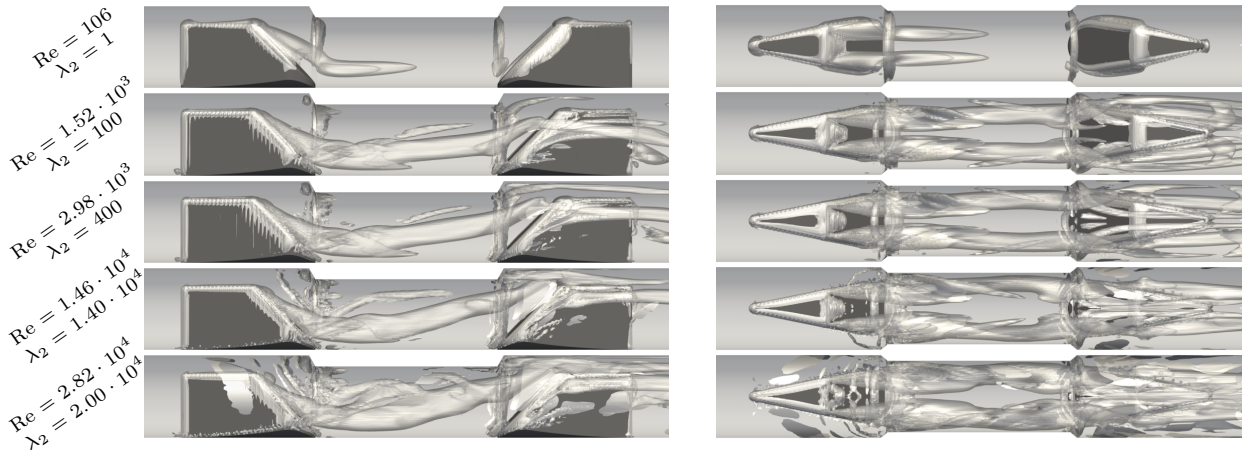

(a) y-normal view. (b) z-normal view

Figure III.6: Isosurfaces of λ_2-criterion for selected cases across the dynamic range. Since a fixed value of λ_2 for all cases is inadequate to visualise the vortices at the constriction for flows at different inflow Re, the isosurface values differ for each case to adequately represent the vortices.

gradients from the lower Re cases is seen until the inflow Re $\approx 1.47 \cdot 10^4$, where the flow becomes qualitatively indistinguishable. Thirdly, the influence of the inflow Re in sections $x \in [-1, 0, 1]D$ displays the formation and propagation of vortices and, finally, a recirculation region at $x = 3D$ is predicted on the bottom section of the pipe, where vortices are predicted on the top section of the downstream stand.

III.3.2 Experimental validation of axial velocity

The simulation framework is tested against experimental LDV for two inflow regimes (laminar and turbulent) displaying the biggest axial velocity differences. In this regard, experiments are taken for Re $= [106, 2.82 \cdot 10^4]$. The aim is to qualitatively identify the flow characteristics predicted by CFD for both cases and to quantify the predictive capabilities by analysis of the axial velocity profiles at regions of interest. Experimental contours are taken through the flow meter constriction at cross-sections $x = [-1, 0, 1]D$ and subsequently compared to the numerical predictions.

Axial velocity contours for inflow Re $= 106$ in Fig. III.8 show a particularly good agreement between experimental and numerical data. High-velocity regions are seen on the upper section of the pipe at $x = -1D$, whereas low-velocity regions are seen on the bottom section near the pipe walls. At $x = 0D$, the flow accelerates in the middle section of the pipe where deceleration regions are seen at the near-wall regions, displaying a more uniform flow distribution. Finally, the velocity contours at $x = 1D$ show a pattern very similar to fully-developed laminar flow, slightly skewed to the upper section of the pipe. Between both methods, there are no noticeable differences in gradients or magnitude predictions. These results are somewhat expected since the lack of turbulence in the flow simplifies the velocity predictions by CFD.

To perform the quantitative analysis, the axial velocity profiles at locations $z = [0.2, 0.1, 0.125]D$ (showed as dotted lines in Fig. III.8) and $y = 0D$ are compared and shown in Fig. III.9. On the one hand, regarding y-profiles (Fig. III.9a), the acceleration and deceleration regions are distinguishable and accurately predicted by CFD for all cases, where negligible

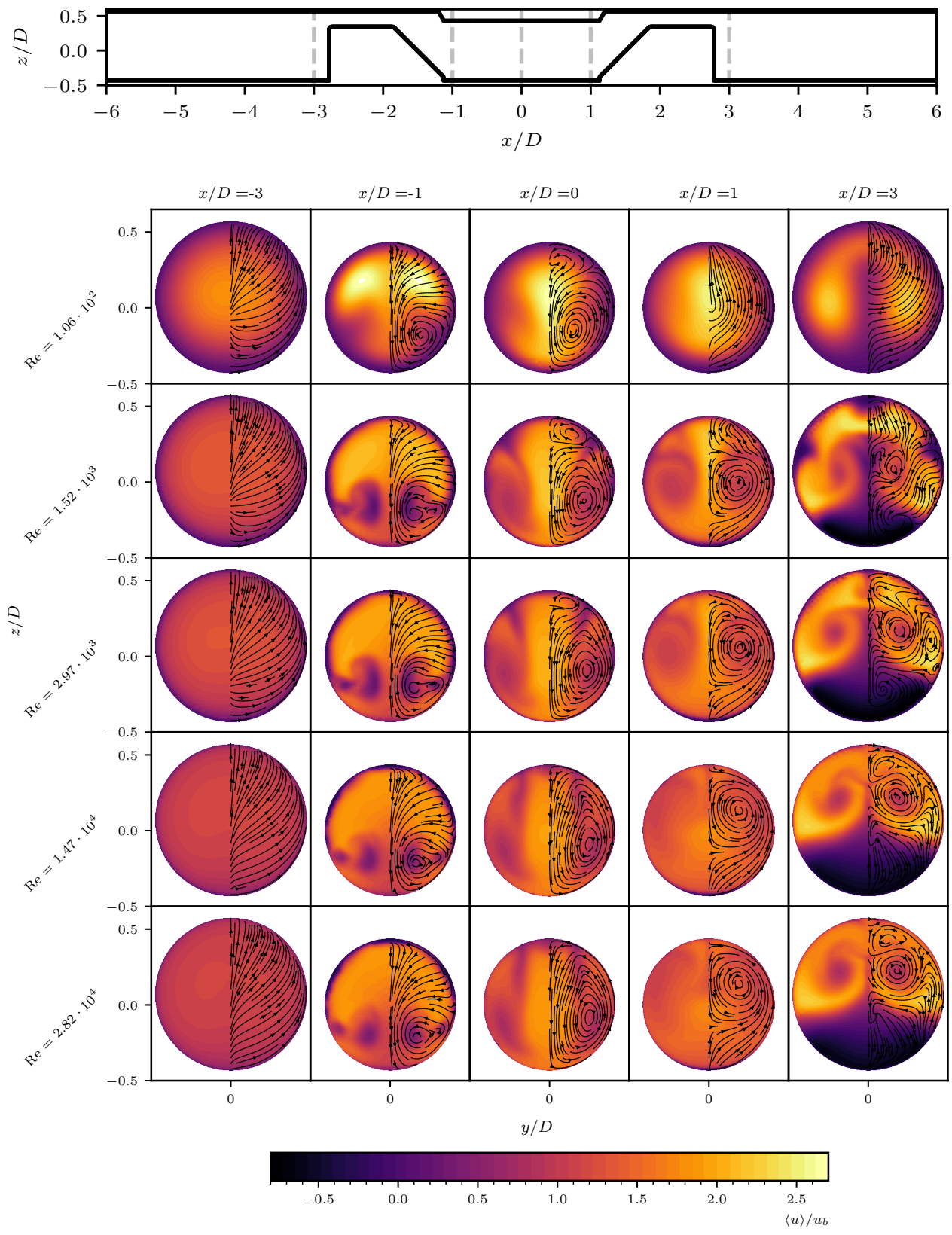

Figure III.7: Axial velocity contours for flow normal slices at $x \in [-3, 3]D$ for selected inflow Re cases.

differences are displayed at the symmetry plane due to the imposition of symmetry in the results. On the other hand, z-profiles predictions of Fig. III.9b show very similar behaviour

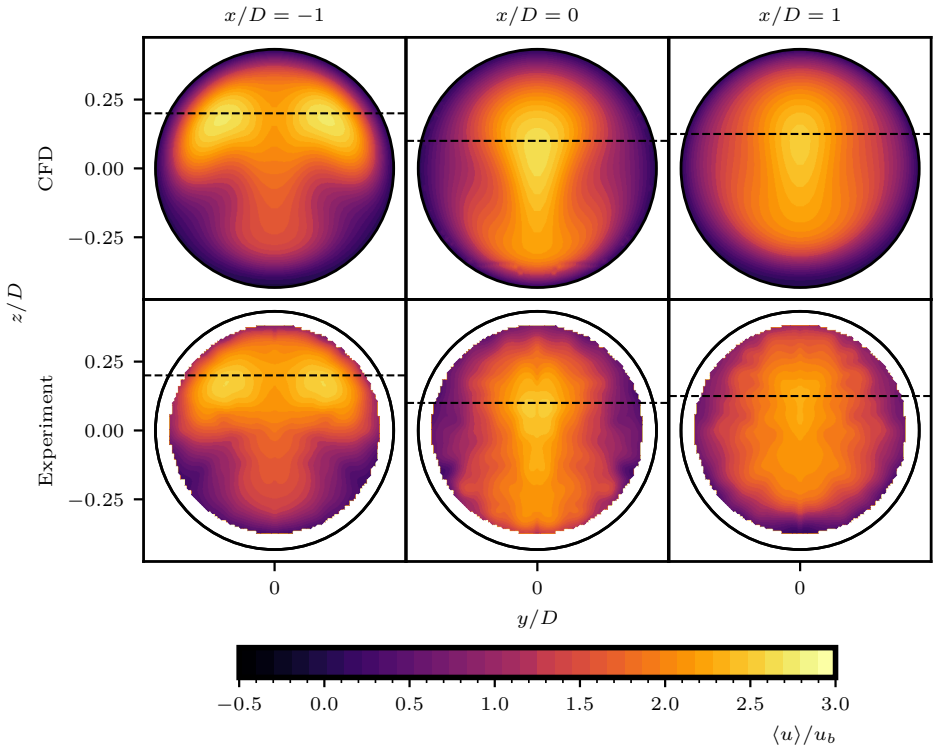

Figure III.8: Comparison of normalised axial velocity flow contours for inflow Re $= 106$ in the three cross-sections for experimental LDV and CFD results. It should be noted that dotted lines represent the location of velocity profiles displayed in the quantitative analysis.

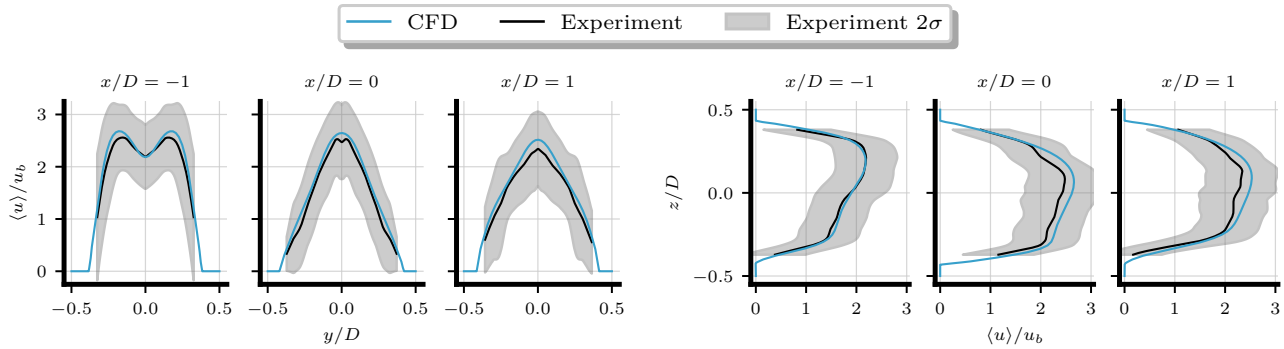

(a) y profiles. It should be noted that all profiles are sampled at $y = 0$.

(b) z profiles. It should be noted that all profiles are sampled at the z locations shown as dashed lines in Fig. III.8.-

Figure III.9: Comparison of normalised axial velocity flow profiles for inflow Re $= 106$ in three flow-normal planes for experimental LDV and CFD simulation results.

and trend, accurately predicting both gradients and magnitude of the velocity and displaying a particularly accurate prediction in agreement with the experiments. Overall, all predictions by CFD show a particularly good agreement with experimental data in both magnitude and gradients, displaying results inside 2σ experimental uncertainty bounds in the analysed profiles.

Regarding inflow Re $= 2.82 \cdot 10^4$, qualitative results shown in Fig. III.10 display similar agreement as previous results, where experimental and numerical data have particularly good agreement. However, the complexity of predicting turbulent flows yields slightly

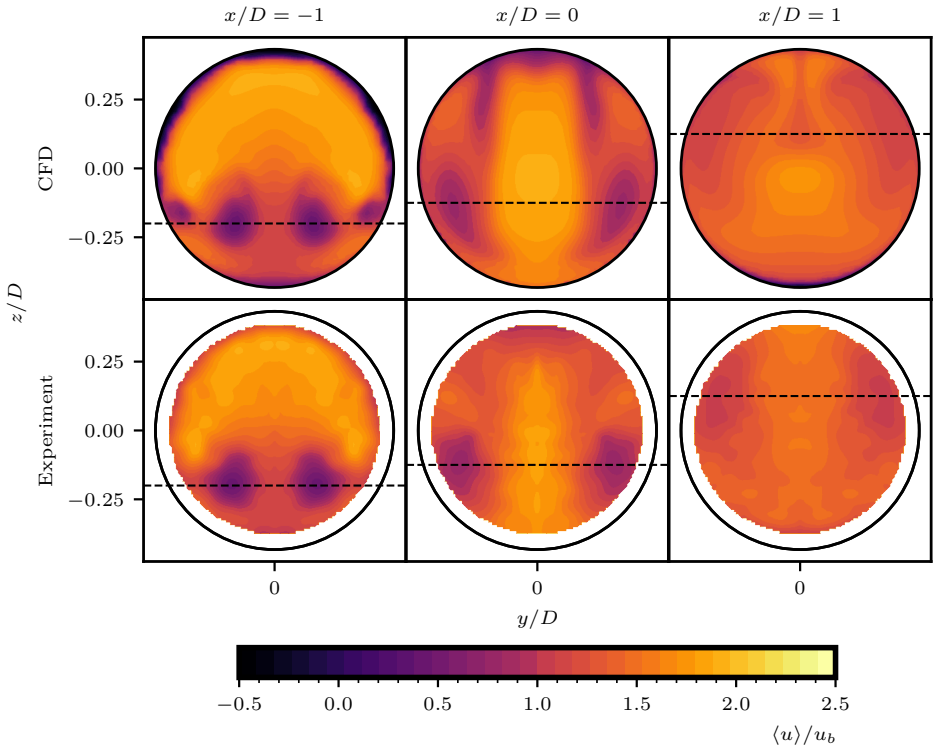

Figure III.10: Comparison of normalised axial velocity flow contours for inflow Re $= 2.82 \cdot 10^4$ in three flow-normal planes for experimental LDV and CFD simulation results. It should be noted that dotted lines represent the location of velocity profiles displayed in the quantitative analysis.

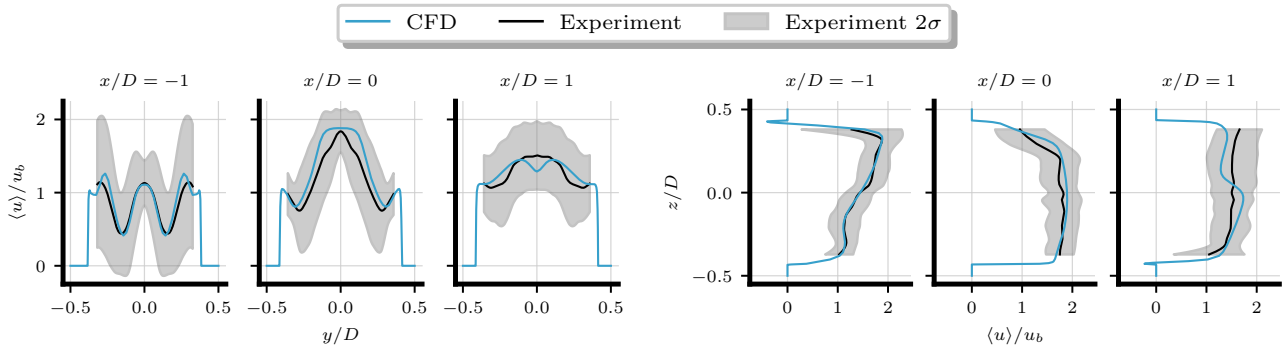

(a) y profiles. It should be noted that all profiles are sampled at $y = 0$.

(b) z profiles. It should be noted that all profiles are sampled at the z locations shown as dashed lines in Fig. III.10.

Figure III.11: Comparison of normalized axial velocity flow profiles for inflow Re $= 2.82 \cdot 10^4$ in three flow-normal planes for experimental LDV and CFD simulation results.

higher differences between experiments and CFD. Although not straightforwardly evident qualitatively, the biggest differences are seen at $x = [0, 1]D$, where the vortices propagation (shown as low-velocity regions) is slightly skewed and stretched by the numerical predictions. Moreover, there is a slightly higher velocity region predicted by CFD at the centre of the pipe in these cross-sections and two slender low-velocity regions are predicted at $x = 0D$ in the top section of the pipe that are not present in the experimental data. Overall, despite the more complex flow conditions presented, the qualitative predictions and vortices locations

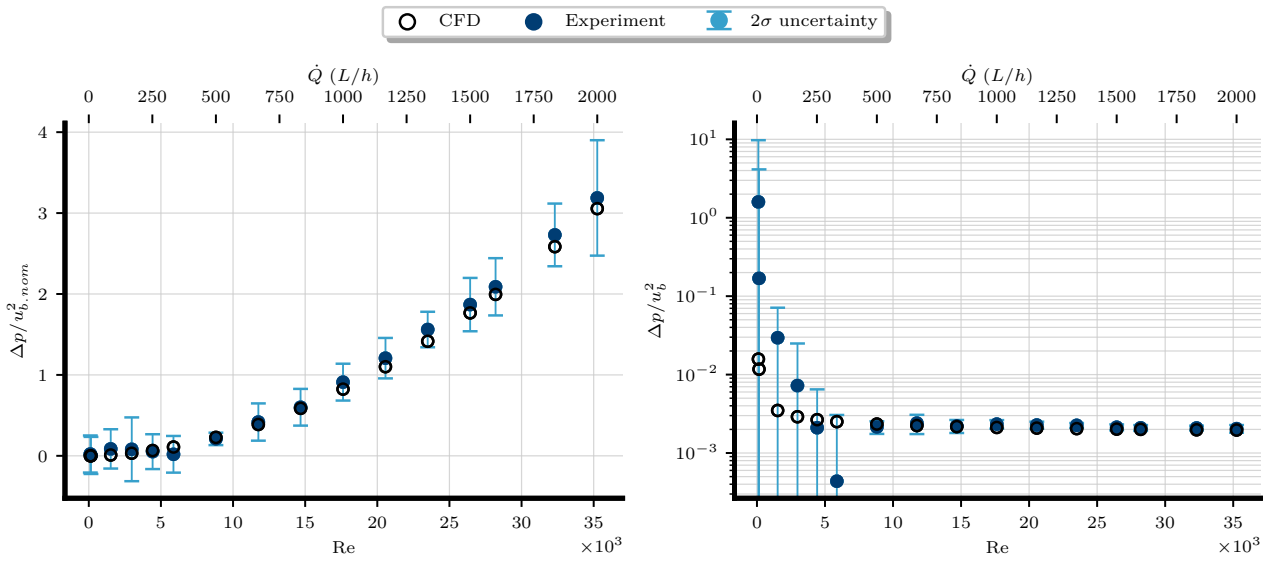

(a) (b)

Figure III.12: Numerical pressure drop prediction compared to experimental results. Figure III.12a: normalised static pressure drop by $u_{b,norm}$ for simulations and experiments with 2σ experimental measurement uncertainty. Figure III.12b: normalised pressure drop by u_b of each case for simulations and experiments with 2σ experimental measurement uncertainty.

are in particularly good agreement between both methods.

Axial velocity profiles at locations $z = [-0.2, -0.0125, 0.125]D$ (showed as dotted lines in Fig. III.10) and $y = 0D$ are likewise compared and shown in Fig. III.11. Similarly to previous results, the quantitative comparison yields particularly good agreement between the numerical and experimental methods both in gradients and magnitudes. There are, however, slight deviations in the mean value of the numerical prediction seen at $x = 1D$. These deviations suggest a slight underprediction of the axial velocity at the centre and top sections of the pipe and could indicate that the CFD methodology underestimates the turbulence diffusion in some regions of the flow as well as boundary-layer detachment and reattachment [29, 86, 87]. Nevertheless, all numerical results are confined inside experimental uncertainty bounds of 2σ in the analysed profiles, where the slight disagreement of high Re cases is expected due to their added physical complexity and the prediction of turbulent fields.

III.3.3 Static pressure drop

Pressure drop serves as a convenient quantity to quantify the amount of energy lost due to momentum loss, which, in turn, influences the flow rate and overall efficiency of internal flow systems [71]. Therefore, pressure drop serves as an excellent bulk quantity to evaluate the overall CFD prediction by comparing the numerical and experimental results.

Figure III.12 displays the direct comparison of static pressure drop with mean and 2σ experimental uncertainty of the full range of Re studied. In order to represent dimensionless static pressure drop, we employ two different normalisation methods: normalising the kinematic static pressure by the square of the inlet bulk velocity of the baseline case at inflow $\mathrm{Re} = 2.82 \cdot 10^4$ (Fig. III.12a); and normalising the kinematic static pressure drop by the square of the bulk inlet velocity of each case (Fig. III.12b).

The pressure drop obtained from CFD simulations complies with the 2σ measurement

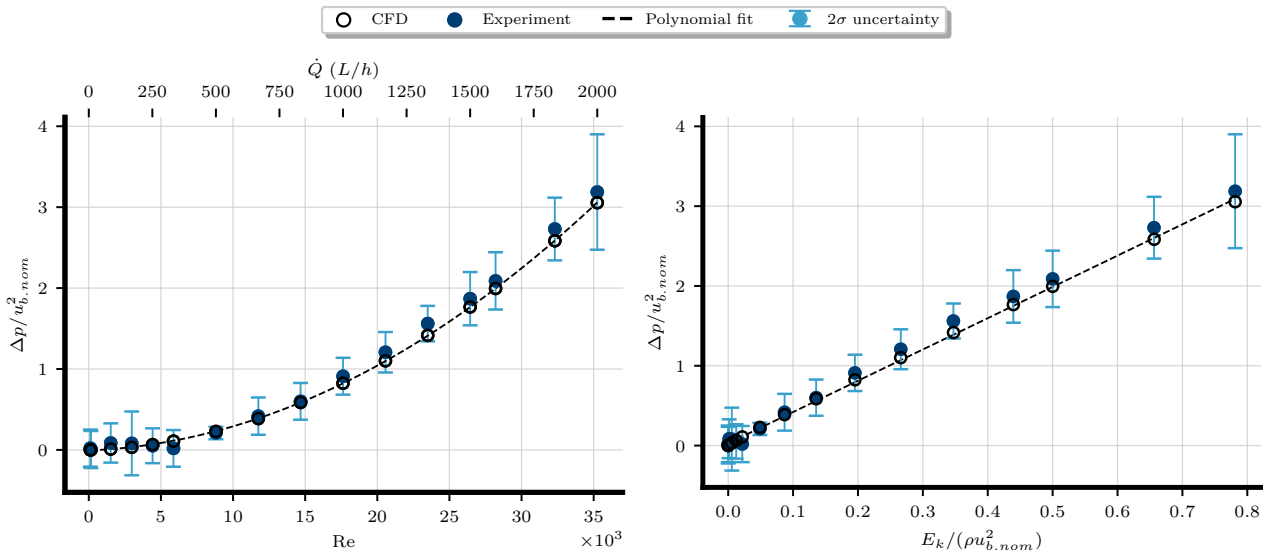

(a) (b)

Figure III.13: Polynomial and linear fits of static pressure drop data. Figure III.13a: Static pressure drop as a function of inflow Re with second-order polynomial fit to CFD data. Figure III.13b: Static pressure drop as a function of the normalised inlet kinetic energy with a linear fit.

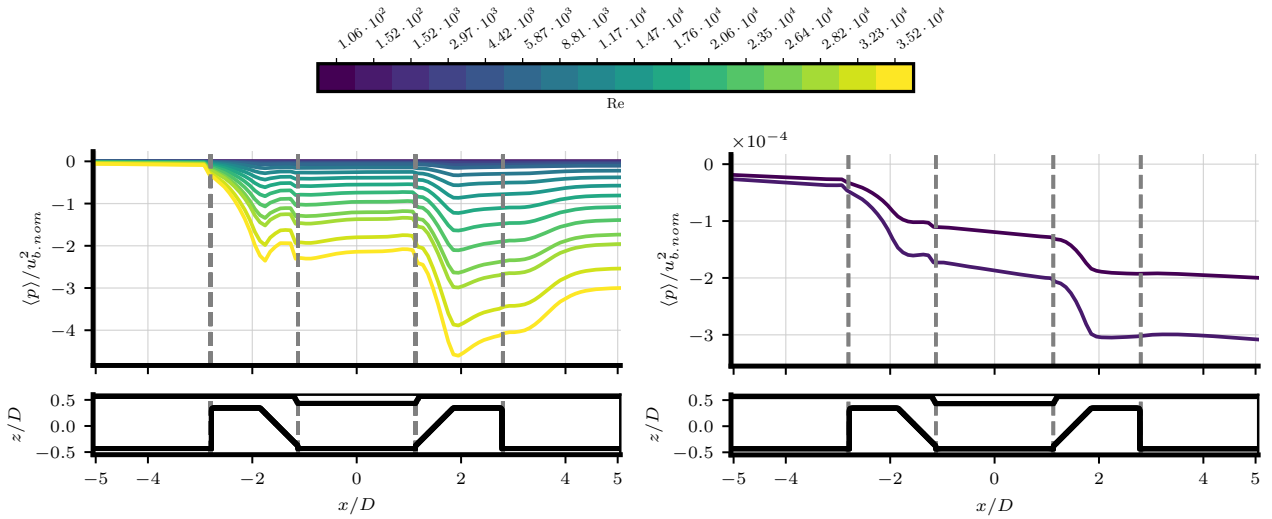

(a) (b)

Figure III.14: Static pressure drop distribution throughout the flow meter geometry for the whole dynamic range. All analysed cases are depicted in Fig. III.14a while only laminar flow cases are depicted in Fig. III.14b.

uncertainty of the experimental results for all tested inflow Re, encompassing the full dynamic range of the tested flowmeter. Results likewise indicate that pressure drop increases exponentially as the inflow Re increases. Initially, at very low Re, the pressure drop is minimal due to a lack of pressure drag, and the predominant presence of a laminar flow regime in the system. However, as the inflow Re increases and the flow becomes more complex and turbulent (with the formation of strong vortical structures, flow separation and recirculation) the pressure drop increases dramatically.

By normalising the pressure drop by the bulk inlet velocity of each case, no qualitative changes in the flow are observed for inflow Re $> 10^4$ where the asymptotic behaviour of the data is seen in Fig. III.12b, coinciding with the constant qualitative behaviour addressed in section III.3.1. The visualisation of the data by normalising the pressure drop in this manner is comparable to displaying the static pressure drop per inlet kinetic energy. Notably, the low Re cases exhibit a larger normalised pressure loss, where the flow is mostly laminar. As the Re increases, the normalised pressure drop converges to a constant value, implying a linear relationship between the inlet kinetic energy and pressure drop. This relationship can be described by a second-order polynomial, as seen in Fig.III.13a.

Such a polynomial fit is defined by $\Delta p/u_{b,nom}^2 = a_2\mathrm{Re}^2 + b_2\mathrm{Re} + c_2$, where $(a_2, b_2, c_2) = (4.5329 \cdot 10^{-9}, 1.4214 \cdot 10^{-5}, -0.0123)$. Similarly, both numerical and experimental results confirm the linear scaling of pressure drop with the kinetic energy of the inlet bulk velocity for each case ($E_k = \frac{1}{2}\rho u_b^2$). Such a fit is given by $\Delta p/u_{b,nom}^2 = a_k E_k / \left(\rho u_{b,nom}^2\right) + b_k$, where $(a_k, b_k) = (3.9206, 0.0280)$ in this study.

In order to investigate where the pressure drop occurs in detail, the pressure distribution throughout the flow meter is assessed by calculating the average static pressure distribution, where mean values of static pressure are calculated in cross-sectional planes along the flow meter axial direction. Cross-sectional average values are calculated with,

$$\Phi_{\text{avg}} = \frac{1}{S}\int \Phi \mathrm{d}S, \tag{III.6}$$

where Φ is the quantity to be averaged, and S is the cross-sectional area. Furthermore, an area-weighted average is utilised to account for different cell sizes.

The static pressure distribution is calculated following Eq. III.6 in the interval $x \in [-5, 5]D$ as seen in Fig. III.14, where the distribution is shown for different inflow Re throughout the flow meter geometry. In this context, the pressure drop increases consistently in magnitude and gradient as the Re increases for all turbulent-dominated cases with no canonical differences. To distinguish both flow regimes, Fig. III.14b depicts the pressure distribution for the two lowest tested inflow Re, where more clear differences are predicted.

At inflow Re > 8808, the impact of viscous effects on the pressure drop is greatly reduced due to flow complexity in turbulence-dominated cases and the occurrence of boundary-layer separation. The majority of the pressure drop is shown to occur as the flow passes the stands for all tested inflow Re where the stands account for the pressure drop almost equally. On the one hand, for turbulent-inflow cases, higher static pressure gradients are predicted at the locations of the stands. Immediately downstream both stands, static pressure recovery takes place. On the other hand, laminar-inflow cases likewise display a high-pressure drop at the stand locations, however, no static pressure recovery is predicted downstream. This lack of recovery is due to the reduced instances of boundary-layer detachment, milder adverse pressure gradients, and the formation of coherent structures present in this system as discussed in Section III.3.1.

III.3.4 Performance in the dynamic range

Following the definition from Rincón *et al.* [76, 82], the performance of the flow meter under the tested inlet conditions, is evaluated. The performance function f_2 evaluates the velocity and turbulence kinetic energy throughout the reflected sound-path volume and provides, solely by the numerical flow solution, a performance value. A high negative value of f_2 indicates a more robust and accurate measurement by the flow meter, whereas a value close to 0 indicates the opposite.

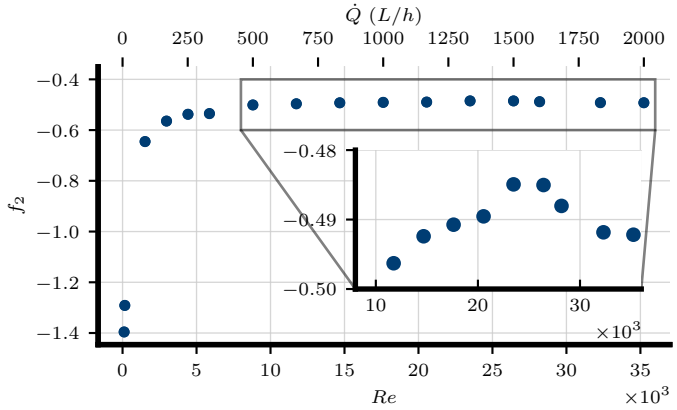

Figure III.15: Estimated flow meter performance performance f_2 as a function of the tested flow rates.

Figure III.15 shows the results of f_2 in function of the inlet Reynolds number for all cases studied. Results show that the estimated measurement performance decreases as the inlet Re increases, with an asymptotic tendency towards $f_2 \approx 0.49$. For low inlet Re cases, the estimated measurement performance improves.

Saturation values of f_2 are reached approximately at Re $= 10^4$. This phenomenon occurs due to the similarity of the flow fields at higher inlet Re. However, the differences in the flow fields of the low flow rate cases yield large deviations in the performance estimates. Excluding the laminar cases, which yield a 286% and 265% better performance than the nominal inlet Re $= 2.82 \cdot 10^4$. These findings point out that these types of flow meters yield a more robust measurement at low inlet Re. Simultaneously, the variation in measurement performance of these meters is highly reduced at higher inlet Re.

III.4 Conclusions

In this study, the dynamic range of a two-stand ultrasonic flow meter is evaluated by RANS $k-\omega$ SST. To validate the numerical predictions, LDV and static pressure drop experiments are performed where data is compared between both methods.

Numerical predictions identify no qualitative changes in the results above inflow Re $> 10^4$ in terms of coherent structures and flow dynamics. A clear distinction in the results is predicted between flow regimes, where a lack of boundary-layer detachment and strong vortical structures are predicted in the presence of laminar inflow.

Axial velocity comparisons between LDV and $k-\omega$ SST at cross-sections throughout the flow meter measurement region show an excellent agreement in both qualitative and quantitative manners. All evaluated velocity profiles concur with the experimental 2σ uncertainty ranges and minor mean deviations are predicted as the inflow Re increases.

Numerical static pressure drop predictions and experimental results show particularly good agreement. The pressure drop prediction in the whole dynamic range conforms with the experimental data and uncertainty bounds of 2σ. Furthermore, the static pressure drop predictions and experiments confirm the linear scaling of pressure drop with inlet kinetic energy and the second-order distribution by varying Re.

Cross-sectional evaluation of the static pressure shows that the regions with the highest influence in pressure drop are the stands. In addition, turbulent-inflow cases display static pressure recovery after high-pressure gradients throughout the stands, whereas laminar-inflow cases do not.

The numerical flow meter performance shows that the velocity field at lower inlet Re yields a more robust and accurate measurement compared to higher inlet Re, where a saturated value of the performance function is observed in inlet Re $> 10^4$.

In conclusion, for its dynamic range, the flow behaviour throughout the flow meter shows complex flow structures such as rolling vortices, detached flow, and recirculation zones. It is predicted that these flow structures are affected by the inflow condition as flows with lower Re yield weaker structures, where no qualitative changes in the flow are observed above inflow Re $> 10^4$. The numerical and experimental methodologies show excellent agreement in results estimating the axial velocity inside the measurement region of the flow meter, and pressure drop throughout within experimental 2σ ranges.

IV

Design Optimisation

Validating the design optimisation of ultrasonic flow meters using computational fluid dynamics and surrogate modelling

ABSTRACT Domestic ultrasonic flow meters with an intrusive two-stand configuration present a complex flow behaviour due to their unique geometry, which offers an interesting case to evaluate optimisation methods in wall-bounded turbulent flows. In this study, the design and analysis of computer models by computational fluid dynamics are used to predict the turbulent flow and to perform robust design optimisation of the flow meter. The optimisation is accomplished by surrogate modelling based on Kriging, Latin hypercube sampling, and Bayesian strategies to ensure a high-quality and space-filled response surface. A novel function to quantify flow meter measurement uncertainty is defined and evaluated together with pressure drop in order to define the multi-objective optimisation problem. The optimisation Pareto front is shown and compared numerically and experimentally against pressure drop and laser Doppler velocimetry experiments, displaying performance gains and geometrical changes in the 3D space. From the various improved designs sampled experimentally, a 4.9% measurement uncertainty reduction and a 37.4% pressure drop reduction have been shown compared to the analysed baseline case. The applied methodology provides a robust and efficient framework to evaluate design changes, improving ultrasonic flow meters and internal flow problems with similar features.

REFERENCE [76]: M. J. Rincón, M. Reclari, X. I. A. Yang, and M. Abkar (2023). "Validating the design optimisation of ultrasonic flow meters using computational fluid dynamics and surrogate modelling," *International Journal of Heat and Fluid Flow*, 100, 109112.

IV.1 Introduction

In the past 50 years, ultrasonic flow metering technology for water measurement has significantly evolved to a democratised state [60]. Due to this fact and the advantages compared to non-ultrasonic metering technologies, cost-efficient and accurate ultrasonic flow meters have become one of the strongest technologies for high-scale flow measurement in the past two decades [88]. Furthermore, the reliability and advantages of low-pressure drop and non-intrusiveness of transient-time ultrasonic flow meters are leading to a high number of these active systems in pipe networks, both for water and district heating applications [73]. Due to the large number of current and future flow meters in operation, there is a significant impact in terms of pressure drop pipe networks. It is then of high relevance to study and provide a methodology to yield an educated improvement of these complex systems.

Standard ultrasonic flow meters send and receive sound waves by means of two piezoelectric transducers. The sensors are capable of estimating volumetric flows by detecting

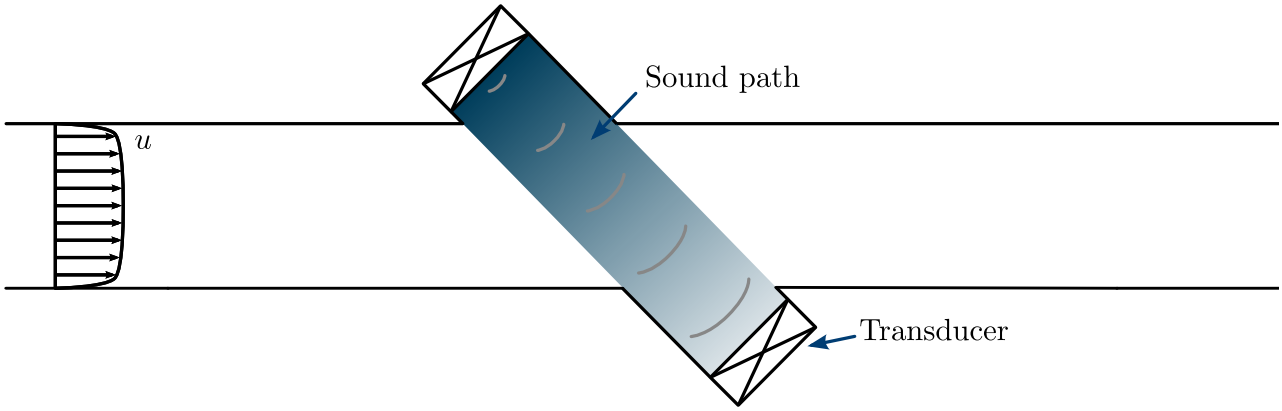

(a) Standard single-path configuration.

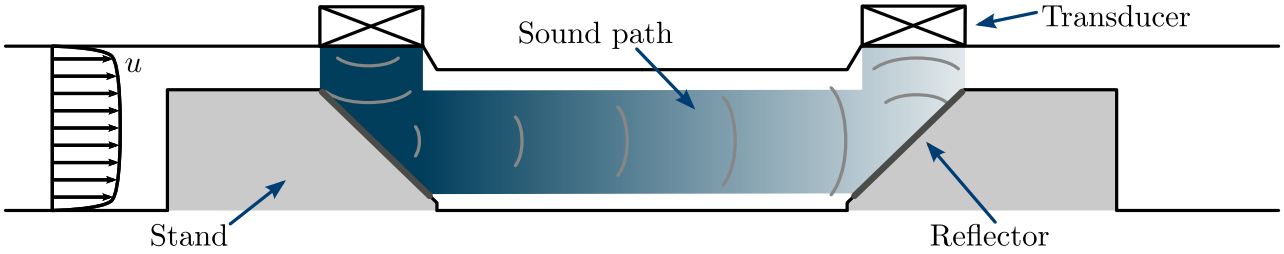

(b) Two-stand configuration and internal reflection of the beams.

Figure IV.1: Schematic of operation and geometries of transient-time ultrasonic flow meters with different configurations. Both figures display the axial cross-section through the centre of the pipe. Note that Fig. IV.1b does not represent the whole 3-dimensional geometry and the blockage of the stands is not as severe as shown.

the time differential generated by the interaction of the waves and the media they travel through (Fig. IV.1a). In order to acquire a more accurate measurement in low-diameter water pipes (below $40\ \mathrm{mm}$ of internal diameter), internal reflections of the beams based on intrusive geometries are commonly introduced in the flow meter (Fig. IV.1b). Although the use of this technique improves the flow meter accuracy significantly, it yields a disruptive and complex interaction with the flow that cannot be analysed straightforwardly by analytical methods [61, 89, 90].

To overcome these limitations, computational fluid dynamics (CFD) with the aid of the latest advances in numerical methods and computer hardware, has facilitated the detailed study of fluid flow in complex systems. These analyses include the prediction of turbulent flow in ultrasonic flow meters with two-stand configuration and internal reflection of the beams [59]. However, CFD methods are nonetheless computationally expensive [91, 92] and, to perform a thorough optimisation analysis of contemporary industrial engineering applications by CFD alone, these costs largely exceed the justifiable time and resources needs for current industrial, academic, and governmental institutions alike [15, 93, 94]. Hence, when comprehensive optimisation studies, diverse methods that rely on mathematical complexity are commonly used to reduce the limitations on resources and time of expensive numerical methods.

Despite the growing market and widespread use of transient-time ultrasonic flow meters, few studies using CFD have been published addressing their improvement. In most cases, ultrasonic flow meters for gas measurement have been studied by CFD with non-intrusive geometries [16, 22, 25, 27]. Nevertheless, the improvements have only been focused on

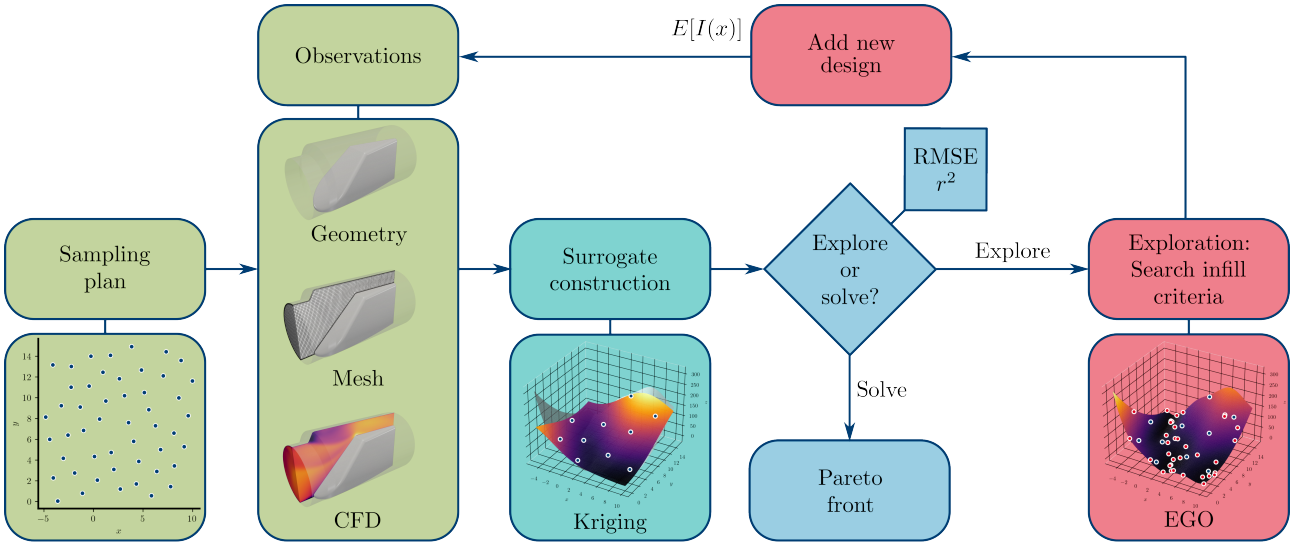

Figure IV.2: Design optimisation strategy adopted. A sampling plan based on Latin hypercube sampling (LHS) is initially applied and solved by CFD. Subsequently, an initial surrogate is constructed based on Kriging. Due to the likelihood of the initial sampling not evaluating the surrogate in extrema, Bayesian strategies based on efficient global optimisation (EGO) and the evaluation of the expected improvement ($E\left[I(x)\right]$) function are applied to further explore the surrogate and improve its quality. Finally, when the quality requirements are met, a genetic algorithm is used to search for an optimum on the response surface of the surrogate model.

finding thresholds of inlet flow conditions (e. g. maximum and minimum flow rate, swirl, and asymmetry) to ensure accurate flow meter operation. The central issue arises when coupling CFD and optimisation techniques, which have been used extensively in the last 20 years as a powerful tool to find the best possible parameters (shape, operating condition, model variables, etc) in industrial and academic applications alike [41].

Design, shape, and topology optimisation methods distinguish geometrical optimisation by the use of CFD. These methods are based on the characterisation of key geometrical parameters [95, 96] and the solution of the adjoint equations in their discrete [49] or continuous [48] versions. Whereas shape and topology optimisation has shown its maturity in applications like structural optimisation [97], the added complexity of flow physics (especially due to turbulence) still adds challenges to democratising and validating these methods adequately. In addition, current shortcomings of optimisation studies have been reported, highlighting the need to perform research based on a thorough understanding of the methods and results, their time-effectiveness, generalisation, scalability, and experimental validation [98]. Hence, nowadays design optimisation presents the biggest potential, most effective, and most well-known approach to yield significant improvements in an ultrasonic flow meter that can be tested and validated with currently available tools.

Algorithms in design optimisation which are based on finding the minimum (or maximum) of one or more given functions in a multidimensional parameter space include slope followers, simplex methods [42], multi-objective evolutionary [43], particle swarm algorithms [44], and many more. An early recognised problem is that these methods require the evaluation of the objective function (i.e. performing a CFD computation) in a large number of test configurations, e.g., $\mathcal{O}(100)$ direct numerical simulations (DNSs) are conducted in Ref. [99], which require considerable computational resources. This led to a distinct development based on the use of a relatively smaller set of CFD simu-

lations (whose parameters are selected using specific methods [45]) to create computationally cost-efficient models (known as response surfaces or surrogates [47]) that are then optimised. These methodologies have been partially applied to various engineering applications such as, but not limited to a laidback fan-shaped hole for film-cooling [100], where a single objective function is optimised with surrogate-based optimisation (SBO) in a 3D case with structured mesh generation; aero-structural optimisation of plane wings [101], where a 3D multi-physics problem is solved by SBO with a structured-grid-deformation algorithm and a multi-objective problem; gas cyclones [102], where CFD observations and experimental data were taken from the literature to perform multi-objective SBO by evolutionary algorithms; centrifugal volute pumps [103], where the impeller and the volute were improved by SBO in different phases and results were supported by experiments; and ground vehicles [104], where a single objective problem was solved by SBO and experiments were used to validate the surrogate model. However, there have not been any studies adopting these optimisation methods applied to an ultrasonic flow meter. In addition, the literature is likewise lacking reliable studies of these methods for complex 3D wall-bounded fluid-flow problems at high Reynolds numbers, the exclusive use of unstructured meshing techniques, and the support of experimental validation of the results.

Table IV.1: Fixed geometry parameters common to all cases. Note that the i, o, m, s, and c subscripts stand for inlet, outlet, meter, stand, and constriction respectively. Moreover, the parameter δ includes a narrow distance between the reflector and the pipe to eliminate possible singularity points which could yield divergences, overlapped, or collapsed edges during the geometry generation.

Parameter	Value
D	20 mm
D_i	$0.865D$
L_i	$5D$
L_o	$5D$
L_m	$9.5D$
L_c	$2.25D$
δ	$0.05D$
α_s (rad)	π / 4
α_c (rad)	π / 3

In this study, optimisation tools based on surrogate modelling with the use of CFD with Reynolds-averaged Navier-Stokes (RANS) turbulence modelling, are applied to improve the performance of a two-stand ultrasonic flow meter with an internal reflection of the beams. The study aims to identify the key parameters and objective functions of the system and obtain a new significantly improved design compared to the baseline case. Section IV.2 presents the numerical and experimental methods and assumptions employed. Section IV.3 shows the results obtained and discusses the findings with experimental validation of the optimisation methods. Finally, a summary and discussion of the findings are presented in Section IV.4.

IV.2 Methodology

To approach the optimisation problem, a surrogate based on Kriging and Gaussian processes (GPs) is generated following the design and analysis of computer experiments (DACE) to obtain the observations, given by the sequence of computer-aided design (CAD) geometry generation, meshing, CFD solution, and post-processing of results [46]. In order to evaluate the performance of the flow meters, two main functions are defined based on the pressure losses and the measurement uncertainty, defining a multi-objective optimisation problem. Furthermore, an efficient sampling plan is described, and an infill criterion constrained by quality metrics is specified. Moreover, the applied methodology is developed entirely with open-source software at all of its stages where a flow diagram of the complete optimisation methodology is depicted in Fig. IV.2.

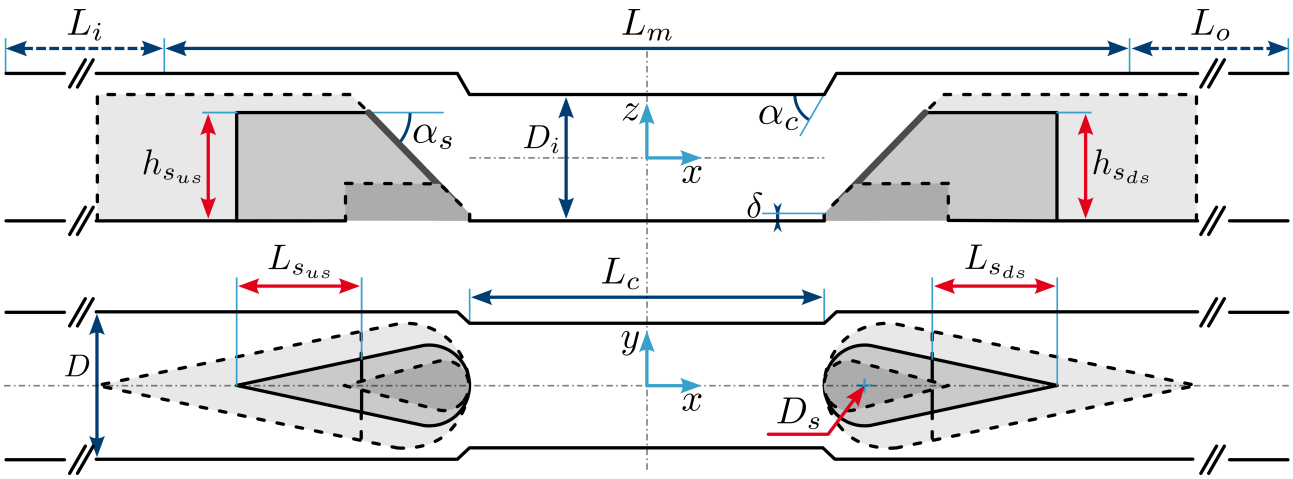

Figure IV.3: Design variables (in red) and parameter description (in blue) of the baseline flow meter geometry for y-normal (top), and z-normal (bottom) planes. All stand edges are filleted with a constant radius of $0.05D$ to aid unstructured-meshing prism layer extrusion. Note that the origin of the coordinates is located at the mid-point of the constriction section. The solid lines show the baseline geometry, and the dotted lines depict the threshold geometries.

IV.2.1 Case parametrisation

The reference flow meter studied is based on a modified version of Kamstrup A/S *flowIQ 2200* with a configuration of two-stand with the internal reflection of the beams. The flow meter geometry is parametrised by CAD and modified to approach studies based on numerical and experimental methods. The parametrisation yields the geometry depicted in Fig. IV.3 with fixed geometric values shown in Table IV.1. This geometry exhibits a compromise between real flow meter fidelity and the suitability of numerical and experimental studies.

A pipe diameter of $D = 20$ mm is selected to be consistent with the pipe diameter of the reference flow meter. Five design variables are chosen to perform the optimisation study due to their impact on flow meter performance and pipe blockage. Furthermore, due to the geometrical constraints of the system and the design variables chosen, certain geometrical constraints must hold to avoid overlapping or collapsed edges during CAD generation:

$$D_{s_{min}} + L_{s_{min}} \geq \frac{h_{s_{max}}}{\tan \alpha_s}, \tag{IV.1a}$$

$$L_{s_{max}} \leq L_m - 2h_{s_{max}} \tan \alpha_s - L_c, \tag{IV.1b}$$

where for Eq. (IV.1a) and Eq. (IV.1b), $D_{s_{min}}$ is the minimum stand diameter, $L_{s_{min}}$ and $L_{s_{max}}$ are respectively the minimum and maximum tail-length of the stands, $h_{s_{max}}$ is the maximum stand height (constrained by the pipe diameter), L_m is the flow meter length, L_c is the constriction length, and α_s is the reflector angle (fixed at $\pi/4$).

The design optimisation is therefore constrained as shown in Table IV.2. The thresholds likewise define the design space for the optimisation, which is normalised by the unit cube to avoid scaling issues as

$$\mathcal{D} = [0, 1]^{\mathcal{K}}, \tag{IV.2}$$

where $\mathcal{D}$ is the design space, and $\mathcal{K} = 5$ is the number of design variables following the normalisation

$$x_{\text{norm}} = \frac{x - x_{\text{min}}}{x_{\text{max}} - x_{\text{min}}}. \tag{IV.3}$$

Table IV.2: Thresholds of the design optimisation and relative variation compared to the baseline case.

Parameter	Value			
	Baseline case	Minimum	Maximum	Relative variation
D_s	$0.6125D$	$0.3655D$	$0.9D$	0.59 - 1.47
$L_{s_{us}}$	$1.25D$	$0.5D$	$2.75D$	0.4 - 2.2
$L_{s_{ds}}$	$1.25D$	$0.5D$	$2.75D$	0.4 - 2.2
$h_{s_{us}}$	$0.7785D$	$0.25D$	$0.865D$	0.32 - 1.11
$h_{s_{ds}}$	$0.7785D$	$0.25D$	$0.865D$	0.32 - 1.11

IV.2.1.1 Objective functions

Flow meters can be distinguished by performance in terms of pressure drop and measurement uncertainty, where both of these quantities are aimed to be minimised. The pressure drop in the system is straightforwardly calculated as

$$\Delta p = \frac{1}{A_i}\int_{A_i} p\, dA - \frac{1}{A_o}\int_{A_o} p\, dA, \tag{IV.4}$$

where Δp is the pressure drop, p is the kinematic static pressure, dA is the cross-sectional area differential, and A_i and A_o are respectively the inlet and outlet cross-sectional pipe areas. However, there is no analytical function in terms of fluid mechanics that defines the measurement uncertainty of a flow meter of these characteristics. In practice, to estimate the time travelled by the sound wave, the mean and peak amplitudes of the sent and received signals are computed by an electronic calculator that reads the signals generated by the piezoelectric transducers, where uncertainty is taken into account. In order to perform a numerical study analogous to an ultrasonic wave travelling through the flow meter, it is theorised that when an ultrasonic signal is sent by a transducer, it gets altered by the flow before it reaches a receiver due to the following conditions (Fig. IV.4):

- **The signal delays or accelerates** its reception by the receiver transducer due to the flow velocity along the sound path. The higher the time difference, the higher the flow meter capability to measure low flows and the higher the measurement resolution:

$$u_\Omega = \frac{1}{V}\int_\Omega u \cdot \hat{e}\, dV. \tag{IV.5a}$$

- **The signal attenuates** due to energy dissipated by the turbulence kinetic energy, **and noise is generated** by the presence of turbulent structures in the flow:

$$u'_\Omega = \sqrt{\frac{2}{3}\frac{1}{V}\int_\Omega k\, dV}. \tag{IV.5b}$$

- **The signal morphs** its original shape due to velocity gradients along the sound path, yielding higher uncertainty in the measurement:

$$\sigma_{u_\Omega} = \sqrt{\frac{1}{V}\int_\Omega \left(u_{\Omega_i} - \langle u_\Omega \rangle\right)^2 \cdot \hat{e}\, dV}; \tag{IV.5c}$$

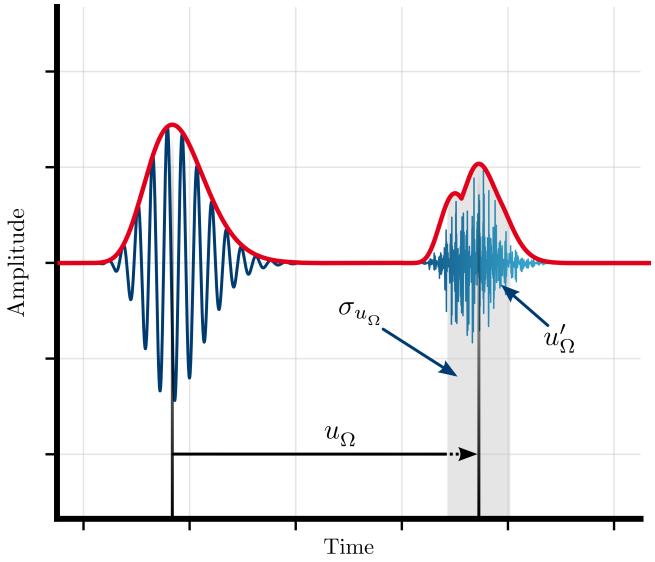

Figure IV.4: Depiction of an altered ultrasonic signal from a sent transducer to a receiver.

in Eqs. (IV.5a), (IV.5b), and (IV.5c), Ω is the reflected sound-path volume, u is the flow velocity vector, u_Ω is the integrated velocity of the fluid in the sound-path volume, $\hat{e}$ is the unitary vector in the sound wave propagation direction, u'_Ω is the integrated velocity fluctuations in the sound-path volume, σ_{u_Ω} is the standard deviation of the integrated velocity distribution in the sound-path volume, k is the turbulence kinetic energy, and dV is the differential of the sound-path volume.

In order to evaluate these metrics, the reflected sound-path volume (Ω) of the system is defined and calculated by extracting three cylinder volumes from the case. The volumes follow the reflected sound beam between the transducers, which varies depending on the stand geometry as seen in Fig. IV.5.

Although the sound travels in both stream and counter-streamwise directions, the analysis of only one of the directions is required to evaluate the objective functions. Hence, for a single streamwise propagating beam, the sound propagation vector equals $\hat{e}_1 = [0, 0, -1]$ for the upstream vertical cylinder, $\hat{e}_2 = [1, 0, 0]$ for the streamwise horizontal cylinder, and $\hat{e}_3 = [0, 0, 1]$ for the downstream vertical cylinder.

Based on the analysis of the metrics from Eqs. (IV.4), (IV.5a), (IV.5b), and (IV.5c); two normalised objective functions are defined which quantify the performance qualities of ultrasonic flow meters:

$$f_1(x) = \frac{\Delta p}{u^2_{\text{inlet}}}, \tag{IV.6a}$$

$$f_2(x) = -\frac{V}{V_{\text{ref}}} \left(\frac{u_\Omega - u'_\Omega - \sigma_{u_\Omega}}{u_{\text{inlet}}} \right), \tag{IV.6b}$$

where $u_{\text{inlet}} = 1.41\ \text{m}\,\text{s}^{-1}$ is the uniform velocity of the fluid at the inlet, and V and $V_{\text{ref}} = 4.704 \cdot 10^{-6}\ \text{m}^3$ are the volume and the reference volume of the reflected sound-path (calculated from the baseline case), respectively. From these objective functions, Eq. (IV.6a) represents the pressure drop across the flow meter whereas Eq. (IV.6b) represents the measurement uncertainties of the flow meter.

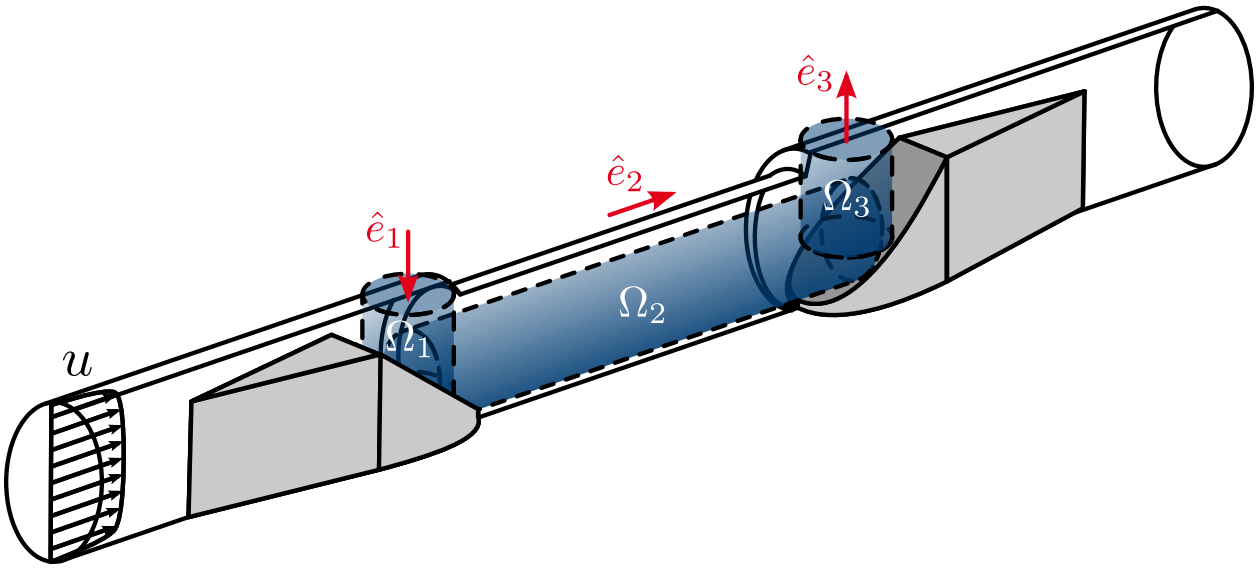

Figure IV.5: Definition of sound path volume by three cylinder-volume decomposition and unitary vectors of the reflected beam.

IV.2.2 Sampling plan

Three main algorithms are used in order to sample observations and data in this study: Monte Carlo, full factorial, and Latin hypercube (Fig. IV.6). Monte Carlo sampling is used when extracting the test subset to compute the surrogate quality, while full factorial sampling is used for visualisation purposes. Since the chosen sampling plan for the initial observations is oriented to be *space-filling*, Latin Hypercube Sampling (LHS) [105] with optimised design by the enhanced stochastic evolutionary (ESE) algorithm [106, 107] is used to obtain an initial sample of the surrogate with a minimum number of observations, and simultaneously, representing the real variability of the parameters. The initial sample by LHS with ESE follows $n_0 = 10\mathcal{K}$, where n_0 is the initial number of observations.

IV.2.3 Observations

Observations are based on the computation and post-process of a RANS $k-\omega$ SST [64] CFD simulation. The governing equations used for the CFD observations in this study are the incompressible form of the RANS equations, excluding heat transfer. These are written following Einstein's summation convention in their convective form [108] as

$$\frac{\partial \langle u_i \rangle}{\partial x_i} = 0, \tag{IV.7a}$$

$$\frac{\partial \langle u_i \rangle}{\partial t} + \langle u_j \rangle \frac{\partial \langle u_i \rangle}{\partial x_j} = -\frac{\partial \langle p \rangle}{\partial x_i} + \nu \frac{\partial^2 \langle u_i \rangle}{\partial x_j \partial x_j} - \frac{\partial \langle u_i' u_j' \rangle}{\partial x_j}, \tag{IV.7b}$$

where x_i is the i^{th} axis in Cartesian coordinates with $i = 1, 2, 3$ corresponding to the stream-wise (x), lateral (y), and vertical (z) directions, respectively. $(u_1, u_2, u_3) = (u, v, w)$ are the components of the velocity field, t is time, p is the kinematic pressure, and ν is the molecular

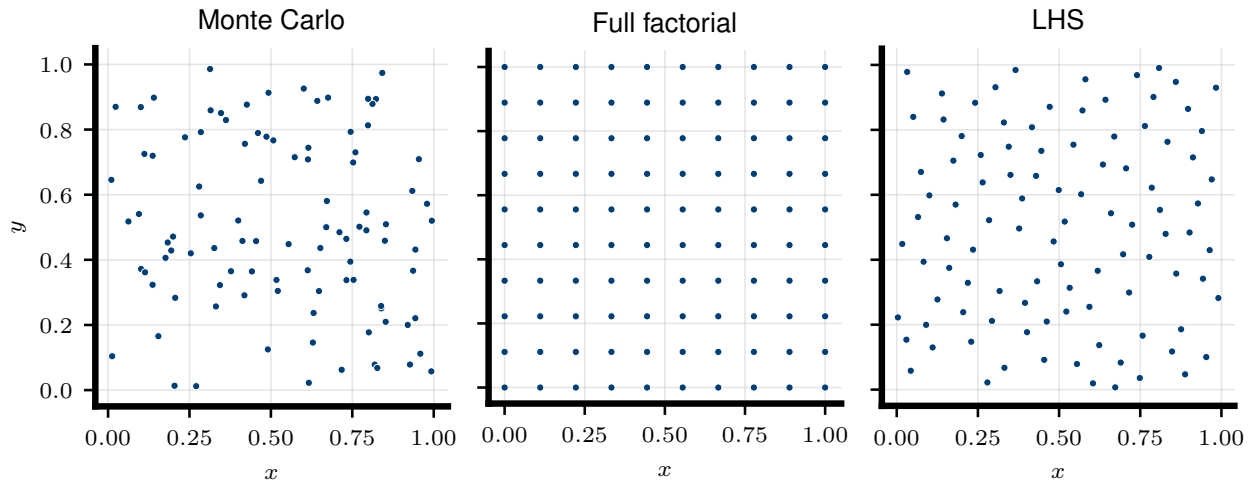

Figure IV.6: Sampling methods: Monte Carlo (left), full factorial (middle), and LHS with genetic algorithm optimisation (right).

kinematic viscosity. The angle $\langle\cdot\rangle$ operators represent the mean value, and the prime superscript $\cdot'$ represents its fluctuating part. Furthermore, the equations of fluid motion are solved numerically by the general-purpose software OpenFOAM [65].

The chosen grid, its grid independence study, and the turbulence model selection follow our previous numerical and experimental investigations in Ref. [59], where a time-efficient wall-modelled hexahedral-based grid is generated for all cases. Walls are considered perfectly smooth and the wall model used is based on the prediction of the turbulence kinematic viscosity (ν_t) based on the turbulent kinetic energy (named *nutkWallFunction* in OpenFOAM). Moreover, symmetry boundary conditions are applied at the $x-z$ plane. For further details on the numerical code, initial and boundary conditions, verification and validation against the experiments, the reader can refer to Ref. [59].

IV.2.4 Surrogate construction

A surrogate attempts to map $y = f(x)$ defined by the optimisation problem with an approximated function $\hat{y} = \hat{f}(x)$ based on the known observations [109]. Of the multiple approaches to generating a surrogate, Kriging (also called spatial correlation modelling) [110, 111] has been chosen due to its well-known implementation, its capability of computing uncertainties, and its computation speed. In this study, Kriging interpolates the observations as a linear combination of a know deterministic term with a constant model and an added realisation of a stochastic process as follows

$$\hat{y} = \sum_{i=1}^{k} \beta_i f_i(x) + Z(x), \tag{IV.8}$$

where $\hat{y}$ is the surrogate prediction, β is a constant deterministic model, $f(x)$ is the known function, and $Z(x)$ is the realization of a stochastic process of zero mean and spatial covariance function given by

$$\operatorname{cov}\left[Z\left(x^{(i)}\right), Z\left(x^{(j)}\right)\right] = \sigma^2 R\left(x^{(i)}, x^{(j)}\right), \tag{IV.9}$$

where R is the spatial correlation function, which controls the smoothness of the Kriging model, the differentiability of the response surface, and the effect of the nearby sampled

points. In this study, the spatial correlation is defined following the squared exponential (Gaussian) function as

$$\prod_{i=1}^{nx} \exp\left\{\left[-\theta_l \left(x_l^{(i)} - x_l^{(j)}\right)^2\right]\right\}, \quad \forall \theta_l \in \mathbb{R}^+, \tag{IV.10}$$

where the correlation scalar θ_l is defined such as, for each point, a hyper-parameter θ_l is given to define the variance of a GP at each point (higher values of θ_l represent higher gradients in the correlation between points). Maximising the *maximum likelihood estimation*, it is possible to find the optimum values for the matrix θ_l and other hyper-parameters of GPs such as the mean μ, and standard deviation σ [112]. Due to the re-meshing operation between samples, discontinuities on the solution space are expected, hence, the methodology evaluates the yielded noise and applies L1 regularisation to obtain a smooth response surface.

IV.2.5 Quality metrics

To ensure the generation of a high-quality surrogate, a number of random test observations $n_t = 0.6n$ $x \rightarrow y$ are taken. The root-mean-square error (RMSE) and Pearson's correlation coefficient squared (r^2) are calculated to evaluate the initial surrogate quality as follows

$$\text{RMSE} = \sqrt{\frac{\sum_{i=1}^{n_t} \left(y^{(i)} - \hat{y}^{(i)}\right)^2}{n_t}}, \tag{IV.11a}$$

$$r^2 = \left(\frac{\text{cov}(y, \hat{y})}{\sqrt{\text{var}(y)\text{var}(\hat{y})}}\right)^2. \tag{IV.11b}$$

Values of 0.1 and 0.8 for RMSE and r^2 respectively are set as thresholds of the quality of surrogates in this study, following [113, 114].

IV.2.6 Infill space exploration

Exploring the surrogate beyond the initial sampling provides an overall lower level of uncertainty and a more accurate approximation in extrema and unexplored regions. To explore the surrogate, Bayesian optimisation strategies based on efficient global optimisation (EGO) [115, 116] are applied. EGO is based on a figure of merit that balances local and global search: the expected improvement ($E[I(x)]$) [117]. If F is the black-box function to be predicted by Kriging, and $X = \{x_1, x_2, \ldots, x_n\}$ are the observed locations, yielding the responses $Y = \{y_1, y_2, \ldots, y_n\}$, the expected improvement is calculated as

$$E[I(x)] = (f_{\text{min}} - \mu(x))\,\Phi\left(\frac{f_{\text{min}} - \mu(x)}{\sigma(x)}\right) + \sigma(x)\phi\left(\frac{f_{\text{min}} - \mu(x)}{\sigma(x)}\right), \tag{IV.12}$$

where $f_{\text{min}} = \min Y$, and $\Phi(\cdot)$ and $\phi(\cdot)$ are respectively the cumulative and probability density functions of $\mathcal{N}(0,1)$, following the distribution $\mathcal{N}(\mu(x), \sigma^2(x))$. Hence, the following sampling point is determined by

$$x_{n+1} = \arg\max_x \left(E[I(x)]\right). \tag{IV.13}$$

The space exploration is performed by sampling new data in each of the objective functions separately, where one sample of $n_{\text{EGO}} = 0.5n_0$ $x \rightarrow y$ for each objective is taken, yielding a total of $10\mathcal{K} = 50$ new sampled points.

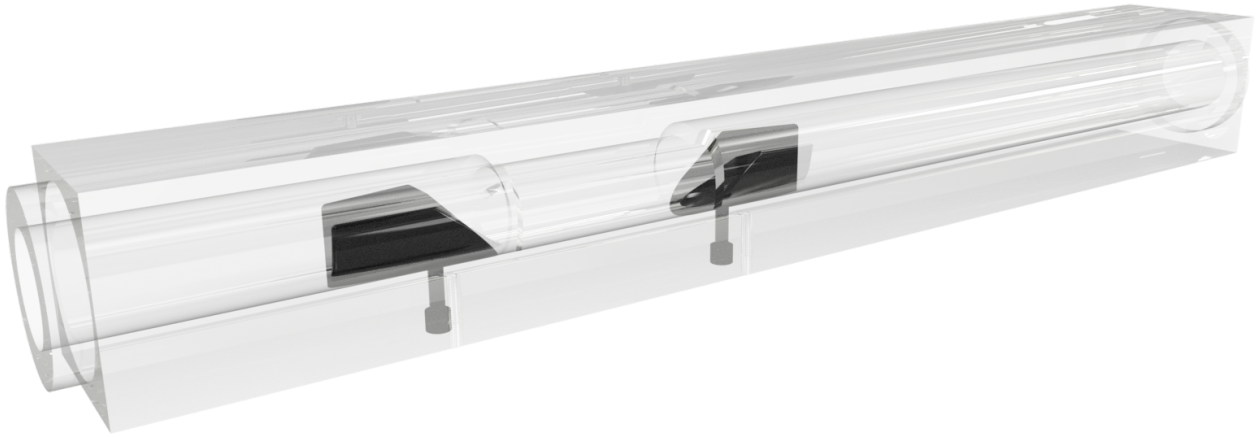

Figure IV.7: Rendered image of the test pipe and baseline-case stands used in the experiments. The pipe is manufactured by drilling a PMMA block whereas the stands are fabricated by additive manufacturing. Two passing holes are drilled with a thread in the stands to accurately fix them in place with screws.

IV.2.7 Multi-objective solution

One of the greatest advantages of the Kriging method is that algorithms that widely explore the objective space can be applied. Hence, in order to find the optima of the surrogate, the multi-objective evolutionary algorithm (MOEA) NSGA-II [118] is chosen. The choice is made due to the versatility, fast and efficient convergence, non-penalty constraint handling, and wide-range search of solutions of the algorithm. This ensures that the improved solutions are non-dominated, do not fall into local minima, and the global optimum is highly likely to be found for the sampled response surface.

IV.2.8 Experimental methods

A polymethyl methacrylate (PMMA) pipe and acrylonitrile butadiene styrene (ABS) powder stand set are used to perform laser Doppler velocimetry (LDV) and pressure drop experiments. The experimental set is manufactured as a 1:1 representation of the numerical simulations. Furthermore, PMMA is chosen to minimise the light refraction between the water and the material due to the similar magnitude of their refractive indices. The experimental set is placed on a test bench with accurate control of temperature and volumetric flow, maintaining constant flow conditions throughout the tests (Fig. IV.7).

LDV experiments are capable of yielding qualitative and quantitative velocity data with minimum influence on the flow. To perform LDV, silver-coated glass-hollow neutrally-buoyant reflective particles of $15\ \mu\mathrm{m}$ in diameter are introduced in the test bench and axial-velocity experiments at x-normal planes are taken. A Nd:YAG (neodymium-doped yttrium aluminium garnet) laser of $100\ \mathrm{mW}$ and a wavelength of $\lambda = 532\ \mathrm{nm}$ is used to obtain the measurements [84]. A data-acquisition grid of 232 uniformly-spaced points is generated where the position of the laser probe is adjusted by means of a 3D traverse unit together with ray-tracing methods to account for the light diffraction of the different media. The traversing unit is motorised and programmable in the y and z axis where the change in the x direction is done manually (Fig. IV.8). Finally, the LDV experiments are taken with a minimum of 500 valid bursts per point, ensuring mean axial-velocity statistical convergence.

Pressure drop experiments are taken by introducing two high-accuracy pressure transduc-

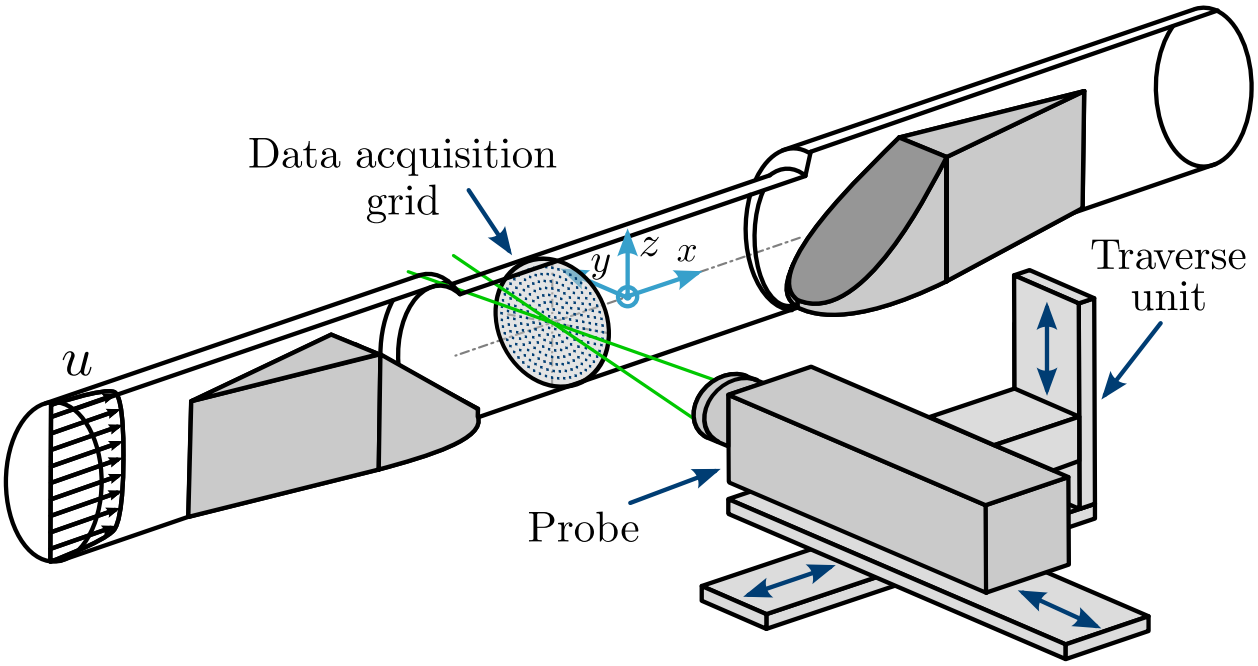

Figure IV.8: LDV experimental setup schematic and cross-sectional data acquisition grid.

ers (model OMEGA PX429-100GI with measuring uncertainty of $\pm 0.08\%$) up and downstream of the measurement pipe. Both sensors are calibrated and measurement repeatability is ensured before the final measurement is taken. Finally, the experiments are taken by sampling pressure data every 5 ms for 150 s, ensuring first and second-order statistical convergence.

IV.3 Results and discussion

Optimisation and experimental results are hereafter depicted and discussed. A surrogate based on the design of experiments by CFD is generated. Contour plots showing the influence of the design variables in the objective functions and quality results of the surrogate concerning optimisation results are shown. The Pareto front solution of both objective functions evaluated is displayed together with the main geometrical differences of the non-dominated cases. Furthermore, a qualitative analysis of the velocity contours between numerical and experimental cases is performed. Finally, numerical validation of the Pareto front results is shown followed by experimental validation of the design space and objective functions defined. All results are shown with their associated uncertainty and are similarly described and discussed followed by their corresponding figures.

IV.3.1 Surrogate quality

The evaluation of the surrogate is based on a direct comparison between the surrogate prediction ($\hat{y}$) and the numerical simulation results (y). The RMSE and r^2 metrics of this analysis present the overall quality of the surrogate. While r^2 shows the capacity of the surrogate model to explain the variability of the dataset, the RMSE represents the average deviation of the predicted and numerical values. These metrics applied to the generated surrogate are shown in Fig. IV.9, where the final quality achieved is shown in Table IV.3.

The prediction of the surrogate for several LHS $n_0 = n_{\text{EGO}} = 50$ yields an overall high agreement with the numerical values. Lower values of the objective functions yield

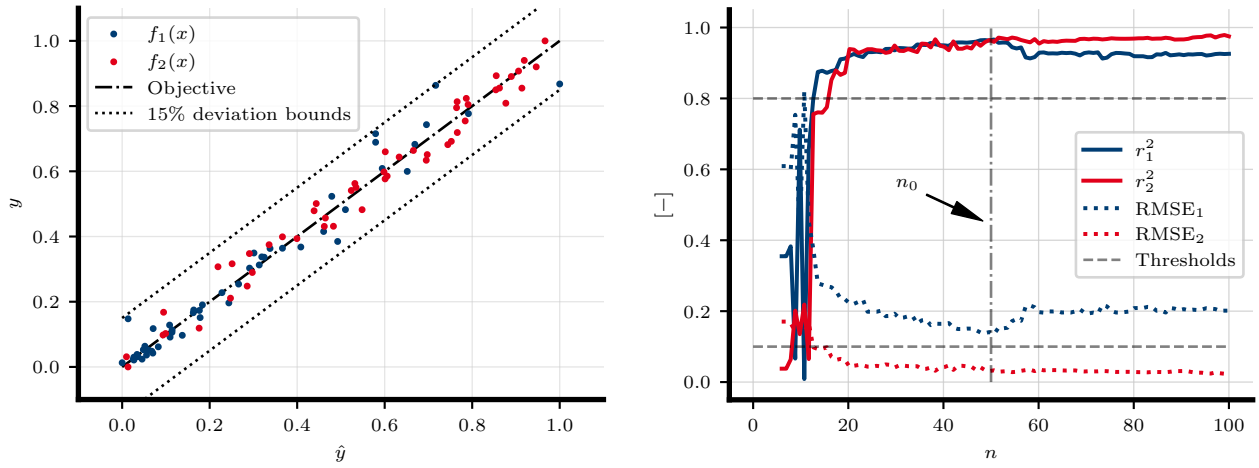

(a) Test values in function of the surrogate prediction with 15% deviation bounds.

(b) Evolution of surrogate quality parameters in function of the number of sampled points where at $n = n_0 = 50$, EGO sampling takes place.

Figure IV.9: Surrogate quality through RMSE and r^2 for the two objective functions analysed. The quality thresholds in Fig. IV.9b are set to 0.8 and 0.1 for r^2 and RMSE respectively.

higher agreement by the surrogate than higher values, where slight deviations are seen (Fig. IV.9a). The surrogate yields all predictions inside the 15% deviation bounds for both objective functions, showing that the surrogate predicts the objective space with reasonable accuracy. However, slight deviations in the surrogate predictions are expected due to the noisy behaviour of the solution space.

Regarding the evolution of the surrogate quality in function of the number of sampled points (Fig. IV.9b), the surrogate model does not yield any conclusive results until $n \approx 15$ points are sampled. Consequently, all quality metrics consistently improve until $n = n_0$ is reached. From $n \in (50, 100]$, the EGO algorithm predicts the new sampling points and a tendency towards convergence is seen in the quality metrics. As seen in the results of Fig. IV.9b, the solution space is noisy due to the introduced discontinuities by the re-meshing operation between samples; therefore, due to this fact and the regularisation applied in the Kriging method, after EGO, both RMSE and r^2 metrics of $f_1(x)$ slightly worsen, while for $f_2(x)$, they slightly improve. This shows the high sensitivity of the boundary layer prediction, wall-shear stress (τ_w), and Δp to geometrical changes in the numerical simulations.

Table IV.3: Final surrogate quality values.

Objective	Quality metric	
	RMSE	r^2
$f_1(x)$	0.202	0.926
$f_2(x)$	0.003	0.975

These results show that by taking a low number of samples ($n = 10\mathcal{K}$), the surrogate quality metrics achieve better values. Moreover, once EGO sampling is done, the quality parameters display noisy behaviour and a higher value of RMSE$_1$ than the initial obtained by LHS. Although counter-intuitive if only these data are taken into consideration, sampling with EGO has shown an overall improvement of the surrogate in terms of lower uncertainty of the final Pareto front results. In addition, since regularisation is applied to handle the noisy solution space and since multiple close proximity points yielding noisy data are evaluated by EGO, the increased value of RMSE$_1$ is justified.

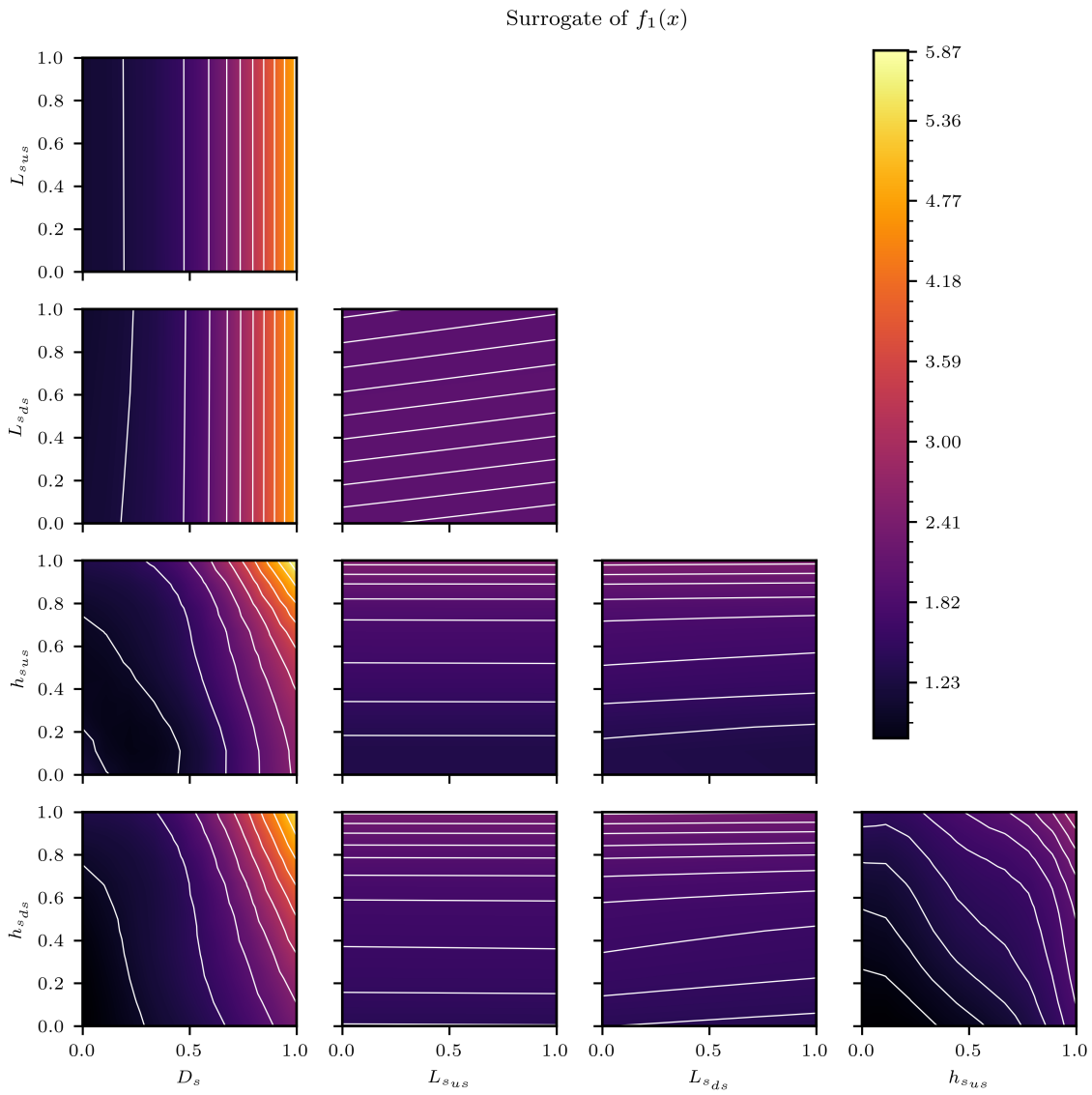

Figure IV.10: Surrogate visualisation of $f_1(x)$. Each tile shows a contour of $f_1(x)$, connected to pressure drop, versus two of the design variables, with the remaining variables held at the baseline value of Table IV.2.

IV.3.2 Surrogate visualisation

The possibility of visualising the response of the different design variables in the objective space gives the advantage of obtaining global knowledge of the optimisation problem and the influence of the design variables. Since the visualisation of a 5-dimensional space is non-trivial, certain simplifications must be applied to visualise the changes in the design variables in function of the objectives. Hence, each pair of design variables is shown in function of each objective in Figs. IV.10 and IV.11, with the remaining design variables, kept at their baseline values. Regarding $f_1(x)$, most of the design variables show a linear or quasi-linear relationship, where the variables showing clear no-linearity are D_s, $h_{s_{us}}$, and $h_{s_{ds}}$ in function of each other. The results show that the variable with higher influence in the pressure drop is D_s, followed by the height of both stands; whereas the rest of the variables show a lower influence in $f_1(x)$. Lower values of all variables show a decrease in Δp, which corresponds to reduced blockage of the stands in the pipe, minimising pressure and viscous

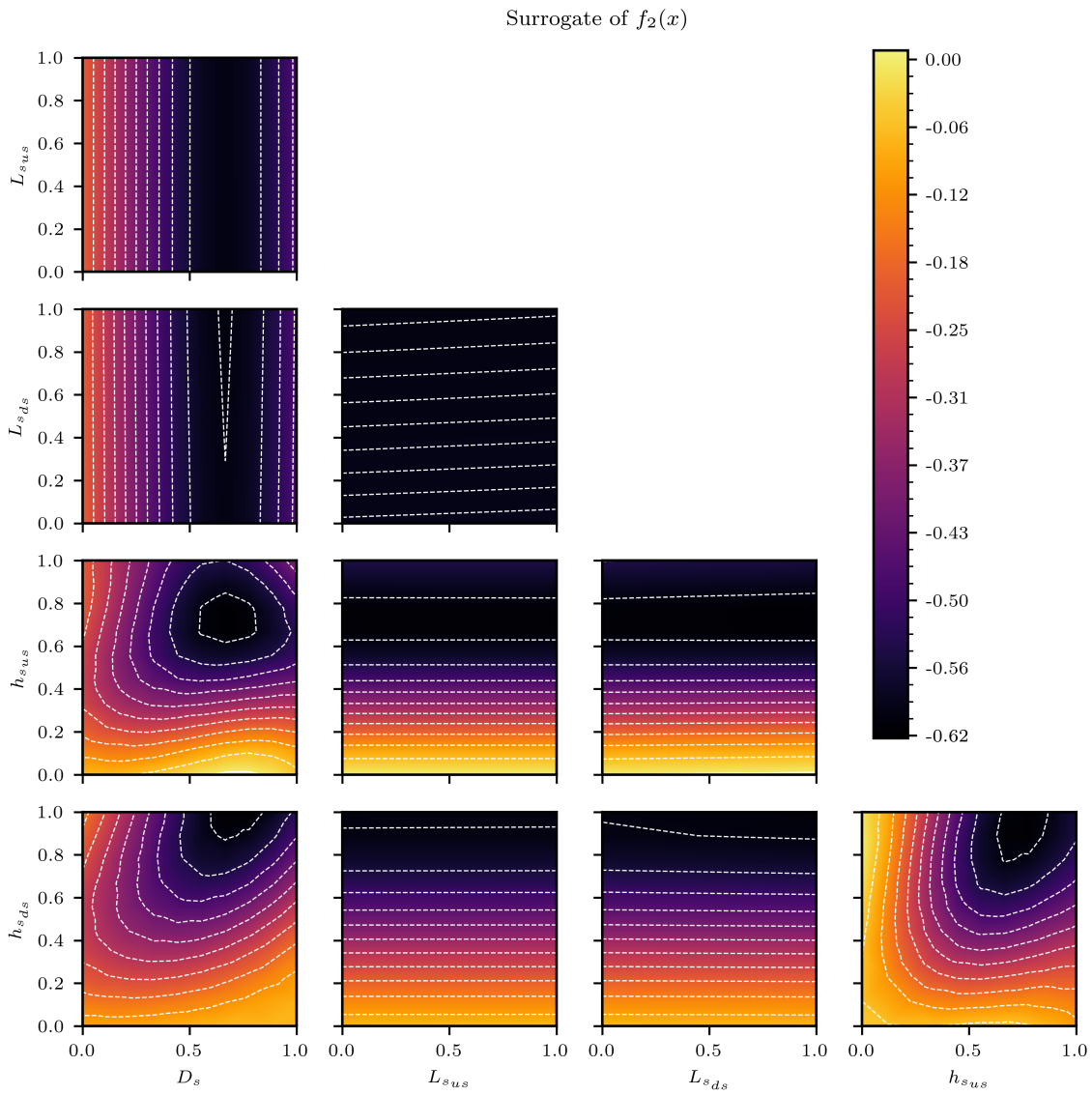

Figure IV.11: Surrogate visualisation of $f_2(x)$. Each tile shows a contour of $f_2(x)$, connected to measurement uncertainty, versus two of the design variables, with the remaining variables held at the baseline value of Table IV.2.

drag. Correspondingly, high values of the variables increase blockage and the formation of complex flow structures, increasing pressure drop. The only variable which shows a decrease in $f_1(x)$ by increasing its value is $L_{s_{ds}}$, where a longer stand length delays flow separation and reduces recirculation at the downstream stand region, yielding lower pressure drag and decreasing Δp. Regarding $f_2(x)$, linear or quasi-linear behaviour is seen between the same variables as with $f_1(x)$, where non-linear behaviour is likewise seen by D_s, $h_{s_{us}}$, $h_{s_{ds}}$ in function of each other. In contrast with pressure drop prediction, $f_2(x)$ displays non-trivial locations of the different minima. In the range of 0.7 to 0.9, values of all design variables except the stand lengths show a tendency towards the global minimum. Furthermore, the stand lengths show a similar behaviour as in $f_1(x)$, where low values of $L_{s_{us}}$ and high values of $L_{s_{ds}}$ show a tendency towards the minimum of $f_2(x)$. The relationship of the variables and $f_2(x)$ is not as trivial as the prediction of pressure drop. Generally, a higher blockage and influence in the bulk flow by the stands does accelerate the fluid in the measurement region and increase the measurement volume, which improves $f_2(x)$. However, the excessive

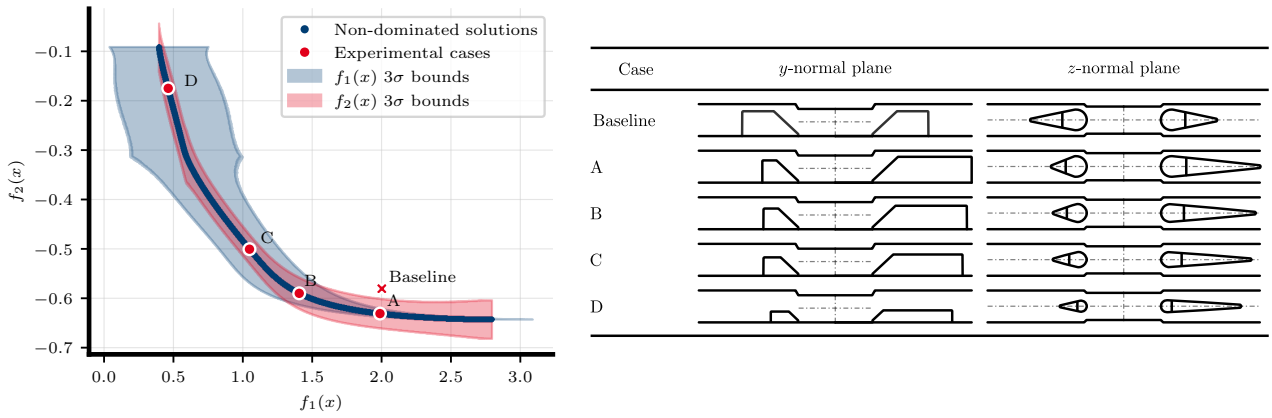

(a) Pareto front.

(b) Comparison of geometries of the experimental cases chosen.

Figure IV.12: Non-dominated solutions from the multi-objective optimisation and chosen experimental cases. Note that the shaded areas in Fig. IV.12a represent the 3σ confidence bounds for each of the objectives.

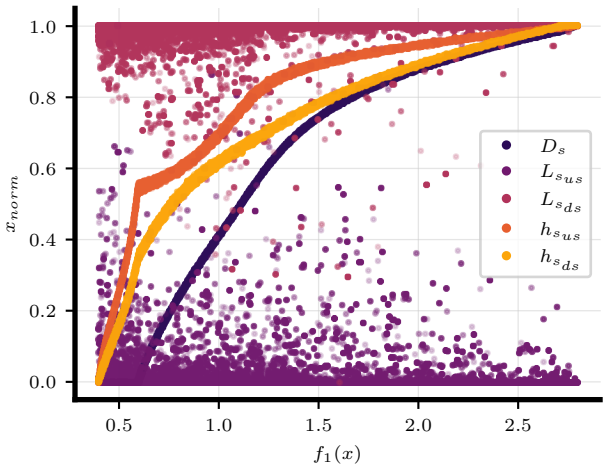

Figure IV.13: Normalised non-dominated design variables variability.

blockage does likewise yield stronger and bigger vortical structures, higher turbulence kinetic energy (TKE), and complex flow conditions which penalise $f_2(x)$.

From the surrogate visualisation, it can be highlighted that both functions display minima at almost opposing values of the design variables, which shows the complexity of designing geometries to improve the system.

IV.3.3 Pareto front solutions

The MOEA yields a front of non-dominated solutions where any change to the design variables cannot improve one objective without further worsening the other. These solutions are known as the Pareto non-dominated front (Fig. IV.12a). Since Kriging is based on GP, the method likewise yields a unique uncertainty range for each objective function and design solution. The uncertainty ranges of both objective functions are taken into consideration since the evaluation of both values is subjected to a validation study. The chosen uncertainty range

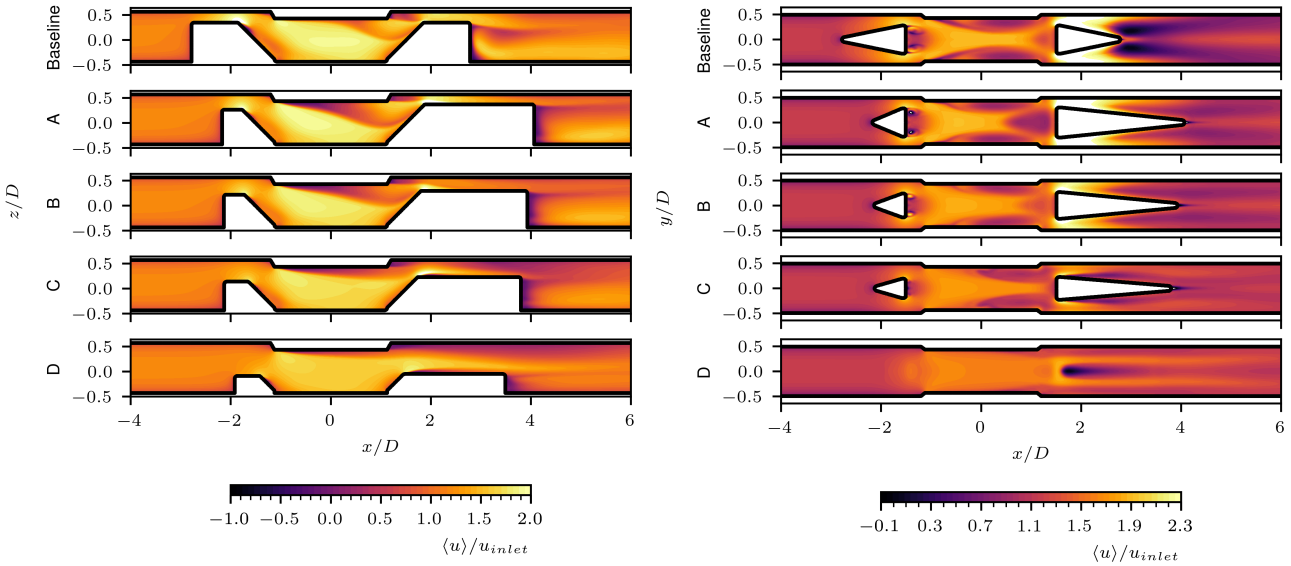

(a) Normalised axial velocity at y-normal plane. (b) Normalised axial velocity at z-normal plane.

Figure IV.14: CFD contours of normalised axial velocity at y- and z-normal planes for different geometrical cases.

for the method is 3σ (equivalent to 99.7% of the distribution) due to the complexity of the case of study, however, more conservative uncertainty ranges could be chosen in other cases depending on the required accuracy and the nature of the system to optimise.

Diverse Pareto fronts have been studied and generated in order to evaluate the convergence and quality of the surrogate in function of the number of samples. After this study, it has been concluded that converged non-dominated results with minimum uncertainty are yielded after EGO sampling and a population of 1000 through 500 generations by NSGA-II.

To experimentally validate the methodology, samples are taken and manufactured of the non-dominated solutions at $f_1(x) = [2, 1.4, 1.05, 0.46]$, which are hereby referred to alphabetically as cases A to D respectively as depicted in Fig. IV.12. These cases are chosen to obtain a representative sample of the Pareto front and to obtain a sample of overall improved (respective to the baseline case) designs for both objective functions (cases A and B). Furthermore, the baseline case is likewise analysed with the applied methodology for reference. The geometry representation of these cases is depicted in Fig. IV.12b where the changes in geometry can be seen.

Regarding the design variable values, D_s, $h_{s_{us}}$, and $h_{s_{ds}}$ show a continuous trend, in contrast to $L_{s_{us}}$ and $L_{s_{ds}}$, where their solution space is discontinuous (Fig. IV.13). While the values of the continuous variables gradually change showing higher gradients at low values of $f_1(x)$, $L_{s_{us}}$ and $L_{s_{ds}}$ tend to yield the highest and lowest values possible, respectively. These results show the high influence of D_s, $h_{s_{us}}$, and $h_{s_{ds}}$ in the solution space compared to the stand tail lengths.

In addition, Fig. IV.14 and IV.15 are shown to provide an overview of the flow behaviour for the baseline and the sampled cases from the Pareto front. The axial velocity distribution (Fig. IV.14) of the baseline case shows an acceleration of the flow through the constriction where two vortices are generated (the reader can refer to [59] for further details). Three main shear layers are seen through the constriction, defining three regions of low velocity (two close to the pipe walls, and one close to the downstream stand) and a main region of high-velocity flow at the centre of the pipe. Downstream, a breakdown of the vortices takes place, the flow greatly accelerates due to the high blockage, and the flow separates after its

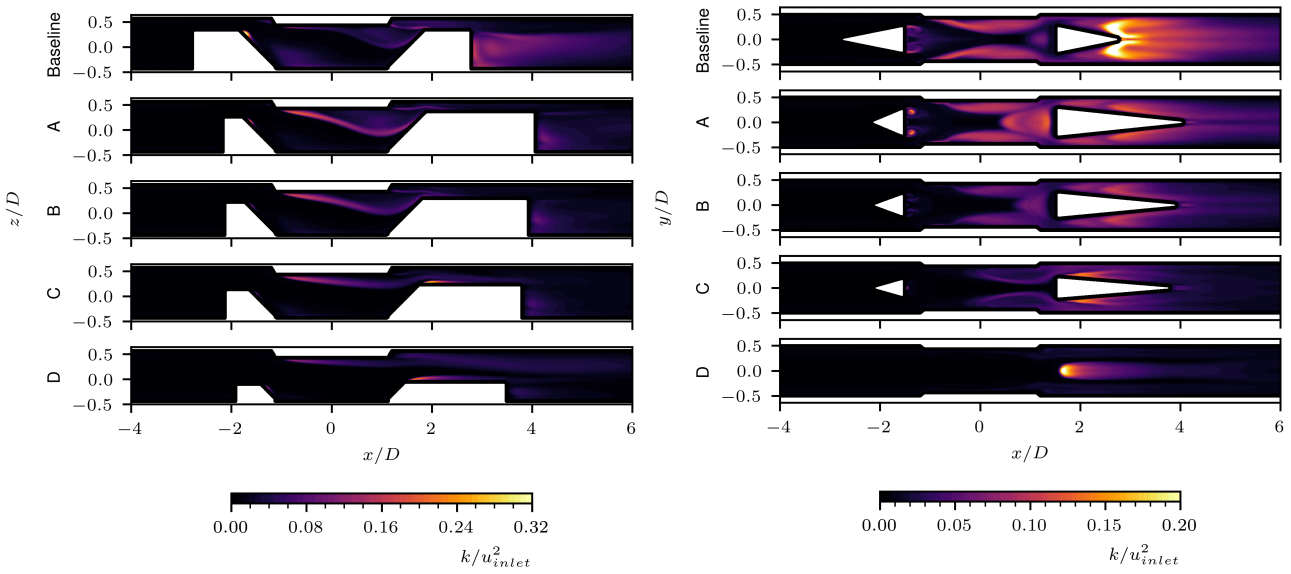

(a) Normalised TKE at y-normal plane.

(b) Normalised TKE at z-normal plane.

Figure IV.15: CFD contours of normalised TKE at y- and z-normal planes for different geometrical cases.

pass through the stand, creating a region where high TKE and mixing take place (Fig. IV.15).

In contrast, for cases A and B, the low-velocity regions at the constriction are smaller, whereas close to the downstream stand, the low-velocity region is bigger. This causes the high-velocity bulk flow region at the constriction to be wider and cover more cross-section of the pipe, favouring $f_2(x)$. A more defined shear layer can be seen in the y-normal plane for cases A and B, together with moderate values of TKE seen in the z-normal planes. This indicates a higher positive vertical velocity (w) at the region close to the downstream reflector, which is likewise favourable to $f_2(x)$.

Cases C and D, which display a best $f_1(x)$ performance, are characterised by a reduced blockage and stand volume. Hence, the flow prediction shows lower disturbances throughout the whole system. These low Δp cases display a delay in the prediction of the shear layers at the constriction, yielding a more uniform and wider high-velocity flow region, resulting in lower TKE generated. Concurrently, cases C and D show reasonably lower velocity gradients (favourable to $f_2(x)$) and lower maximum velocity magnitudes (against $f_2(x)$).

IV.3.4 Velocity field validation

Experimental LDV results are compared to numerical wall-modelled $k-\omega$ SST simulations in Fig. IV.16. The experiments are taken at three different cross-sections throughout the flow meter constriction at $x \in [-1, 0, 1]\ D$ for each of the optimised and baseline cases described in Fig. IV.12b.

At $x = -1D$, the location and magnitude of the vortices are accurately predicted in all cases. Similarly, the bulk flow is likewise predicted in agreement with the experiments for all cases and no major differences can be observed qualitatively.

A high level of agreement at $x = 0D$ can likewise be observed between experiments and simulations. However, slight differences can be recognised, predominantly in the axial velocity magnitude predicted by CFD at the uppermost pipe region for all cases except the baseline. For A to D cases, the axial velocity at the upper pipe section is underestimated

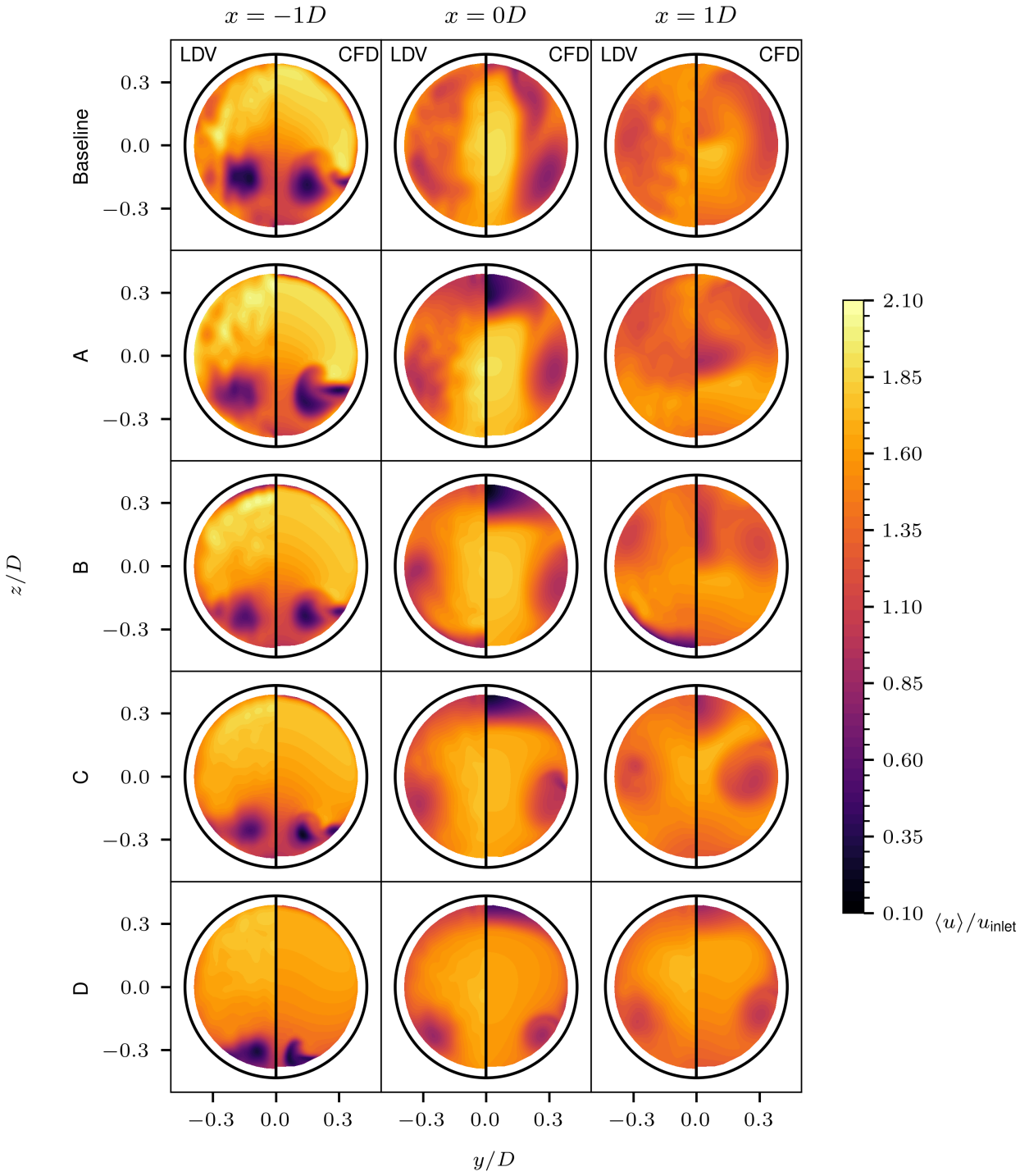

Figure IV.16: LDV and CFD results for normalised axial velocity. The left half of the cross-sections shows the LDV experimental results, whereas the right half shows the numerical results.

compared to LDV data. Despite these differences, there is a high level of qualitative agreement in terms of velocity gradients and vortices propagation in all cases.

Finally, at $x = 1D$, cases representing lower values of $f_1(x)$ (cases C and D) tend to show higher agreement between experimental and numerical results than cases at higher $f_1(x)$ (Baseline, A, and B cases). The main differences are seen at the baseline, case A, and case B, where the numerical simulations generally tend to marginally underestimate the velocity at

the centre of the pipe.

Overall, the LDV results show high agreement with the numerical simulations, qualitatively predicting the magnitude and gradients of the axial velocity regardless of the stand geometry; as well as the position, propagation, and magnitude of the vortices throughout the constriction with the different shear layers seen in the experiments.

IV.3.5 Pareto front validation

The validation of the optimisation methodology is performed by means of numerical simulations at diverse points in the Pareto front, and through the experimental values acquired for the sampled cases (Baseline, and A to D cases). The whole set of validation results is depicted in Fig. IV.17.

On one hand, the sampled numerical simulations are spaced linearly by 25 points in function of $f_1(x)$ from its minimum to maximum non-dominated values (Fig IV.17a). Numerical results show that predictions are inside the uncertainty ranges and a slight and expected noisy behaviour is observed. The region of $f_1(x) \in [1.6, 1.9]$ yields the highest deviation from the mean Pareto values, where RANS simulations predict three values of $f_2(x)$ outside the uncertainty bounds. These outliers show a slight overestimation of $f_1(x)$ and a reasonably high underestimation of $f_2(x)$. RANS models the turbulence instead of resolving it and levels of known uncertainties in RANS turbulence models (including $k-\omega$ SST) have been documented against high-fidelity methods [30, 31, 119–121]. Therefore, marginal inaccuracies when modelling complex turbulence are expected as seen in the results.

On the other hand, the comparison of experimental values is depicted in Fig. IV.17b and IV.17c, where the prediction of mean values of $f_1(x)$ is inside the uncertainty bounds of the surrogate model for all cases. Furthermore, results show that designs that aim to reduce pressure loss incur lower uncertainty.

Regarding $f_2(x)$, since it is not equitable to evaluate directly the function due to the limitations of the present experimental methodology, a modified version of the objective function and its associated uncertainty is defined as

$$\mathcal{F}_2(x) = -\left(\frac{u_\Omega - u'_\Omega - \sigma_{u_\Omega}}{u_{\text{inlet}}}\right)\Bigg|_{x \in [-1,0,1]D}, \tag{IV.14a}$$

$$\epsilon_{\mathcal{F}_2(x)} = \mathcal{F}_2(x)_{\text{LDV}} \left|1 - \frac{\mathcal{F}_2(x)_{\text{LDV}}}{\mathcal{F}_2(x)_{\text{CFD}}}\right|, \tag{IV.14b}$$

where $\epsilon_{\mathcal{F}_2(x)}$ is the associated uncertainty of the $\mathcal{F}_2(x)$ function and the subscripts LDV and CFD denote the evaluation of the function by experimental and numerical methods, respectively. The new function is evaluated for both CFD and LDV in order to perform a trustworthy comparison of the numerical and experimental results evaluated and averaged at the sampled cross-sections ($x \in [-1, 0, 1]D$). The objective of this evaluation is to validate experimentally the axial velocity and TKE predictions by CFD to ensure a correct estimation of $f_2(x)$.

Regarding the experimental validation (Fig. IV.17b), although the results yield high agreement for all $f_1(x)$ values, where the mean value of the experiments fits inside the surrogate uncertainty in all cases, there are higher associated uncertainties when approximating $\mathcal{F}_2(x)$ by experimental methods. The higher uncertainties are most likely due to the inability of current LDV hardware to obtain the same resolution as CFD methods, and the approximation of $u'_{\Omega\text{LDV}} \approx I_x u_x$ (where I_x is the axial turbulence intensity) due to the 1-dimensional data yield by LDV experiments.

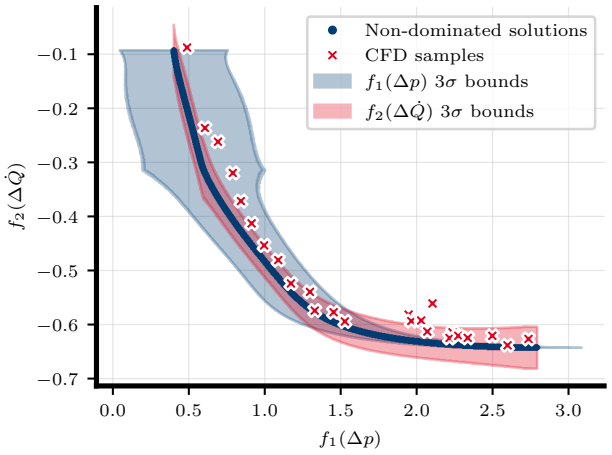

(a) Numerical validation by CFD with 3σ Gaussian uncertainty.

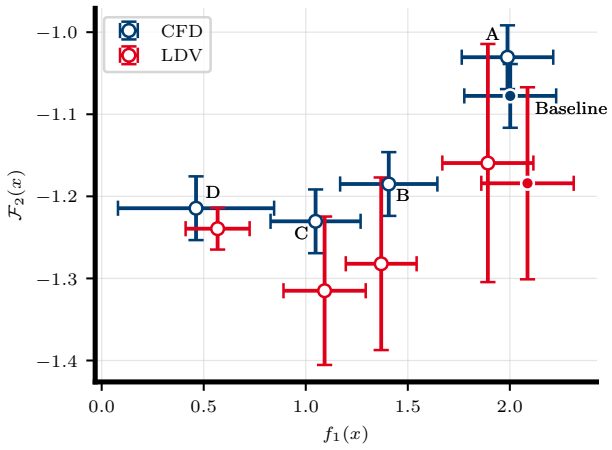

(b) Experimental validation with 3σ Gaussian uncertainty for $f_1(x)$ and ϵ uncertainty for $\mathcal{F}_2(x)$ as defined in Eq. IV.14b.

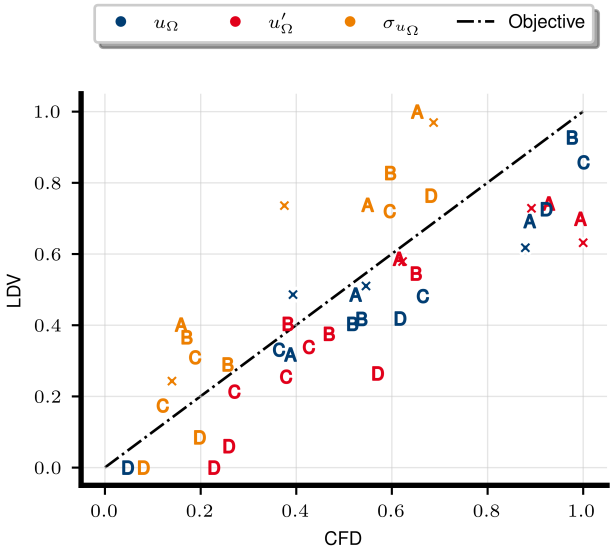

(c) Experimental and numerical comparative of normalised values of u_Ω, u'_Ω, and σ_{u_Ω} for each evaluated cross-section. Note that the baseline case results are represented by the cross marker and the rest of the cases by their corresponding letter.

Figure IV.17: Pareto front validation results with their dedicated uncertainty.

Despite these limitations, the mean experimental value of $\mathcal{F}_2(x)$ for case A is inside the uncertainty bounds. Nevertheless, the rest of the cases overestimate the mean value outside the numerical uncertainty. Concurrently, designs that aim to reduce $\mathcal{F}_2(x)$ suffer from significant uncertainty due to the complex flow behaviour throughout the flow meter and the limited accuracy of the present LDV and RANS simulations. Notwithstanding, the combined uncertainty of the experiments and the surrogate is partly inside the conformity bounds in all cases.

A more detailed analysis for the experimental validation is shown in Fig. IV.17c, where a comparison is performed between CFD and LDV results of the variables defining $\mathcal{F}_2(x)$ for

each cross-section and case. Whereas values of u_Ω are reasonably well-predicted in all cases, values of u'_Ω are overall slightly over-predicted and values of σ_{u_Ω} are under-predicted by the numerical simulations. Case B shows the best agreement with experimental results whereas the rest of the cases display a similar deviation from the experimental data.

IV.4 Conclusions

This study showed the suitability of design optimisation methods based on Kriging surrogate models to efficiently optimise residential ultrasonic flow meters. It has likewise been shown that these flow meters display a complex flow behaviour that wall-modelled RANS $k-\omega$ SST is able to predict with relatively good agreement even for diverse configurations of the baseline geometry evaluated.

Two characteristic functions based purely on fluid mechanics have been defined to analytically evaluate the performance of ultrasonic flow meters. One of the functions evaluates the pressure drop of the flow meter, whereas the other function evaluates the measurement uncertainties with a novel approach by analysing the flow complexities and unsteadiness throughout the flow meter sound path.

An approach of sampling by LHS together with an optimisation search infill criteria based on Bayesian strategies and the expected improvement ($E[I(x)]$) function have shown to be an efficient methodology to reach a high-quality response surface in a 5-dimensional design space yielding noisy results on the objective space. The optimal sampling found in this study suggests the use of $n_0 = n_{\text{EGO}} = 10\mathcal{K}$ to obtain a high-quality and space-filled surrogate.

The MOEA algorithm NSGA-II has shown its effectiveness to obtain a non-dominated front of solutions for the multi-objective problem, minimising both the pressure losses and measurement uncertainties of the flow meter and maximising the objective space exploration while avoiding local minima.

On one hand, the combination of numerical samples and LDV experiments have validated the surrogate and CFD predictions at the Pareto front with a relatively good agreement for $f_1(x)$ and its association with pressure losses, where all results are inside the established uncertainty bounds of 3σ. On the other hand, predictions of the measurement uncertainty function $f_2(x)$ have incurred higher uncertainties in connection to the limitations of current LDV hardware and low-fidelity RANS methods. Nevertheless, $f_2(x)$ validation results are partly inside the conformity bounds of the numerical and experimental data obtained. These results show that from an engineering standpoint, applied optimisation can be acted upon in industrial cases following the methodology of this study. Nonetheless, more detailed and accurate tools both numerically and experimentally can be employed if a more precise prediction of the flow is required.

Concerning the optimisation results, it has been shown that diverse geometries of the flow meter yield improved performance and lower pressure losses than the baseline case. A set of improved designs is found where non-dominated solutions range from a 67% pressure drop reduction to an 8.7% measurement uncertainty reduction relative to the baseline case. Specifically for case B in this study, improvements show a numerical 37.4% pressure drop reduction and a 4.9% measurement uncertainty reduction relative to the baseline case.

Finally, the work done in this study has shown the efficiency, robustness, and accuracy of CFD-RANS $k-\omega$ SST model applied to DACE design optimisation based on Kriging surrogate modelling to improve the design of ultrasonic flow meters where a thorough validation has been performed based on numerical simulations, pressure drop, and LDV experiments. The methodology applied in this study has the potential to likewise improve

wall-bounded systems governed by fluid motion with similar features.

V

Shape Optimisation

CFD-aided morphing and design optimisation of ultrasonic flow meters

ABSTRACT Ultrasonic flow meters with an intrusive two-stand configuration present a complex flow behaviour due to their unique geometry, which offers an interesting and challenging case to evaluate optimisation methods in wall-bounded flows. In this study, the design and analysis of computer models and shape optimisation by mesh morphing are utilised to predict the turbulent flow and perform a robust two-step geometry optimisation of the flow meter. Design optimisation is accomplished by surrogate modelling based on Kriging, Latin hypercube sampling, and Bayesian strategies. A novel function to quantify flow meter measurement robustness is evaluated together with pressure drop in order to define a multi-objective optimisation problem. The design optimisation Pareto front is shown and compared numerically and experimentally. Subsequently, one of the non-dominated designs is further improved by mesh morphing with the aid of the adjoint method, acquiring a novel topology with further optimisation gains. The final results display performance gains, and the final geometrical changes in the 3D space are shown. The applied methodology provides a robust and efficient framework to evaluate design changes and improve complex internal-flow geometries with similar features.

REFERENCE [82] : M. J. Rincón, M. Reclari, X. I. A. Yang, and M. Abkar (2023). "CFD-aided morphing and design optimisation of ultrasonic flow meters," *14th ERCOFTAC Symposium on Engineering Turbulence Modelling and Measurements*. Barcelona, Spain.

V.1 Introduction

Ultrasonic flow meters employing an intrusive two-stand configuration exhibit intricate flow characteristics owing to their distinctive geometry. This feature presents an interesting and demanding scenario for assessing optimisation techniques in wall-bounded flows.

The operational principle of these meters relies on measuring the time differential of sound waves transmitted by piezoelectric transducers in both directions relative to the flow. The interaction between the waves and the flowing medium results in wave acceleration and deceleration, leading to a time disparity that enables precise estimation of the volumetric flow passing through the flow meter.

The fluid flow throughout these systems has been thoroughly studied with the use of computational fluid dynamics (CFD) thanks to the advancements in computer hardware, numerical, and experimental methods [59]. However, CFD methods are nonetheless computationally expensive and, in order to perform comprehensive optimisation studies, diverse

methodologies that rely on mathematical complexity rather than considerable computational power are generally preferred in order to reduce limitations on resources and time.

In this regard, design, shape, and topology optimisation methods can be used with the aid of CFD to geometrically improve similar systems [122]. On the one hand, design optimisation methods are based on the characterisation of key geometrical parameters, their evaluation by design analysis of computer experiments (DACE), statistical methods, and diverse optimisation algorithms which are problem-specific [76, 95, 96]. On the other hand, shape and topology optimisation allows a cost-effective evaluation of the gradient of an objective in function of a higher number of design variables by the use of the adjoint formulation in their discrete or continuous versions [48, 49].

There are several studies which employ design and shape optimisation methods to optimise the shape of diverse engineering applications. These studies are generally applied to problems where structured meshes are commonly used, such as canonical flow cases and simplified external aerodynamics [58], which allows for flexible and accessible mesh morphing. However, in the literature, internal flow and highly constrained problems with the use of unstructured meshing (as in the case of ultrasonic flow meters) are lacking comprehensive studies and the analysis of the results obtained with these methods.

In this study, a two-step geometrical optimisation of a small-diameter flow meter is performed. Starting from a baseline geometry, the first step employs design optimisation by DACE and the second, the use of shape morphing by the adjoint method. The optimised results obtained are numerically verified by means of high-quality CFD simulations. Section 2, elaborates on the background and application of the design and shape optimisation methods in ultrasonic flow meters, while Section 3 showcases the results obtained and discusses the findings. Finally, Section 4 concludes this study with final remarks and future considerations.

V.2 Methodology

V.2.1 Design optimisation

To approach the optimisation problem, the performance parameters to optimise the system must be defined. In this regard, two objective functions for design optimisation are defined as

$$f_1(x) = \frac{\Delta p}{u_{\text{inlet}}^2}, \tag{V.1a}$$

$$f_2(x) = -\frac{V}{V_{\text{ref}}} \left(\frac{u_\Omega - u'_\Omega - \sigma_{u_\Omega}}{u_{\text{inlet}}} \right), \tag{V.1b}$$

where u_Ω is the integrated velocity of the fluid in the sound-path volume, u'_Ω is the integrated velocity fluctuations in the sound-path volume, and σ_{u_Ω} is the standard deviation of the integrated velocity distribution in the sound-path volume. Additionally, $u_{\text{inlet}} = 1.41\ \text{m}\,\text{s}^{-1}$ is the uniform velocity of the fluid at the inlet, and V and $V_{\text{ref}} = 4.704 \cdot 10^{-6}\ \text{m}^3$ are the volume and the reference volume of the reflected sound-path respectively. For an inlet pipe diameter of $D = 20\ \text{mm}$ and a kinematic viscosity of $\nu = 1.00341 \cdot 10^{-6}$, the case displays a $\text{Re}_D = 2.82 \cdot 10^4$ and $\text{Re}_\tau = 760$. From these objective functions, Eq. (V.1a) represents the pressure drop across the flow meter whereas Eq. (V.1b) represents the measurement robustness of the flow meter. More information about the calculation of these quantities can be found in [76].

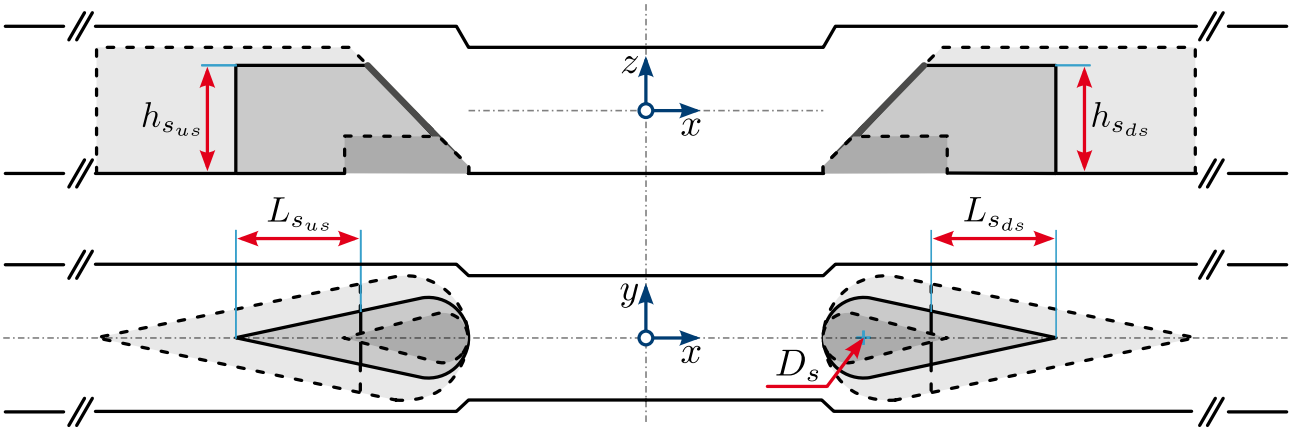

Figure V.1: Depiction of flow meter geometry with design variables to optimise and the baseline flow meter geometry for y-normal (top), and z-normal (bottom) planes. The solid lines show the baseline geometry, and the dotted lines depict the threshold geometries.

Table V.1: Thresholds of the design optimisation and relative variation compared to the baseline case.

Parameter	Value			
	Baseline case	Minimum	Maximum	Relative variation
D_s	$0.6125D$	$0.3655D$	$0.9D$	$0.59 - 1.47$
$L_{s_{us}}$	$1.25D$	$0.5D$	$2.75D$	$0.4 - 2.2$
$L_{s_{ds}}$	$1.25D$	$0.5D$	$2.75D$	$0.4 - 2.2$
$h_{s_{us}}$	$0.7785D$	$0.25D$	$0.865D$	$0.32 - 1.11$
$h_{s_{ds}}$	$0.7785D$	$0.25D$	$0.865D$	$0.32 - 1.11$

To approach the design optimisation problem, firstly, a surrogate based on Kriging is generated following DACE, and secondly, the multi-objective evolutionary algorithm NSGA-II [118] is used to optimise the surrogate, obtaining a non-dominated Pareto front of solutions.

To construct the surrogate, the Latin Hypercube sampling strategy is used to perform an initial investigation of the objective space, where Bayesian optimisation is further implemented to explore areas of high variance and possible minimum locations. The surrogate is built by a sequence of computer-aided design (CAD) geometry generation, meshing, CFD solution, and post-processing of results [46].

Five design parameters and their thresholds are defined (Figure V.1 and Table V.1) respecting the geometry constraints.

For the second part of the optimisation, one of the results from the Pareto front is chosen and subsequently improved by shape optimisation.

V.2.2 Adjoint shape optimisation

Taking into consideration the primal Navier-Stokes equations, continuity and momentum, which are in function of

$$f\left(u, p, b_n\right), \tag{V.2}$$

where u is the velocity vector, p is the kinematic pressure, and b_n is a set of design variables. Ideally, in shape optimisation problems, each grid point is considered a state variable. This

offers great flexibility to explore the objective space and find optimised solutions, however, the cost of the computation of local derivatives by traditional methods (e.g. direct or finite differentiation) is not justified, since the cost of these methods scales linearly with the number of design variables. Hence this is clearly unfeasible for the typical number of grid points that a flow problem requires. To circumvent this issue, the adjoint method is applied. The adjoint method is a cost-effective methodology based on Lagrange multipliers to compute the gradient of a function with respect to the design variables in numerical optimisation problems. Hence, the adjoint objective function is defined as a linear combination of each objective as

$$J\left(b_n\right) = \omega_1 j_1\left(b_n\right) + \omega_2 j_2\left(b_n\right), \tag{V.3}$$

where $j_1(b_n)$ and $j_2(b_n)$ are the 2 objective functions defined in this study, and ω_i is the associated weight given to each objective. Due to the added complexity of the adjoint method in the numerical methodology and to ease the computation of the results, the objective functions from Eqs. (V.1a) and (V.1b) are slightly modified as follows

$$j_1(b_n) = \frac{\int_{\text{inlet}}^{\text{outlet}} \left(p + \rho u^2\right) \mathrm{d}S}{2 S u_{\text{inlet}}^2}, \tag{V.4a}$$

$$j_2(b_n) = -\frac{V}{V_{\text{ref}}} \frac{\|u_\Omega\| - u'_\Omega - \sigma_{u_\Omega}}{u_{\text{inlet}}}, \tag{V.4b}$$

where $j_1(b_n)$ evaluates the normalised total pressure drop between inlet and outlet patches, and $j_2(b_n)$ evaluates the measurement robustness of the flow meter throughout the measurement volume Ω by the calculation of the velocity magnitude $\|u_\Omega\|$ instead of its calculation by its components as seen in Eq. (V.1b).

The adjoint method enables the computation of

$$\frac{\mathrm{d}J}{\mathrm{d}b_n} = \frac{\partial J}{\partial b_n} + \frac{\partial J}{\partial x_k}\frac{\mathrm{d}x_k}{\mathrm{d}b_n}, \tag{V.5}$$

without computing $\frac{\partial u}{\partial b_n}$ and $\frac{\partial p}{\partial b_n}$ first. This requires solving the set of equations for the adjoint pressure (q), adjoint velocity (v), and the associated adjoint variables of the chosen turbulence model ($k-\omega$ SST in this study). Once the gradient $\frac{\mathrm{d}J}{\mathrm{d}b_n}$ has been computed, the steepest descent gradient-based optimisation method is used to update the state variables iteratively, constraining the maximum grid displacement to $0.01D$ (0.2 mm) per iteration. Hence, the problem is approached by first solving the primal RANS $k-\omega$ SST equations and then solving the respective adjoint equations to obtain the sensitivities with respect to the objective function J. For more information about the applied continuous adjoint method and adjoint wall functions, the reader is referred to [123].

While the initial flexibility gained from morphing all available grid points is appealing, it can lead to challenges associated with numerical stability and potential self-intersected edges in the geometry. To mitigate these problems, it is common practice to impose mesh morphing constraints and control points to restrict and smooth the displacement. Control points are introduced in order to constrain the displacement of the flow meter reflectors and pipe, allowing movement only on the surfaces of both stands without deforming the reflectors and pipe walls. The sensitivities calculated on these surfaces are then interpolated to the control points, which are organised into nonuniform rational B-splines (NURBS) using the methodology proposed by [124, 125]. For this purpose, two separate 3D control boxes are defined, each comprising one of the stands. These control boxes consist of $(x, y, z) = (7, 5, 5)$ points and have B-spline basis function degrees of $(p_u, p_v, p_w) = (5, 4, 4)$. Finally, a

laplacian mesh morphing algorithm is employed to deform the mesh, achieving the desired modifications.

Since the downstream stand has a little-to-none influence on the flow in the flow meter constriction ($x \in [-1, 1]\, D$) and upstream, the shape optimisation is performed in two steps: an initial optimisation of the upstream stand, and subsequent optimisation of the downstream stand starting from the obtained geometry from the upstream stand optimisation. Thus, the final geometry obtained is a superposition of these two steps.

The final geometries obtained are extracted and re-meshed to minimise possible numerical uncertainties created by mesh morphing, and the results are compared with the baseline, design optimisation, and shape optimisation cases utilising the same mesh refinement used in the adjoint shape optimisation.

V.3 Results

A set of 150 RANS simulations (50 by LHS to create an initial surrogate and 100 by Bayesian optimisation) is performed to build the complete surrogate. The results of the multi-objective optimisation applied to the Kriging-based surrogate yield a Pareto front with estimated uncertainties (Figure V.2a). From the non-dominated solutions, 4 cases displaying diverse gains for each of the objective functions are extracted and experimentally validated following the study by [76] (Figure V.2b).

The results and methodology of the design optimisation show that various geometries of the flow meter lead to increased performance and lower pressure losses compared to the baseline design. A group of improved non-dominated designs are identified ranging from a 67% reduction in pressure drop to an 8.7% increase in measurement robustness compared to the baseline design.

Regarding the geometrical changes, the results display a general tendency to enlarge the tail of the downstream stand as much as possible and to reduce the tail length of the upstream stand compared to the baseline case. Intuitively, cases leading towards an improvement of $f_1(x)$ (C and D), show a reduced blockage ratio in the pipe and the stand volume is dramatically reduced to minimise interactions leading to pressure drag in the flow. Alternatively, cases focusing on improving $f_2(x)$ (A and B) display a larger blockage ratio where the upstream stand is slightly smaller in height compared to the downstream stand. A globally favourable case representing a compromise of both objectives is case B, with a numerical decrease of 37.4% in pressure drop and an increase of 4.9% in measurement robustness relative to the baseline case and according to Eqs. (V.1a) and (V.1b), respectively.

Subsequently, optimised case B from design optimisation is chosen to be evaluated and improved by shape optimisation and the adjoint method. The first-step optimisation, taking into consideration only the upstream stand, shows an objective functions evolution leading to the minimisation of both functions with the asymptotic behaviour of $\langle J \rangle / J_0 \approx 0.925$ after 27 primal-adjoint iterations (Figure V.3a). Performing another shape optimisation to the yielded geometry of the last iteration of this first step, only the downstream stand is optimised. Since the downstream stand has little-to-no influence on the upstream flow, the objective j_2 only changes marginally where the objective j_1 gets minimised displaying an asymptotic behaviour at $\langle J \rangle / J_0 \approx 0.97$ after iteration 25 (Figure V.3b).

According to the objective function evaluation, the geometry of iteration 25 is chosen as a converged and optimised case. This case is therefore compared and analysed against the baseline and the design optimisation cases.

Regarding j_1, the analysis of the function results is broken down into static, dynamic, and

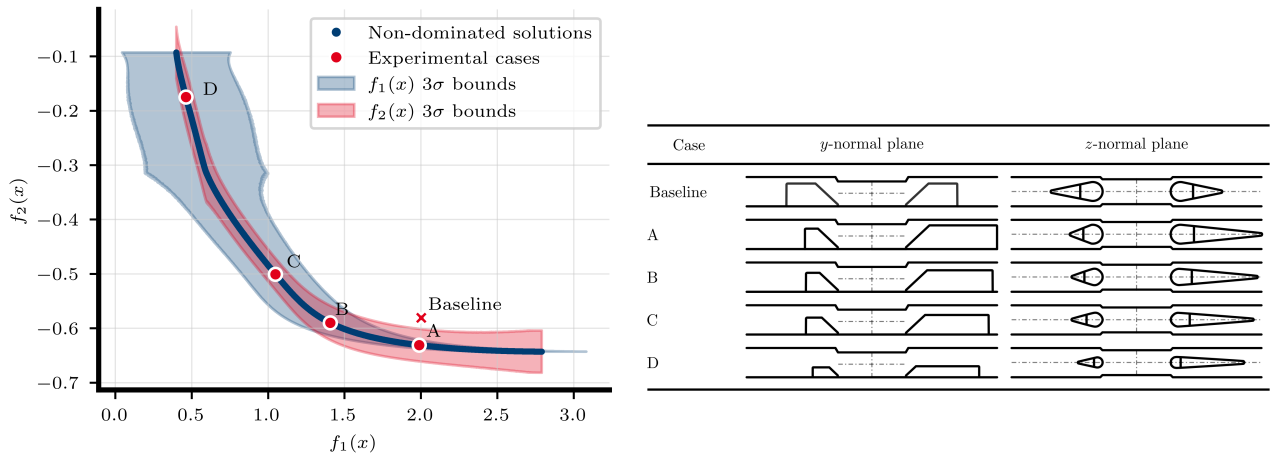

(a) Non-dominated solutions from the design optimisation and chosen experimental cases.

(b) Comparison of geometries of the experimental cases chosen.

Figure V.2: Design optimisation results. Note that in Fig. V.2a, $f_1(x)$ represents the static pressure losses and $f_2(x)$ represents the measurement robustness of the flow meter.

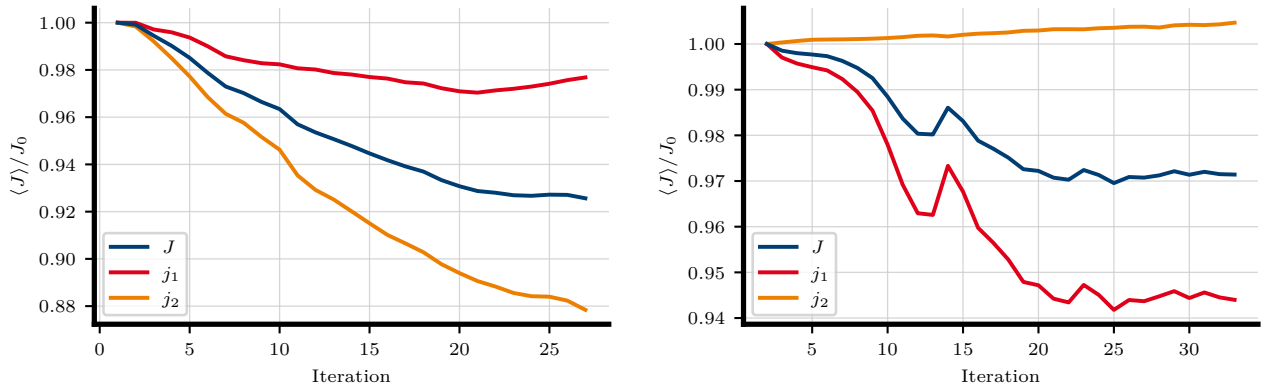

(a) Upstream stand.

(b) Downstream stand.

Figure V.3: Objective functions evolution for both stands during their shape optimisation. It should be noted that j_1 represents the total pressure loss and j_2 represents the flow meter's measurement robustness.

stagnation pressures. Results in Fig. V.4a show that the dynamic pressure contribution in total pressure drop is negligible compared to the static pressure contribution. The design optimisation case yields a 24.24% total pressure drop reduction whereas the adjoint optimisation case yields a 23.2% reduction compared to the baseline case. However, the dynamic pressure losses of the design optimisation and adjoint optimisation cases are 1.95 and 11.73 times respectively higher than the baseline. This again showcases the negligible effect of the dynamic pressure on the total pressure drop.

Similarly, for j_2, the function is broken down into its components: the measurement volume velocity magnitude u_Ω, the measurement volume velocity fluctuations due to TKE u'_Ω, and the spatial flow uniformity in the measurement region σ_{u_Ω}. The results in Fig. V.4b showcase the improvement of the measurement robustness by both design and adjoints optimisation cases. The design optimisation case yields an overall 0.3% improvement whereas the adjoint case yields a 7.07% improvement in measurement robustness compared to the baseline case. Both the design optimisation and adjoint cases slightly compromise the

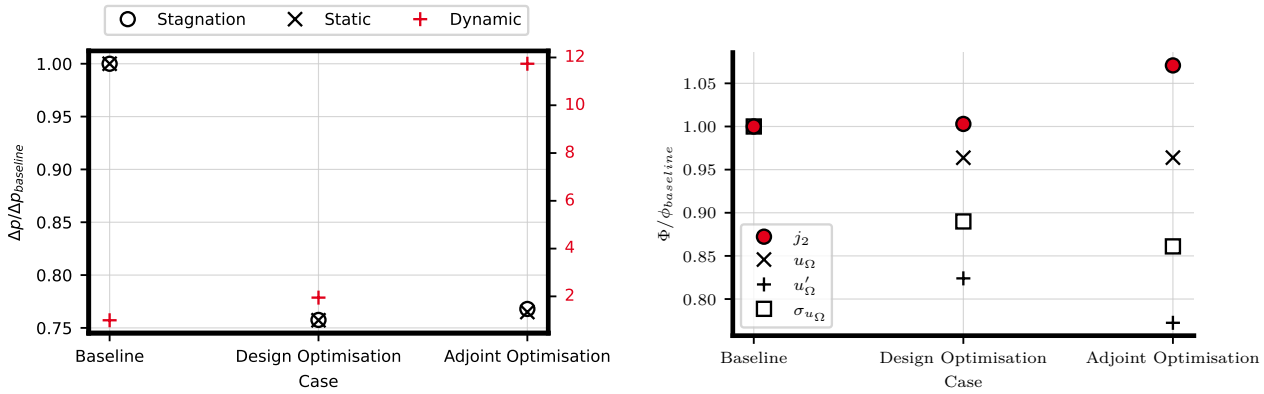

(a) j_1 and associated pressure losess.

(b) j_2 and associated components.

Figure V.4: Objective functions comparison between cases with their associated components. It should be noted that in Fig. V.4a, the stagnation pressure is equal to the objective function j_1.

velocity magnitude in order to greatly decrease the velocity fluctuations and increase the flow uniformity in the measurement volume. The adjoint case displays the best measurement robustness by decreasing u_Ω by 3.6%, u'_Ω by 22.75%, and σ_{u_Ω} by 13.9%, respectively, to the baseline case.

Qualitatively, the differences in the predicted axial velocity fields are not clearly visible in the measurement region. The most remarkable variation between cases is the minimisation of the recirculation zones downstream, which leads to a pressure drag reduction. It is remarkable to highlight the main differences between the new wall-resolved results obtained in this study and the wall-modelled results from [76] for the design optimisation case. These results suggest that the use of wall models cannot predict the impending boundary layer detachment when using the $k-\omega$ SST model. Simultaneously, $k-\omega$ SST is known to overestimate boundary layer separation and re-attachment by the literature [86, 87]. Future work suggests performing high-fidelity numerical simulations and/or experimentally investigating these regions to validate the results and which methodology is more accurate.

Regarding the measurement robustness, since the flow mechanics between the stands are very complex (displaying clear areas of non-equilibrium and adverse pressure gradients, strong vortices, and separation and reattachment of flow [59]), it is not straightforward to envision an improvement of j_2 with the yielded geometries by traditional engineering knowledge.

The mesh morphing of the adjoint case is considerable and clearly visible compared to the initial geometry of the design optimisation case (Figure V.6). The surface normal displacement shows the inwards and outwards deformation generated by the method on the original surface. On the one hand, it can be seen that the upstream stand tail is marginally enlarged and generally, the blockage ratio of the stand in the pipe is increased. The shape displays a more streamlined topology and the upper section of the stand is slightly filleted. On the other hand, the downstream stand shows a general volume reduction, yielding a more streamlined topology with few changes from the original shape. The upper section of the stand is likewise filleted and the length of the tail is not changed.

It is critical to remark on the possible drawbacks of the adjoint method and mesh morphing. As initially seen, the optimisation gains calculated during the adjoint optimisation process (Figure V.3) are higher than the yielded results of the re-meshed final geometry simulation (Figure V.4). This is suggested to be due to the re-meshing procedures, the deterioration of

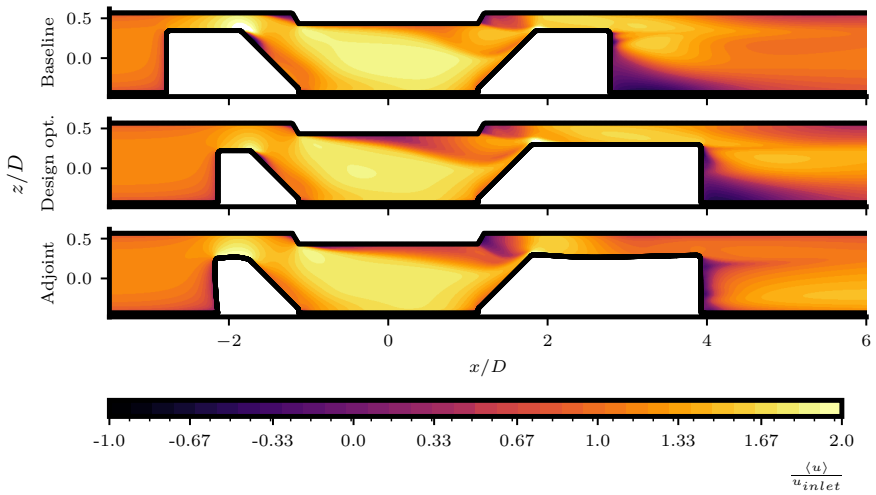

Figure V.5: Normalised axial velocity contours of the different analysed cases.

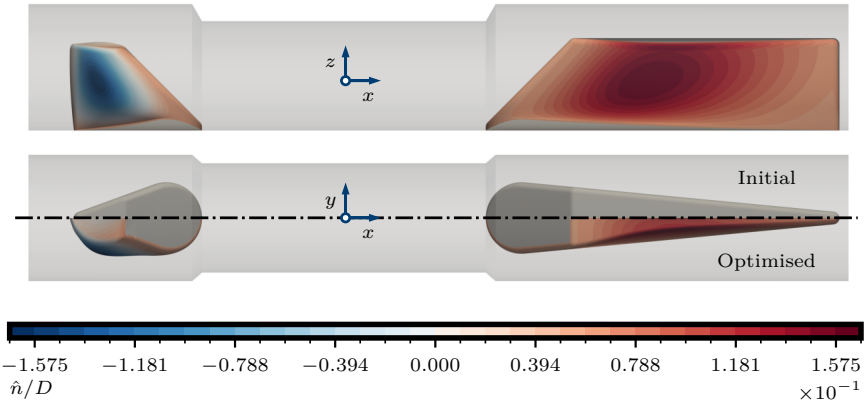

Figure V.6: Normalised surface normal displacement ($\hat{n}/D$) contours at y-normal plane of final morphed geometry and comparison against design optimisation case. Top: y-normal plane. Bottom: z-normal plane.

the mesh quality during the adjoint optimisation, and the possible predictive inaccuracies of boundary layer detachment and reattachment by RANS $k-\omega$ SST. Nevertheless, the final geometry obtained does yield overall improved numerical results compared to the initial design.

V.4 Conclusions

The results and methodology of the optimisation have demonstrated that various geometries of a small-diameter flow meter lead to higher measurement robustness and lower pressure losses compared to the baseline design. The chosen optimisation methodology has improved the baseline design by employing design optimisation with the aid of surrogates and, subsequently, shape optimisation with mesh morphing.

A group of improved non-dominated designs have been identified and validated numerically and experimentally regarding design optimisation. One of these cases has been further optimised by employing mesh morphing and the fast calculation of derivates by the adjoint

method.

The final design has been achieved by employing a 2-step shape optimisation procedure, improving first the upstream stand and, secondly, the downstream stand, where a final superposed geometry has been obtained. The analysis of the baseline, design, and adjoint optimisation geometries has shown that a gradual improvement of the objectives is achieved by CFD simulations. However, the expected improvements by the adjoint optimisation method are compromised when the mesh gets too deformed.

Due to the complexity of the system and the current implementation limitations of the adjoint method, the objective function results obtained during the shape optimisation do not completely agree with the final results once re-meshing and high-quality simulations are performed. Nonetheless, the adjoint method has yielded improved geometries in measurement robustness while only slightly increasing pressure drop with respect to the initial case. These results are showcasing the implications of this methodology for future engineering applications.

In conclusion, this study has demonstrated the numerical effectiveness, reliability, and precision of using a 2-step global optimisation method with CFD-RANS $k-\omega$ SST model to enhance the design of ultrasonic flow meters. The first step is built on DACE design optimisation and Kriging surrogate modelling, whereas the second step is based on the adjoint method and mesh morphing. A comprehensive verification process has been conducted through numerical simulations, yielding improved designs. Finally, the methodology employed in this study has the potential to improve other wall-bounded systems with similar fluid motion characteristics.

VI

Turbulence Modelling for Secondary Flows

Progressive augmentation of turbulence models for secondary flow prediction by computational fluid dynamics driven surrogate optimisation

ABSTRACT Generalisability and the consistency of the *a posteriori* results are the most critical points of view regarding data-driven turbulence models. This study presents a progressive improvement of turbulence models using simulation-driven Bayesian optimisation with Kriging surrogates where the optimisation of the models is achieved by a multi-objective approach based on duct flow quantities. We aim for the augmentation of secondary-flow prediction capability in the linear eddy-viscosity model $k-\omega$ SST without violating its original performance on canonical cases e.g. channel flow. Progressively data-augmented explicit algebraic Reynolds stress correction models (PDA-EARSMs) for $k-\omega$ SST are obtained enabling the prediction of secondary flows that the standard model fails to predict. The new models are tested on channel flow cases guaranteeing that they preserve the successful performance of the original $k-\omega$ SST model. Subsequently, numerical verification is performed for various test cases. Regarding the generalisability of the new models, results of unseen test cases demonstrate a significant improvement in the prediction of secondary flows and streamwise velocity. These results highlight the potential of the progressive approach to enhance the performance of data-driven turbulence models for fluid flow simulation while preserving the robustness and stability of the solver.

REFERENCE [126]: M. J. Rincón, A. Amarloo, M. Reclari, X. I. A. Yang, and M. Abkar (2023). "Progressive augmentation of Reynolds stress tensor models for secondary flow prediction by computational fluid dynamics driven surrogate optimisation," *International Journal of Heat and Fluid Flow*, 104, 109242.*.

VI.1 Introduction

Reynolds-averaged Navier-Stokes (RANS) equations are widely preferred over high-fidelity methods like direct numerical simulation (DNS) and large-eddy simulation (LES) for the industrial applications of computational fluid dynamics (CFD) due to their robustness and computational speed. In RANS, the physics of turbulence is predicted by a Reynolds stress tensor (RST) model; hence, the results obtained are dependent on the performance of these model predictions. Despite the popularity of RANS simulations, the common empirical models have been found to have shortcomings [29], particularly in capturing Prandtl's second kind of secondary flow [127]. This limitation is accentuated in the most commonly used

*M.J. Rincón and A. Amarloo contributed equally to this study.

RANS turbulence models (e.g. two-equation models based on the Boussinesq assumption like $k-\varepsilon$ and $k-\omega$) due to their inability to predict complex turbulence anisotropy.

Although the development of reliable RANS turbulence models has remained stagnant for decades [30], the recent advances in data-driven techniques have motivated a new wave of studies aiming at improving the performance of RANS turbulence models [31]. The majority of these studies have used available high-fidelity data of the RST values to train a model and improve the predictions obtained from empirical models [32–37]. These studies have mainly focused on obtaining ways to correct the RST prediction [87, 121, 128–130], or to modify the available empirical models [40, 131, 132]. Taking into consideration a different approach, CFD-driven models [38, 39] have shown promising results in finding reliable variants of RANS turbulence modelling. Hence, CFD-driven models can guarantee consistency and robustness in *a posteriori* results (i.e. by a model-consistent training method [40]), as opposed to other data-driven RANS models (i.e. by a *a priori*-training method [40]) since they are optimised while performing simulations to guarantee the improvement of the results obtained by new models.

In order to improve these models by a CFD-driven approach, it is necessary to solve a complex optimisation problem. In this regard, the use of optimisation algorithms that aim to minimise or maximise one or more functions in a multi-dimensional parameter space is essential. Some of the commonly used optimisation algorithms include slope followers [133], simplex methods [42], multi-objective evolutionary [43], and particle swarm algorithms [44], among others. However, these algorithms require the evaluation of an objective function, which can be computationally expensive if CFD simulations are involved, especially in cases where a large number of test configurations are required.

To address this issue, development has been made towards the use of a relatively smaller set of simulations to create computationally efficient surrogate models, also known as response surfaces, that can then be fastly optimised [134]. Response surfaces are mathematical models that approximate the behaviour of the objective function in the parameter space and can be used to predict the function values at untested configurations. This approach has been applied to various engineering applications, such as optimising complex internal-flow systems based on ultrasonic flow metering [59, 76], improving the efficiency of gas cyclones [102], optimising the aero-structural design of plane wings [101], and improving the performance of ground vehicles [104], among others.

There are only a few studies that have investigated the use of optimisation algorithms and data-driven models for the improvement of the RANS turbulence models. Reference [38] combined CFD-driven optimisation with gene expression programming to obtain a correction for the RST modelled by the $k-\omega$ SST model. They showed that the CFD-driven model had an improved performance compared to the data-driven model trained on the same case. They concluded that CFD-driven models have a great potential for developing reliable improved RANS models even though their new model is limitedly optimised for wake mixing flow. In another study, Ref. [39] used response surfaces to find the best linear combination of candidate functions to correct the RST values modelled by the $k-\omega$ SST model for the cases with flow separation. They also showed that a CFD-driven approach yields models that perform better than the data-driven models trained on the same set of data. In Ref. [99], the authors resort to Kriging and obtained wall models for boundary layer flows subjected to system rotation in an arbitrary direction. The model was shown to predict deviations in the mean flow from the equilibrium law of the wall. In Ref. [135], the authors employed an evolutionary neural network and arrived at numerical strategies for the pressure Poisson equation with density discontinuities. Furthermore, the CFD-driven methodology is extended to a multi-objective optimisation for coupled turbulence closure models by [136].

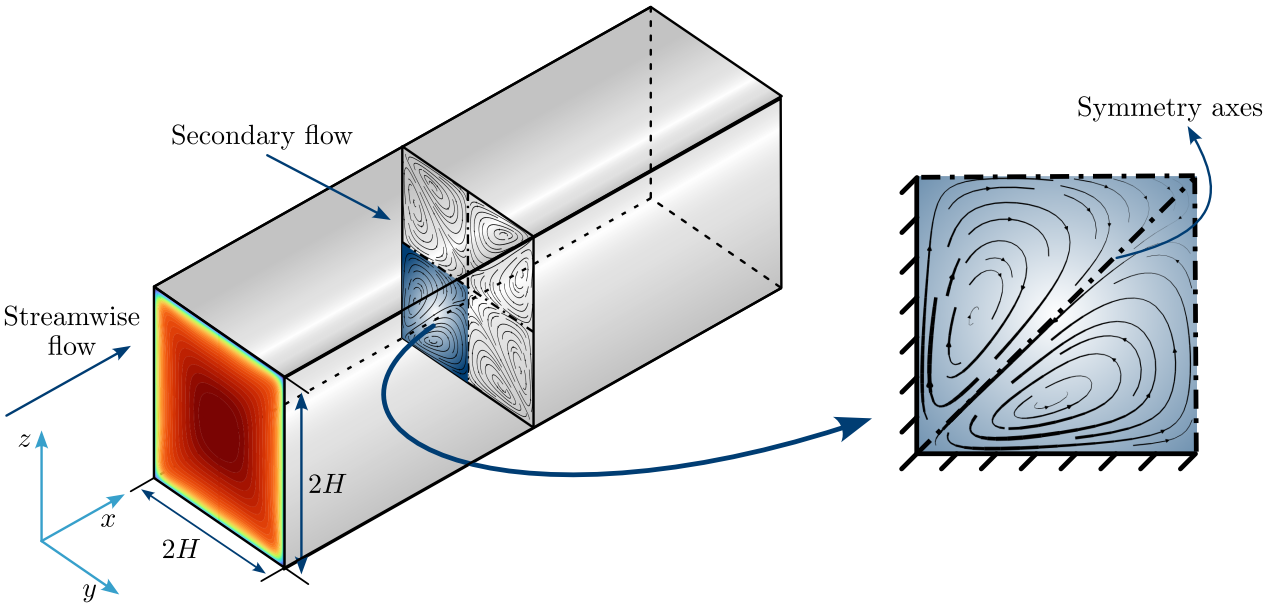

Figure VI.1: Flow characteristics of a duct flow with AR $= 1$ and height and width of 2H. Note the formation of secondary motions and their symmetry.

However, the application of surrogate-based optimisation (SBO) and Bayesian optimisation methods [137] to improve complex mathematical tools such as RANS turbulence modelling has not been widely explored. In this regard, SBO and Bayesian optimisation methods show potential in evaluating problems based on design and analysis of computer experiments (DACE) [46] with a low-to-medium number of parameters to optimise.

One of the most important topics in data-driven RANS modelling is the generalisability of the new models for unseen cases [138]. It has been suggested that using a multi-case CFD-driven approach to consider different turbulent phenomena during the optimisation process can help with the generalisability of the new model [139]. However, even these new models are still specific to either wall-free or wall-bounded flows; therefore, the generalisability problem requires further investigation.

The generalisability is the ability of data-driven models to perform well both with unseen cases (out of the training cases range) and with canonical cases like channel flow. The combination of a conventional progressive approach with data-driven approaches has been proposed to address this issue [140]. In the progressive approach, the starting point is a baseline model that is already performing adequately for simple flows and adds more complexity step by step without violating the model's performance for flow cases that the model was calibrated against. In this study, we use the progressive approach to add the capability of secondary flow reconstruction to a linear eddy-viscosity model without violating its successful performance in a channel flow simulation.

Since the CFD-driven technique ensures the consistency of the *a posteriori* results and the progressive approach aids with the generalisability of the new models, in this study we combine the CFD-driven surrogate and Bayesian optimisation technique with the progressive approach to obtain a progressively data-augmented explicit algebraic Reynolds stress model (PDA-EARSM) to the $k-\omega$ SST [64] model for exclusively predicting secondary flows. We likewise investigate the potential of a progressive approach in the development of generalisable CFD-driven RANS models. Since standard linear eddy-viscosity models have difficulty predicting secondary flows [127], we use the Pope's decomposition of RST [141] to add a non-linear term of the RST to the model, and we optimise the new models for the prediction

of secondary flows induced by a duct flow with an aspect ratio (AR) of 1 (squared) at bulk Reynolds number of 3500 (depicted in Fig. VI.1). The new models' boundary-layer prediction is tested on the channel flow to ensure that they do not affect the successful performance of the original model. Considering the generalisability, the new models are verified on duct flow cases with different Reynolds numbers and aspect ratios. Furthermore, we test the new models against an extremely disadvantageous case regarding accurate flow prediction by RANS models, we verify the models in a case where the secondary flow is induced by roughness patches in a channel flow [142, 143] with a nominally infinite Reynolds number. Finally, we test the performance of the models against two novel data-driven EARSMs and the traditional BSL-EARSM based on the constitutive relation of Wallin and Johansson [144].

VI.2 Methodology

This section presents the structure of the progressive correction model for RANS modelling and the optimisation technique for training the correction model. By using the Reynolds decomposition of velocity and pressure, the Navier-Stokes equation for an incompressible steady flow can be written as [108]

$$u_i = \langle u_i \rangle + u_i', \;\; p = \langle p \rangle + p', \tag{VI.1}$$

$$\partial_i \langle u_i \rangle = 0, \;\; \partial_j (\langle u_i \rangle \langle u_j \rangle) = -\frac{1}{\rho} \partial_i \langle P \rangle + \partial_j \left(\nu \partial_j \langle u_i \rangle - A_{ij} \right), \tag{VI.2}$$

where $i, j = 1, 2, 3$ are indicating the streamwise (x), spanwise (y), and vertical (z) directions, respectively. u_i and p are velocity and pressure decomposed to a temporal mean term, indicated by $\langle \cdot \rangle$, and fluctuations, indicated by $\cdot'$. The kinematic viscosity is denoted by ν, and ρ is the fluid density. $A_{ij} = \langle u_i' u_j' \rangle - \frac{1}{3} \langle u_k' u_k' \rangle \delta_{ij}$ is the anisotropic part of RST, and pressure is modified with the isotropic part of the RST as $\langle P \rangle = \langle p \rangle + \frac{1}{3} \rho \langle u_i' u_i' \rangle$.

In this study, the $k - \omega$ SST [64] model is used as a baseline model to be progressively corrected to predict secondary flows. In the standard $k - \omega$ SST model, A_{ij} is modelled as

$$A_{ij}^{BL} = -2 \nu_t S_{ij}, \tag{VI.3}$$

where $S_{ij} = \frac{1}{2} (\partial_i \langle u_j \rangle + \partial_j \langle u_i \rangle)$ is the strain rate tensor, ν_t is the turbulent viscosity which is calculated by values of turbulent kinetic energy (TKE) (i.e. k), and the specific dissipation rate (i.e. ω), which are modelled by the original two-equation model [77].

VI.2.1 Progressively data-augmented EARSM

We extend the structure of the linear eddy-viscosity model (Eq.VI.3) by following Pope's decomposition [141] of the RST and considering the two first terms of the decomposition,

$$A_{ij} = 2k\alpha^{(1)} \frac{S_{ij}}{\omega} + 2k\alpha^{(2)} \frac{S_{ik}\Omega_{kj} - \Omega_{ik}S_{kj}}{\omega^2}, \tag{VI.4}$$

where $\Omega_{ij} = \frac{1}{2} (\partial_i \langle u_j \rangle - \partial_j \langle u_i \rangle)$ is the rotation rate tensor, and $\alpha^{(n)}$ are unknown functions of 5 invariants defined as,

$$\begin{aligned} I_1 &= \frac{\mathrm{tr}(S_{ik}S_{kj})}{\omega^2}, \quad I_2 = \frac{\mathrm{tr}(\Omega_{ik}\Omega_{kj})}{\omega^2}, \quad I_3 = \frac{\mathrm{tr}(S_{ik}S_{km}S_{mj})}{\omega^3}, \\ I_4 &= \frac{\mathrm{tr}(\Omega_{ik}\Omega_{km}S_{mj})}{\omega^3}, \quad I_5 = \frac{\mathrm{tr}(\Omega_{ik}\Omega_{km}S_{ml}S_{lj})}{\omega^4}. \end{aligned} \tag{VI.5}$$

A comparison between Eq. VI.3 and Eq. VI.4 shows that the $k-\omega$ SST model is already providing the first term in Pope's decomposition of the RST (i.e., the turbulent viscosity); therefore following the progressive approach, only the second term is trained in this study. The reason behind this decision is to preserve the original performance of the $k-\omega$ SST model in the prediction of the turbulent viscosity (i.e., ν_t) while the second basis tensor's coefficient is determined with the exclusive purpose of secondary flow prediction. Hence, the new RST model can be written as

$$A_{ij} = -2\nu_t \left(S_{ij} - \alpha^{(2)} \frac{S_{ik}\Omega_{kj} - \Omega_{ik}S_{kj}}{\omega} \right), \tag{VI.6}$$

where ν_t and ω are modelled by the standard $k-\omega$ SST model, where Eq. VI.6 is used for the production term by the Reynolds stress tensor instead of Eq. VI.3, and the unknown function of $\alpha^{(2)}$ is determined by the CFD-driven optimisation technique. It should be mentioned that the linear part of the new model is treated implicitly as turbulent viscosity, and the non-linear part of the RST is added explicitly to the RANS equations. The assumption behind the progressive approach is that using only the second basis tensor does not affect the incompressible parallel shear flow, either in the momentum equation or via production in the k-equation; therefore, the performance of $k-\omega$ SST is preserved in cases where secondary flow is not present.

Inspired by a sparse regression of candidate functions (SpaRTA) [87] used for $\alpha^{(n)}$, we use a set of candidate functions to describe $\alpha^{(2)}$ as

$$\alpha^{(2)} = \theta_0 + \sum_{i=1}^{20} \theta_i \mathcal{D}_i, \tag{VI.7}$$

$$\begin{aligned} \mathcal{D} = \{ & I_1, I_2, I_3, I_4, I_5, I_1^2, I_2^2, I_3^2, I_4^2, I_5^2, \\ & I_1I_2, I_1I_3, I_1I_4, I_1I_5, I_2I_3, I_2I_4, \\ & I_2I_5, I_3I_4, I_3I_5, I_4I_5 \}, \end{aligned} \tag{VI.8}$$

where θ_i are constant coefficients to be determined by the CFD-driven optimisation process. To achieve a more efficient sparse optimisation, the normalised candidate functions are normalised and defined as

$$\mathcal{B}_i = \frac{\mathcal{D}_i - \mu_i}{\sigma_i}, \tag{VI.9}$$

where μ_i, σ_i are the mean and the standard deviation of each candidate function $\mathcal{D}_i$, respectively. These statistics are calculated based on high-fidelity data from the optimisation case. Therefore, Eq. VI.7 is rewritten as,

$$\alpha^{(2)} = C_0 + \sum_{i=1}^{20} C_i \mathcal{B}_i, \tag{VI.10}$$

where an optimisation technique determines the coefficients C_i based on the performance of the correction model for the reconstruction of the high-fidelity velocity field of an optimisation case.

In this study, only 2D canonical flow cases are considered, since they are computationally cost-effective. However, reducing the dimensionality of the optimisation problem and using computational parallelisation is key if a complex 3D case is used in the training process.

Since considering 21 optimisation variables is impractical, making the model unnecessarily complex and exposed to solution instabilities, two approaches are chosen:

1. Selecting only the first m leading candidate functions.
2. Reducing the dimensionality of the problem using a statistical technique.

Both of these approaches are compared, and for the purpose of dimensionality reduction, principal component analysis (PCA) is applied on the $\mathcal{B}_i$ functions to obtain the first m principal components as,

$$\varphi_j = \sum_{i=1}^{20} a_i^{(j)} \mathcal{B}_i, \tag{VI.11}$$

where the coefficients $a_i^{(j)}$ are obtained by performing PCA on the high-fidelity data from the optimisation case. It should be mentioned that PCA also determines which features among all the 20 features have a higher importance in the variability of $\alpha^{(2)}$ by determining the $a_i^{(j)}$ coefficients for each of them. By considering this transformation equation, Eq. VI.10 is rewritten as,

$$\alpha^{(2)} = C_0 + \sum_{i=1}^{m} C_i \varphi_i. \tag{VI.12}$$

Based on the high-fidelity data of the optimisation case, in Sec. VI.3.1 it is shown that the first two principal components are enough to represent a high percentage of the variability of the dataset (i.e. $m = 2$). Therefore, two different structures for $\alpha^{(2)}$ are considered:

$$\alpha_I^{(2)} = C_0 + C_1 \mathcal{B}_1 + C_2 \mathcal{B}_2, \tag{VI.13a}$$

$$\alpha_{II}^{(2)} = C_0 + C_1 \varphi_1 + C_2 \varphi_2, \tag{VI.13b}$$

which are described as *model* ***I*** and *model* ***II***, respectively. Where a unique set of three coefficients C_0, C_1, and C_2 are determined by a multi-objective optimisation technique for each of the models.

VI.2.2 Optimisation methods

To approach the optimisation problem, a surrogate based on Kriging and Gaussian processes (GPs) is built. The surrogate is based on DACE, using observations obtained from a sequence of CFD solutions and post-processing of results. SBO has shown its advantages for these types of problems, minimising the number of required observations, and allowing the use of goal-seeking algorithms such as Bayesian optimisation [115]. To assess the model's performance, two main objective functions are established that involve streamwise velocity and streamwise vorticity, defining a multi-objective optimisation problem. An effective sampling plan is also outlined, and an infill criterion constrained by quality metrics is specified. Finally, the methodology is implemented using the general-purpose software OpenFOAM [65]. A flow diagram of the complete optimisation methodology is depicted in Fig. VI.2.

VI.2.2.1 Objective functions

The principal issue that is assessed in this study is the complete lack of prediction of secondary flows in RANS turbulence models based on the Boussinesq assumption. In the chosen optimisation case, the addition of these secondary flow motions is strong enough to also incur changes in the streamwise direction of the flow. In addition, once the corrections are made, the mean streamwise flow is simultaneously modified. Since the aim of this study is

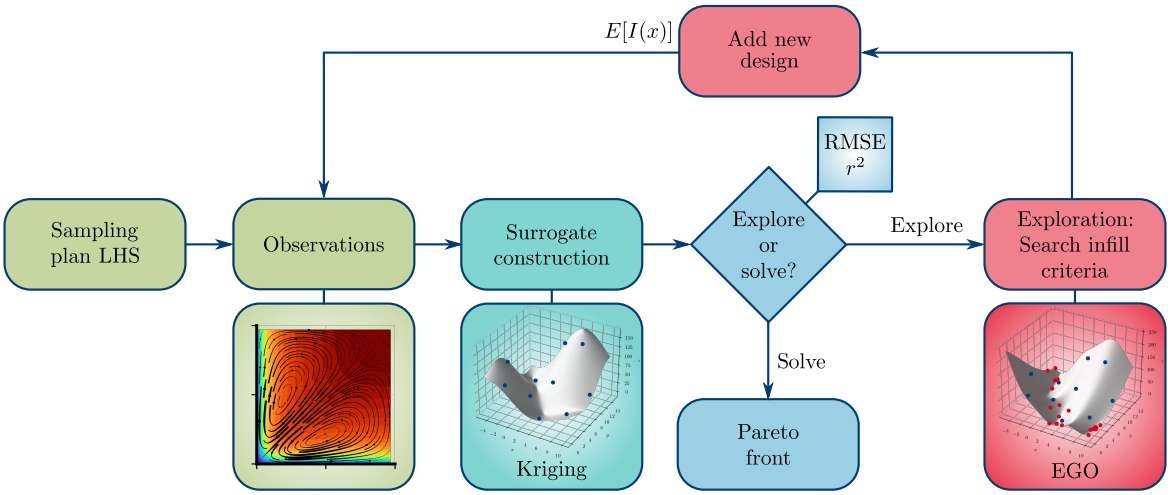

Figure VI.2: Optimisation strategy employed involving an initial sampling plan based on Latin hypercube sampling (LHS) which is solved by CFD. Subsequently, an initial surrogate is constructed using Kriging. Since it is likely that the initial sampling may not evaluate the surrogate in extrema, Bayesian strategies based on efficient global optimisation (EGO) and the evaluation of the expected improvement ($E\left[I(x)\right]$) function are then applied to further explore the surrogate and improve its quality. Finally, once the quality requirements have been met, a genetic algorithm is employed to search for non-dominated optima on the surrogate model.

to improve the overall flow prediction, it is important to not disregard possible predictions that could improve secondary flow but worsen streamwise velocity. Hence, two objective functions that physically describe the streamwise flow and the secondary flow prediction are defined and evaluated.

In this regard and to holistically evaluate the flow prediction, the normalised error of both the streamwise velocity and vorticity with respect to high-fidelity data, are evaluated and taken as objectives to be minimised. To yield a fair and accurate single value representing these quantities, the volumetric average of each field is computed as the objective functions, following

$$j_1 = \frac{\int_V \left(\langle u_1\rangle_{\text{PDA-EARSM}} - \langle u_1\rangle_{\text{HF}}\right) \mathrm{d}V}{\int_V \left(|\langle u_1\rangle_{k-\omega} - \langle u_1\rangle_{\text{HF}}|\right) \mathrm{d}V}, \tag{VI.14a}$$

$$j_2 = \frac{\int_V \left(\langle \omega_1\rangle_{\text{PDA-EARSM}} - \langle \omega_1\rangle_{\text{HF}}\right) \mathrm{d}V}{\int_V \left(|\langle \omega_1\rangle_{k-\omega} - \langle \omega_1\rangle_{\text{HF}}|\right) \mathrm{d}V}, \tag{VI.14b}$$

where $|\cdot|$ is the absolute value operation, $\langle\omega_i\rangle = \varepsilon_{ilk}\partial_l\langle u_k\rangle$ is the vorticity of the mean flow, where ε_{ilk} is the alternating unit tensor, HF stands for high fidelity, and $k-\omega$ refers to the solution of the standard $k-\omega$ SST model. The definition of these functions yields a value of 1 when their output matches the prediction of $k-\omega$ SST and 0 when the predictions match the high-fidelity data. Subsequently, to evaluate the overall results of the method, a global fitness function is defined as

$$J = \frac{1}{2}\left(j_1 + j_2\right). \tag{VI.15}$$

VI.2.2.2 Sampling plan

Two main algorithms are used in order to sample observations and data in this study: Monte Carlo and Latin hypercube. Monte Carlo sampling is used when extracting a test subset to compute the surrogate quality. Since the chosen sampling plan for the initial observations is oriented to be *space-filling*, Latin Hypercube Sampling (LHS) [105] with optimised design by the enhanced stochastic evolutionary (ESE) algorithm [106, 107] is used to obtain an initial sample of the surrogate with a minimum number of observations, and simultaneously, representing the real variability of the parameters. This deterministic sampling technique is a type of stratified Monte Carlo that divides each dimension space representing a variable into n_0 sections, and only one point is placed in each partition. The initial sample by LHS with ESE follows $n_0 = 30\mathcal{K}$, where n_0 is the initial number of observations, and $\mathcal{K}$ is the number of design variables.

VI.2.2.3 Surrogate construction

In the context of a sparse optimisation problem, surrogates are commonly used to approximate a function $y = f(x)$ based on known observations. In this study, the Kriging method is chosen for generating the surrogate based on CFD-driven observations. Kriging is one of the most common surrogate construction methods due to its well-known implementation, ability to compute uncertainties and speed. Furthermore, it has been proven useful in physical, uncertainty quantification, and engineering applications [76, 145]. Kriging interpolates the observations as a linear combination of a deterministic term and a stochastic process, which is represented by

$$\hat{f}(x) = \sum_{i=1}^{k} \beta_i f_i(x) + Z(x), \tag{VI.16}$$

where $\hat{f}(x)$ is the surrogate prediction, β is a linear deterministic model, $f(x)$ is the known function, and $Z(x)$ is the realisation of a stochastic process with zero mean and spatial covariance function given by

$$\operatorname{cov}\left[Z\left(x^{(i)}\right), Z\left(x^{(j)}\right)\right] = \sigma^2 R\left(x^{(i)}, x^{(j)}\right). \tag{VI.17}$$

Here, the spatial correlation function R determines how smooth the Kriging model is, how easily the response surface can be differentiated, and how much influence the nearby sampled points have on the model. In this study, the spatial correlation is defined following the squared exponential (Gaussian) function as

$$\prod_{i=1}^{nx} \exp\left\{\left[-\theta_l \left(x_l^{(i)} - x_l^{(j)}\right)^2\right]\right\}, \quad \forall \theta_l \in \mathbb{R}^+, \tag{VI.18}$$

where the correlation scalar θ_l is used to define the variance of a Gaussian process at each point, with higher values indicating a stronger correlation between points. By maximising the maximum likelihood estimation, optimal values for hyper-parameters as θ_l, mean, and standard deviation can be found [112].

VI.2.2.4 Quality metrics

The quality of the surrogate refers to how accurately it approximates the true function being modelled. In order to evaluate this quality, a number of random test observations

$n_t = n_0\ x \rightarrow y$, are taken. where n_t is a function of the number of initial observations. Once the test observations have been generated, they are used to compare the surrogate's predictions to the true values of the function being modelled. The root-mean-squared error (RMSE) and Pearson's correlation coefficient squared (r^2), defined as

$$\text{RMSE} = \sqrt{\frac{\sum_{i=1}^{n_t} \left(y^{(i)} - \hat{y}^{(i)}\right)^2}{n_t}}, \tag{VI.19a}$$

$$r^2 = \left(\frac{\text{cov}(y, \hat{y})}{\sqrt{\text{var}(y)\text{var}(\hat{y})}}\right)^2, \tag{VI.19b}$$

are two common metrics used to evaluate the quality of surrogates. While the RMSE measures the difference between the surrogate's predictions and the true values, r^2 measures the strength of its linear relationship. A high RMSE and a low r^2 indicate that the surrogate is performing poorly and needs to be refined, while a low RMSE and a high r^2 indicate that the surrogate is performing accurately and can be used with confidence. Hence, these values serve as reference points to determine whether the surrogate model is accurate enough to be used in the optimisation process.

In this study, thresholds of 0.2 for RMSE and 0.8 for r^2 are established as indicators of good surrogate quality, based on previous studies [113, 114].

VI.2.2.5 Infill space exploration

Efficient global optimisation (EGO) based on Bayesian optimisation strategies is used to improve the accuracy of surrogate models and decrease overall uncertainty [115, 116]. This is achieved by exploring the surrogate beyond the initial sampling. EGO is a well-known algorithm that employs both local and global searches to find the optimal solution by means of the expected improvement ($E[I(x)]$) function as a key metric to direct its search. The function calculates the potential improvement that can be obtained by evaluating a new observation point based on the current best solution and the overall uncertainty of the surrogate model [117]. The implementation of this function provides the necessary sparsity-promoting behaviour to explore the design space in regions where their initial sampling was not sufficient. The expected improvement function is defined as

$$E[I(x)] = (f_{\text{min}} - \mu(x))\,\Phi\left(\frac{f_{\text{min}} - \mu(x)}{\sigma(x)}\right) + \sigma(x)\phi\left(\frac{f_{\text{min}} - \mu(x)}{\sigma(x)}\right), \tag{VI.20}$$

where $f_{\text{min}} = \min Y$, and $\Phi(\cdot)$ and $\phi(\cdot)$ are respectively the cumulative and probability density functions of $\mathcal{N}(0, 1)$, following the distribution $\mathcal{N}(\mu(x), \sigma^2(x))$. Using EGO to explore the surrogate beyond the initial sampling aids in decreasing the overall uncertainty and improving the precision of the surrogate model, especially in the unexplored and extreme regions of the design space. Consequently, the algorithm can effectively balance local and global searches and locate the optimal solution more proficiently. Hence, the following sampling point is determined by

$$x_{n+1} = \arg\max_x \left(E[I(x)]\right). \tag{VI.21}$$

In order to fully explore the design space, new data is collected for each objective function separately. This involves taking one sample of $n_{\text{EGO}} = n_0\ x \rightarrow y$ for each objective, resulting in a total of 180 new sampled points (n_0 for each of the objectives). With the addition of

the initial LHS, the total number of observations sums to 270 per model, yielding a cost-efficient computational problem to be analysed by Kriging. However, since the design space explored is large and the use of Bayesian optimisation might sample observations in very close proximity, the gradients between points may be high, yielding possible noise. Therefore, the surrogate is regularised following the methodology by [146], where noise is considered to be Gaussian distributed and its homoscedastic variance is evaluated based on the performed observations to obtain a smooth response surface.

VI.2.2.6 Multi-objective solution

The Kriging method offers a significant benefit since it allows the application of algorithms that can thoroughly explore the objective space. Consequently, the objective of this study is to find the optimal solution for the surrogate model. To achieve this, the multi-objective evolutionary algorithm (MOEA) NSGA-II has been chosen. This algorithm is known for its versatility, fast and efficient convergence, and ability to handle non-penalty constraints. It also has a wide-range search for solutions, which implies that it can explore the objective space more thoroughly and is less likely to get grounded in local optima [118]. By using the MOEA NSGA-II algorithm, the improved solutions are ensured to be non-dominated, meaning that they are not worse than any other feasible solution in all objective functions. This also ensures that the solutions avoid local minima and are highly likely to discover the global optimum for the sampled response surface. This makes the algorithm able to search a large portion of the objective space and find the best possible solution for the surrogate model while avoiding suboptimal solutions.

VI.2.3 High-fidelity data

Since the main purpose of this study is to obtain a PDA-EARSM for capturing the secondary flow, the DNS data of a canonical case with this flow characteristic is chosen. A duct flow case of AR $= 1$ and bulk Reynolds number of $\mathrm{Re}_b = 3500$ is used for the training process (depicted in Fig. VI.1). The DNS data is obtained from Ref. [147] curated by Ref. [148]. Following the progressive approach, the trained PDA-EARSMs are tested on two cases of channel flow with friction Reynolds number of $\mathrm{Re}_\tau = 395$ and $\mathrm{Re}_\tau = 5200$ for which data is obtained from Refs. [149] and [150], respectively. Considering the generalisability of the new models, we likewise test them on four unseen cases containing secondary flows, including duct secondary flow cases with AR $= 1$ and higher bulk Reynolds numbers of $\mathrm{Re}_b = 5700$ [151], and $\mathrm{Re}_b = 10320$ [152], a duct secondary flow case with AR $= 3$, a lower bulk Reynolds number of $\mathrm{Re}_b = 2600$ [151], and a roughness-induced secondary flow with nominally infinite Reynolds number (more information about the geometry and properties of this case is available at Refs. [121, 143].

VI.3 Results and discussion

In this section, the results are presented in two subsections. In the first one, the results of the optimisation process and training of the two best PDA-EARSMs are presented, whereas, in the second, the performance of the trained models is evaluated on the test cases with different geometries, Reynolds numbers, and boundary conditions. Associated contours and velocity profiles accompany all results which are similarly described and discussed, followed by their corresponding figures.

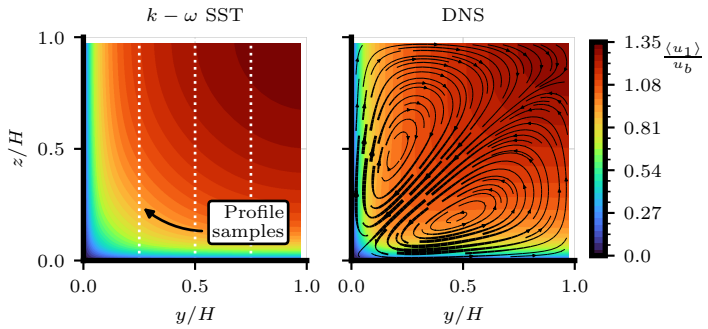

Figure VI.3: Contours of streamwise velocity and secondary flow streamlines for duct flow optimisation case at AR $= 1$ and $\mathrm{Re}_b = 3500$ for RANS $k-\omega$ SST (left) and DNS (right) data. DNS data obtained from Ref. [147]. The dotted white lines denote the location of the velocity profiles evaluated throughout this study to perform a quantitative comparison. It should be noted the varying thickness of the secondary flow streamlines denotes their magnitude.

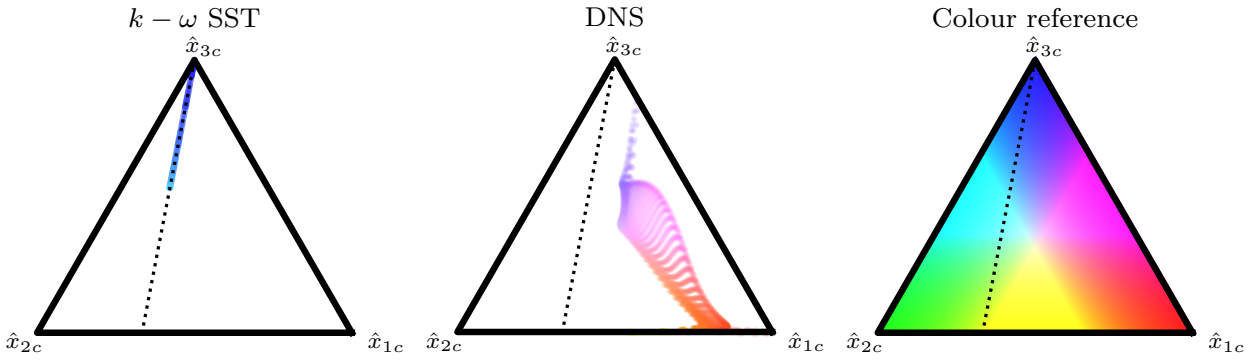

Figure VI.4: Barycentric representation of RSTs' shape for $k-\omega$ SST (left) and DNS (centre) for training duct flow case with AR $= 1$ at $\mathrm{Re}_b = 3500$. DNS data obtained from Ref. [147]. The plain-strain limit is represented by the dotted line, and the colour representation (right) follows the work by [153].

VI.3.1 Surrogate-based optimisation

VI.3.1.1 Optimisation case: k–ω SST performance

It is essential to qualitatively indicate the original performance of $k-\omega$ SST against high-fidelity data prior to any modifications. For both fidelity levels, the results for the square duct case show the progressive deceleration of the streamwise flow as it approaches the walls of the duct, exhibiting higher gradients in the near-wall regions as a consequence of the boundary layer and the fully developed turbulent flow. Whereas this behaviour can be predicted by $k-\omega$ SST, the presence of a secondary flow predicted by DNS is completely neglected by the RANS model (Fig. VI.3), as expected [127]. Two antisymmetric rotational regions are generated diagonally at the duct's vertex, preserving their symmetry at the 4 quadrants of the duct. This secondary flow is strong enough to drive the streamwise flow towards the duct vertices, skewing the streamwise velocity field in the domain through an impinging-like flow behaviour. Since $k-\omega$ SST does not predict these rotational motions, the streamwise velocity distribution is not skewed and the spanwise and vertical components of the velocity are zero.

Figure VI.4 compares the barycentric plots representing the shape of RSTs for the optimisation case. The location of each point is calculated based on the eigenvalues of the

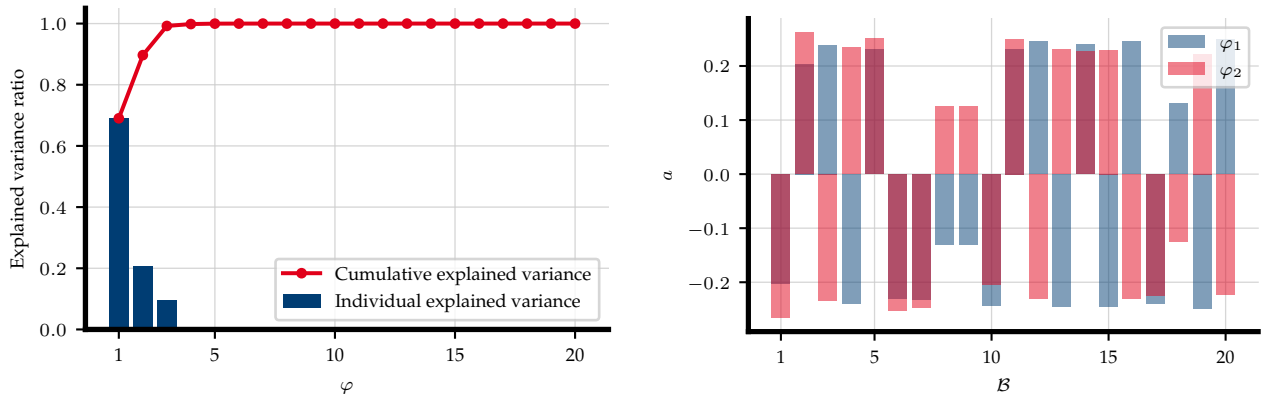

(a) Explained variance ratio of each principal component.

(b) Coefficients associated with the first two principal components.

Figure VI.5: PCA results of the candidate functions calculated by DNS data of the optimisation case.

normalised anisotropic part of the RST (more information about barycentric plots available at Refs. [153, 154]). While $k-\omega$ SST yields all results within the plain-strain limit as expected from a linear eddy-viscosity RANS model, DNS shows a more complex stress anisotropy distribution as a combination of states toward one-component turbulence fluctuations $\hat{x}_{1_c}$ (also known as rod-like or cigar-like turbulence) and an offset from the plain-strain limit with a tendency towards isotropic (or spherical) turbulence $\hat{x}_{3_c}$.

VI.3.1.2 Optimisation case: PDA-EARSMs

Since $k-\omega$ SST is not able to predict the secondary flow of the optimisation case, CFD-driven optimisation is applied following the models described in Eqs. VI.13a and VI.13b focusing on predicting secondary flows and correct streamwise velocity.

Regarding model **II**, PCA is applied to the set of candidate functions (listed in Eq. VI.8) using the high-fidelity data of the optimisation case. Figure VI.5 presents the PCA results and shows that only the first 2 principal components (φ_1 and φ_2) yield an explained variance ratio of 0.90 (Fig. VI.5a), where φ_1 is the main principal component explaining the variability. Figure VI.5b presents the coefficients corresponding to the two first principal components used for model **II**.

As mentioned in Sec. VI.2, the two first principal components for model **II** are chosen. To compare model **I** in an analogous manner, the two first leading candidate functions are likewise chosen where the coefficients of these two models are determined by surrogate and Bayesian optimisation.

The surrogate model is generated using the RANS simulations results to find the optimal values of the optimisation variables. Regarding the optimisation process and since cases with high values of the objective functions are not of interest, the MOEA optimisation is performed by imposing the constraints $j_1 \leq 0.5$ and $j_2 \leq 0.4$, therefore, the analysed non-dominated solutions only take place in the regions of highest interest and potential global minimisation. To yield a smooth non-dominated solution front, 5000 samples are required by the MOEA in this study. This showcases the cost advantages of surrogates, where 270 CFD observations are required, yielding a cost reduction of 18.4 times.

Regarding both models' results, an optimal design space of $[-2,-1,-1] \leq C_i \leq [0,1,1]$ is chosen for model **I**, and an optimal design space of $[-1.75,-0.25,-0.25] \leq C_i \leq$

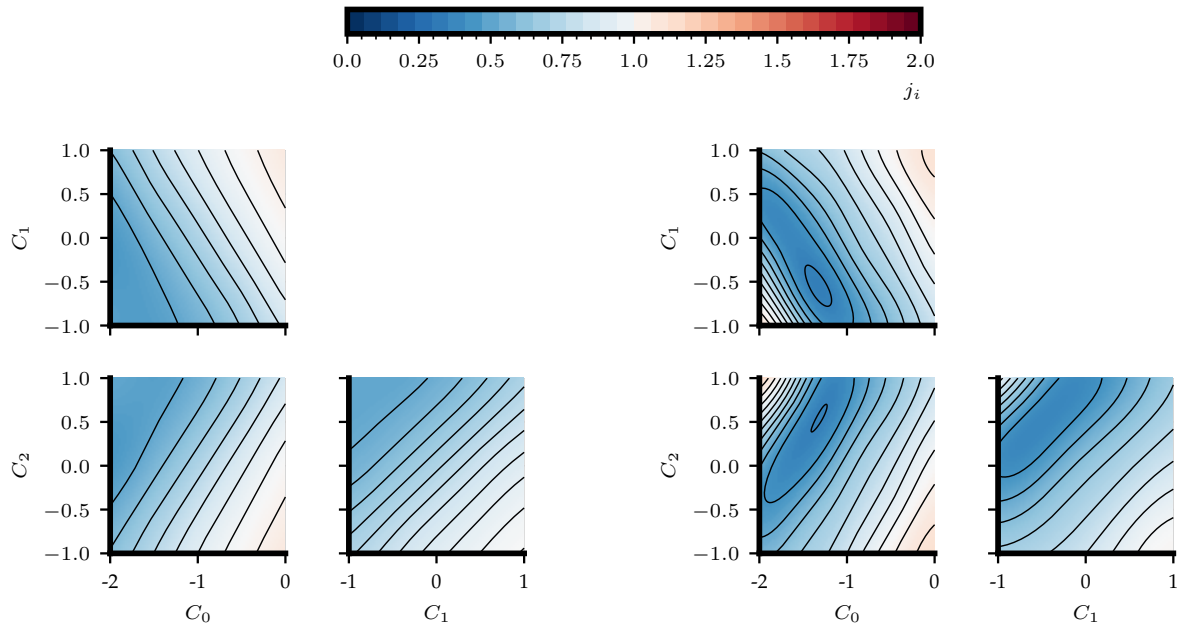

(a) Surrogate for j_1.

(b) Surrogate for j_2.

Figure VI.6: Surrogate contour visualisation for model **I**. It should be noted that each pair of variables is shown by holding the other variable at the mid-value of their range.

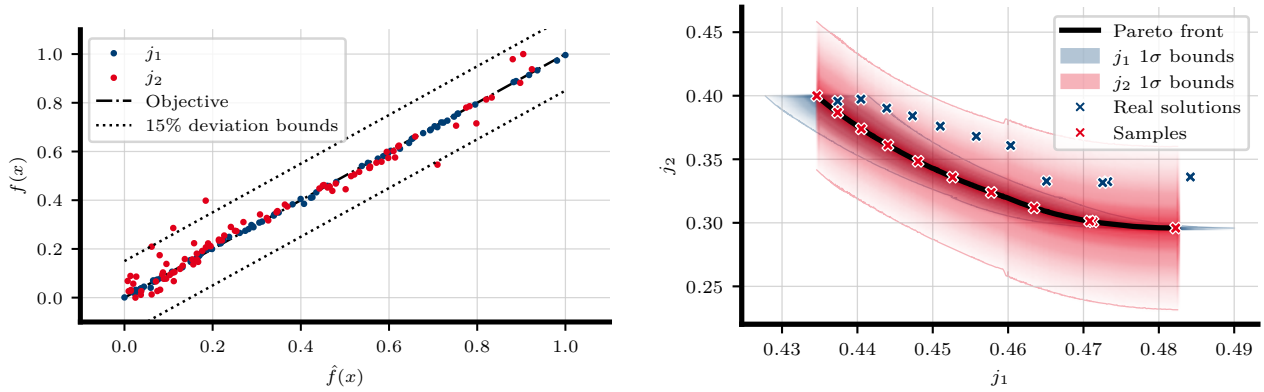

(a) Surrogate quality.

(b) Pareto front.

Figure VI.7: Surrogate quality against test set (Fig. VI.7a), and Pareto-front validation with 1σ uncertainty bounds (Fig. VI.7b) for model **I**.

$[-1.25, 0.25, 0.25]$ is chosen for model **II** after various progressive surrogate iterations. The iterations re-define the design space limits by analysing the non-dominated values of the coefficients after optimisation. If these values reach the imposed limits, the objective space is reset, and the design space is adapted.

VI.3.1.2.1 MODEL **I** Contour plots in Fig. VI.6b illustrate how the optimisation variables affect the objective functions. On the one hand, the surrogate visualisation for j_1 (Fig. VI.6a) shows a quasi-linear tendency for all variables. The global minimum for j_1 is shown towards negative values for all C_i without clear visualisation of extrema. On the other hand, there is a clear global minimum seen for j_2 values, shown by a non-linear surrogate for C_0 and C_1, where quasi-linear behaviour is predicted by the relationship between C_1 and C_2 (Fig. VI.6b). It is important to highlight that, although the lowermost values for the coefficients predict an

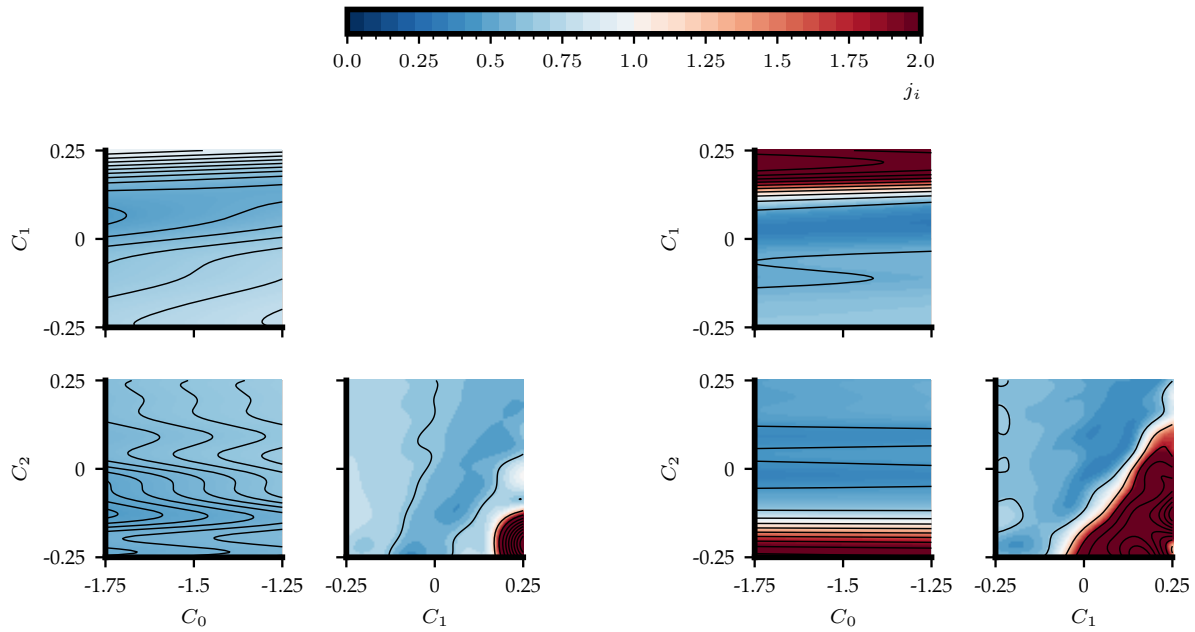

(a) Surrogate for j_1.

(b) Surrogate for j_2.

Figure VI.8: Surrogate contour visualisation for model **II**. It should be noted that each pair of variables is shown by holding the other variable at the mid-value of their range.

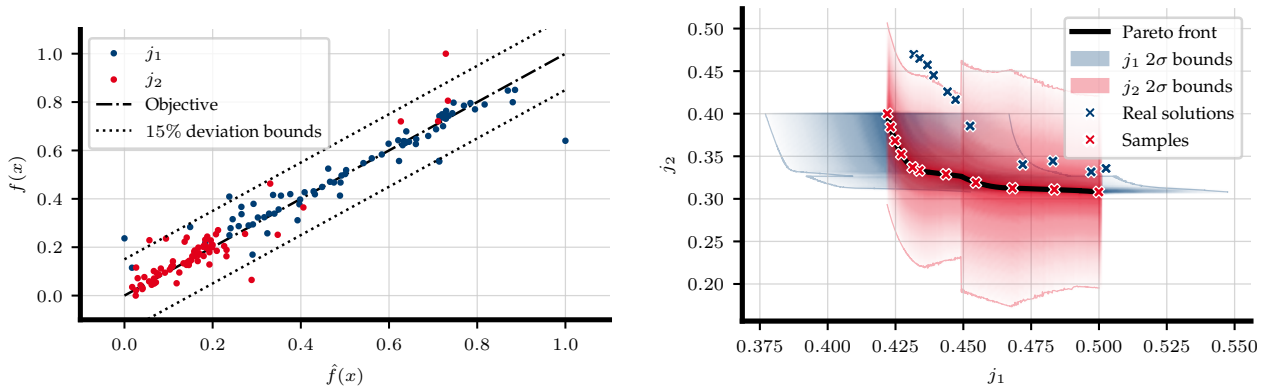

(a) Surrogate quality.

(b) Pareto front.

Figure VI.9: Surrogate quality against test set (Fig. VI.9a), and Pareto front validation with 2σ uncertainty bounds (Fig. VI.9b) for model **II**.

improvement for j_1, the tendency is not completely followed by j_2 prediction. This implies that a more accurate prediction of the streamwise flow does not necessarily correlate with the secondary flow prediction in this case.

Regarding the surrogate quality (Fig. VI.7a), and Pareto front prediction and numerical validation (Fig. VI.7b), the surrogate predicts the test set with great accuracy for the whole design space tested, which is likewise reflected by a highly accurate Pareto front prediction, where all numerical tests simulated are able to predict the objective space within 1σ uncertainty bounds for both objective functions.

VI.3.1.2.2 MODEL **II** In contrast with model **I**, the surrogate visualisation for both objective functions (Fig. VI.8) in model **II** shows a non-linear prediction for all variables. This behaviour is somewhat expected due to the added complexity of the model with the PCA.

Table VI.1: Objective function results, coefficients, and quality for best models and surrogates of each approach.

Model	J	j_1	j_2	C_0	C_1	C_2	RMSE_1	RMSE_2	r_1^2	r_2^2
I	0.387	0.455	0.319	-1.653	0.625	1	0.004	0.048	0.999	0.966
II	0.398	0.457	0.339	-1.613	0.074	0.015	0.032	0.079	0.895	0.880

The global minimum for j_1 does not have a straightforward location. Instead, there are diverse regions where the global extrema can be found. Specifically, negative values of C_0, and near-zero values of C_1 and C_2 predict generally lower values of j_1 and j_2 (Figs. VI.8a and VI.8b). Similarly to model **I**, although the objective spaces for both functions follow similar tendencies, there are visible differences in the predicted locations of the minima, reflecting once more that a more accurate prediction of the streamwise flow does not necessarily correlate with the secondary flow prediction.

Regarding the surrogate quality (Fig. VI.9a), and Pareto front prediction and numerical validation (VI.8b), the surrogate predicts the test set with high accuracy for the whole design space tested. These lower-confidence regions are not reflected in the non-dominated solutions nor in their numerical validation. Since the expected improvement function prioritises good confidence in the near-extrema region and the complexity of the model is higher, a certain level of uncertainty is expected in far-away regions of the global minimum. Nevertheless, the surrogate shows a good level of confidence at the Pareto front (within 2σ in Fig. VI.9b).

VI.3.2 Comparison of models

The final results for each model are shown in Table VI.1, where the best cases per model are shown, followed by their C_i values and surrogate quality parameters. Both models significantly improved the standard $k-\omega$ SST by 61.3% and 60.2% for model **I** and **II** respectively. Differences in performance for the objective values are considered negligible. As seen in Fig VI.7a and VI.9a, the surrogate quality is slightly worse for model **II**. This is due to the higher complexity added by PCA and the inclusion of higher order terms in α_2, yielding more non-linear behaviour in the design space and, thus, a higher RMSE and lower r^2 for model **II**.

Regarding qualitative results for the optimisation case, both models are able to accurately predict the direction and symmetry of the secondary motions while improving the streamwise flow prediction. However, the streamwise vorticity error is generally higher in the near-wall regions (Fig. VI.10). As a consequence of the prediction of a correct secondary flow direction, the streamwise flow prediction likewise improves. Regions of slight overprediction of $\langle u_1 \rangle$ are seen in the near-wall vicinity as well as the middle section of the computational volume, whereas regions of $\langle u_1 \rangle$ underprediction are seen in the bulk flow close to the channel vertex. Regarding the prediction of $\langle \omega_1 \rangle$, anti-symmetric predictions are seen with respect to the diagonal symmetry line with a general over and underprediction in the near-wall region.

As expected from the objective function results, qualitative differences between models (Fig. VI.11) are not clearly seen. For the streamwise velocity prediction, no significant differences can be seen in the contours of the error function, whereas for the vorticity prediction, slight variations in the error can be seen between models without a significant impact on the overall performance of the models. In summary, both models are able to predict the secondary flow with high accuracy.

Concerning the quantitative analysis of the velocity profiles at $y/H = [0.25, 0.5, 0.75]$, an

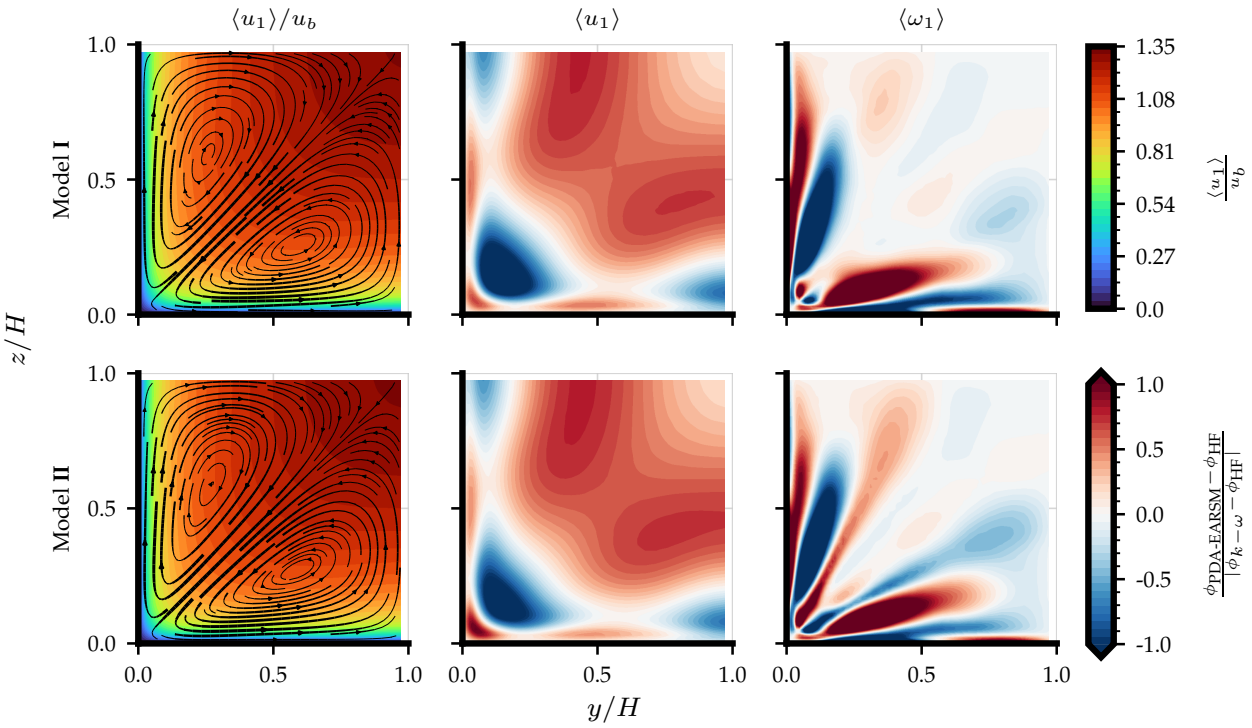

Figure VI.10: Qualitative streamwise and secondary flow prediction of the best cases for each of the models. Left: streamwise flow contours with stream function lines depicting secondary flow prediction and direction. Centre: streamwise flow error compared to DNS data. Right: streamwise vorticity error compared to DNS data. It should be noted that the stream function line thickness denotes the secondary flow intensity. In the colourbar, ϕ indicates either $\langle u_1\rangle$ or $\langle \omega_1\rangle$.

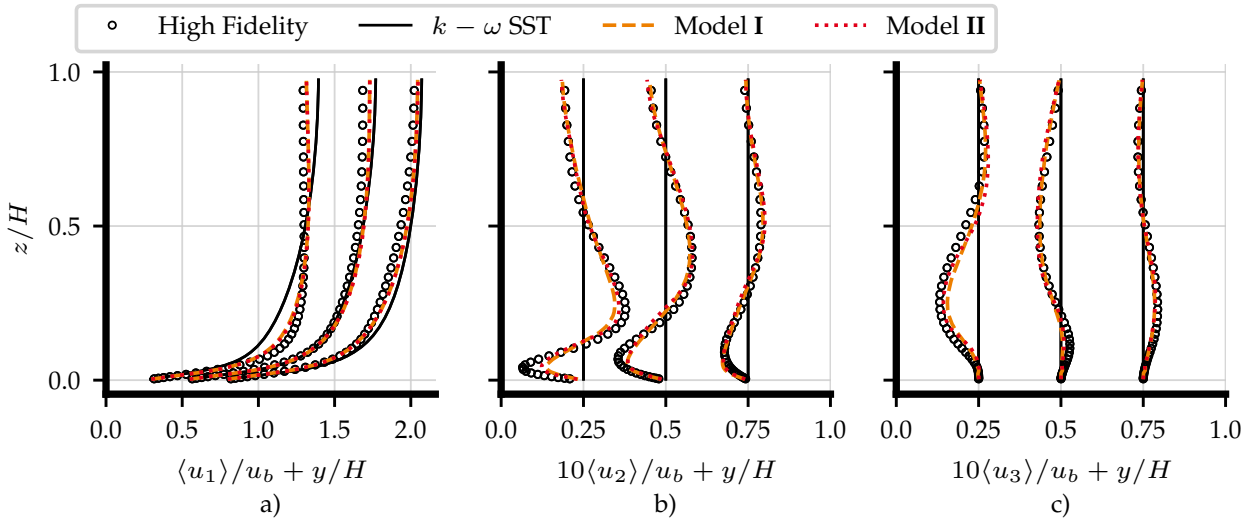

Figure VI.11: Profiles of velocity components for duct flow case with AR $= 1$ and $\text{Re}_b = 3500$. High-fidelity data obtained from Ref. [147].

overall and significant improvement in the prediction of both models against standard $k-\omega$ SST, can be seen. Although the prediction of both models displays minor differences between each other, they both predict with high accuracy the DNS data. Some light discrepancy can be

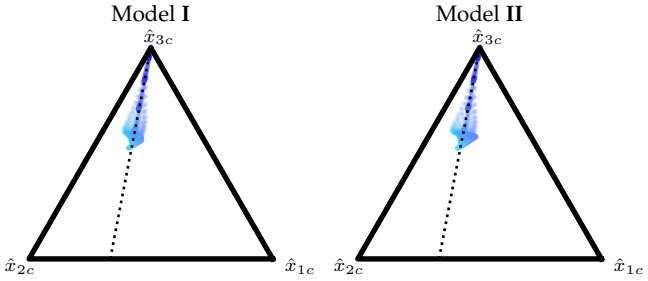

Figure VI.12: Barycentric map showing the physical reliasability and turbulence anisotropy of the developed models following the colour representation by [153].

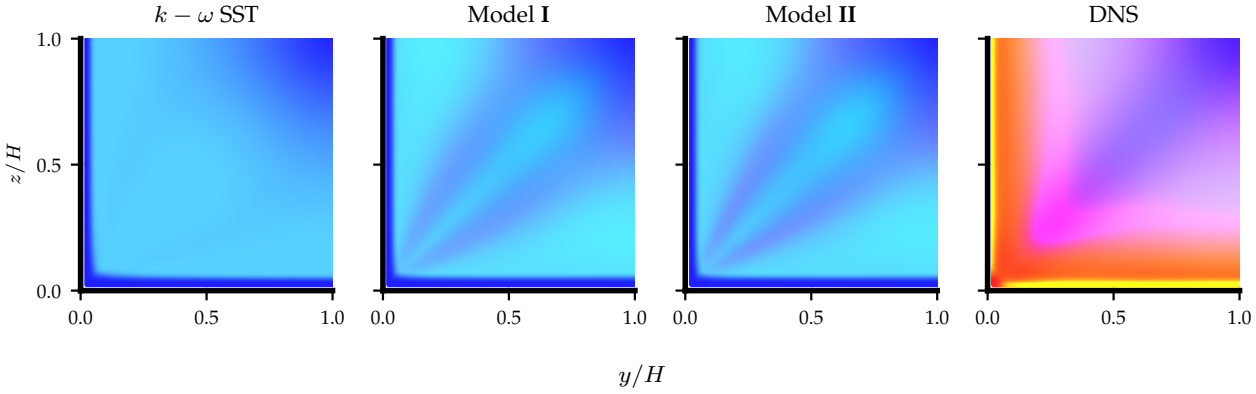

Figure VI.13: Contours of RSTs' shape for duct flow case with AR $= 1$ and $\mathrm{Re}_b = 3500$. The colours follow the reference barycentric map in Fig.VI.4. DNS data from Ref. [147].

seen in the magnitudes at near-wall regions, where the gradient of $\langle u_2 \rangle$ is high. Nevertheless, gradients of velocity are accurately predicted, only displaying a slight underprediction in the velocity magnitude in near-wall regions.

The turbulence shape of the developed models is represented in Figs. VI.12 and VI.13, where the reliasability for both models is conserved. A certain level of anisotropy is added to the models, yielding results in the vicinity of the plain-strain limit. Both models predict a very similar turbulence shape while model **II** slightly yields results farther away from the plain-strain limit. Nonetheless, results are distant from $\hat{x}_{1_c}$ and DNS anisotropy. Although these results are expected, the integration of the whole Pope's decomposition with its 10 tensors and a more thorough definition of $\mathcal{B}$ could be able to further improve the RANS anisotropy prediction.

Figure VI.14 presents the profiles of RST components obtained by new models and shows that new correction models improve the prediction of RST components. It should be mentioned that the Reynolds stress tensor is calculated as

$$R_{ij} = A_{ij} + \frac{2}{3} k \delta_{ij}. \tag{VI.22}$$

The results of R_{ij} show that the introduced correction does not change the original R_{11} prediction by $k-\omega$ SST while the 2 other principal components of the tensor (R_{22} and R_{33}) are predicted in better agreement with high-fidelity data. Predictions of the off-diagonal components of R_{ij} are overall displaying an improvement in prediction, highlighting the non-zero prediction of R_{23}, which shows a certain level of mismatch with high-fidelity data in the near-wall regions.

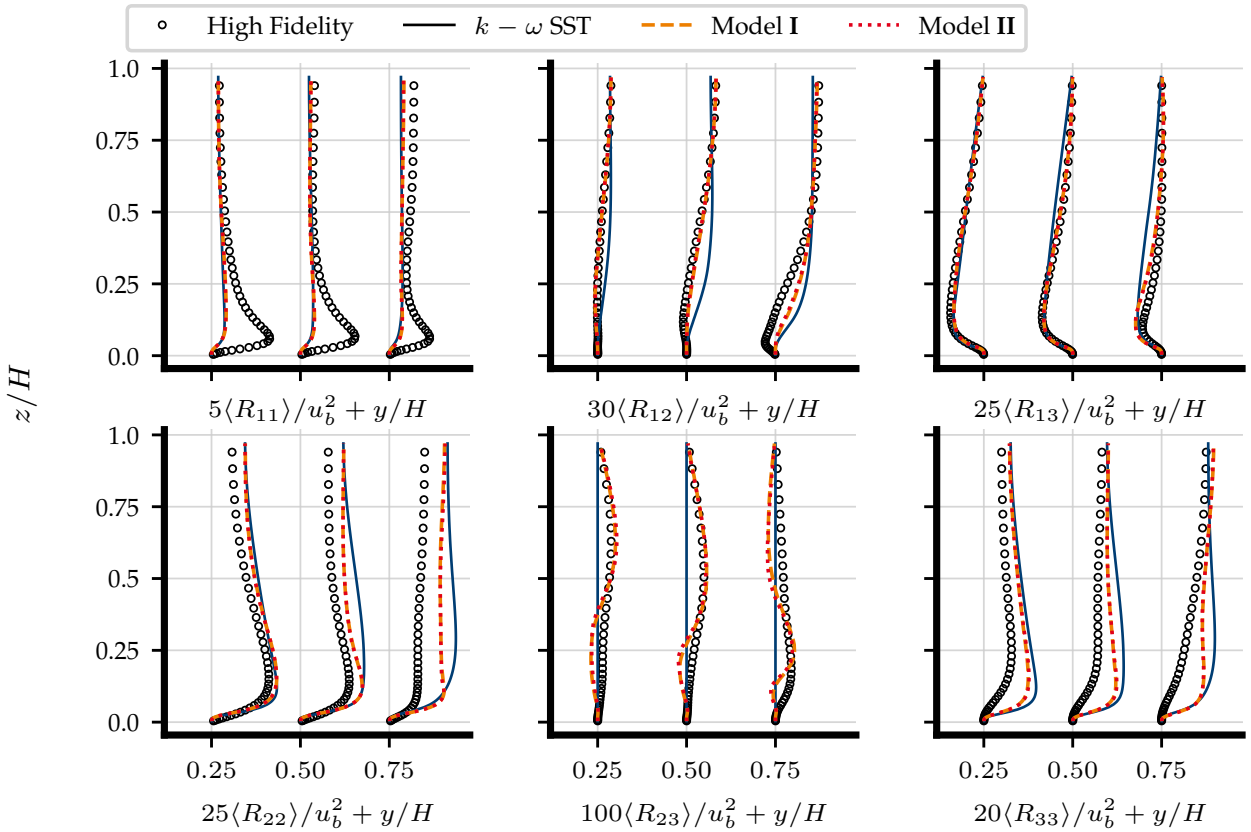

Figure VI.14: Profiles of Reynolds stress components for duct flow case with AR $= 1$ and $\mathrm{Re}_b = 3500$. High-fidelity data obtained from Ref. [147].

Qualitatively and quantitatively, both models improve the prediction and agreement with high-fidelity Reynolds stresses while not showing significant differences in the prediction of Reynolds stresses between models.

VI.3.3 Verification and generalisability on test cases

In this subsection, the best-found models are tested against diverse canonical cases in which secondary flow is an important component as well as cases where secondary flow is not present. This verification is performed in order to provide a performance overview of the models' generalisability, stability, and robustness to preserve canonical flow features. Firstly, validation of the channel case and the boundary layer is performed at different Reynolds numbers. Secondly, the models are tested against diverse cases of ducts with different aspect ratios and Reynolds numbers. Lastly, the models are tested against a wall-modelled nominally infinite Reynolds number case in which secondary flow is roughness-induced. Similarly as in section VI.3, all results are shown and discussed with their respective velocity contour plots with stream functions and qualitative flow analysis of the velocity profiles.

VI.3.3.1 Channel flow and law of the wall

The addition of $T_{ij}^{(2)}$ and further modifications in this study must not destabilise $k-\omega$ SST and yield unphysical results. Therefore, both models are tested in a channel flow case at friction Reynolds numbers 395 and 5200 to verify that the law of the wall is preserved. The

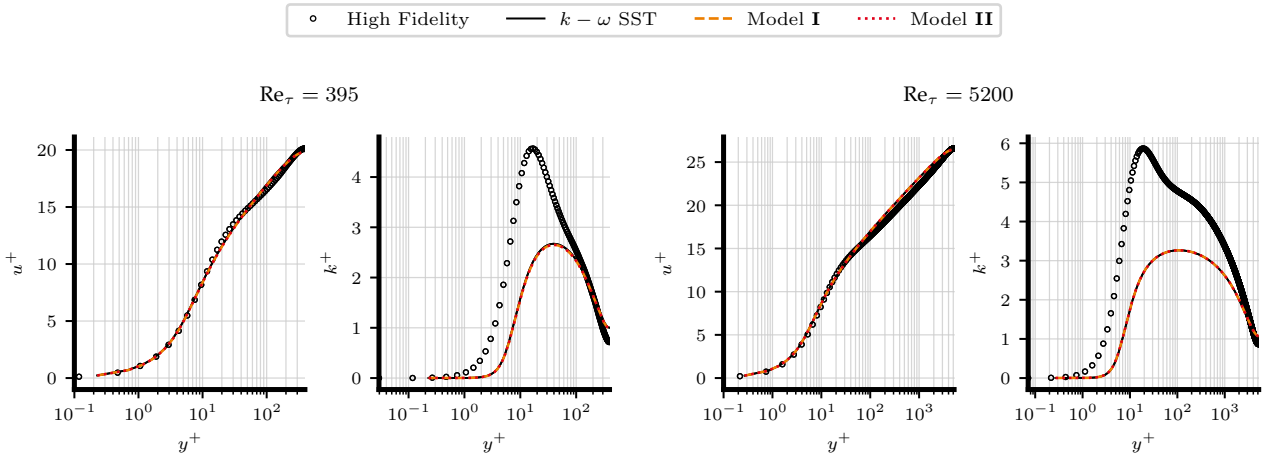

(a) (b)

Figure VI.15: Mean streamwise velocity and turbulent kinetic energy profiles for channel flow: $\mathrm{Re}_\tau = 395$ (Fig. VI.15a), and $\mathrm{Re}_\tau = 5200$ (Fig. VI.15b). High-fidelity data obtained from Ref. [149].

canonical channel flow cases are driven by a constant pressure gradient in order to match the friction Reynolds number from DNS.

Results shown in Fig. VI.15 depict the streamwise velocity as $u^+ = u/u_\tau$ and $k^+ = k/u_\tau^2$ in function of $y^+ = u_\tau y/\nu$, where u_τ is the friction velocity. The results show a consistent prediction of the law of the wall with $k-\omega$ SST without introducing any noticeable changes. Both models yield the same results for both the streamwise velocity and the turbulence kinetic energy, and no improvements or diminishments in the prediction of these variables are seen compared to standard $k-\omega$ SST.

VI.3.3.2 Duct cases

To showcase the generalisability of the models, diverse duct cases are tested. The first case is the flow through a duct of AR $= 1$ and a considerably higher $\mathrm{Re}_b = 5700$ compared to the optimisation case.

A qualitative depiction of the results is shown in Fig. VI.16, where both models are able to predict the gradients of the secondary flow and improve the prediction of the streamwise velocity compared to $k-\omega$ SST. In agreement with the baseline results of the models, the magnitude of the secondary motion is weaker than the high-fidelity data although the motion's antisymmetry and location of the vortices centres are predicted accurately.

Regarding the velocity profiles of the case (Fig. VI.17), a similar trend is observed where the gradients and magnitude of the profiles are predicted with high accuracy in both models, only displaying some discrepancies in the wall-near regions, where the high-fidelity data yields slightly higher velocity gradients.

In order to verify the performance of the models in diverse cases with similar features, the models are likewise tested against a duct of AR $= 3$ and a slightly lower $\mathrm{Re}_b = 2600$ compared to the optimisation case.

The qualitative results shown in Fig. VI.18 indicate a similar performance for both models: gradients, symmetry, and direction of secondary flow are predicted accurately with slight inaccuracies regarding the secondary flow magnitude in the near-wall regions. The location of the vortices centres is likewise predicted with high accuracy, agreeing with high-fidelity data (Fig. VI.18).

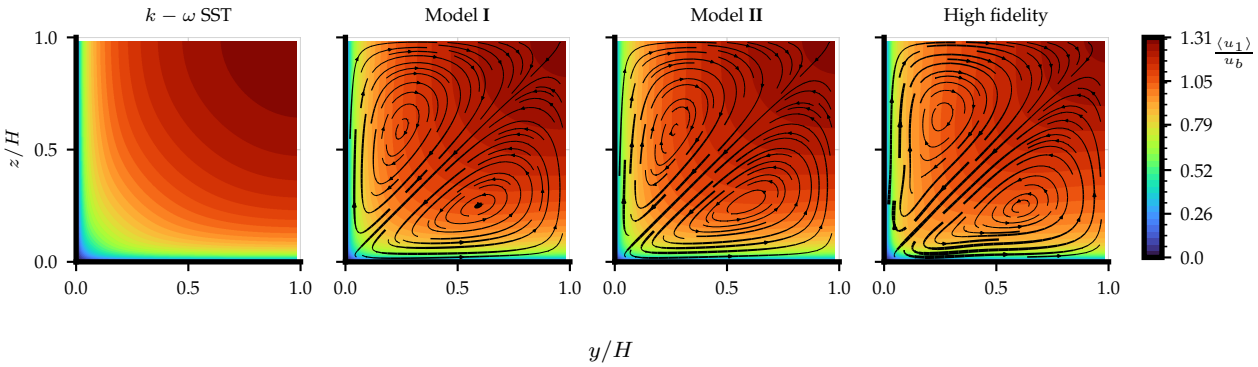

Figure VI.16: Streamwise flow contours with stream function iso-lines depicting secondary flow prediction and direction: Duct flow case with AR $= 1$ and $\mathrm{Re}_b = 5700$. High-fidelity data obtained from Ref. [151].

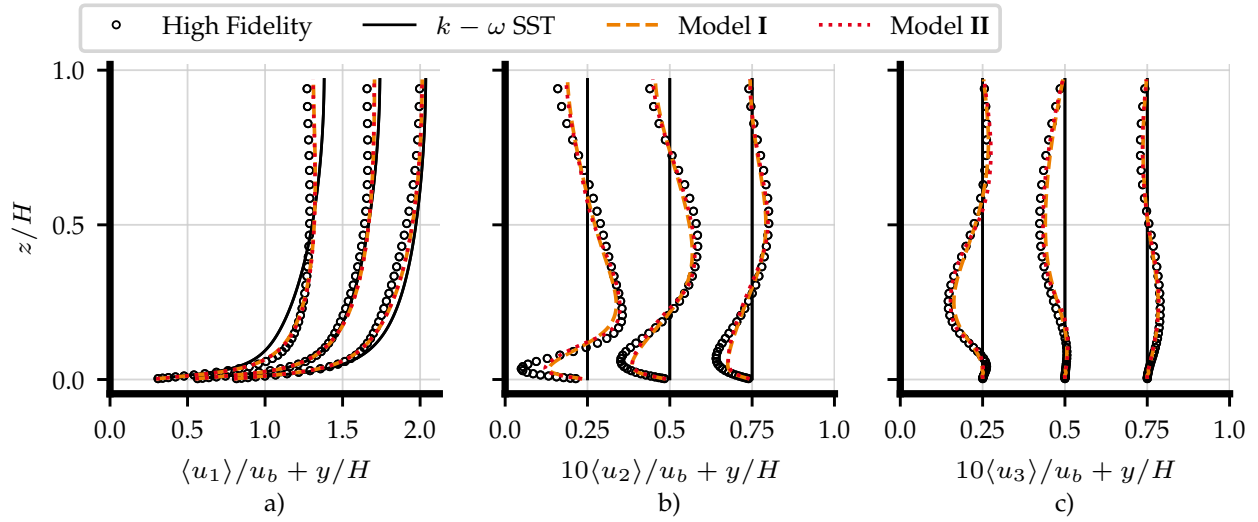

Figure VI.17: Profiles of velocity components for duct flow case with AR $= 1$ and $\mathrm{Re}_b = 5700$. High-fidelity data obtained from Ref. [151].

In terms of the quantitative analysis and the evaluation of the velocity profiles, the results shown in Fig. VI.19 likewise follow a similar trend compared to previous results in this study. The region in the vicinity of the duct vertex shows some discrepancy in the velocity prediction. Nevertheless, the bulk flow away from the near wall is accurately predicted.

VI.3.3.3 Roughness-induced secondary flow case

Finally, the verification of the models is tested on a roughness-induced secondary flow case. The case is based on the studies by [142, 143], and is characterised by displaying a nominally infinite Reynolds number. It should be noted that due to the very high Reynolds number, the use of wall models is inevitable with current hardware, therefore, the atmospheric wall models [155] have been used. The secondary flows generated in this case are recognised as Prandtl's second kind of secondary flow, similar to the square duct flow [127]. The roughness-induced case is chosen to showcase the models' performance in a more complex and challenging to predict case, mostly by two-equation RANS turbulence models.

For a better analysis of roughness-induced secondary flow, dispersive velocity compo-

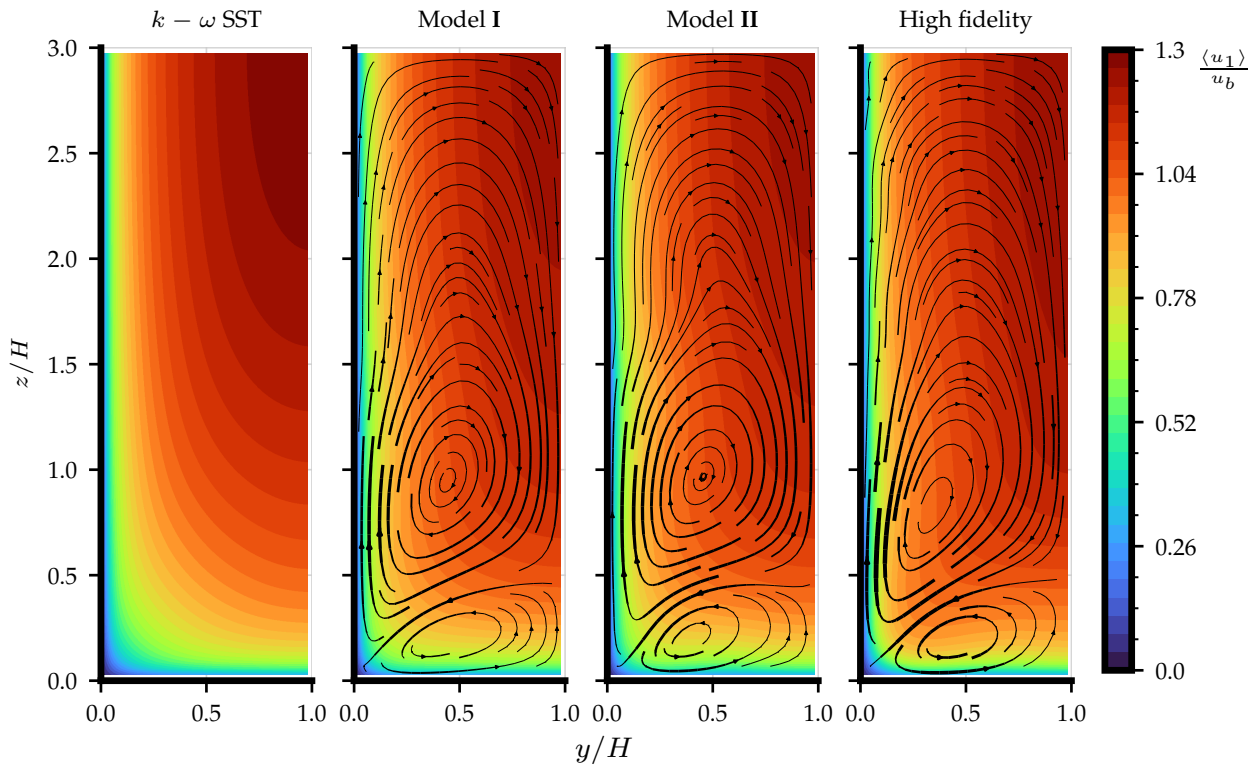

Figure VI.18: Streamwise flow contours with stream function iso-lines depicting secondary flow prediction and direction: Duct flow case with AR $= 3$ and $\mathrm{Re}_b = 2600$. High-fidelity data obtained from Ref. [151].

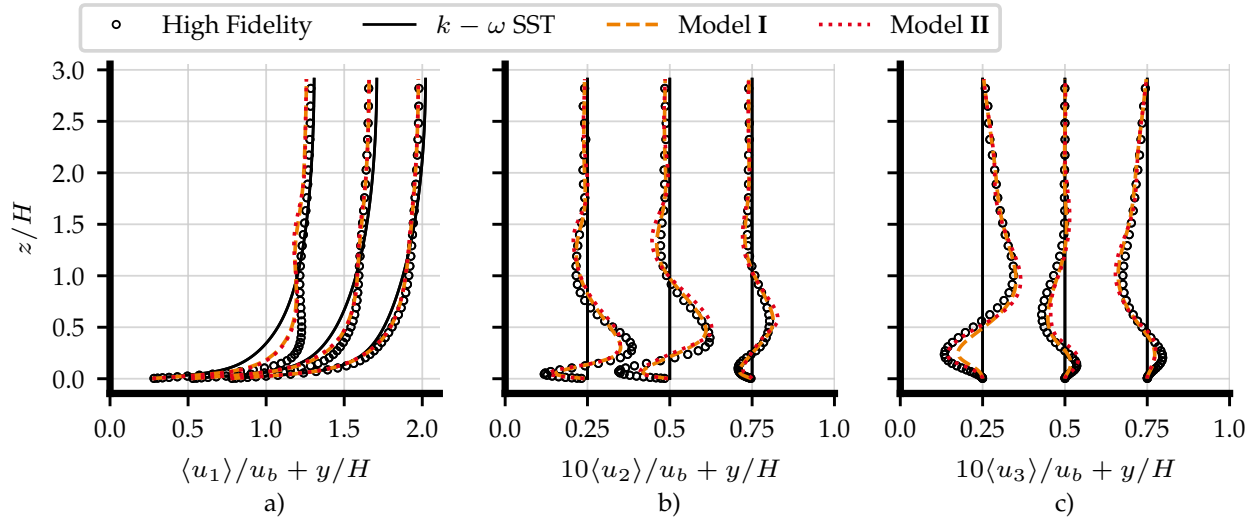

Figure VI.19: Profiles of velocity components for duct flow case with AR $= 3$ and $\mathrm{Re}_b = 2600$. High-fidelity data obtained from Ref. [151].

nents are defined as,

$$\langle u_i'' \rangle = \langle u_i \rangle - \langle \tilde{u}_i \rangle, \tag{VI.23}$$

where $\langle u_i'' \rangle$ is the dispersive velocity components, and $\langle \tilde{u}_i \rangle$ is the spatial spanwise-averaged mean velocity.

Following previous verification, the qualitative results of the streamwise dispersive velocity ($\langle u_1'' \rangle$) are shown in Fig. VI.20. On the one hand, results show that standard $k-\omega$

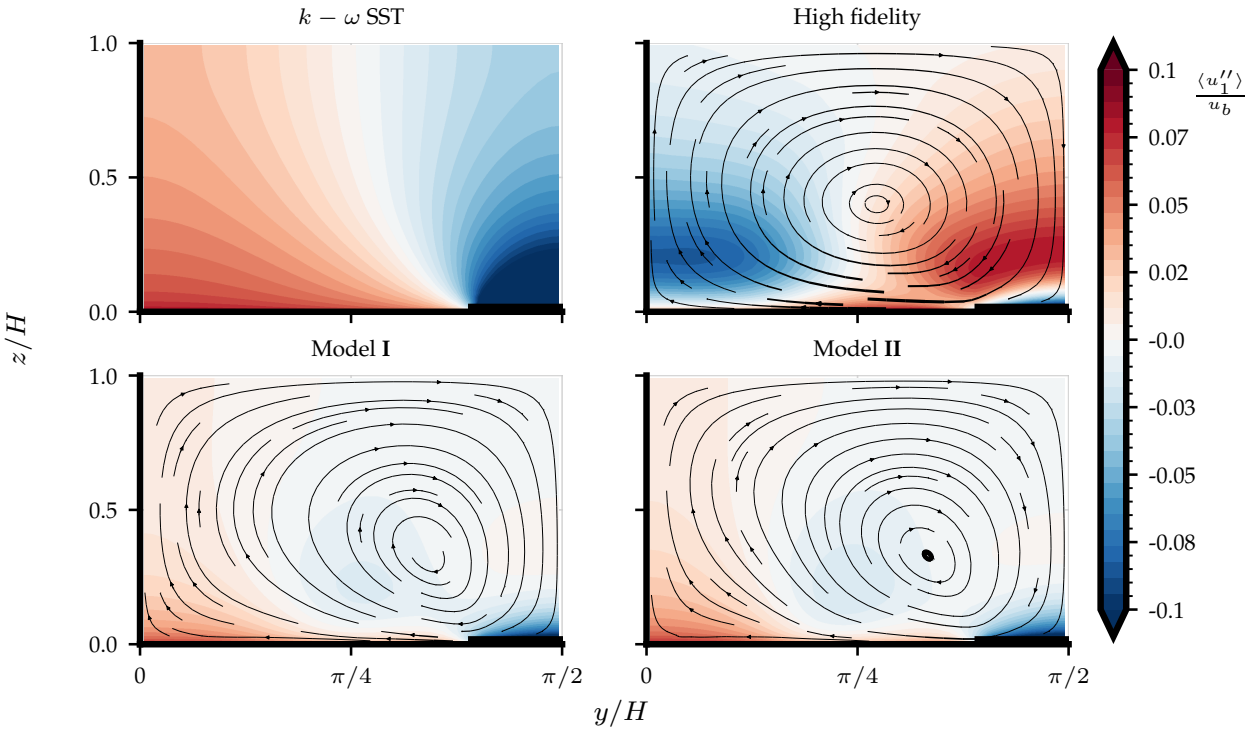

Figure VI.20: Streamwise dispersive velocity contours with stream function iso-lines depicting secondary flow prediction and direction: Roughness-induced secondary flow case with $\mathrm{Re}_b = 2 \times 10^8$. High-fidelity data obtained from Ref. [143].

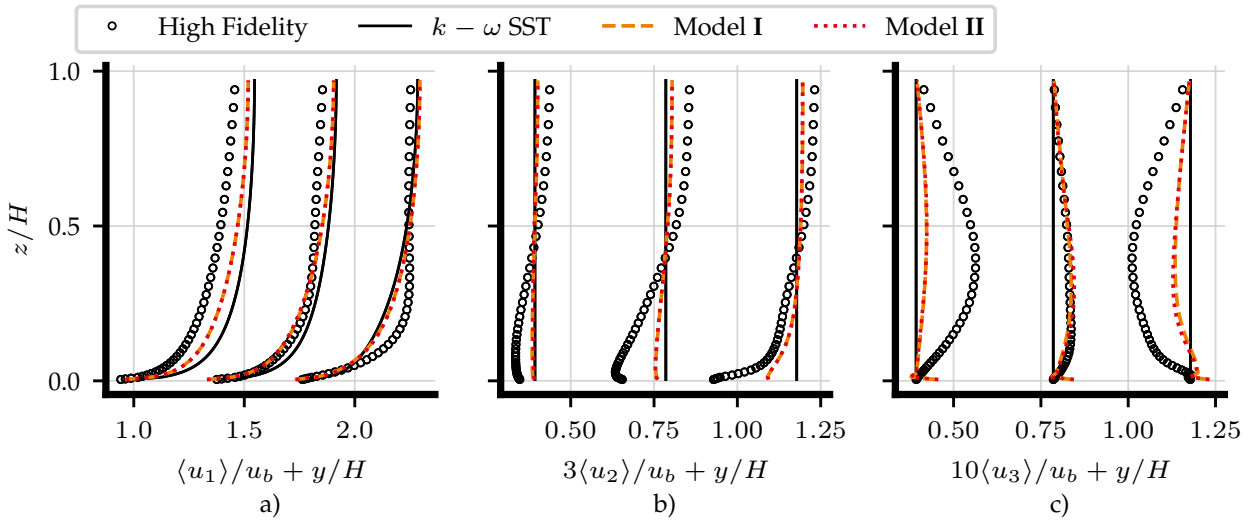

Figure VI.21: Profiles of velocity components for roughness-induced secondary flow with $\mathrm{Re}_b = 2 \times 10^8$. High-fidelity data obtained from Ref. [143].

SST does not predict any secondary motion that drives the flow to display a high-momentum path on top of the high-roughness patch and a low-momentum path at $y/H = 0$, as the high-fidelity data predicts. On the other hand, the enhanced models are both capable of predicting the secondary motion, although at a lower intensity compared to high-fidelity results. The direction of the rotation (clockwise) is correctly predicted although the vortex centre does not visibly match the high-fidelity counterpart. Even though the predicted secondary flow

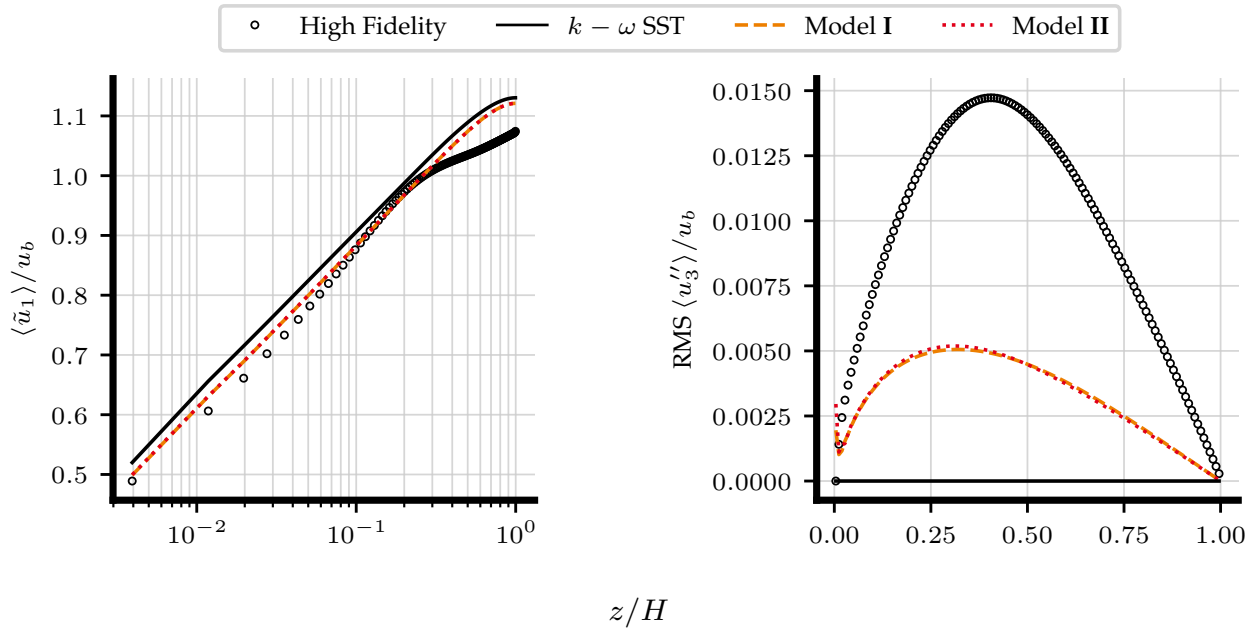

Figure VI.22: Roughness-induced secondary flow quantitative results of spanwise-averaged streamwise velocity (left), and root-mean-squared dispersive vertical velocity (right). High-fidelity data obtained from Ref. [143].

is not strong enough to move the low-momentum path to the top of the low-roughness patch ($y/H = 0$), the existence of a weak high-momentum path is visible on top of the high-roughness patch. Since the source of vorticity production lies at roughness-heterogeneity existing at the bottom wall (more information at Ref. [143]), the authors believe that further investigations about wall models regarding the secondary flow can help a better prediction of the secondary flow.

Quantitive results reflect the previous qualitative analysis. Figure VI.21 shows the velocity profiles at $y/H = [\pi/8, \pi/4, 3\pi/8]$, where the improvement of the models can be seen. In contrast to other verification cases in this study, both models' predictions improve the performance of standard $k-\omega$ SST, however, the secondary flow intensity is weaker compared to the high-fidelity data. The predicted tendencies are correct, although there is a discrepancy in the gradients and magnitudes predictions relative to previous verification cases.

To provide a complete and holistic comparative study for this case, the spatial average of the streamwise, as well as vertical root-mean-squared (RMS) dispersive velocity ($\langle \tilde{u}_1 \rangle$ and RMS $\langle u_3'' \rangle$, respectively), are calculated. These results are shown in Fig. VI.22, where the prediction of $\langle \tilde{u}_1 \rangle$ shows a considerable improvement compared to standard $k-\omega$ SST. However, the bulk flow for the developed models is still overpredicted as a consequence of the underpredicted secondary flow and its derived under-subtraction of the streamwise momentum. Regarding the RMS $\langle u_3'' \rangle$, a clear improvement in the prediction can be seen by the developed models, where $k-\omega$ SST is unable to predict any vertical dispersive velocity. The predictive profiles are underpredicted and slightly skewed towards $z/H = 0$ compared to the high-fidelity data, which verifies the mismatched location of the predicted secondary flow vortices. Both developed models yield an almost identical prediction of the flow, and a similar improvement is seen by models at their prediction of RMS $\langle u_3'' \rangle$. Overall, the applicability of the models to this case shows their generalisability, where robust and improved predictions are obtained in more complex cases at very high Reynolds numbers.

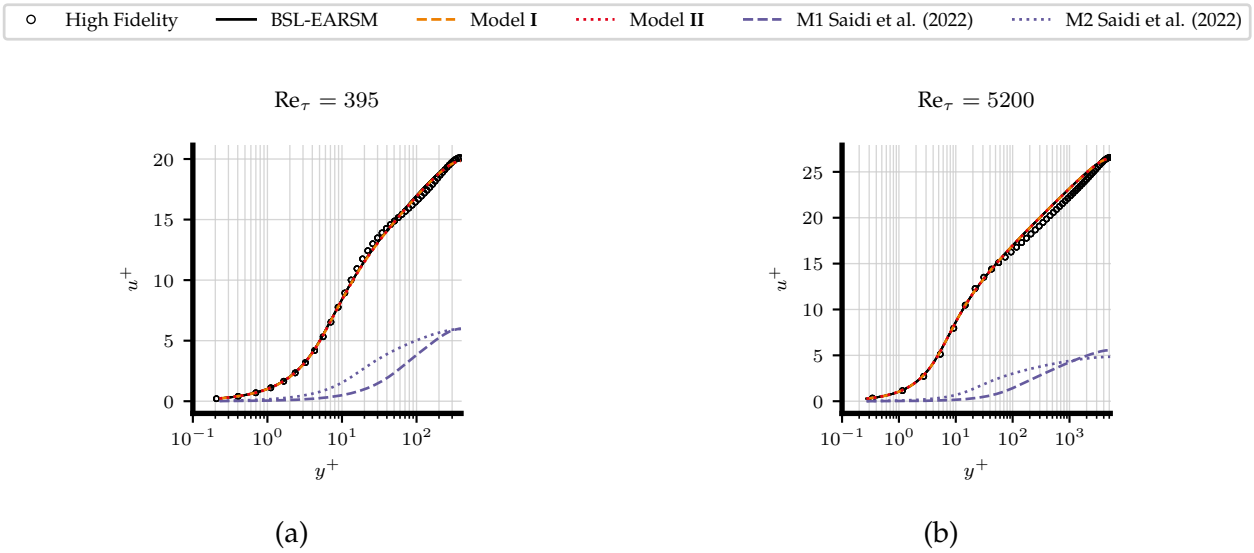

(a) (b)

Figure VI.23: Model comparison of mean streamwise velocity and turbulent kinetic energy profiles for channel flow: $\mathrm{Re}_\tau = 395$ (Fig. VI.23a), and $\mathrm{Re}_\tau = 5200$ (Fig. VI.23b). High-fidelity data obtained from Ref. [149].

VI.4 Comparison with other EARSMs

To provide a complete and updated performance of the developed models, a comparison is made against the two novel machine-learned EARSMs developed by Saidi et al. [39] denoted as M1 (Model 1) and M2 (Model 2); and the classical (not machined-learned) EARSM BSL-EARSM based on $k-\omega$ SST model and on the explicit constitutive relation by Ref. [144] and developed by Menter et al. [156]. The comparison is made on CF_{395}, CF_{5200}, and duct flow with $\mathrm{Re}_b = 10320$ and AR$= 1$.

As shown in the comparative results of Fig. VI.23, Saidi et al. models mispredict the prediction of boundary layers due to its modification of $T_{ij}^{(1)}$ in their models. These modifications improve the prediction of separated flows at the expense of modifying the successful prediction of the law of the wall by standard $k-\omega$ SST. This undesirable effect, however, can be avoided by deactivating the $T_{ij}^{(1)}$ correction in the regions corresponding to equilibrium boundary layers (e.g., a space-dependant aggregation in Ref. [157]). Since the work performed in this study only adds the contributions of $T_{ij}^{(2)}$, the developed models are able to preserve the successful predictions of $k-\omega$ SST for equilibrium boundary layers.

Finally, a comparison showing the prediction of the $\langle u_2 \rangle$ component along the $y = z$ line of a square duct at $\mathrm{Re}_b = 10320$ is shown in Fig. VI.24. It can be seen that the PDA-EARSMs outperform the models by Saidi et al. and yield similar performance compared to BSL-EARSM.

VI.5 Conclusions

This study employs CFD-driven surrogate and Bayesian optimisation to enhance the $k-\omega$ SST turbulence model focusing on predicting Prandtl's second kind of secondary flow. A progressive approach is adopted to enhance the linear eddy-viscosity model with the ability to predict secondary flows while maintaining its effective performance in canonical flow cases. The enhancement is based on the introduction of explicit algebraic Reynolds stress

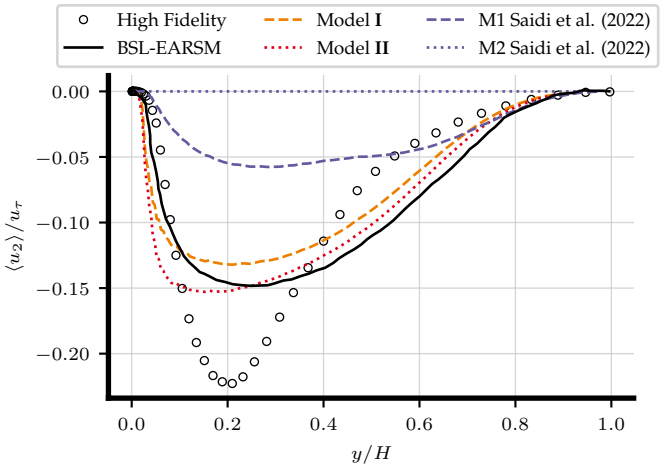

Figure VI.24: Normalised vertical velocity component comparison between models for DF_{10320} with AR$=1$ along line $y=z$. High-fidelity data obtained from Ref. [152].

correction models with two levels of complexity: introducing a linear combination of the first two candidate functions and introducing a linear combination of the first two principal components obtained from PCA on all candidate functions. These two models are optimised to reach the best prediction of both secondary flow and streamwise flow in the optimisation case of a duct flow with an aspect ratio of 1 and $Re_b = 3500$.

Considering the progressive approach, the enhanced models are tested against channel flow cases at different friction Reynolds numbers, where the enhanced models preserve the original performance of the $k-\omega$ SST model in a successful reproduction of the velocity and TKE profiles.

For the purpose of generalisability investigation, new models are tested against verification duct-flow cases with different Reynolds numbers and different aspect ratios. Both enhanced models show a successful prediction of secondary flow and improvement of streamwise velocity prediction in the unseen cases. The third and final verification case is a roughness-induced secondary flow case at a nominally infinite Reynolds number, where the enhanced models are able to predict the secondary motion, although at a lower intensity compared to high-fidelity data due to the limitations of wall modelling for this type of cases.

Table VI.2: Objective function results for optimisation case and all verification cases tested. Results are presented by the case abbreviation and characteristics: Duct flow cases as $DF_{AR,\,Re}$ and roughness-induced secondary flow as RI_{Re}. It should be noted that $DF_{1,\,3500}$ is the optimisation case. $J=1$ indicates the $k-\omega$ SST original prediction and $J=0$ indicates a match of the high-fidelity data.

Case	Model	J	j_1	j_2
$DF_{1,\,3500}$	**I**	0.387	0.455	0.319
	II	0.398	0.457	0.339
$DF_{1,\,5700}$	**I**	0.405	0.482	0.328
	II	0.392	0.461	0.323
$DF_{3,\,2600}$	**I**	0.458	0.551	0.365
	II	0.502	0.580	0.424
$RI_{2\times10^8}$	**I**	0.693	0.663	0.723
	II	0.698	0.666	0.730
Average	**I**	**0.486**	**0.538**	**0.434**
	II	**0.498**	**0.541**	**0.454**

Overall, the results, summarised in Table VI.2, show that the developed models perform substantially better than the standard $k-\omega$ SST model in all verification cases. The enhanced models are able to predict secondary flow features, showing global improvements in the velocity field prediction. Both

models show similar performance in successfully predicting secondary flows and streamwise velocity. Therefore, more invariants combined with PCA do not necessarily improve the performance of the models in the 2-dimensional cases considered in this study. Nevertheless, considering scaling up the complexity of the model in 3-dimensional cases, the combination with PCA dimensionality reduction could further improve the predictions. It should be noted that the optimisation process and the nature of the PDA-EARSMs yield a certain level of turbulence anisotropy while always maintaining solution robustness and stability. This fact results in some discrepancies between the PDA-EARSMs and high-fidelity data in the predicted turbulence shape.

These findings suggest that the use of CFD-driven optimisation with surrogate modelling and Bayesian optimisation is a robust approach to enhance linear-eddy-viscosity turbulence models to predict more complex physics. The enhanced PDA-EARSMs developed greatly improve the prediction of turbulence anisotropy in wall-bounded flows, especially in cases where the standard $k-\omega$ SST presents difficulties in accurately predicting the secondary flow. The progressive nature of this development as a first step focuses on the prediction of secondary flows, allowing further improvement of the models by adding more predictive physics and verifying them on other test cases.

VII

Turbulence Modelling for Separated Flows

Progressive augmentation of turbulence models for flow separation by multi-case computational fluid dynamics driven surrogate optimisation

ABSTRACT In the field of data-driven turbulence modelling, the consistency of the *a posteriori* results and generalisability are the most critical aspects of new models. In this study, we combine a multi-case surrogate optimisation technique with a progressive augmentation approach to enhance the performance of the popular $k-\omega$ Shear Stress Transport (SST) turbulence model in the prediction of flow separation. We introduce a separation factor into the transport equation of turbulent specific dissipation rate (ω) to correct the underestimation of turbulent viscosity by the $k-\omega$ SST model in the case of flow separation for 2-dimensional cases. The new model is optimised based on their performance on the training cases including periodic hills and curved backward-facing step flow. Simulation of channel flow is likewise included in the optimisation process to guarantee that the original performance of $k-\omega$ SST is preserved in the absence of separation. The new model is verified on multiple unseen cases with different Reynolds numbers and geometries. Results show a significant improvement in the prediction of the recirculation zone, velocity components, and distribution of friction coefficient in both training and testing cases, where flow separation is expected. The performance of the new models on the test case with no separation shows that they preserve the successful performance of $k-\omega$ SST when flow separation is not expected.

REFERENCE [158]: A. Amarloo, M. J. Rincón, M. Reclari, and M. Abkar (2023). "Progressive augmentation of turbulence models for flow separation by multi-case computational fluid dynamics driven surrogate optimization," *Physics of Fluids*, vol.35, p. 125154, 12 2023 † ‡.

VII.1 Introduction

Compared to direct numerical simulations (DNS) and large-eddy simulations (LES), Reynolds-averaged Navier-Stokes (RANS) simulations are quite popular and cost-effective in industrial applications of computational fluid dynamics (CFD). In RANS, the accuracy of the results relies on the performance of the RANS models in modelling the physics of turbulence (i.e., Reynolds stress tensor, RST). Despite the popularity of RANS, it is well established that the common empirical models (e.g. linear eddy viscosity models like $k-\varepsilon$ and $k-\omega$) have

†M.J. Rincón and A. Amarloo contributed equally to this study.

shortcomings in simulations of specific phenomena like secondary flows [127] and flows with boundary-layer separation and reattachment [29].

The recent progress in data-driven methods has inspired a new wave of studies aimed at improving the performance of RANS models [31]. Most of these investigations have been focused on utilising available high-fidelity data (like LESs and DNSs) to enhance the results produced by common empirical models [32–37, 40, 131, 132] or to find correction models to the RST prediction [87, 121, 128–130, 159]. These studies use high-fidelity data by *a priori*-training methods to find a better RANS model [40], where the main concern is the generalisability and consistency of the new data-driven models for unseen cases [138].

In a different approach, models obtained by model-consistent training methods have shown promising results in finding a reliable RANS turbulence model [40]. In these methods, the performance of models (i.e., *a posteriori* results) is involved during the training process; hence, these methods can guarantee the consistency and robustness of final models. In this regard, using optimisation algorithms in CFD-driven techniques has shown promising performance in finding new reliable RANS models [38, 39].

Optimisation algorithms, which are of paramount importance in engineering and scientific domains, are designed to minimise or maximise functions within multi-dimensional parameter spaces. These algorithms play a pivotal role in a wide array of fields, ranging from the design of efficient engineering systems to the optimisation of intricate scientific models. Commonly employed optimisation algorithms encompass slope followers [133], simplex methods [42], multi-objective evolutionary [43], and particle swarm algorithms [44], among others. Nevertheless, a notable challenge arises due to the considerable computational expense associated with evaluating objective functions, particularly when engaging in CFD simulations and dealing with an extensive range of test configurations.

To address this challenge and expedite the optimisation process, significant strides have been made towards the implementation of a relatively smaller set of simulations to construct computationally efficient surrogate models, also referred to as response surfaces [47, 137]. These response surfaces are mathematical approximations of the objective function's behaviour within the parameter space, thus enabling the prediction of function values for untested configurations. By capitalising on these response surfaces, engineers and scientists can effectively explore the parameter space with reduced computational burden, rendering the optimisation process both feasible and efficient. This approach finds wide application within various engineering fields, such as the optimisation of complex internal-flow systems using ultrasonic flow metering [59, 76], the enhancement of gas cyclone efficiency [102], the optimisation of aero-structural designs of aircraft wings [101], and the improvement of ground vehicle performance [104], among other notable applications. As the demand for efficient optimisation algorithms continues to grow, the development of surrogate models and response surface techniques assumes increasing importance in streamlining the design and analysis processes of complex engineering systems and scientific models.

Surrogate-based optimisation (SBO) methods yet have not been widely investigated for improving RANS turbulence models, and there are a few works that have explored the potential of using optimisation techniques for the development of data-driven RANS modelling. For example, Zhao *et al.* [38] used a gene expression programming tool to evolve a correction model for the $k-\omega$ Shear Stress Transport (SST) model. They showed that CFD-driven optimisation has a significant potential for finding reliable RANS models. Their new models showed better performance compared to the data-driven (i.e., *a priori*-trained) models trained on the same high-fidelity data, but the new model's performance was limited to the training cases. Later, this methodology was extended to a coupled turbulence closure model by multi-objective optimisation [136]. In another study, Saïdi *et al.* [39] applied the

response surfaces method to obtain a sparse regression of candidate functions for correcting the $k-\omega$ SST model trained on the cases with recirculation zone. They also reported better performance of their CFD-driven models when they compared their model-consistent trained method with *a priori*-trained models. Most of these studies show that the model-consistent method has the potential to solve the consistency problem attached to all data-driven RANS models, yet new models are limited to their trained high-fidelity data and not generalisable to unseen cases.

As a solution to this issue, Fang *et al.* [139] suggested including more cases in the training process of CFD-driven optimisation which means that in each evaluation of the optimisation algorithm, more CFD simulations have to be completed to include more *a posteriori* results in the training process. Fang *et al.* [139] investigated this solution with a multi-case CFD-driven optimisation including different turbulent phenomena. They reported that this solution helped with the generalisability of the new model, however, their new models still have to be separated into either wall-free or wall-bounded flows.

The new data-driven models' inability to generalise is not only limited to unseen cases extrapolated out of the training data but they also might not be able to perform well on simple canonical cases like channel flow for which common empirical models have been tuned. In a different solution, Bin *et al.* [140] suggested including the conventional progressive approach of empirical models in new data-driven models. In the progressive approach, a common RANS model, which has adequate performance for canonical simple flows, is progressively augmented with new physical corrections for more complex flow cases without violating its original performance in simple flow cases. Rincón *et al.* [126] combined this progressive augmentation with a CFD-driven optimisation to improve the standard $k-\omega$ SST with a data-driven correction for predicting secondary flows without violating the successful performance of standard $k-\omega$ in channel flow.

In this study, we use the progressive augmentation method to improve the standard $k-\omega$ SST with a data-driven correction factor for the flows with separation and reattachment phenomena. This correction model consists of a correction term in the transport equation of the turbulent specific dissipation rate (ω) with an activation function for the flows with separation and adverse pressure gradient. In the case of flow separation, the ratio of production (P_k) to dissipation (ε) of turbulent kinetic energy (i.e, $\frac{P_k}{\varepsilon}$) is much higher than 1 [64]; therefore, we use this criterion for activation functions of new correction models. As an example, Fig. VII.1 shows that in periodic hills flow where flow separation is expected, the standard $k-\omega$ SST model overestimates the size of the recirculation zone, and the separation phenomenon induces an area where $\frac{P_k}{\varepsilon} > 1$. In the data-driven approach, we use periodic hills flow and curved backwards-facing step cases for the training process. The training process includes a multi-case CFD-driven optimisation technique to guarantee the reliability and consistency of the obtained model. We also include a channel flow case in the training process to preserve the original law-of-the-wall prediction of $k-\omega$ SST [77]. The newly developed models are verified on unseen test cases with different Reynolds numbers and geometries where flow separation is expected. Regarding the progressive method, we likewise test the new models where flow separation is not expected.

VII.2 Methodology

This section presents the methodology behind the progressive augmentation of a RANS model for flow separation and training correction models by CFD-driven optimisation techniques. The RANS equations for an incompressible steady flow, by using the Reynolds decomposition

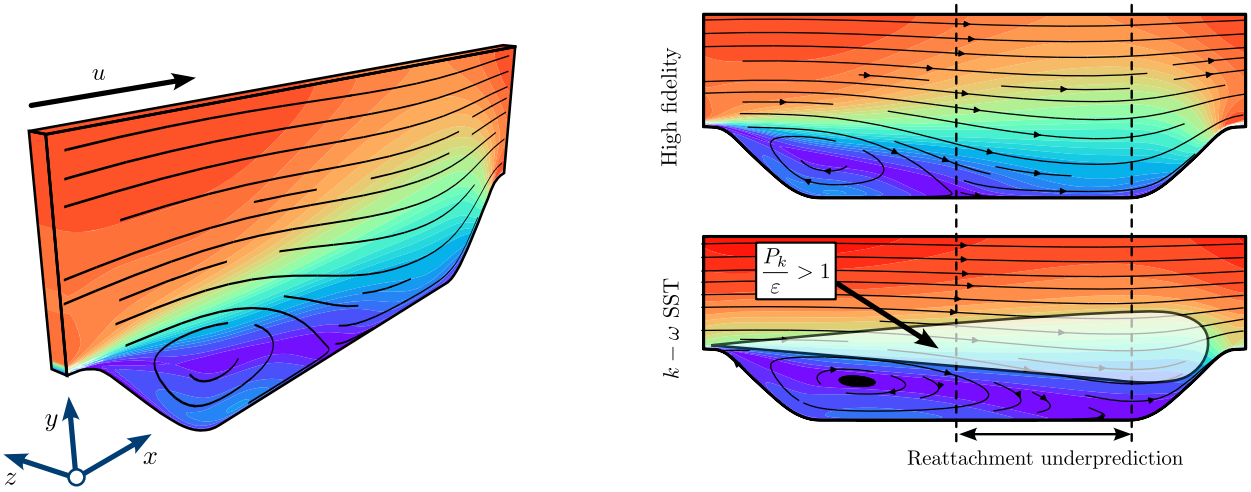

Figure VII.1: Streamwise velocity and stream function of flow separation at periodic hills case with RANS $k-\omega$ SST turbulence model and high-fidelity simulation results. The ratio of turbulent kinetic energy production to dissipation P_k/ε is used as an indication of flow separation. High-fidelity data from Ref. [160].

of velocity and pressure, can be written as [108]

$$u_i = \langle u_i \rangle + u_i', \;\; p = \langle p \rangle + p', \tag{VII.1}$$

$$\partial_i \langle u_i \rangle = 0, \;\; \partial_j (\langle u_i \rangle \langle u_j \rangle) = -\frac{1}{\rho} \partial_i \langle P \rangle + \partial_j \left(\nu \partial_j \langle u_i \rangle - A_{ij} \right), \tag{VII.2}$$

where $i, j = 1, 2, 3$ indicate the streamwise (x), spanwise (y), and vertical (z) directions, respectively. u_i and p are velocity components and pressure, respectively, decomposed to a mean value, indicated by $\langle \cdot \rangle$, and fluctuations, indicated by $\cdot'$. ν and ρ are the kinematic viscosity and the fluid density, respectively. $\langle P \rangle = \langle p \rangle + \frac{1}{3}\rho \langle u_i' u_i' \rangle$ is the modified pressure, and $A_{ij} = \langle u_i' u_j' \rangle - \frac{1}{3} \langle u_k' u_k' \rangle \delta_{ij}$ is the anisotropic part of RST.

By using the Boussinesq approximation, A_{ij} is modelled as

$$A_{ij} = -2\nu_t S_{ij}, \tag{VII.3}$$

where $S_{ij} = \frac{1}{2}(\partial_i \langle u_j \rangle + \partial_j \langle u_i \rangle)$ is the strain rate tensor, ν_t is the turbulent viscosity which is determined by a RANS model. In this study, the $k-\omega$ SST [64] model is chosen as a baseline model to be progressively corrected for flow separation prediction. In the standard $k-\omega$ SST model, ν_t is calculated as

$$\nu_t = \frac{a_1 k}{\max(a_1 \omega, F_2 S)}, \tag{VII.4}$$

where k is the turbulent kinetic energy, and ω is the specific dissipation rate. In the standard $k-\omega$ SST model, these quantities are calculated based on two transport equations as

$$\partial_j \left(\langle u_j \rangle k \right) = P_k - \beta^* \omega k + \partial_j \left((\nu + \sigma_k \nu_t) \partial_j k \right), \tag{VII.5}$$

$$\partial_j \left(\langle u_j \rangle \omega \right) = \frac{\gamma}{\nu_t} P_k - \beta \omega^2 + \partial_j \left((\nu + \sigma_\omega \nu_t) \partial_j \omega \right) + CD_{k\omega}, \tag{VII.6}$$

where $P_k = \partial_i \langle u_j \rangle (2\nu_t S_{ij})$ is the production of turbulent kinetic energy by the RST. In this study, we intend to modify Eq. VII.6; therefore for the sake of brevity, we skip the extra details of the standard $k-\omega$ SST model for which one can refer to Ref. [77].

VII.2.1 Progressive $k-\omega$ SST

In this study, the production term in the transport equation for ω (Eq. VII.6) is modified by introducing a correction term R as

$$\partial_j\left(\langle u_j\rangle\omega\right) = \frac{\gamma}{\nu_t}(P_k + R) - \beta\omega^2 + \partial_j\left((\nu + \sigma_\omega\nu_t)\partial_j\omega\right) + CD_{k\omega}. \tag{VII.7}$$

Since R can have both positive and negative values, this term could be considered either a production or a dissipation term in Eq. VII.7. This term could be modelled as a production term of a hypothetical RST following Pope's decomposition [141] of the RST; therefore, we introduce this correction as

$$R = \partial_i\langle u_j\rangle(2\nu_t\alpha S_{ij})\mathcal{X} = P_k\alpha\mathcal{X}, \tag{VII.8}$$

where only the first tensor in Pope's decomposition is considered. α is an unknown function of the first two invariants including $I_1 = \text{tr}(S_{ik}S_{kj})/\omega^2, I_2 = \text{tr}(\Omega_{ik}\Omega_{kj})/\omega^2$, where $\Omega_{ij} = \frac{1}{2}(\partial_i\langle u_j\rangle - \partial_j\langle u_i\rangle)$ is the rotation rate tensor. $\mathcal{X}$ is an activation function for R to activate the correction in case of flow separation. By placing Eq. VII.8 in Eq. VII.7, Eq. VII.7 can be rewritten as

$$\partial_j\left(\langle u_j\rangle\omega\right) = \frac{\gamma}{\nu_t}P_k\left(1 + F_{\text{sep}}\right) - \beta\omega^2 + \partial_j\left((\nu + \sigma_\omega\nu_t)\partial_j\omega\right) + CD_{k\omega}, \tag{VII.9a}$$

$$F_{\text{sep}} = \alpha\mathcal{X}, \tag{VII.9b}$$

where F_{sep} is the new separation factor to modify the original transport equation from the standard $k-\omega$ SST model (i.e., Eq. VII.6).

Inspired by the sparse regression method used by Schmelzer *et al.*[87], we consider a set of candidate functions to define α as

$$\alpha = \theta_0 + \sum_{i=1}^{27}\theta_i\mathcal{D}_i, \tag{VII.10}$$

$$\begin{aligned}\mathcal{D} = \{&I_1, I_2,\\ &I_1^2, I_1I_2, I_2^2,\\ &I_1^3, I_1^2I_2, I_1I_2^2, I_2^3,\\ &I_1^4, I_1^3I_2, I_1^2I_2^2, I_1I_2^3, I_2^4,\\ &I_1^5, I_1^4I_2, I_1^3I_2^2, I_1^2I_2^3, I_1I_2^4, I_2^5\\ &I_1^6, I_1^5I_2, I_1^4I_2^2, I_1^3I_2^3, I_1^2I_2^4, I_2^5I_2, I_2^6\},\end{aligned} \tag{VII.11}$$

where θ_i are unknown coefficients to be determined by a CFD-driven optimisation technique. To obtain a holistic sparse optimisation, the candidate functions are normalised as

$$\mathcal{B}_i = \frac{\mathcal{D}_i - \mu_i}{\sigma_i}, \tag{VII.12}$$

where μ_i is the mean, and σ_i is the standard deviation of each candidate function $\mathcal{D}_i$. These statistics are obtained from high-fidelity data from the training cases. Therefore, Eq. VII.10 is rewritten as,

$$\alpha = C_0 + \sum_{i=1}^{27}C_i\mathcal{B}_i. \tag{VII.13}$$

Since optimisation with 28 design variables is impractical, and it makes the model exposed to instabilities, two approaches are considered in this study including selecting only the first m leading functions and reducing the dimensionality of the problem. We utilised principal component analysis (PCA) as a dimensionality reduction on the $\mathcal{B}_i$ values from high-fidelity data to find the first m principal components as,

$$\varphi_j = \sum_{i=1}^{27} a_i^{(j)} \mathcal{B}_i, \tag{VII.14}$$

where $a_i^{(j)}$ are calculated by PCA on high-fidelity data of the training cases. It is shown in Sec. VII.3.1 that the first two principal components represent the variability of all 27 candidate functions sufficiently (i.e., $m = 2$). Therefore, here two structures are considered for α as

$$\alpha = C_0 + C_1\mathcal{B}_1 + C_2\mathcal{B}_2, \tag{VII.15a}$$

$$\alpha = C_0 + C_1\varphi_1 + C_2\varphi_2, \tag{VII.15b}$$

where C_0, C_1, C_2 are the three optimisation variables for determining α inside the separation factor (Eq. VII.9b). It should be mentioned that both φ_1 and φ_2 include a combination of all the candidate functions (listed in Eq. VII.11), where $\mathcal{B}_1$ and $\mathcal{B}_2$ are the normalised versions of the linear terms I_1 and I_2, respectively.

Considering the activation function, Menter [64] mentions that in the case of flow separation, the ratio of production to dissipation of k (i.e, $\frac{P_k}{\varepsilon}$) is much higher than 1; therefore, they modified the ν_t definition in Eq. VII.4. From this fact, we can use the value of ν_t for defining a linear activation function as

$$\mathcal{X}_{\text{linear}} = 1 - \nu_t \frac{\omega}{k}. \tag{VII.16}$$

In other words, turbulent viscosity ν_t is equal to $\frac{k}{\omega}$ when there is no separation or adverse pressure gradient (e.g. channel flow); therefore, the activation function is $\mathcal{X} = 0$, and the standard $k-\omega$ SST is used. Otherwise, $\nu_t < \frac{k}{\omega}$ an activation function $0 < \mathcal{X} < 1$ activates the correction term R in the transport equation of ω. Equation VII.16 is a linear activation function considered in this study, and for a more general activation function, we also considered the following form as

$$\mathcal{X}_{\text{power}} = \left(1 - \left(\nu_t \frac{\omega}{k}\right)^{\lambda_1}\right)^{\lambda_2}, \tag{VII.17}$$

where λ_1 and λ_2 are considered as two extra optimisation variables. In this study, we considered two equations for α (Eqs. VII.15a and VII.15b) and two equations for $\mathcal{X}$ (Eqs. VII.16 and VII.17); therefore, four models listed in Table VII.1 are compared in this study. It should be mentioned that all of these correction models integrate only a few algebraic calculations to each iteration in the simulations, which do not affect the computational cost of the simulations compared to the original $k-\omega$ SST model.

VII.2.2 Optimisation methods

To tackle the optimisation challenge, a surrogate is constructed using Kriging and Gaussian processes (GPs). This surrogate relies on the principles of Design and Analysis of Computer Experiments (DACE) [46, 113, 114], utilising data from a series of CFD simulations and subsequent result analysis. The model's effectiveness is gauged through two primary objective functions tied to velocity magnitude and friction coefficient at the walls, thereby

Table VII.1: Four different models for the separation factor considered in this study

Name	Model Equation		Optimisation variables
Model I	$F_{sep} = (C_0 + C_1\mathcal{B}_1 + C_2\mathcal{B}_2)\left(1 - \nu_t\frac{\omega}{k}\right)$	(VII.18a)	C_0, C_1, C_2
Model II	$F_{sep} = (C_0 + C_1\varphi_1 + C_2\varphi_2)\left(1 - \nu_t\frac{\omega}{k}\right)$	(VII.18b)	C_0, C_1, C_2
Model III	$F_{sep} = (C_0 + C_1\mathcal{B}_1 + C_2\mathcal{B}_2)\left(1 - \left(\nu_t\frac{\omega}{k}\right)^{\lambda_1}\right)^{\lambda_2}$	(VII.18c)	$C_0, C_1, C_2, \lambda_1, \lambda_2$
Model IV	$F_{sep} = (C_0 + C_1\varphi_1 + C_2\varphi_2)\left(1 - \left(\nu_t\frac{\omega}{k}\right)^{\lambda_1}\right)^{\lambda_2}$	(VII.18d)	$C_0, C_1, C_2, \lambda_1, \lambda_2$

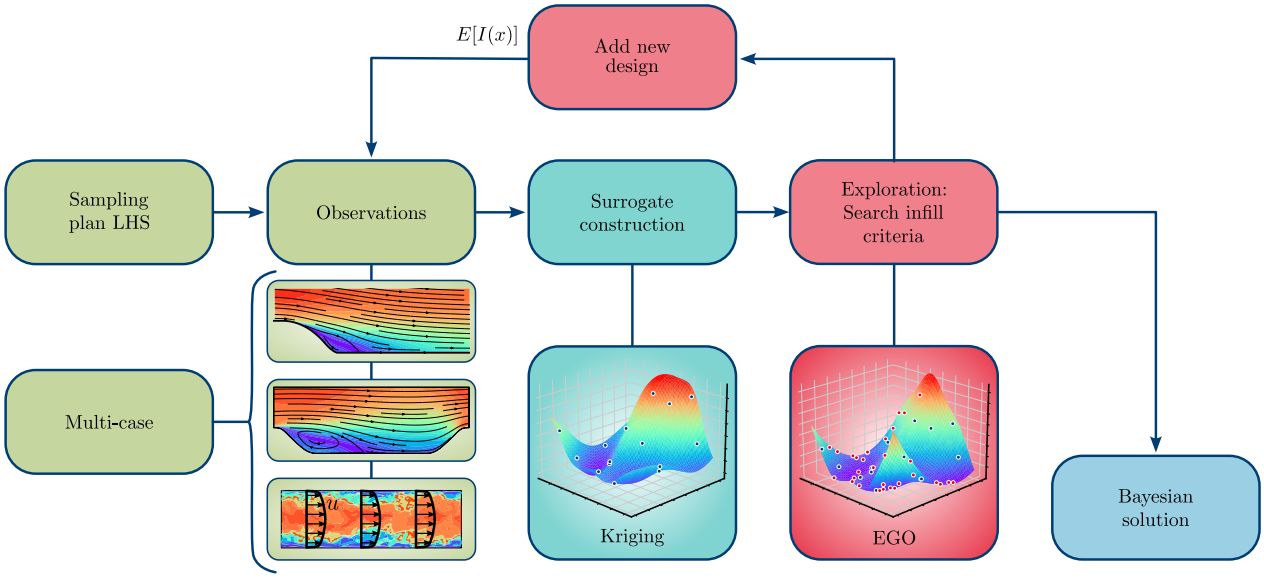

Figure VII.2: Optimisation approach involving an initial sampling plan using Latin hypercube sampling, resolved through CFD. A multi-case methodology is adopted, wherein observations are simultaneously conducted across three cases: $CBFS_{13700}$, PH_{2800}, and CF_{5200}. Subsequent to this, an initial surrogate model is formulated using Kriging and improved using Bayesian optimisation techniques.

framing a multi-objective optimisation task. A well-designed sampling plan is delineated based on Latin hypercube sampling (LHS), with an infill criterion that adheres to quality measures. Acknowledging the possibility that the initial sampling might not cover the surrogate's extreme values, Bayesian techniques rooted in efficient global optimisation are employed, coupled with the evaluation of the expected improvement ($E\left[I(x)\right]$) function. These strategies are aimed at further exploring the surrogate model, enhancing its reliability, and obtaining optimal observations. The practical implementation employs the open-source software OpenFOAM [65]. For a comprehensive view of the optimisation process, the reader can refer to Fig. VII.2.

The primary concern addressed in this study involves the overestimation of boundary-layer detachment within the $k-\omega$ SST turbulence model. In the selected optimisation scenario, rectifying the velocity field and boundary-layer detachment introduces alterations in the friction coefficient along the walls. Consequently, ensuring accurate prediction of the friction coefficient becomes an equally key parameter to evaluate. Hence, to comprehensively assess flow prediction, the normalised error of both velocity magnitude and friction coefficient

with respect to high-fidelity data is computed and adopted as minimisation objectives. For a comprehensive and reliable representation of these quantities, the volumetric average of each field is computed as the objective functions, following

$$j_1 = \frac{\int_V \left(|\langle u \rangle - \langle u \rangle^{\mathrm{HF}}|\right) \mathrm{d}V}{\int_V \left(|\langle u \rangle^{k-\omega} - \langle u \rangle^{\mathrm{HF}}|\right) \mathrm{d}V}, \tag{VII.19a}$$

$$j_2 = \frac{\int_x \left(|c_f - c_f^{\mathrm{HF}}|\right) \mathrm{d}x}{\int_x \left(|c_f^{k-\omega} - c_f^{\mathrm{HF}}|\right) \mathrm{d}x}, \tag{VII.19b}$$

where $\langle u \rangle$ is the velocity magnitude, c_f is the friction coefficient, $|\cdot|$ is the absolute value operation, the superscript $\cdot^{HF}$ stands for *high-fidelity*, and $\cdot^{k-\omega}$ refers to the solution of the standard $k-\omega$ SST model. The formulation of these functions results in a value of 1 when their output aligns with the prediction of the $k-\omega$ SST model, and 0 when the predictions correspond to the high-fidelity data. To enhance the generalisability of the developed models, these objective functions are evaluated in multiple 2-dimensional canonical flow cases, therefore, to comprehensively assess the method's overall outcomes, a global fitness function (J^{OPT}) is subsequently established as follows

$$J^{OPT} = \frac{\sum_{i=1}^{N}(J_i) + J^{CF}}{N+1}, \tag{VII.20a}$$

$$J = \frac{1}{2}(j_1 + j_2), \tag{VII.20b}$$

where J is an averaged fitness function describing the performance of the models in the prediction of velocity magnitude and friction coefficients, N is the number of training cases for multi-case optimisation (2 in this study), and J^{CF} is an objective filtering value given by the convergence of a channel flow case defined as

$$J^{CF} = \begin{cases} 0 & \text{if} \quad \text{Converged to } k-\omega \text{ SST result,} \\ 1 & \text{if} \quad \text{Not converged to } k-\omega \text{ SST result.} \end{cases} \tag{VII.21}$$

This study employs the Latin hypercube sampling (LHS) for sampling observations and data. For the initial observations, a *space-filling* sampling plan is realised using LHS [105], which is optimised through the enhanced stochastic evolutionary (ESE) algorithm [106, 107]. This approach yields an initial surrogate sample with a minimal number of observations while effectively capturing parameter variability. The initial LHS with ESE sample consists of $n_0 = 50\mathcal{K}$ observations, where n_0 signifies the initial number of observations and $\mathcal{K}$ denotes the number of design variables.

In this study, the Kriging method is selected to construct a surrogate model based on data-driven by CFD [76, 145]. The Kriging method interpolates observations by forming a linear combination of a deterministic term and a stochastic process, given by

$$\hat{f}(x) = \sum_{i=1}^{k} \beta_i f_i(x) + Z(x), \tag{VII.22}$$

where $\hat{f}(x)$ denotes the surrogate prediction, β represents a linear deterministic model, $f(x)$ corresponds to the known function, and $Z(x)$ reflects the realisation of a stochastic process with zero mean and spatial covariance function provided as

$$\mathrm{cov}\left[Z\left(x^{(i)}\right), Z\left(x^{(j)}\right)\right] = \sigma^2 R\left(x^{(i)}, x^{(j)}\right). \tag{VII.23}$$

Within this context, the spatial correlation function R determines the smoothness of the Kriging model, the ease of differentiating the response surface, and the extent of influence that nearby sampled points exert on the model. In this study, the spatial correlation adheres to the squared exponential (Gaussian) function

$$\prod_{i=1}^{nx} \exp\left\{\left[-\theta_l \left(x_l^{(i)} - x_l^{(j)}\right)^2\right]\right\}, \quad \forall \theta_l \in \mathbb{R}^+, \tag{VII.24}$$

where the correlation scalar θ_l determines the Gaussian process variance at each point. Through maximising the maximum likelihood estimation, optimal hyper-parameter values, such as the matrix θ_l, mean, and standard deviation, can be determined [112].

Efficient global optimisation (EGO) employing Bayesian optimisation strategies is used to enhance surrogate model accuracy and reduce overall uncertainty [115, 116]. This is achieved by extending the exploration of the surrogate model beyond the initial LHS. EGO is a recognised algorithm that blends both local and global searches to identify the optimal solution, driven by the expected improvement ($E[I(x)]$) function, given as

$$E[I(x)] = (f_{\text{min}} - \mu(x))\, \Phi\left(\frac{f_{\text{min}} - \mu(x)}{\sigma(x)}\right) + \sigma(x)\phi\left(\frac{f_{\text{min}} - \mu(x)}{\sigma(x)}\right), \tag{VII.25}$$

where, $f_{\text{min}} = \min Y$, and $\Phi(\cdot)$ and $\phi(\cdot)$ respectively represent the cumulative and probability density functions of $\mathcal{N}(0,1)$, conforming to the distribution $\mathcal{N}(\mu(x), \sigma^2(x))$. This function gauges the potential enhancement attainable by assessing a new observation point, factoring in the current best solution and the overall uncertainty of the surrogate model [117]. The algorithm adeptly balances local and global searches, resulting in more proficient identification of the optimal solution. Consequently, the subsequent sampling point is determined by

$$x_{n+1} = \arg\max_x \left(E[I(x)]\right). \tag{VII.26}$$

To comprehensively explore the design space, new data is sampled for each objective function individually. This entails collecting a single sample of $n_{\text{EGO}} = n_0$ for each objective, resulting in a cumulative $n = N \cdot 50\mathcal{K}$ new sampled points (with $N = 2$ in this study). The optimised models to evaluate are obtained by the best (J^{OPT} solution gathered during Bayesian optimisation.

VII.2.3 High-fidelity data

Following the objective of this study to find an optimised correction model for flows with separation and reattachment, the high-fidelity data of canonical cases including these phenomena are considered for both training and testing.

For the training process (i.e., multi-case optimisation of the separation factor models), we use the DNS data of periodic hills with bulk Reynolds number of $\text{Re}_b = 2800$ [160] (PH_{2800}) and the LES data of curved backwards-facing step flow with bulk Reynolds number of $\text{Re}_b = 13700$ [161] (CBFS_{13700}). Also, we use the DNS data of channel flow with friction Reynolds number of $\text{Re}_\tau = 5200$ [150] (CF_{5200}) during the training process to guarantee that the new models do not change the performance of standard $k-\omega$ SST model in the absence of flow separation.

For the testing of the final four models found from the training process, all of the models are tested on six unseen cases and the performance of the models is compared with the high-fidelity of these six cases including LES data of periodic hills with bulk Reynolds number of

Table VII.2: Characteristic properties used for training and testing cases.

Cases	Characteristic properties
$CBFS_{13700}$	u_c: the center-channel inlet velocity L: the height of the backward-facing step $\nu = 1/Re_b$
PH_{2800} PH_{10595}	u_c: the average velocity on top of the hill L: the height of the hill $\nu = 1/Re_b$
CD_{12600} CD_{20580}	u_c: the center-channel inlet velocity L: the half-height of the channel $\nu = 1/Re_b$
$BUMP_{20}$ $BUMP_{42}$	$u_c = 16.77\ \mathrm{m\,s^{-1}}$: the inlet free-stream velocity $L = 0.305\ \mathrm{m}$: the width of the bump $\nu = 2.53 \times 10^{-5}\ \mathrm{m^2\,s^{-1}}$ $Re_b = 1.01 \cdot 10^5$

$Re_b = 10595$ [162] (PH_{10595}), DNS data of converging-diverging channel with bulk Reynolds number of $Re_b = 12600$ [163] (CD_{12600}), LES data of converging-diverging channel with bulk Reynolds number of $Re_b = 20580$ [164] (CD_{20580}), and LES data of parametric bump [165] with bump heights of $h = 20$ mm ($BUMP_{20}$) and $h = 42$ mm ($BUMP_{42}$).

For all of the training and testing cases, the characteristic properties used in simulations and the presentation of results are listed in Table VII.2, where u_c is the characteristic velocity, and L is the characteristic length.

VII.3 Results and discussion

In this section, the results are divided into two subsections. In the first one, all four structures listed in Table. VII.1 are optimised with multi-case optimisation, and the performance of those models on the training cases is evaluated. In the second subsection, the performance of the trained models is investigated on the unseen test cases with different Reynolds numbers and geometries. Associated contours and velocity profiles for all of the training and test cases are similarly described and discussed in each subsection. A summary of the performance of each model on each case is presented in Table VII.3. It should be mentioned that according to Eq. VII.19, j_1 and j_2 show the averaged error of mean velocity magnitude ($\langle u \rangle$) and friction coefficient (c_f), respectively, through the whole domain compared to the standard $k-\omega$ SST error values. In other words, values of $j_1, j_2 = 1$ refer to a performance of the new model similar to the standard $k-\omega$ SST, and values of $j_1, j_2 = 0$ refer to a performance of the new model similar to high-fidelity data.

VII.3.1 Multi-case surrogate-based optimisation

For the purpose of multi-case surrogate optimisation, two cases PH_{2800} and $CBFS_{13700}$ are selected as training cases. For a more efficient optimisation, the candidate functions listed in Eq. VII.11 are normalised by the mean and standard deviation values. For each candidate function, these values are calculated based on the high-fidelity data of PH_{2800} and $CBFS_{13700}$ and reported in Fig. VII.3. As mentioned in Sec. VII.2, for models **II** and **IV**, we employ PCA to reduce the dimensionality of the α function. Similarly, we use the high-fidelity data of

Table VII.3: Summary of the performance of using the trained models on the training and testing cases. j_1 is the volumetric-averaged error of velocity magnitude, j_2 is the mean error of friction coefficient at the bottom wall, and $J = 1/2(j_1 + j_2)$

Cases		$\mathcal{X}_{\text{linear}}$						$\mathcal{X}_{\text{power}}$					
		Model I			**Model II**			**Model III**			**Model IV**		
		j_1	j_2	J	j_1	j_2	J	j_1	j_2	J	j_1	j_2	J
Training	**CBFS**$_{13700}$	0.45	0.46	0.46	0.48	0.41	0.45	0.51	0.30	0.40	0.50	0.30	0.40
	PH$_{2800}$	0.38	0.43	0.41	0.36	0.44	0.40	0.35	0.42	0.39	0.35	0.42	0.38
Testing	**PH**$_{10595}$	0.45	0.51	0.48	0.41	0.52	0.47	0.33	0.50	0.42	0.34	0.49	0.41
	CD$_{12600}$	0.49	0.84	0.67	0.49	0.84	0.66	0.31	0.79	0.55	0.32	0.80	0.56
	CD$_{20580}$	0.61	0.85	0.73	0.60	0.84	0.72	0.46	0.79	0.63	0.46	0.79	0.63
	BUMP$_{20}$	0.96	0.83	0.90	0.96	0.82	0.89	0.95	0.71	0.83	0.95	0.73	0.84
	BUMP$_{42}$	0.42	0.85	0.64	0.41	0.86	0.64	0.32	0.76	0.54	0.32	0.73	0.53
Average Training		0.42	0.45	**0.43**	0.42	0.43	**0.42**	0.43	0.36	**0.39**	0.43	0.36	**0.39**
Average Testing		0.55	0.85	**0.70**	0.55	0.84	**0.69**	0.39	0.79	**0.59**	0.39	0.79	**0.59**
Total Average		0.48	0.65	**0.56**	0.48	0.63	**0.56**	0.41	0.57	**0.49**	0.41	0.58	**0.49**

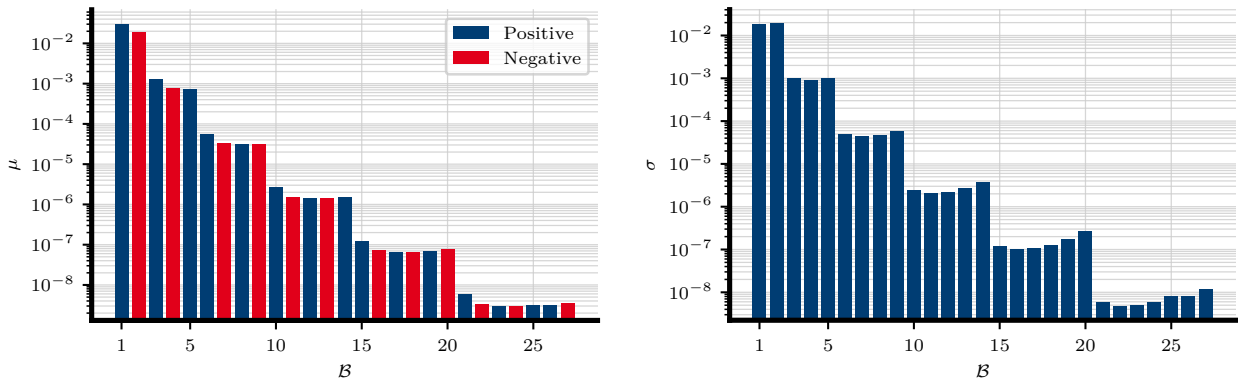

Figure VII.3: Mean (left) and standard deviation (right) values of each candidate functions calculated based on the training cases, PH_{2800} and $CBFS_{13700}$.

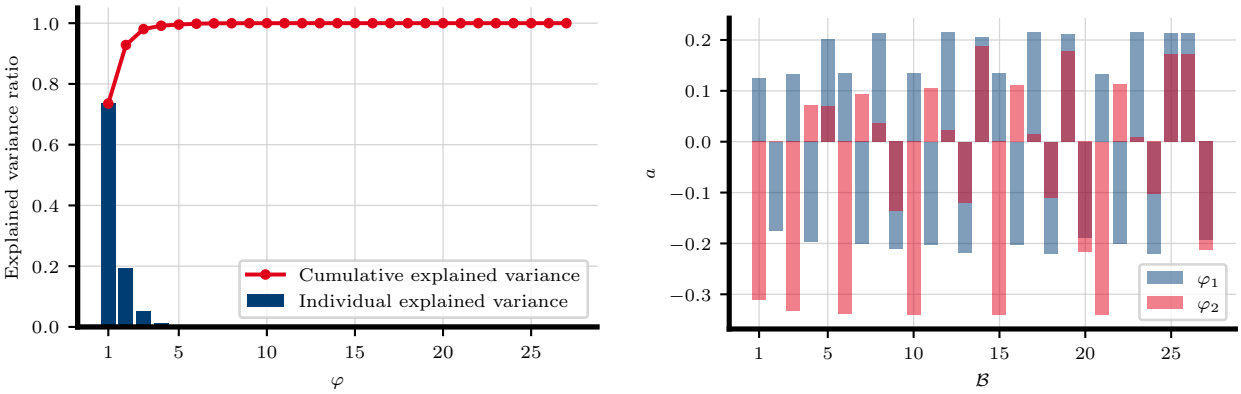

Figure VII.4: Explained variance ratio of each principal component (left) and coefficients associated with the first two principal components (right) calculated by high-fidelity data of PH_{2800} and $CBFS_{13700}$.

PH_{2800} and $CBFS_{13700}$ in the PCA process. Figure VII.4 presents the explained variance of each principal component, and it shows that the first two principal components are adequate enough to represent the variance of the function. Figure VII.4 also reports the $a_i^{(1)}$ and $a_i^{(2)}$ values corresponding to the two first principal components (i.e., φ_1 and φ_2, respectively).

In the training process, we optimise the 4 equations listed in Table. VII.1 by the multi-case surrogate optimisation technique. As depicted in Fig. VII.5, these models are optimised with 450 observations for Models **I** and **II**, and 750 observations for Models **III** and **IV** (i.e., RANS simulations of the training cases), and obtained equations are listed in Table. VII.4. All four models have $C_0 < 0$ which makes the separation factor have negative values. Hence, the new models try to reduce the production (i.e., increase the dissipation) in the ω transport equation (Eq. VII.9a). This changes the results in lower values of ω, and therefore, the turbulent viscosity (Eq. VII.4) is increased by these new correction models.

For Models **I** and **II**, we choose a linear activation function whereas for Models **III** and **IV**, the activation function is optimised during the CFD-driven surrogate optimisation. Figure VII.6 compares the non-linear activation functions with the linear activation function, showing that the optimal activation functions yield a higher gradient to switch between 0 and 1, instead of a linear behaviour. The enhanced activation functions also show zero gradients close to the non-separation point (i.e., where $\nu_t \frac{\omega}{k} \approx 1$), which makes the model more stable in cases when there is no separation phenomenon.

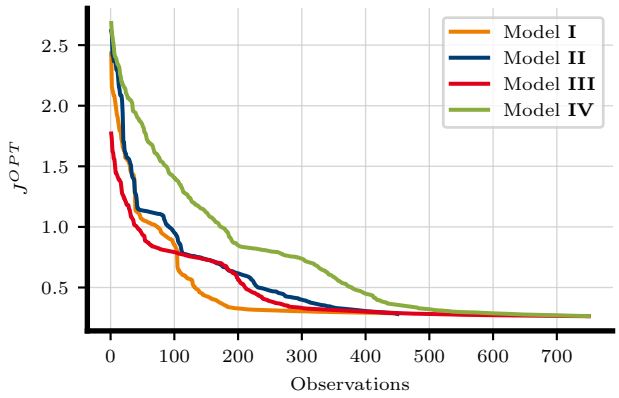

Figure VII.5: Global objective function of the training cases obtained during the optimisation process.

Table VII.4: Optimised model obtained by multi-case surrogate optimisation on high-fidelity data of PH_{2800} and $CBFS_{13700}$.

Model Name	Model Equation	
Model I	$F_{sep} = (-1.08 - 0.38\mathcal{B}_1 + 0.063\mathcal{B}_2)\left(1 - \nu_t\frac{\omega}{k}\right)$	(VII.27a)
Model II	$F_{sep} = (-1.86 + 0.063\varphi_1 + 0.016\varphi_2)\left(1 - \nu_t\frac{\omega}{k}\right)$	(VII.27b)
Model III	$F_{sep} = (-0.25 - 0.44\mathcal{B}_1 - 0.025\mathcal{B}_2)\left(1 - \left(\nu_t\frac{\omega}{k}\right)^{16.47}\right)^{4}$	(VII.27c)
Model IV	$F_{sep} = (-0.87 + 0.013\varphi_1 - 0.077\varphi_2)\left(1 - \left(\nu_t\frac{\omega}{k}\right)^{20}\right)^{7.25}$	(VII.27d)

All four models, listed in Table. VII.4, are optimised for the best performance in RANS simulations of the training cases. Therefore at first, their performance in the reconstruction of separation and reattachment is investigated for the training cases. As stated in Table VII.3, the averaged normalised errors are $0.40 < J < 0.46$ by all 4 obtained models for the case $CBFS_{13700}$. The comparison of the error values (Model **I** vs. **II** and Model **III** vs. **IV**) shows that using the first two principal components has the same performance as using the first two leading functions. These similarities in the performance of PCA and linear structures of function α are an indication that the effect of higher order linear combinations of I_1 and I_2 is negligible for model improvement in this study. However, the PCA analysis can decrease the optimisation cost when more invariants are involved in complex and 3-dimensional cases. Therefore, Models **I** and **III** which have simpler formats are chosen to be compared throughout this paper to highlight the effect of non-linear (i.e., power) activation function versus linear activation function. For the $CBFS_{13700}$, it is shown that using a power activation function over a linear one (i.e., Models **III** and **IV**) improves the reconstruction of both velocity and friction coefficient.

By using the new correction models, the separation factor is expected to have a negative value to reduce the production of ω, and Fig. VII.7 illustrates the values of F_{sep} and the area in which activation function is activated. Therefore, as illustrated in Fig. VII.7, it is expected that the values of predicted ν_t increase compared to the standard $k-\omega$ SST model. Furthermore, due to the higher gradients of the optimised activation function $\mathcal{X}$, the results of F_{sep} for Model **III** show more extreme values.

Since the objective function of the optimisation process is defined based on averaged error

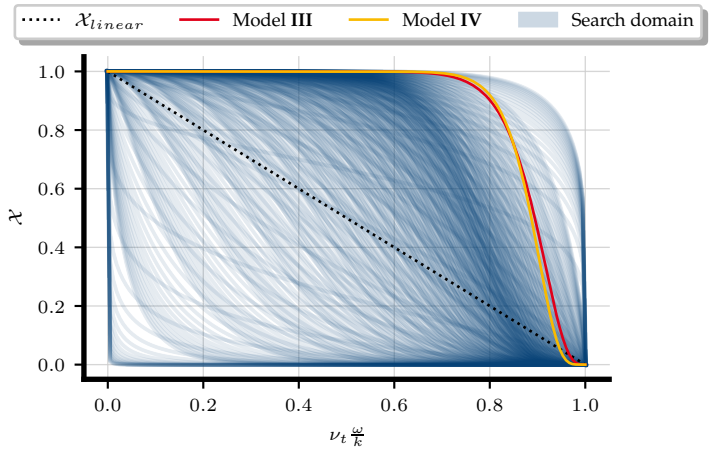

Figure VII.6: Activation function search area. Blue lines represent possible activation functions with diverse combinations of λ_1 and λ_2.

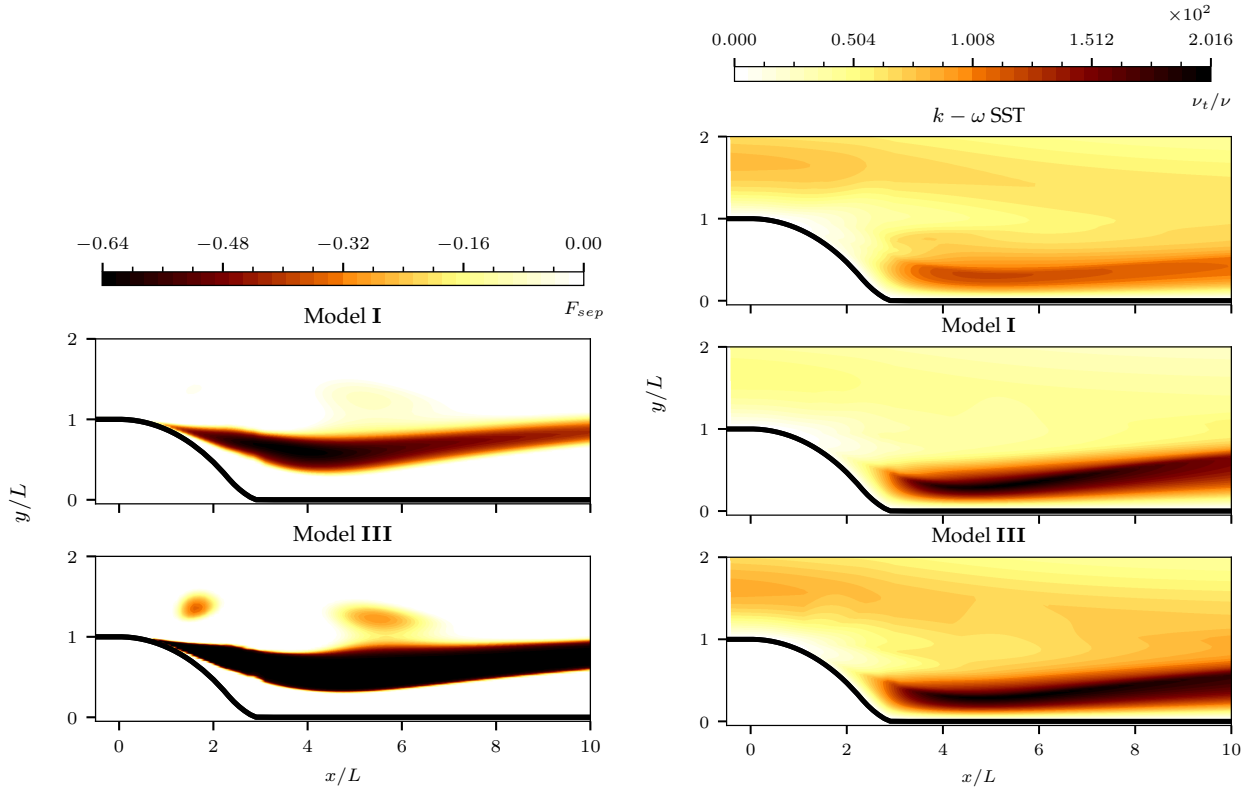

Figure VII.7: Contours of separation factor F_{sep} (left) and turbulent viscosity ν_t (right) for the training case CBFS_{13700}.

values of velocity magnitude and friction coefficient (Eq. VII.19), we compare these quantities obtained by the new models with high-fidelity data and the standard $k-\omega$ SST model. In this regard, Fig. VII.8 shows that the recirculation zone predicted by the standard $k-\omega$ SST model is larger than that of the high-fidelity method due to underprediction of ν_t by the standard $k-\omega$ SST model. The recirculation zone resulting from RANS simulations corrected by Models **I** and **III** are smaller which shows that the increment of ν_t by new separation factors helps to shrink the recirculation zone. For a better comparison, Fig. VII.9 presents the profiles of stream-wise velocity, wall-normal velocity, and bottom-wall friction coefficient.

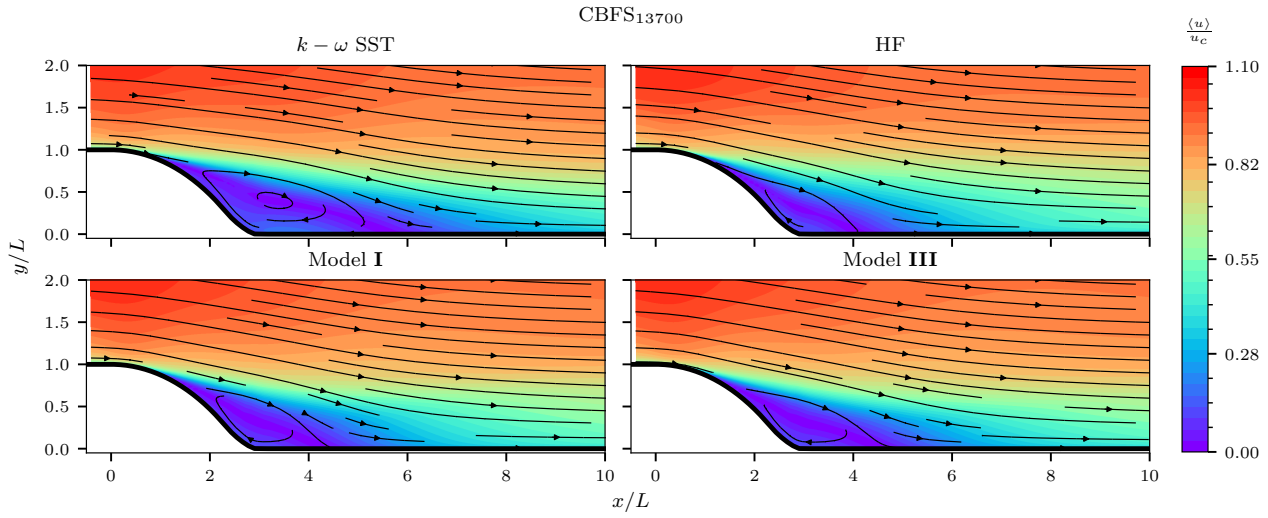

Figure VII.8: Contours of velocity magnitude with streamlines depicting separation and reattachment for the training case CBFS_{13700}. High-fidelity data obtained from Ref. [161].

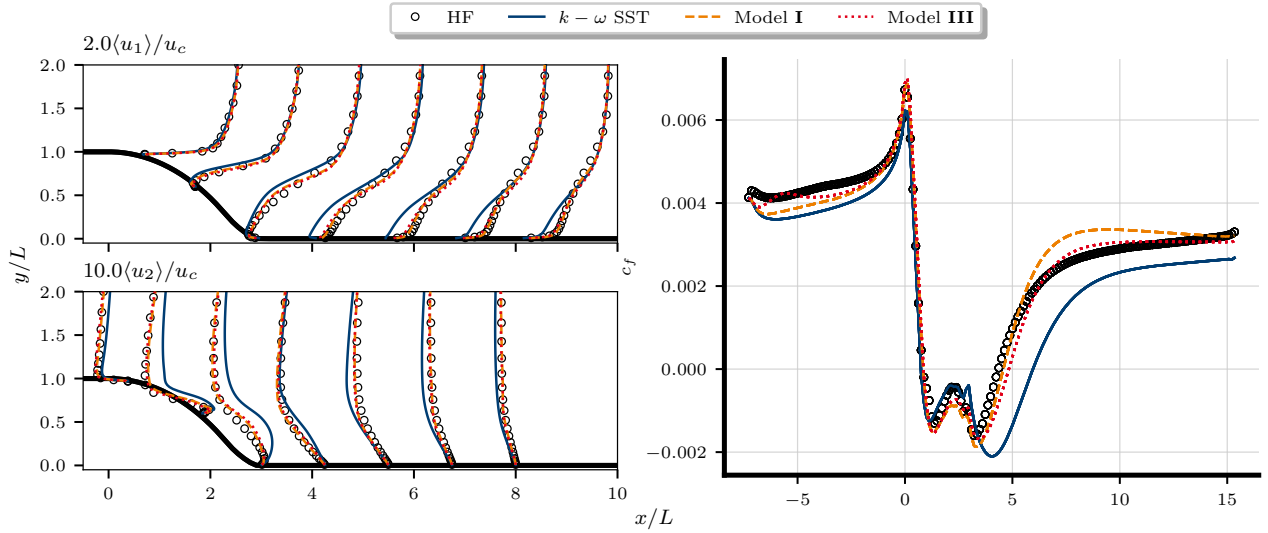

Figure VII.9: Profiles of streamwise velocity (upper left), wall-normal velocity (lower left) at seven locations $x/L = [0.5, 1.75, 3, 4.25, 5.5, 6.75, 8]$, and distribution of bottom-wall friction coefficient (right) for the training case CBFS_{13700}. High-fidelity data obtained from Ref. [161].

These results confirm the improvement of velocity prediction obtained by using Models **I** and **III**. It likewise shows an improvement of the friction coefficient prediction by new models, where Model **III** displays a better performance in the prediction of c_f compared to Model **I**. Furthermore, the results show that the size of the recirculation zone (i.e., where $c_f < 0$) is predicted with higher agreement between the new correction models and high-fidelity data.

For the other training case (PH_{2800}), Table VII.3 shows that averaged error values are $0.39 < J < 0.41$ which indicates a successful training of new models for PH_{2800}. Similar to CBFS_{13700}, using PCA (in Models **II** and **IV**) does not show particular improvement, however, using the non-linear (i.e., power) activation function improves the models' performance. Figure VII.10 shows that similar to CBFS_{13700} case, the size of the recirculation zone is overpredicted by the standard $k-\omega$ SST model compared to DNS data for PH_{2800}, and the new models reduce the size of the otherwise overpredicted recirculation zone. Results in Fig. VII.11 show a higher agreement in the prediction of stream-wise velocity, wall-normal

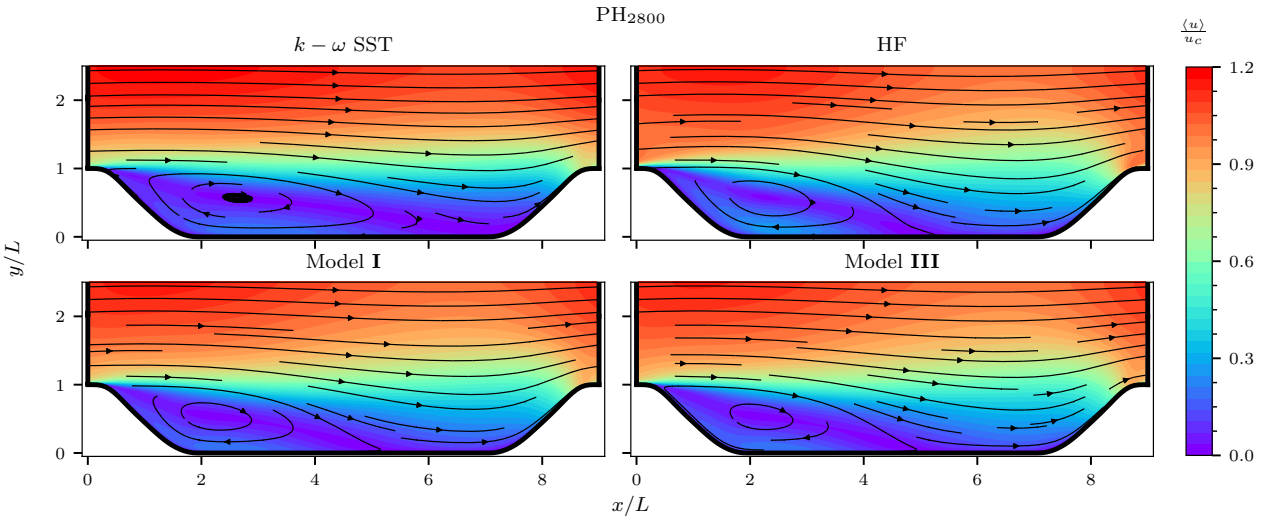

Figure VII.10: Contours of velocity magnitude with streamlines depicting separation and reattachment for the training case PH_{2800}. High-fidelity data obtained from Ref. [160].

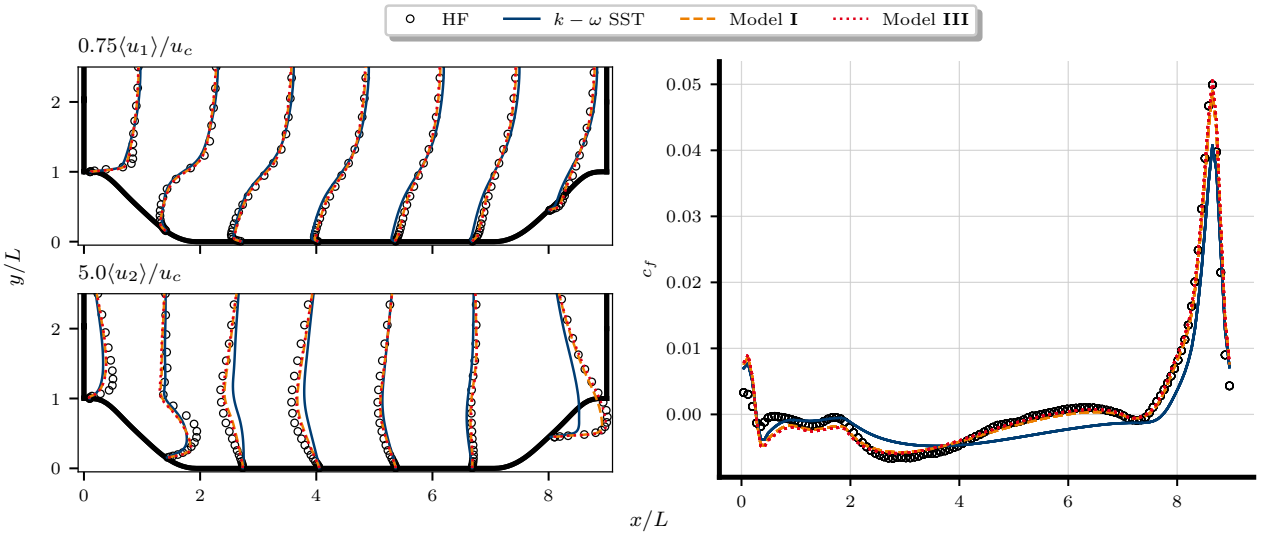

Figure VII.11: Profiles of streamwise velocity (upper left), wall-normal velocity (lower left) at seven locations $x/L = [0.1, 1.42, 2.73, 4.05, 5.36, 6.68, 8]$, and distribution of bottom-wall friction coefficient (right) for the training case PH_{2800}. High-fidelity data obtained from Ref. [160].

velocity, and bottom-wall friction coefficient with high-fidelity data. New models show a successful improvement in the prediction of velocity and friction coefficient, specifically in the reattachment area (i.e., $x/L > 4$).

Following the progressive approach, the activation function inside the separation factor guarantees that the performance of the $k-\omega$ SST is preserved when new correction models are applied in cases with no flow separation like the channel flow. Figure VII.12 shows that the new models obtain identical results to the standard $k-\omega$ SST for the case of channel flow CF_{5200}. In this figure, $u^+ = \langle u_1 \rangle / u_\tau$ is the normalised streamwise velocity by friction velocity u_τ, and $y^+ = y u_\tau / \nu$ is the normalised wall distance.

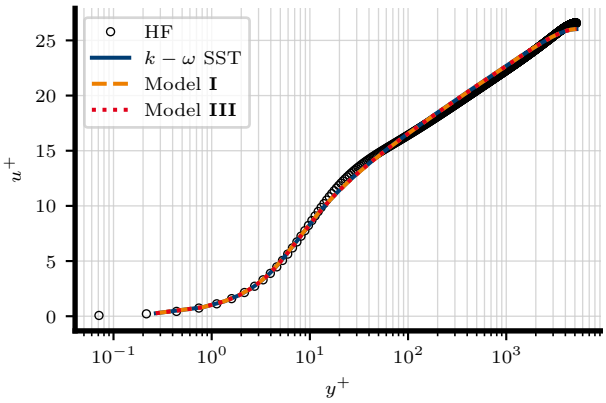

Figure VII.12: Velocity profiles of the channel flow case CF_{5200}.

VII.3.2 Verification on testing cases

In this subsection, the performance of new correction models is investigated for unseen test cases. The case of periodic hills with bulk Reynolds number of $Re_b = 2800$ (PH_{2800}) is included in the training process; therefore at first, new models are tested on the unseen case of higher Reynolds number of the same case (PH_{10595}). Table. VII.3 reports a successful improvement in this unseen case ($0.41 < J < 0.48$), similar to the training case PH_{2800}.

A comparison between the results in Fig. VII.13 and Fig. VII.10 shows that a higher Reynolds number yields a smaller recirculation zone for this case, however, the standard $k-\omega$ SST model still overpredicts the size of this recirculation zone compared to high-fidelity data. Results in Fig. VII.13 likewise show that new models successfully correct the prediction of the recirculation zone in the unseen case of a higher Reynolds number, where results in Fig. VII.14 confirm the successful improvement in the prediction of velocity components and bottom-wall friction coefficient in the unseen case of PH_{10595}; which is similar to the improvement in the training case PH_{2800}.

The performance of the models is also evaluated on unseen cases with different geometries. For this purpose, the new models are employed in the case of converging-diverging channel flow at two different Reynolds numbers including CD_{12600}, and CD_{20580}. Figures VII.15 and VII.16 compare the performance of new models in the reconstruction of separation and reattachment of flow for the cases of CD_{12600} and CD_{20580}, respectively. In both cases, there is not a large recirculation zone in the high-fidelity data, but the standard $k-\omega$ SST model overpredicts the separation phenomenon. The new correction models are successfully able to correct $k-\omega$ SST to shrink this area.

For a better comparison, Figs. VII.17 and VII.18 present the profiles of velocity components and friction coefficient for cases of CD_{12600} and CD_{20580}, respectively. These figures confirm the ability of new models to successfully capture the velocity profiles in a case with a different geometry than the training cases. The distribution of the bottom-wall friction coefficient shows a small separation zone at $5.5 < x/L < 6.5$ which is overstretched by the standard $k-\omega$ SST to $6 < x/L < 9$. Both Models **I** and **III** can improve the prediction of c_f values by shrinking the separation zone.

In another verification case, we choose the $BUMP_{20}$ from the cases of parametric bumps, studied by Matai and Durbin [165], to be tested by our new models to evaluate the performance of new models in cases where separation is weak or non-existent. According to Ref. [165], no separation of the flow is expected in this case of $BUMP_{20}$. Figure VII.19 shows the performance of standard $k-\omega$ SST and our new models compared to high-fidelity data.

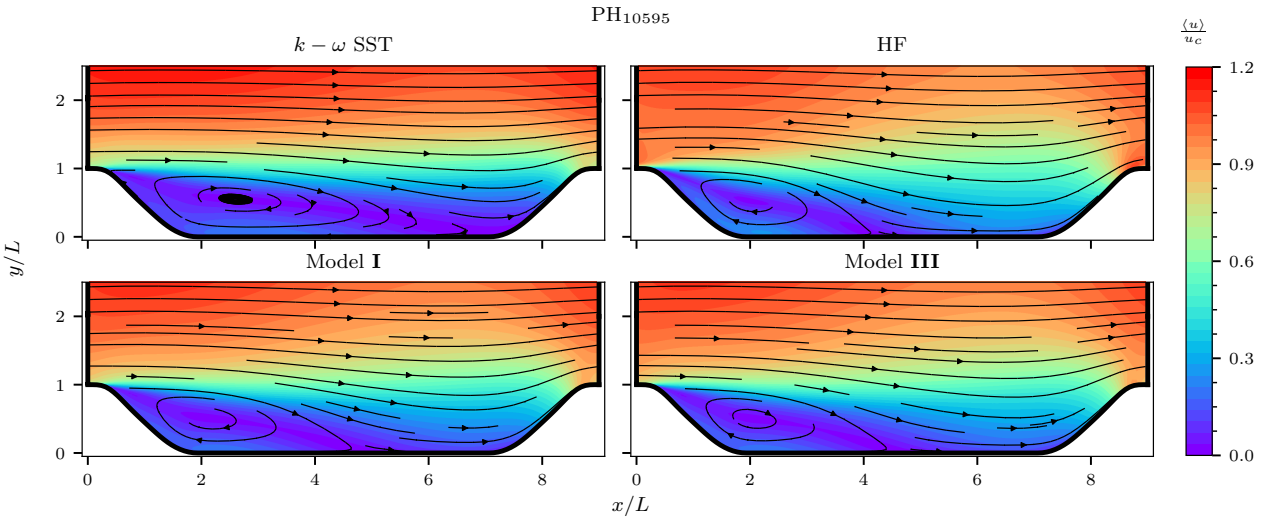

Figure VII.13: Contours of velocity magnitude with streamlines depicting separation and reattachment for the test case PH_{10595}. High-fidelity data obtained from Ref. [162].

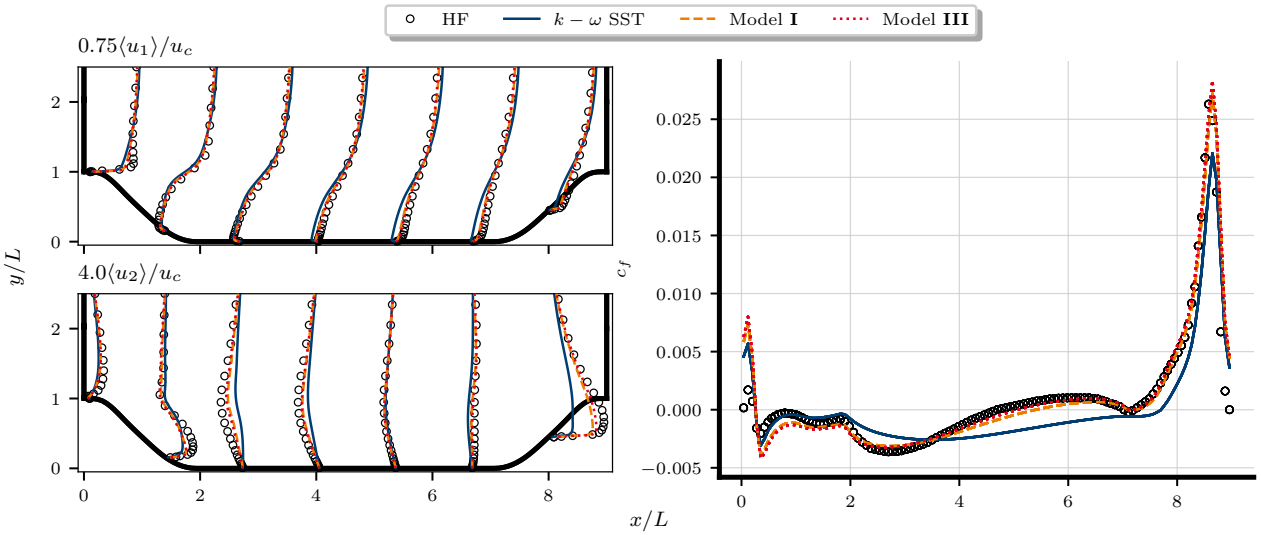

Figure VII.14: Profiles of streamwise velocity (upper left), wall-normal velocity (lower left) at seven locations $x/L = [0.1, 1.42, 2.73, 4.05, 5.36, 6.68, 8]$, and distribution of bottom-wall friction coefficient (right) for the test case PH_{10595}. High-fidelity data obtained from Ref. [162].

Since there is no separation in this case, the standard $k-\omega$ has a successful performance in the reconstruction of the velocity domain. Figure VII.19 likewise shows that new models have similarly a successful performance, and the averaged error values, reported in Table. VII.3, indicate that new models improve the performance of $k-\omega$ SST slightly (i.e., the error values $0.95 < j_1 < 0.96$). Therefore following the progressive approach, the activation function inside the new models prevents jeopardising the successful performance of the standard $k-\omega$ SST in the cases where the separation phenomenon is very weak or non-existent.

Figure VII.20 compares the profiles of velocity components and distribution of the bottom-wall friction coefficient. This figure confirms that the new models keep the successful performance of the standard $k-\omega$ SST model in the prediction of velocity profiles while improving the prediction of friction coefficients after the separation area.

We likewise try the new models on the case $BUMP_{42}$ which has similar geometry to $BUMP_{20}$, however, due to the higher height of the bump, flow separation is expected in

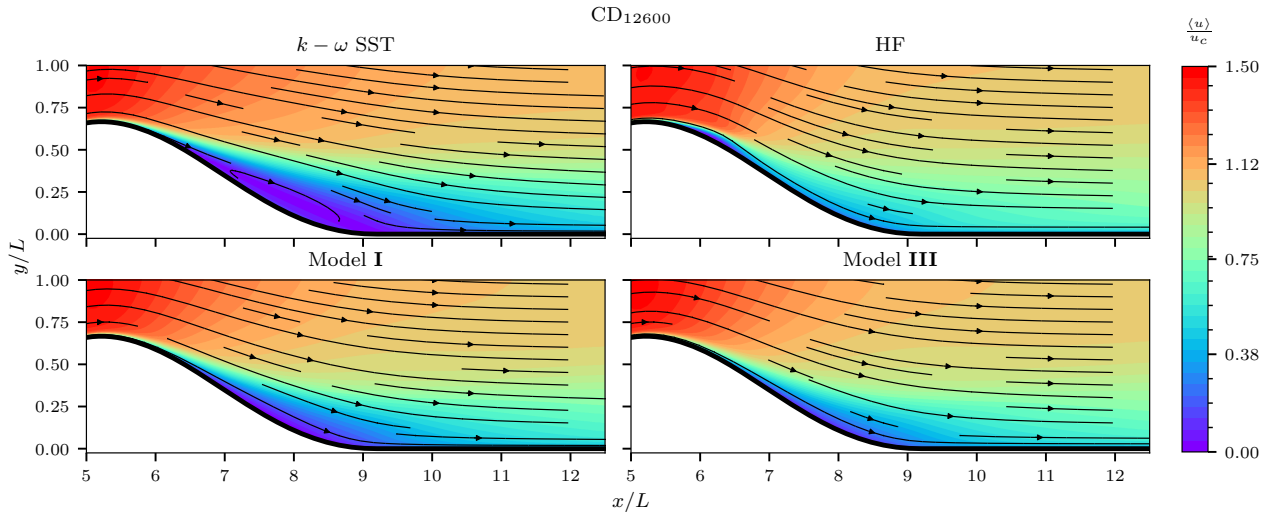

Figure VII.15: Contours of velocity magnitude with streamlines depicting separation and reattachment for the test case CD_{12600}. High-fidelity data obtained from Ref. [163].

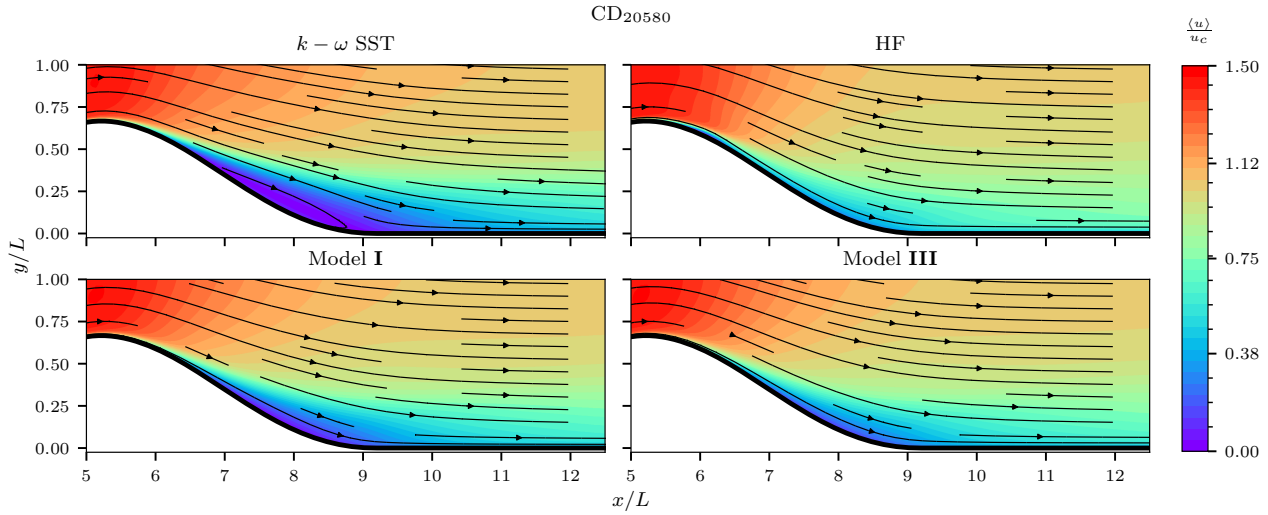

Figure VII.16: Contours of velocity magnitude with streamlines depicting separation and reattachment for the test case CD_{20580}. High-fidelity data obtained from Ref. [164].

this case. Figure. VII.21 compares the separation zone predicted by the standard $k-\omega$ SST and our new models with that of high-fidelity data. The recirculation zone in high-fidelity is placed approximately in $0.8 < x/L < 1.2$, and the standard $k-\omega$ SST overstretches the recirculation zone ($0.6 < x/L < 1.4$) whereas new correction models successfully predict the size of the recirculation zone in this unseen test case. The profiles of velocity components and distribution of bottom-wall friction coefficient are compared in Fig. VII.22. The averaged error values in Table VII.3 ($0.53 < J < 0.64$) and the comparison in Fig. VII.22 confirms the improvement resulting from the new correction models.

It should be mentioned that the mismatch in values of c_f at the inlet shown in Figs. VII.20 and VII.22, which are also present in Figs. VII.17 and VII.18, are due to the underestimation of friction coefficient by the standard $k-\omega$ SST. Since the purpose of the new correction models is to only modify the $k-\omega$ SST when separation flow exists, this mismatch is also present in the predictions by the corrected models.

Fig. VII.22 shows that the c_f in the $0.2 < x/L < 0.6$ is slightly overpredicted compared to

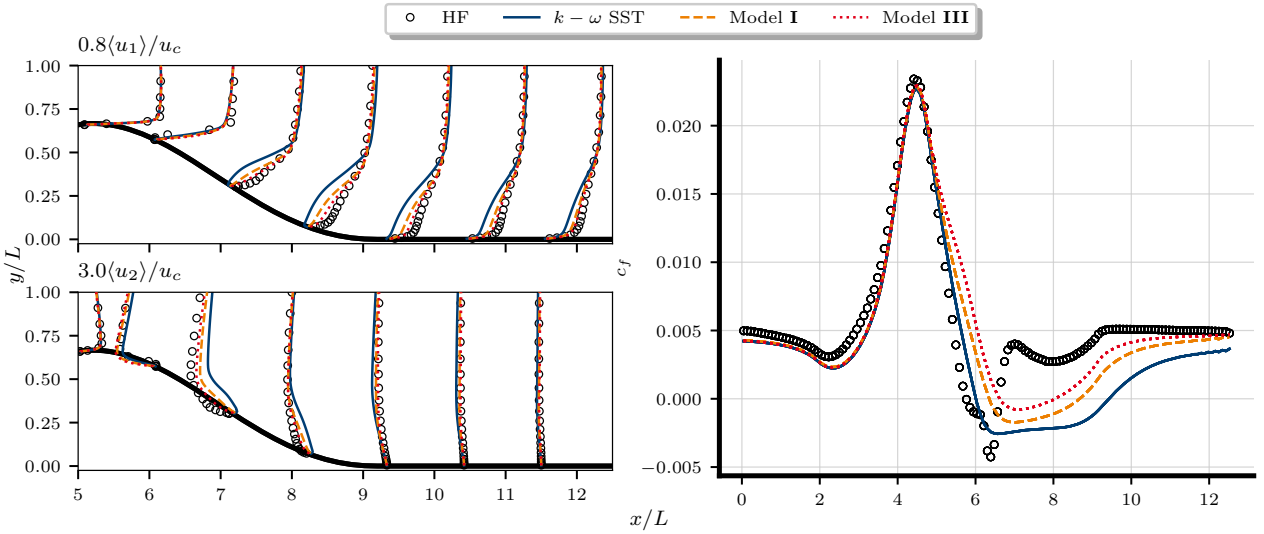

Figure VII.17: Profiles of streamwise velocity (upper left), wall-normal velocity (lower left) at seven locations $x/L = [5, 6.08, 7.17, 8.25, 9.33, 10.42, 11.5]$, and distribution of bottom-wall friction coefficient (right) for the test case CD_{12600}. High-fidelity data obtained from Ref. [163].

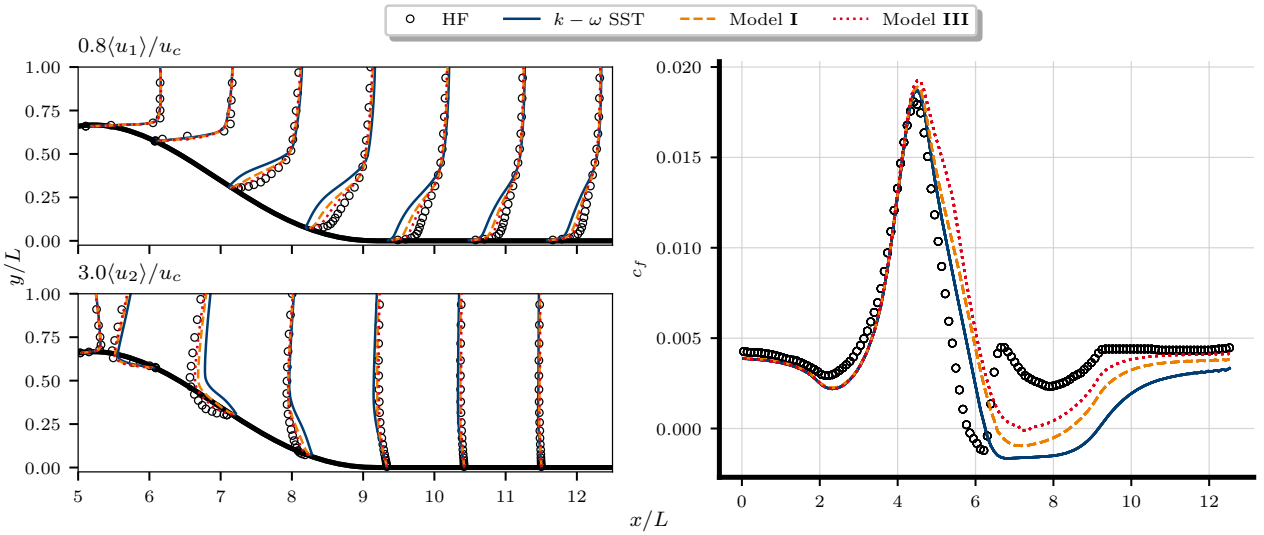

Figure VII.18: Profiles of streamwise velocity (upper left), wall-normal velocity (lower left) at seven locations $x/L = [5, 6.08, 7.17, 8.25, 9.33, 10.42, 11.5]$, and distribution of bottom-wall friction coefficient (right) for the test case CD_{20580}. High-fidelity data obtained from Ref. [164].

the standard $k-\omega$ SST. For a better analysis of the new models' effect in this case, Fig. VII.23 presents the F_{sep} values and the effect of new models on the values of turbulent viscosity (i.e., ν_t). The values of ν_t are similar to the standard $k-\omega$ SST before the bump. The main changes in ν_t happen after the apex of the bump, where a strong adverse pressure gradient causes a high ratio of production to dissipation and a higher value of ν_t can help the prediction of the velocity profiles. Also, Fig. VII.23 shows that F_{sep} is not activated where c_f is overestimated (i.e., bottom-wall boundary at $0.2 < x/L < 0.6$). It should be mentioned that even though F_{sep} value is varied locally, its effect can be transported within the domain by convection and diffusion in the ω transport equation, and it is unavoidable that we see the effect of F_{sep} on c_f in this region of an unseen test case.

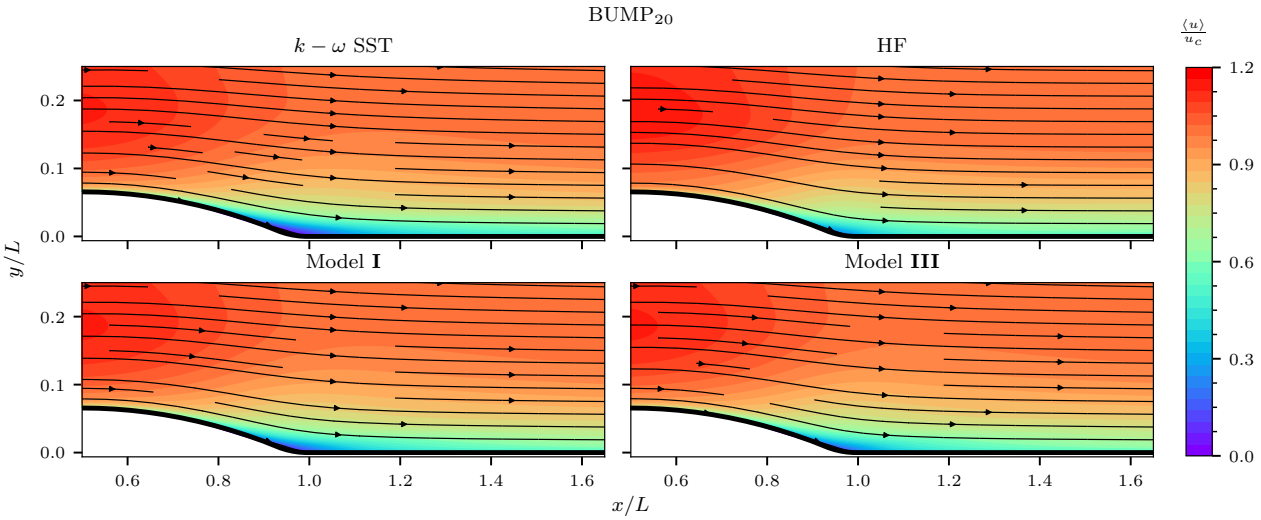

Figure VII.19: Contours of velocity magnitude with streamlines depicting separation and reattachment for the test case BUMP_{20}. High-fidelity data obtained from Ref. [165].

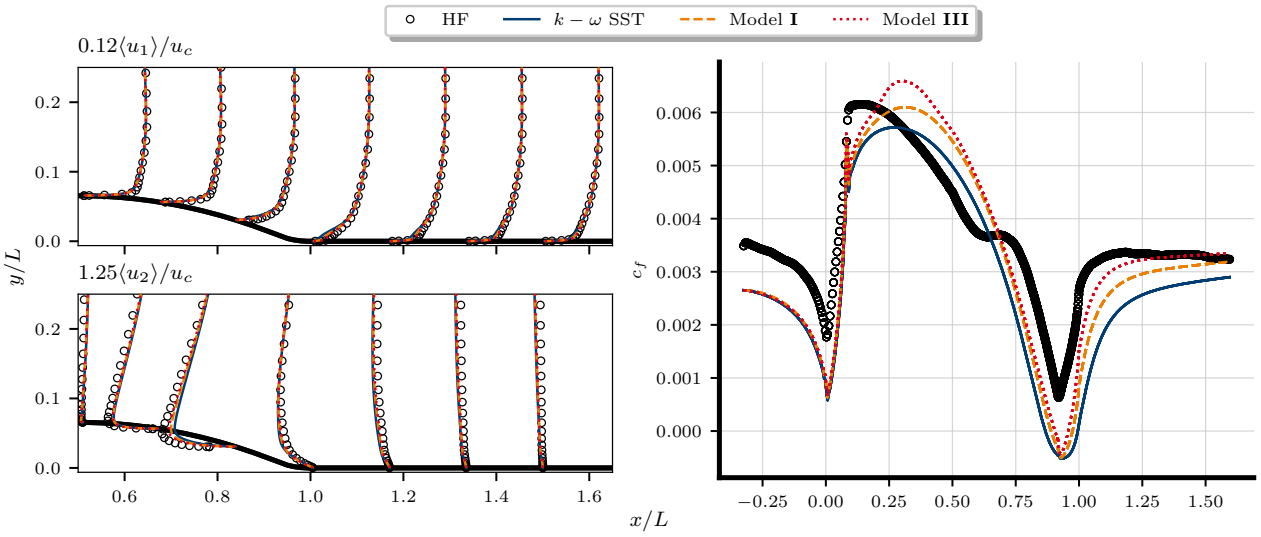

Figure VII.20: Profiles of streamwise velocity (upper left), wall-normal velocity (lower left) at seven locations $x/L = [0.51, 0.675, 0.84, 1.005, 1.17, 1.335, 1.5]$, and distribution of bottom-wall friction coefficient (right) for the test case BUMP_{20}. High-fidelity data obtained from Ref. [165].

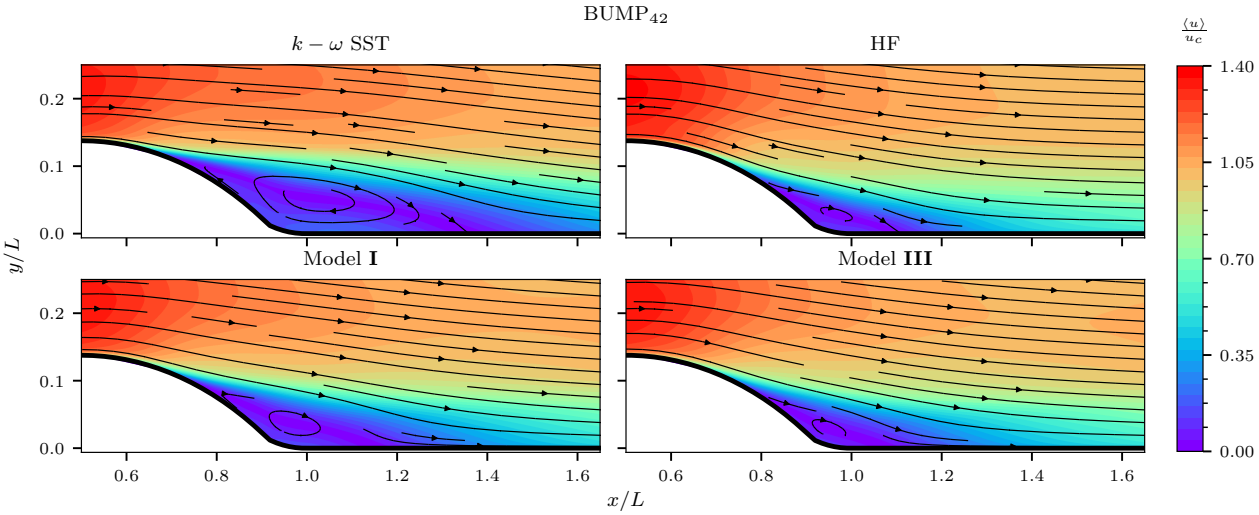

Figure VII.21: Contours of velocity magnitude with streamlines depicting separation and reattachment for the test case BUMP$_{42}$. High-fidelity data obtained from Ref. [165].

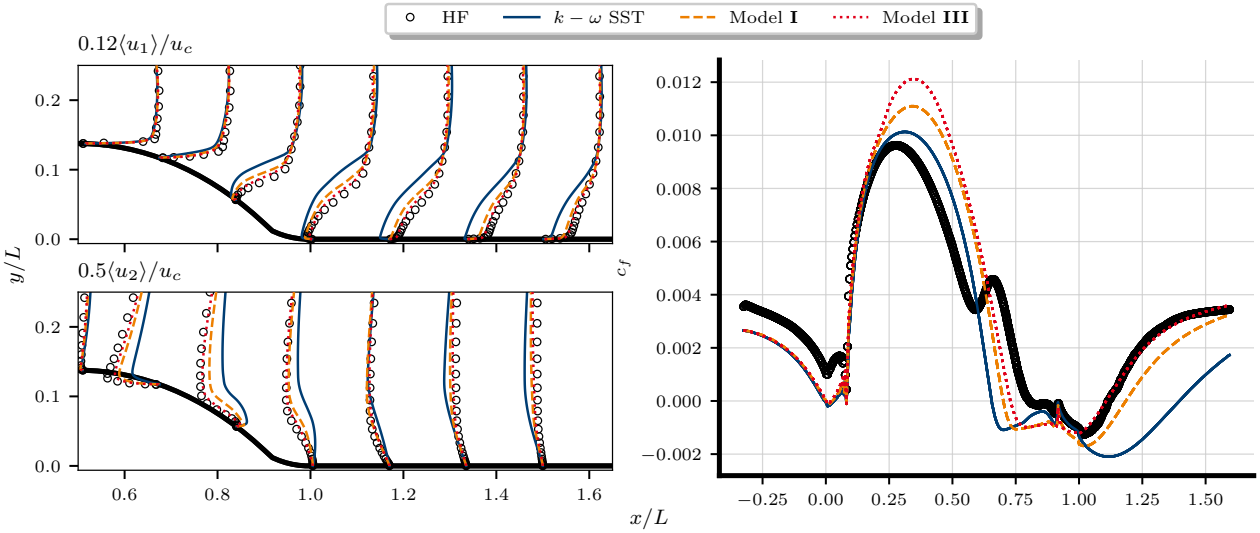

Figure VII.22: Profiles of streamwise velocity (upper left), wall-normal velocity (lower left) at seven locations $x/L = [0.51, 0.675, 0.84, 1.005, 1.17, 1.335, 1.5]$, and distribution of bottom-wall friction coefficient (right) for the test case BUMP$_{42}$. High-fidelity data obtained from Ref. [165].

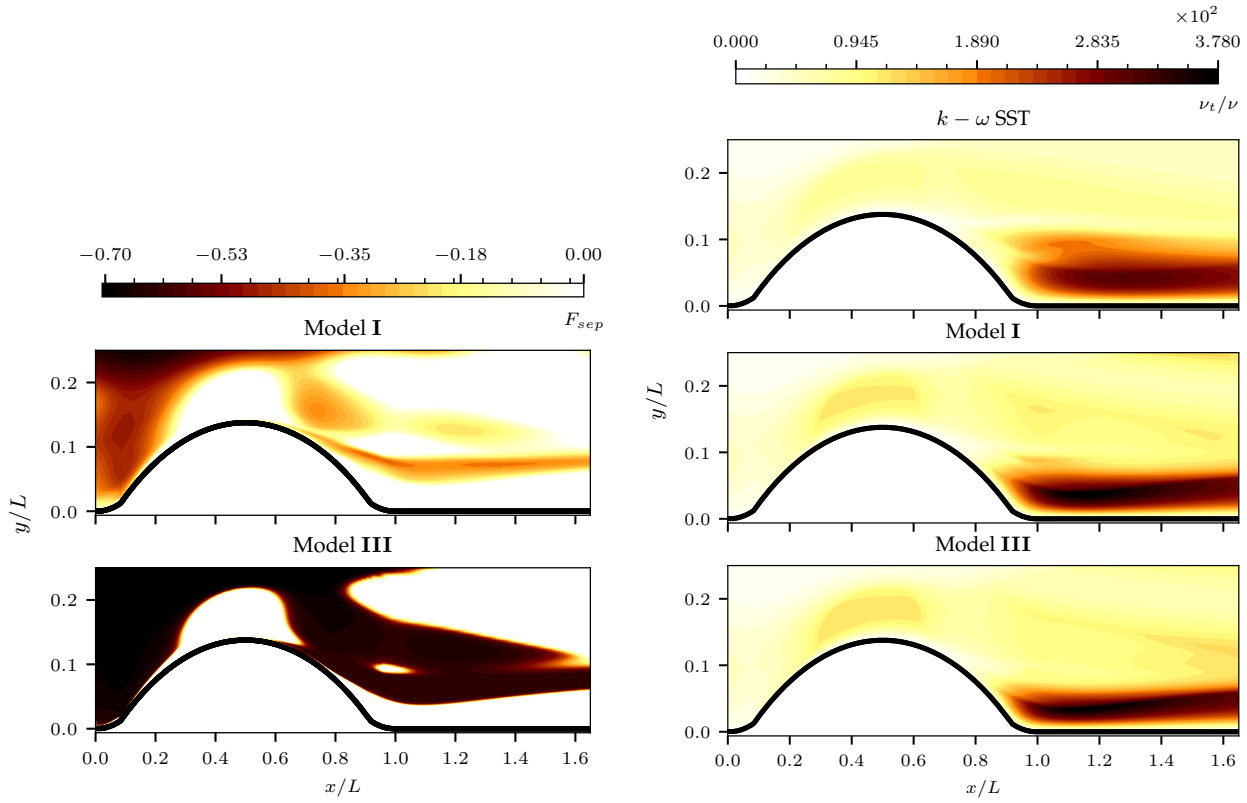

Figure VII.23: Contours of separation factor F_{sep} (left) and turbulent viscosity ν_t (right) for the testing case BUMP_{42}.

VII.4 Accountability of flow transition effects

To finalise this study, a short discussion is done regarding the influence of flow transition in separation and reattachment. In 2-dimensional cases where favourable and adverse pressure gradients are present; boundary-layer transition, laminar separation bubbles, and flow re-laminarisation play an important role in flow physics. In this study, these physics take place in test cases CD_{12600}, CD_{20580}, BUMP_{20}, and, BUMP_{41}.

Due to the limitations of standard $k-\omega$ SST, it is not possible to account for the predictions of all flow physics and complexities. Specifically, for the BUMP cases, it has been reported that the flow does not re-laminarise through the favourable pressure gradient region, nevertheless, boundary-layer transition effects that affect separation are predicted by the high-fidelity simulations in the adverse pressure gradient region [165]. Such effects cannot be predicted by standard $k-\omega$ SST.

On the one hand, these issues are encapsulated as part of a different physical phenomenon (i.e., the transition effect) than boundary-layer separation. On the other hand, the corrections added to $k-\omega$ SST improve the overall separation and reattachment prediction of not only training but also the test cases in which this extra phenomenon occurs. Nevertheless, the prediction of the velocity profiles is improved, although the mismatch in c_f is due to the abovementioned physics.

In order to showcase the transition effects inside linear eddy-viscosity models, simulations with the transition model $k-\omega$ SST $\gamma-\text{Re}_\theta$ [166, 167] have been performed for these cases. Results in Fig. VII.24 display the differences in flow prediction when turbulence transition is modelled for BUMP_{42}. The $k-\omega$ SST $\gamma-\text{Re}_\theta$ transition model is capable of slightly predicting

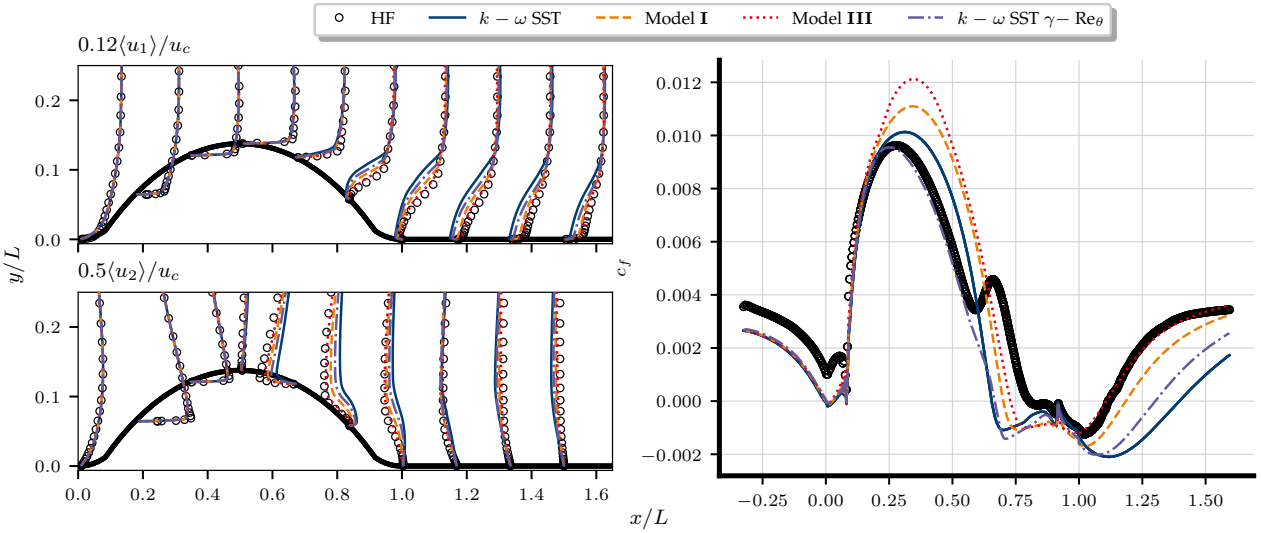

Figure VII.24: Profiles of streamwise velocity (upper left), wall-normal velocity (lower left) at ten locations $x/L = [0.01, 0.17, 0.34, 0.51, 0.672, 0.84, 1.003, 1.17, 1.335, 1.5]$, and distribution of bottom-wall friction coefficient (right) for the test case BUMP$_{42}$. High-fidelity data obtained from Ref. [165].

transition effects and accurately predicting the c_f upstream the bump's apex (at $x/L \approx 0.6$); however, the prediction still displays the overstretched flow separation and reattachment issue that standard $k-\omega$ SST has. Regarding velocity profiles, $k-\omega$ SST $\gamma-$ Re$_\theta$ enhances the prediction by the standard model although it does not improve it as much as the new correction models developed in this study.

A comparison of c_f values in range $0.2 < x/L < 0.6$ in Fig. VII.24 shows that accounting for the transition effect has improved the $k-\omega$ SST performance and has the potential to help new correction models to overcome the overprediction of c_f in that range. Therefore in a future study, it would be interesting to perform an enhanced model optimisation for $k-\omega$ SST $\gamma-$ Re$_\theta$ since the results based on Fig. VII.24 show the model's potential to be improved in a generalisable manner following the progressive methodology of this study.

VII.5 Conclusions

In this study, we use a multi-case CFD-driven surrogate optimisation to enhance the standard $k-\omega$ SST in the prediction of flow separation. We employ a progressive approach to introduce a correction to ω transport equations which is activated in the case of separation and guarantees the original performance of the $k-\omega$ SST in the absence of separation.

The performance of standard $k-\omega$ SST in 6 different tested cases, where flow separation is expected, shows that the recirculation zone is predicted larger than that of high-fidelity data. This overstretched recirculation zone is due to the underestimation of turbulent viscosity (ν_t) by standard $k-\omega$ SST. Therefore, all optimised models introduce a separation factor (F_{sep}) to the transport equation of ω, leading to lower values of ω and higher values for ν_t in localised regions of the flow field. This modification enhances the prediction of the velocity field and friction coefficient.

Considering the structure of the separation factor, we investigate two forms of dimensionality reduction including the first two leading components and the first two principal components. We likewise investigate two forms of activation functions, including a linear

function and a non-linear (i.e., power) function inside the separation factor formulation. The comparison of results in both training and testing cases shows that in general, using PCA does not improve the performance of the models in this case whereas using the power activation functions improves such performance; hence, Model **III** in this study has shown the best performance and generalisability in the tested cases.

All of the models are optimised for the lowest averaged error for the training cases (PH_{2800} and $CBFS_{13700}$) while the channel flow case (CF_{5200}) is used to guarantee the original performance of the standard $k-\omega$ SST in the absence of separation. We use 5 cases with different geometries and Reynolds numbers (PH_{10595}, CD_{12600}, CD_{20580}, $BUMP_{20}$, and $BUMP_{42}$) as unseen test cases to evaluate the generalisability of the new models. All of the new models show significant improvement in the prediction of velocity domain and friction coefficient in both training and testing cases.

For the test cases where flow separation is expected (PH_{10595}, CD_{12600}, CD_{20580}, and $BUMP_{42}$), the new separation factors successfully increase the values of ν_t to shrink the overestimated size of the recirculation zone by the standard $k-\omega$ SST. In the test case of $BUMP_{20}$, where flow separation is not expected, the new models preserve the successful performance of the standard $k-\omega$ SST in the prediction of the velocity domain while improving the prediction of friction coefficient distribution at the walls.

The results of this study suggest that the progressive augmentation methodology combined with CFD-driven optimisation is a consistent and generalisable approach to enhance common popular RANS models (e.g., standard $k-\omega$ SST model) for their shortcomings while preserving their original favourable aspects.

VIII

Final Remarks

This thesis shows the current status of the application of fluid mechanics, turbulence modelling, data-driven methods, and optimisation in complex industrial internal flows. The principal objective is to develop methods to evaluate and improve ultrasonic flow meters and popular turbulence models. With these methods, robust predictions of the flow fields throughout ultrasonic flow meters are used to improve these or any other system with similar characteristics. The applicability of these simulation-based tools allows the improvement of engineered systems in ways that would not be possible with the use of traditional technical knowledge.

The flow physics throughout a baseline two-stand ultrasonic flow meter geometry is generally complex, yielding a combination of rolling vortices generation and breakup, boundary-layer separation and reattachment, recirculation zones, and high shear and rotational regions in the flow. These flow characteristics are common for most of the flow meter dynamic range and mostly predominant for inlet turbulent flows. Furthermore, no qualitative changes in terms of coherent structures and flow dynamics are seen above an inflow Re $> 10^4$. These findings show that two-stand ultrasonic flow meters display non-canonical and intricate flow dynamics, presenting an excellent case to prove the latest methods in flow prediction and optimisation.

With the use of CFD methods and RANS $k-\omega$ SST turbulence modelling, these complex flows are predicted with particularly good agreement in the whole dynamic range of the flow meter. These predictions are compared to LDV and pressure drop experiments with an uncertainty agreement in results of 1 and 3 standard deviations, respectively. Predictions in the baseline flow meter geometry show an incipient pressure drop due to boundary-layer detachment. Moreover, high flow non-uniformities and turbulence kinetic energy are predicted in the flow meter measurement region, where the ultrasound waves travel between transducers. These facts are clear indicators of opportunities for improvement in the baseline geometry.

The use of steady-state RANS allows the relatively fast computation of results, which is a determinant factor when approaching geometrical optimisation and the practical usability of methods. In this regard, a two-step geometrical optimisation strategy is applied. Firstly, a design optimisation method is developed, parametrising the flow meter geometry and employing surrogate and Bayesian optimisation to define a response surface. This surrogate is subsequently searched for optima with a multi-objective evolutionary algorithm in a fast-paced manner. Secondly, the design optimisation method results are further improved by applying shape optimisation with the adjoint method and a custom control-point box to morph the geometry in the 3D space. This last step allows the refinement of the obtained geometry, further improving the system. This optimisation strategy shows the coupled use of CFD and optimisation to provide improved and experimentally validated designs by means of computational simulations. The repercussions of these findings open the door to the optimisation of systems with similar geometries and flow physics.

Previous optimisation efforts could not be possible without an accurate prediction of

the flow fields. Nevertheless, although accurate, eddy-viscosity RANS models have shown shortcomings in the prediction of anisotropy-based secondary flow and boundary-layer separation and reattachment in canonical flow cases. Expanding the use of the previous optimisation methodology into RANS $k-\omega$ SST, the model is enhanced by the use of a sparse regression of basis tensors and their invariants together with coefficients, where the coefficients' values are calibrated by surrogate and Bayesian optimisation.

On the one hand, regarding secondary flow prediction, a set of principal components based on the invariant functions and coefficients are defined into the second basis tensor of Pope's decomposition, adding a non-linear term into the Reynolds stress prediction that accounts for a certain level of turbulence anisotropy. Performing surrogate optimisation in a simplified square duct case and comparing the results to high-fidelity data, a set of optimal coefficients is found. On the other hand, regarding the prediction of boundary-layer separation and reattachment, a combination of the first and second invariants and coefficients is used to correct the production of dissipation. To not alter the correct law of the wall prediction of the original model, an activation function defined by two exponents is likewise defined and added to the correction. Performing simultaneous Bayesian optimisation to a series of canonical flows in which separation is expected, an optimal set of coefficients and exponents is likewise found.

All models are tested in diverse canonical cases with different geometries and Reynolds numbers, generally showing excellent generalisability in 2-dimensional cases. Hence, these approaches have shown to be consistent and generalisable methods for enhancing popular RANS models by data-driven techniques.

The methods developed throughout this thesis have been able to evaluate, characterise key metrics, and optimise two-stand ultrasonic flow meters via numerical simulation tools, while experimentally validating the obtained results. In addition, the data-driven optimisation methods developed have been expanded and used to progressively enhance common RANS turbulence models in an accurate and generalised manner.

VIII.1 Future prospects

The work done in this thesis likewise leads to certain insights to keep advancing the state-of-the-art of fluid-based optimisation and data-driven RANS modelling. The most relevant research topics to be studied as a consequence of this thesis are discussed as follows:

- For the specific case of ultrasonic flow metering, there are gaps in the literature that must be filled in order to ensure an optimal evaluation of flow meter performances. The performance functions defined in this thesis are based on empirical and previous industrial technical knowledge. Although their base shows physical significance, these functions have not been experimentally validated. Hence, it is required to develop the experimental hardware to evaluate the ultrasound-fluid interaction and validate the performance functions.

- During the timeframe of this thesis, it was not possible to experimentally evaluate wide fields of view. Although very accurate, LDV is a time-consuming experimental technique that evaluates velocity locally. In this regard, the experimental evaluation of 2D or 3D velocity fields by PIV or similar techniques throughout the flow meter would be desirable to validate the numerical methodology at other locations.

- It would be desirable to perform an extended design optimisation in the flow meter

where more geometrical degrees of freedom are allowed based on the results of this thesis and a refined performance function is validated.

- The final results of shape optimisation by mesh morphing and the adjoint method obtained during this thesis do not fully agree with the calculated gains by the method. To this end, it would be desirable to perform experimental validation on the final geometry and implement careful re-meshing between optimisation iterations to maintain consistency in the results.

- Regarding data-driven RANS turbulence modelling enhancement, the progressive approach has proven to be very useful in the generalisability and robustness of the models. However, the introduction of a non-linear term into the Reynolds stress has shown certain tendencies towards solver divergence that should not be overlooked. One suggestion to improve the models' convergence is the inclusion of a sparsity-promoting function with regularisation during optimisation that penalises the final objective the bigger the coefficient values are. This approach would minimise the non-linear correction to the model while still being accurate in the prediction of secondary flows.

- All enhanced turbulence models have been trained in 2D canonical flow cases. It is expected that certain terms in the yielded functions and invariants would be insignificant due to the limited dimensionality of the training cases. Therefore, using a 3D case with significant complexity (such as a two-stand ultrasonic flow meter or the 3D Boeing Gaussian speed bump) to perform the training would probably yield more generalisable and accurate models for both 2D and 3D cases alike.

IX

Epilogue from the Author

To conclude, I would like to share some light-hearted reflections on our past, our present, and our future based on what I have learned during my Ph.D journey.

Nowadays, every little improvement in society and technology involves solving a very complex *knowledge* problem. One can only imagine then that big changes do not come easy, and when they come, they are the result of small incremental contributions by a lot of people. Some would say that knowledge is power due to this fact, but I believe that knowledge is something more: *opportunity*. An opportunity to dare to try, an opportunity to change and make things better, an opportunity to feel safe in a world full of uncertainties...

We should not neglect the importance of knowledge (and research) in today's world. I found it very interesting that knowledge showcases a feedback loop. Showing that every answer just leads to more questions, therefore, we must not stop learning, so we can always find the answers to the questions, and most importantly: the solutions to the lurking problems.

Throughout history, it has been seen that the correct use of physical laws in favour of human aid enables changes to increase the well-being of society as a whole. To this end, I hope that the research performed in this thesis places a little grain of sand in the mountain of knowledge and societal progress that will *improve* the well-being of current and future generations.

If you have followed this thesis, you must have noticed the problem that we are trying to solve: mitigating or completely avoiding the collateral damages of climate change, mostly, water scarcity. To do so, a substantial amount of engineering-based efforts must be placed in the improvement of the water distribution networks at a global scale. That is why fluid mechanics knowledge is very important if we need to understand the flow of fluids in current distribution networks.

Extrapolating this fact, we live surrounded by the consequences of fluid mechanics, thus improving our prediction of fluid motion is very relevant to solving a staggering amount of engineering challenges. But simultaneously, we should not forget the need for collaboration and multi-disciplinary synergies between fields, not only from technical disciplines but also from humanities and social sciences. Ultimately, we all live in society and the contemporary landscape requires understanding each other while cooperating.

A fundamental matter that I have learned during these years is that, in the current scene of engineering and physics research, the applicability of state-of-the-art methods and technologies is the holy grail of progress. With this, I have the feeling that applying the methods developed and *knowledge* uncovered during my years of research opens the door to a fascinating *opportunity* for continuous *improvement*. My final hope is that this opportunity is welcomed with open arms and used wisely in the years to come.

Thank you for the time to go through my thesis, my dear reader. Let us all remember to make this world a better place, together.

Appendices

A

Erratum

Everyone makes mistakes (even in a Ph.D. thesis), hence, this appendix includes various updates to the Ph.D. Thesis titled *Robust Optimisation of Ultrasonic Flow Meters by Computational Fluid Dynamics and Enhanced Turbulence Modelling* by the author Mario Javier Rincón. The thesis was originally submitted for assessment to the Graduate School of Technical Sciences (GSTS) of Aarhus University (AU) on October 30th, 2023 and, according to:

Rules & Regulations 11.7 "*Corrections to the thesis: The thesis available for the defence must in principle be identical to the version submitted for assessment. However, the PhD student is allowed to incorporate small corrections and changes provided that a detailed description of these corrections and changes is included as well; this also applies to corrections and changes incorporated after the defence.*"

Following this rule, certain updates are made to the submitted thesis version due to the final publication and acceptance of 2 out of 6 manuscripts composing the thesis. These manuscripts compose Chapters 3, and 7 of the thesis. The minor changes included following the suggestions of the journal reviewers, who pointed out improvements to the text and some figures. In addition, the reference of these chapters is updated to match them with reference journals in which these are now published.

Hence, all updates are based on the reviewer's comments and have been peer-reviewed after their implementation in the articles. Changes are made to provide a finished and complete version of the studies made during the Ph.D. prior to the thesis defence and printing by the University Library.

A.1 List of Changes

A.1.1 Chapter II

1. Title has changed: Flow investigation of two-stand ultrasonic flow meters in a wide dynamic range by numerical and experimental methods.

2. Reference changed with the new title.

3. Paragraph added at the end of Section 1: The previous studies regarding two-stand ultrasonic flow meters have only focused on a single nominal inlet flow in the turbulent regime, resulting in a gap in the literature when assessing the robustness and accuracy of common RANS models in their prediction of the dynamic range of complex internal flows. This study thus presents a comprehensive numerical and experimental investigation of the dynamic range of operation of a typical two-stand ultrasonic flow meter by industry standards. By using numerical methods, we aim to understand, accurately predict, and investigate the flow dynamics within the device and evaluate its performance under varying flow rates within its dynamic range. Furthermore, with a well-documented and grounded numerical foundation of the flow physics of the

dynamic range in these systems, we aim to provide the knowledge to analyse the performance of ultrasonic flow meters and improve their performance based on numerical data.

4. Paragraph added at the end of section 2: In addition, the performance of the flow meter is numerically evaluated in the dynamic range following the work by Rincón *et al.* [76, 82]. This performance function is defined as

$$f_2 = -\left(\frac{u_\Omega - u'_\Omega - \sigma_{u_\Omega}}{u_b}\right), \tag{A.1}$$

where Ω is the estimated sound propagation volume, u_Ω is the integrated velocity of the fluid in the sound-path volume, u'_Ω is the integrated velocity fluctuations in the sound-path volume, σ_{u_Ω} is the standard deviation of the integrated velocity distribution in the sound-path volume. For more information about the performance function calculation, the reader is referred to [76].

5. Line is added at the beginning of Section 3: Experimental uncertainties follow the convention by ISO/IEC Guide 98-3 Part 3: GUM [85], displaying 2σ ranges. All results are similarly discussed and described followed by their corresponding figures.

6. Paragraph is added at the beginning of Subsection 3.1: It is remarkable to highlight that there is not a single geometrical parameter that holistically governs the flow physics present in this type of ultrasonic flow meter. It is very complex to determine and evaluate in detail the geometrical causes of all the physics present in this case, therefore, the results section of this study focuses on the qualitative and quantitative description of the physics and phenomena. For more information about the parameter influence in this case, the reader is referred to the study by Rincón *et al.* (2023) [76].

   And after Figure 6 of Subsection 3.1: The λ_2 values represent a good criterion to identify vortical structures. The criterion is defined as the second biggest eigenvalue (in magnitude) of the matrix $S_{ik}S_{kj} + \Omega_{ik}\Omega_{kj}$, where S_{ij} is the rate-of-strain tensor and Ω_{ij} is the rate-of-rotation tensor, defined as

$$S_{ij} = \frac{1}{2}\left(\frac{\partial u_i}{\partial x_j} + \frac{\partial u_j}{\partial x_i}\right) \tag{A.2a}$$

$$\Omega_{ij} = \frac{1}{2}\left(\frac{\partial u_i}{\partial x_j} - \frac{\partial u_j}{\partial x_i}\right). \tag{A.2b}$$

7. Figure 7 has been updated showing a schematic on top of it.

8. Figure 9 has been updated showing darker uncertainty bounds to improve its printability. Uncertainty bounds are now showing 2σ.

9. Figure 11 has been updated showing darker uncertainty bounds to improve its printability. Uncertainty bounds are now showing 2σ.

10. Figure 12 has been updated showing now 2σ uncertainty bounds.

11. Figure 13 has been updated showing now 2σ uncertainty bounds.

12. Subsection 3.4 has been added: Following the definition from Rincón *et al.* [76, 82], the performance of the flow meter under the tested inlet conditions, is evaluated. The performance function f_2 evaluates the velocity and turbulence kinetic energy throughout the reflected sound-path volume and provides, solely by the numerical flow solution, a performance value. A high negative value of f_2 indicates a more robust and accurate measurement by the flow meter, whereas a value close to 0 indicates the opposite.

    Figure 15 shows the results of f_2 in function of the inlet Reynolds number for all cases studied. Results show that the estimated measurement performance decreases as the inlet Re increases, with an asymptotic tendency towards $f_2 \approx 0.49$. For low inlet Re cases, the estimated measurement performance improves.

    Saturation values of f_2 are reached approximately at Re $= 10^4$. This phenomenon occurs due to the similarity of the flow fields at higher inlet Re. However, the differences in the flow fields of the low flow rate cases yield large deviations in the performance estimates. Excluding the laminar cases, which yield a 286% and 265% better performance than the nominal inlet Re $= 2.82 \cdot 10^4$. These findings point out that these types of flow meters yield a more robust measurement at low inlet Re. Simultaneously, the variation in measurement performance of these meters is highly reduced at higher inlet Re.

13. Figure 15 has been added to support the claims of Subsection 3.4.

14. A line has been added to Section 4: The numerical flow meter performance shows that the velocity field at lower inlet Re yields a more robust and accurate measurement compared to higher inlet Re, where a saturated value of the performance function is observed in inlet Re $> 10^4$. .

A.1.2 Chapter VII

1. Paper title changed from British to American spelling to be consistent with the published version, e.g. the word *optimisation* has been changed to the word *optimization*. These changes of British to American spelling in the title are changed throughout the whole text.

2. The article reference has been changed to be consistent with the published manuscript.

3. Lines added in Section 2.1: It should be mentioned that both φ_1 and φ_2 include a combination of all the candidate functions (listed in Eq. VII.11), where $\mathcal{B}_1$ and $\mathcal{B}_2$ are the normalised versions of the linear terms I_1 and I_2, respectively.

4. Lines added after Eq. II.17: It should be mentioned that all of these correction models integrate only a few algebraic calculations to each iteration in the simulations, which do not affect the computational cost of the simulations compared to the original $k-\omega$ SST model.

5. Lines added in section 2.2: A well-designed sampling plan is delineated based on Latin hypercube sampling (LHS), with an infill criterion that adheres to quality measures. Acknowledging the possibility that the initial sampling might not cover the surrogate's extreme values, Bayesian techniques rooted in efficient global optimisation are employed, coupled with the evaluation of the expected improvement ($E\left[I(x)\right]$) function. These strategies are aimed at further exploring the surrogate model, enhancing its reliability, and obtaining optimal observations.

6. Caption changed in Fig. II.2: Optimisation approach involving an initial sampling plan using Latin hypercube sampling, resolved through CFD. A multi-case methodology is adopted, wherein observations are simultaneously conducted across three cases: CBFS_{13700}, PH_{2800}, and CF_{5200}. Subsequent to this, an initial surrogate model is formulated using Kriging and improved using Bayesian optimisation techniques.

7. Line added at the end of table II.2: $Re_b = 1.01 \cdot 10^5$.

8. Lines added after Fig. II.6: These similarities in the performance of PCA and linear structures of function α are an indication that the effect of higher order linear combinations of I_1 and I_2 is negligible for model improvement in this study. However, the PCA analysis can decrease the optimisation cost when more invariants are involved in complex and 3-dimensional cases. Therefore, Models **I** and **III** which have simpler formats are chosen to be compared throughout this paper to highlight the effect of non-linear (i.e., power) activation function versus linear activation function... Furthermore, due to the higher gradients of the optimised activation function $\mathcal{X}$, the results of F_{sep} for Model **III** show more extreme values.

9. Caption of Fig. II.7: Contours of separation factor F_{sep} (left) and turbulent viscosity ν_t (right) for the training case CBFS_{13700}.

10. Paragraph added at the end of section 3.2: It should be mentioned that the mismatch in values of c_f at the inlet shown in Figs. 20 and 22, which are also present in Figs. 17 and 18, are due to the underestimation of friction coefficient by the standard $k-\omega$ SST. Since the purpose of the new correction models is to only modify the $k-\omega$ SST when separation flow exists, this mismatch is also present in the predictions by the corrected models.

    Fig. 22 shows that the c_f in the $0.2 < x/L < 0.6$ is slightly overpredicted compared to the standard $k-\omega$ SST. For a better analysis of the new models' effect in this case, Fig. 22 presents the F_{sep} values and the effect of new models on the values of turbulent viscosity (i.e., ν_t). The values of ν_t are similar to the standard $k-\omega$ SST before the bump. The main changes in ν_t happen after the apex of the bump, where a strong adverse pressure gradient causes a high ratio of production to dissipation and a higher value of ν_t can help the prediction of the velocity profiles. Also, Fig. 23 shows that F_{sep} is not activated where c_f is overestimated (i.e., bottom-wall boundary at $0.2 < x/L < 0.6$). It should be mentioned that even though F_{sep} value is varied locally, its effect can be transported within the domain by convection and diffusion in the ω transport equation, and it is unavoidable that we see the effect of F_{sep} on c_f in this region of an unseen test case.

11. Section 4: Accountability of flow transition effects, has been added with two new figures.

Bibliography

[1] C. J. Vorosmarty, P. Green, J. Salisbury, and R. B. Lammers, "Global water resources: vulnerability from climate change and population growth," *science*, vol. 289, no. 5477, pp. 284–288, 2000.

[2] United Nations, "Population division, world population prospects 2019: Highlights," March 2019.

[3] R. Frauendorfer and R. Liemberger, "The issues and challenges of reducing non-revenue water," *Asian Development Bank*, 2010.

[4] European Environment Agency, *Water scarcity conditions in Europe (Water exploitation index plus) (8^{th} EAP)*. European Environment Agency, 2023.

[5] R. Liemberger and A. Wyatt, "Quantifying the global non-revenue water problem," *Water Supply*, vol. 19, no. 3, pp. 831–837, 2019.

[6] R. Liemberger and M. Farley, "Developing a nonrevenue water reduction strategy part 1: Investigating and assessing water losses," in *Paper to IWA Congress*, 2004.

[7] Organisation for Economic Co-operation and Development (OECD), "Infrastructure to 2030: Telecom, land transport, water and electricity," June 2006.

[8] D. Vicente, L. Garrote, R. Sánchez, and D. Santillán, "Pressure management in water distribution systems: Current status, proposals, and future trends," *Journal of Water Resources Planning and Management*, vol. 142, no. 2, p. 04015061, 2016.

[9] Kamstrup A/S, "User guide of kamstrup water solutions and analytics in leak detection," *Kamstrup A/S customer information*, 2023.

[10] J. Yoder, *The World market for ultrasonic flowmeters*. Flow Research, 2017.

[11] E. Mandard, D. Kouame, R. Battault, J.-P. Remenieras, and F. Patat, "Methodology for developing a high-precision ultrasound flow meter and fluid velocity profile reconstruction," *IEEE Transactions on Ultrasonics, Ferroelectrics, and Frequency Control*, vol. 55, no. 1, pp. 161–172, 2008.

[12] B. Lüscher, T. Staubli, T. Tresch, and P. Gruber, "Accuracy analysis of the acoustic discharge measurement using analytical, spatial velocity profiles," *Proceedings of Hydro07, Granada, Spain*, 2007.

[13] A. N. Kolmogorov, "A refinement of previous hypotheses concerning the local structure of turbulence in a viscous incompressible fluid at high reynolds number," *Journal of Fluid Mechanics*, vol. 13, no. 1, pp. 82–85, 1962.

[14] U. Frisch, *Turbulence: the legacy of AN Kolmogorov*. Cambridge university press, 1995.

[15] X. I. Yang and K. P. Griffin, "Grid-point and time-step requirements for direct numerical simulation and large-eddy simulation," *Physics of Fluids*, vol. 33, no. 1, p. 015108, 2021.

[16] A. Hilgenstock and R. Ernst, "Analysis of installation effects by means of computational fluid dynamics—CFD vs experiments?," *Flow Measurement and Instrumentation*, vol. 7, no. 3-4, pp. 161–171, 1996.

[17] R. S. Martins, G. S. de Aquino, M. F. Martins, and R. Ramos, "Sensitivity analysis for numerical simulations of disturbed flows aiming ultrasonic flow measurement," *Measurement*, vol. 185, p. 110015, 2021.

[18] A. Weissenbrunner, A. Fiebach, S. Schmelter, M. Bär, P. U. Thamsen, and T. Lederer, "Simulation-based determination of systematic errors of flow meters due to uncertain inflow conditions," *Flow Measurement and Instrumentation*, vol. 52, pp. 25–39, 2016.

[19] A. Weissenbrunner, A.-K. Ekat, M. Straka, and S. Schmelter, "A virtual flow meter downstream of various elbow configurations," *Metrologia*, 2023.

[20] R. S. Martins, J. R. Andrade, and R. Ramos, "On the effect of the mounting angle on single-path transit-time ultrasonic flow measurement of flare gas: a numerical analysis," *Journal of the Brazilian Society of Mechanical Sciences and Engineering*, vol. 42, no. 1, p. 13, 2020.

[21] D. Zheng, P. Zhang, and T. Xu, "Study of acoustic transducer protrusion and recess effects on ultrasonic flowmeter measurement by numerical simulation," *Flow Measurement and Instrumentation*, vol. 22, no. 5, pp. 488–493, 2011.

[22] E. Liu, H. Tan, and S. Peng, "A CFD simulation for the ultrasonic flow meter with a header," *Tehnički Vjesnik - Technical Gazette*, vol. 24, no. 6, p. 1797, 2017.

[23] W. Chen, J. Wu, and C. Li, "The investigation on the flow distortion effect of header to guarantee the measurement accuracy of the ultrasonic gas flowmeter," *Applied Sciences*, vol. 11, no. 8, p. 3656, 2021.

[24] H. Zhao, L. Peng, S. A. Stephane, H. Ishikawa, K. Shimizu, and M. Takamoto, "Cfd aided investigation of multipath ultrasonic gas flow meter performance under complex flow profile," *IEEE Sensors Journal*, vol. 14, no. 3, pp. 897–907, 2013.

[25] S. Peng, W. Liao, and H. Tan, "Performance optimization of ultrasonic flow meter based on computational fluid dynamics," *Advances in Mechanical Engineering*, vol. 10, no. 8, 2018.

[26] A. Hallanger, K. Froysa, and P. Lunde, "Cfd-simulation and installation effects for ultrasonic flow meters in pipes with bends," *International Journal of Applied Mechanics and Engineering*, vol. 7, no. 1, pp. 33–64, 2002.

[27] M. Simão, M. Besharat, A. Carravetta, and H. M. Ramos, "Flow velocity distribution towards flowmeter accuracy: CFD, UDV, and field tests," *Water*, vol. 10, no. 12, p. 1807, 2018.

[28] V. Leontidis, C. Cuvier, G. Caignaert, P. Dupont, O. Roussette, S. Fammery, P. Nivet, and A. Dazin, "Experimental validation of an ultrasonic flowmeter for unsteady flows," *Measurement Science and Technology*, vol. 29, no. 4, p. 045303, 2018.

[29] J. Slotnick, A. Khodadoust, A. Juan, D. Darmofal, W. Gropp, E. Lurie, and D. Mavriplis, "CFD vision 2030 study: A path to revolutionary computational aerosciences," Technical Report NASA/CR-2014-218178, NASA, 2014.

[30] H. Xiao and P. Cinnella, "Quantification of model uncertainty in RANS simulations: A review," *Progress in Aerospace Sciences*, vol. 108, pp. 1–31, 2019.

[31] K. Duraisamy, G. Iaccarino, and H. Xiao, "Turbulence modeling in the age of data," *Annual Review of Fluid Mechanics*, vol. 51, pp. 357–377, 2019.

[32] B. Tracey, K. Duraisamy, and J. Alonso, "Application of supervised learning to quantify uncertainties in turbulence and combustion modeling," in *51st AIAA aerospace sciences meeting including the new horizons forum and aerospace exposition*, p. 259, 2013.

[33] J.-X. Wang, J.-L. Wu, and H. Xiao, "Physics-informed machine learning approach for reconstructing Reynolds stress modeling discrepancies based on DNS data," *Phyical Review Fluids*, vol. 2, no. 3, p. 034603, 2017.

[34] J.-L. Wu, H. Xiao, and E. Paterson, "Physics-informed machine learning approach for augmenting turbulence models: A comprehensive framework," *Physical Review Fluids*, vol. 3, no. 7, p. 074602, 2018.

[35] J. Ling, A. Kurzawski, and J. Templeton, "Reynolds averaged turbulence modelling using deep neural networks with embedded invariance," *Journal of Fluid Mechanics.*, vol. 807, pp. 155–166, 2016.

[36] M. L. Kaandorp and R. P. Dwight, "Data-driven modelling of the Reynolds stress tensor using random forests with invariance," *Computers & Fluids*, vol. 202, p. 104497, 2020.

[37] R. McConkey, E. Yee, and F.-S. Lien, "Deep structured neural networks for turbulence closure modeling," *Physics of Fluids*, vol. 34, no. 3, p. 035110, 2022.

[38] Y. Zhao, H. D. Akolekar, J. Weatheritt, V. Michelassi, and R. D. Sandberg, "RANS turbulence model development using CFD-driven machine learning," *Journal of Computational Physics*, vol. 411, p. 109413, 2020.

[39] I. B. H. Saïdi, M. Schmelzer, P. Cinnella, and F. Grasso, "CFD-driven symbolic identification of algebraic Reynolds-stress models," *Journal of Computational Physics*, vol. 457, p. 111037, 2022.

[40] K. Duraisamy, "Perspectives on machine learning-augmented Reynolds-averaged and large eddy simulation models of turbulence," *Physical Review Fluids*, vol. 6, no. 5, p. 050504, 2021.

[41] D. Thévenin and G. Janiga, *Optimization and computational fluid dynamics*. Springer Science & Business Media, (2008).

[42] J. A. Nelder and R. Mead, "A Simplex Method for Function Minimization," *The Computer Journal*, vol. 7, no. 4, pp. 308–313, 1965.

[43] C. A. C. Coello, G. B. Lamont, D. A. Van Veldhuizen, *et al.*, *Evolutionary algorithms for solving multi-objective problems*, vol. 5. Springer, (2007).

[44] R. Eberhart and J. Kennedy, "Particle swarm optimization," in *Proceedings of the IEEE international conference on neural networks*, vol. 4, pp. 1942–1948, Citeseer, 1995.

[45] G. E. Box, "The exploration and exploitation of response surfaces: some general considerations and examples," *Biometrics*, vol. 10, no. 1, pp. 16–60, 1954.

[46] J. Sacks, S. B. Schiller, and W. J. Welch, "Designs for Computer Experiments," *Technometrics*, vol. 31, no. 1, pp. 41–47, 1989.

[47] R. H. Myers, D. C. Montgomery, and C. M. Anderson-Cook, *Response surface methodology: process and product optimization using designed experiments*. John Wiley & Sons, (2016).

[48] J. Alexandersen and C. S. Andreasen, "A review of topology optimisation for fluid-based problems," *Fluids*, vol. 5, no. 1, p. 29, 2020.

[49] G. K. Kenway, C. A. Mader, P. He, and J. R. Martins, "Effective adjoint approaches for computational fluid dynamics," *Progress in Aerospace Sciences*, vol. 110, p. 100542, 2019.

[50] E. Kontoleontos, E. Papoutsis-Kiachagias, A. Zymaris, D. Papadimitriou, and K. Giannakoglou, "Adjoint-based constrained topology optimization for viscous flows, including heat transfer," *Engineering Optimization*, vol. 45, no. 8, pp. 941–961, 2013.

[51] G. H. Yoon, "Topology optimization for turbulent flow with spalart–allmaras model," *Computer Methods in Applied Mechanics and Engineering*, vol. 303, pp. 288–311, 2016.

[52] J. Reuther, A. Jameson, J. Farmer, L. Martinelli, and D. Saunders, "Aerodynamic shape optimization of complex aircraft configurations via an adjoint formulation," in *34^{th} Aerospace Sciences Meeting and Exhibit*, p. 94, 1996.

[53] G. Carpentieri, B. Koren, and M. J. van Tooren, "Adjoint-based aerodynamic shape optimization on unstructured meshes," *Journal of Computational Physics*, vol. 224, no. 1, pp. 267–287, 2007.

[54] A. Jameson, "Aerodynamic design via control theory," *Journal of Scientific Computing*, vol. 3, no. 3, pp. 233–260, 1988.

[55] S. Thomas, O. Carsten, *et al.*, "Adjoint optimization for vehicle external aerodynamics," *International Journal of Automotive Engineering*, vol. 7, no. 1, pp. 1–7, 2016.

[56] C. Othmer, "Adjoint methods for car aerodynamics," *Journal of Mathematics in Industry*, vol. 4, no. 1, p. 6, 2014.

[57] S. B. Dilgen, C. B. Dilgen, D. R. Fuhrman, O. Sigmund, and B. S. Lazarov, "Density based topology optimization of turbulent flow heat transfer systems," *Structural and Multidisciplinary Optimization*, vol. 57, pp. 1905–1918, 2018.

[58] Z. Lyu, G. K. Kenway, and J. R. Martins, "Aerodynamic shape optimization investigations of the common research model wing benchmark," *AIAA Journal*, vol. 53, no. 4, pp. 968–985, 2015.

[59] M. J. Rincón, M. Reclari, and M. Abkar, "Turbulent flow in small-diameter ultrasonic flow meters: A numerical and experimental study," *Flow Measurement and Instrumentation*, vol. 87, p. 102227, 2022.

[60] L. Lynnworth and Y. Liu, "Ultrasonic flowmeters: Half-century progress report, 1955–2005," *Ultrasonics*, vol. 44, pp. e1371–e1378, 2006.

[61] E. Thompson, "Fundamentals of multipath ultrasonic flow meters for gas measurement," *Proceedings of the American School of Gas Measurement Technology*, p. 23, 2011.

[62] S. B. Pope, *Turbulent flows*. IOP Publishing, 2001.

[63] B. E. Launder and D. B. Spalding, "The numerical computation of turbulent flows," in *Numerical prediction of flow, heat transfer, turbulence and combustion*, pp. 96–116, Elsevier, 1983.

[64] F. R. Menter, "Two-equation eddy-viscosity turbulence models for engineering applications," *AIAA journal*, vol. 32, no. 8, pp. 1598–1605, 1994.

[65] H. G. Weller, G. Tabor, H. Jasak, and C. Fureby, "A tensorial approach to computational continuum mechanics using object-oriented techniques," *Computers in Physics*, vol. 12, no. 6, pp. 620–631, 1998.

[66] P. K. Sweby, "High resolution schemes using flux limiters for hyperbolic conservation laws," *SIAM Journal on Numerical Analysis*, vol. 21, no. 5, pp. 995–1011, 1984.

[67] R. M. Beam and R. F. Warming, "An implicit finite-difference algorithm for hyperbolic systems in conservation-law form," *Journal of Computational Physics*, vol. 22, no. 1, pp. 87–110, 1976.

[68] D. C. Wilcox *et al.*, *Turbulence modeling for CFD*, vol. 2. DCW industries La Canada, CA, (1998).

[69] J. E. Bardina, P. G. Huang, and T. J. Coakley, "Turbulence modeling validation, testing, and development," tech. rep., AIAA, 1997.

[70] J. Jeong and F. Hussain, "On the identification of a vortex," *Journal of Fluid Mechanics*, vol. 285, pp. 69–94, 1995.

[71] R. C. Baker, *Flow measurement handbook*, vol. 99. Cambridge University Press Cambridge, 2000.

[72] M. J. Rincón, A. Caspersen, N. T. Ingwersen, M. Reclari, and M. Abkar, "Flow investigation of two-stand ultrasonic flow meters in a wide dynamic range by numerical and experimental methods," *Flow Measurement and Instrumentation*, vol. 96, p. 102543, 2024.

[73] G. Rajita and N. Mandal, "Review on transit time ultrasonic flowmeter," in *2nd International Conference on Control, Instrumentation, Energy & Communication (CIEC)*, pp. 88–92, IEEE, (2016).

[74] D. W. Spitzer, *Flow Measurement: practical guides for measurement and control*. Instrument Society of America, 1991.

[75] M. Straka, A. Weissenbrunner, C. Koglin, C. Höhne, and S. Schmelter, "Simulation uncertainty for a virtual ultrasonic flow meter," *Metrology*, vol. 2, no. 3, pp. 335–359, 2022.

[76] M. J. Rincón, M. Reclari, X. I. Yang, and M. Abkar, "Validating the design optimisation of ultrasonic flow meters using computational fluid dynamics and surrogate modelling," *International Journal of Heat and Fluid Flow*, vol. 100, p. 109112, 2023.

[77] F. R. Menter, M. Kuntz, and R. Langtry, "Ten years of industrial experience with the sst turbulence model," *Turbulence, Heat and Mass Transfer*, vol. 4, no. 1, pp. 625–632, 2003.

[78] F. G. Schmitt, "About boussinesq's turbulent viscosity hypothesis: historical remarks and a direct evaluation of its validity," *Comptes Rendus Mécanique*, vol. 335, no. 9-10, pp. 617–627, 2007.

[79] J. H. Ferziger, M. Perić, and R. L. Street, *Computational methods for fluid dynamics*. springer, 2019.

[80] S. Patankar, *Numerical heat transfer and fluid flow*. Taylor & Francis, 2018.

[81] A. D. McNaught, A. Wilkinson, *et al.*, *Compendium of chemical terminology*, vol. 1669. Blackwell Science Oxford, 1997.

[82] M. J. Rincón, M. Reclari, X. Yang, and M. Abkar, "CFD-aided morphing and design optimisation of ultrasonic flow meters," in *The 14th International ERCOFTAC Symposium on Engineering Turbulence Modelling and Measurements*, pp. 109–114, 2023.

[83] International Organisation of Legal Metrology, *R-49: Water meters intended for the metering of cold potable water and hot water*. OIML, 2006.

[84] K. Shirai, C. Bayer, A. Voigt, T. Pfister, L. Büttner, and J. Czarske, "Near-wall measurements of turbulence statistics in a fully developed channel flow with a novel laser Doppler velocity profile sensor," *European Journal of Mechanics-B/Fluids*, vol. 27, no. 5, pp. 567–578, 2008.

[85] ISO/IEC, "Guide 98–3: 2008-09: Uncertainty of measurement – part 3: Guide to the expression of uncertainty in measurement (GUM)," *ISO/EIC*, 1995.

[86] S. Cherroud, X. Merle, P. Cinnella, and X. Gloerfelt, "Sparse bayesian learning of explicit algebraic reynolds-stress models for turbulent separated flows," *International Journal of Heat and Fluid Flow*, vol. 98, p. 109047, 2022.

[87] M. Schmelzer, R. P. Dwight, and P. Cinnella, "Discovery of algebraic reynolds-stress models using sparse symbolic regression," *Flow, Turbulence and Combustion*, vol. 104, pp. 579–603, 2020.

[88] J. Yoder, "Ultrasonic flowmeter market is expected to grow strongly," *Pipeline & Gas Journal*, vol. 229, no. 4, p. 22, 2002.

[89] J. G. Drenthen and G. de Boer, "The manufacturing of ultrasonic gas flow meters," *Flow Measurement and Instrumentation*, vol. 12, no. 2, pp. 89–99, 2001.

[90] T. Vontz and V. Magori, "An ultrasonic flow meter for industrial applications using a helical sound path," in *IEEE Ultrasonics Symposium. Proceedings*, vol. 2, pp. 1047–1050, IEEE, (1996).

[91] H. H. Xu, S. Lynch, and X. I. Yang, "Direct numerical simulation of slot film cooling downstream of misaligned plates," *Flow*, vol. 2, 2022.

[92] S. Altland, X. Zhu, S. McClain, R. Kunz, and X. Yang, "Flow in additively manufactured super-rough channels," *Flow*, vol. 2, 2022.

[93] A. Apon, S. Ahalt, V. Dantuluri, C. Gurdgiev, M. Limayem, L. Ngo, and M. Stealey, "High performance computing instrumentation and research productivity in US universities," *Journal of Information Technology Impact*, vol. 10, no. 2, pp. 87–98, 2010.

[94] T. Sterling, M. Brodowicz, and M. Anderson, *High performance computing: modern systems and practices*. Morgan Kaufmann, (2017).

[95] A. Keane and P. Nair, *Computational approaches for aerospace design: the pursuit of excellence*. John Wiley & Sons, (2005).

[96] A. I. Forrester, N. W. Bressloff, and A. J. Keane, "Optimization using surrogate models and partially converged computational fluid dynamics simulations," *Proceedings of the Royal Society A: Mathematical, Physical and Engineering Sciences*, vol. 462, no. 2071, pp. 2177–2204, 2006.

[97] M. P. Bendsoe and O. Sigmund, *Topology optimization: theory, methods, and applications*. Springer Science & Business Media, (2003).

[98] R. V. Woldseth, N. Aage, J. A. Bærentzen, and O. Sigmund, "On the use of artificial neural networks in topology optimisation," *Structural and Multidisciplinary Optimization*, vol. 65, no. 10, pp. 1–36, 2022.

[99] X. L. Huang and X. I. Yang, "A bayesian approach to the mean flow in a channel with small but arbitrarily directional system rotation," *Physics of Fluids*, vol. 33, no. 1, p. 015103, 2021.

[100] K.-D. Lee and K.-Y. Kim, "Surrogate based optimization of a laidback fan-shaped hole for film-cooling," *International Journal of Heat and Fluid Flow*, vol. 32, no. 1, pp. 226–238, 2011.

[101] X. Lam, Y. Kim, A. Hoang, and C. Park, "Coupled aerostructural design optimization using the kriging model and integrated multiobjective optimization algorithm," *Journal of Optimization Theory and Applications*, vol. 142, no. 3, pp. 533–556, 2009.

[102] P. Singh, I. Couckuyt, K. Elsayed, D. Deschrijver, and T. Dhaene, "Multi-objective geometry optimization of a gas cyclone using triple-fidelity co-kriging surrogate models," *Journal of Optimization Theory and Applications*, vol. 175, no. 1, pp. 172–193, 2017.

[103] L. Zhang, G. Davila, and M. Zangeneh, "Multi-objective optimization of a high specific speed centrifugal volute pump using three-dimensional inverse design coupled with computational fluid dynamics simulations," *Journal of Fluids Engineering*, vol. 143, no. 2, p. 021202, 2021.

[104] M. Urquhart, M. Varney, S. Sebben, and M. Passmore, "Aerodynamic drag improvements on a square-back vehicle at yaw using a tapered cavity and asymmetric flaps," *International Journal of Heat and Fluid Flow*, vol. 86, p. 108737, 2020.

[105] M. D. McKay, R. J. Beckman, and W. J. Conover, "A comparison of three methods for selecting values of input variables in the analysis of output from a computer code," *Technometrics*, vol. 42, no. 1, pp. 55–61, 2000.

[106] R. Jin, W. Chen, and A. Sudjianto, "An efficient algorithm for constructing optimal design of computer experiments," *Journal of Statistical Planning and Inference*, vol. 134, no. 1, pp. 268–287, 2005.

[107] G. Damblin, M. Couplet, and B. Iooss, "Numerical studies of space-filling designs: optimization of Latin Hypercube Samples and subprojection properties," *Journal of Simulation*, vol. 7, no. 4, pp. 276–289, 2013.

[108] S. B. Pope, *Turbulent flows*. Cambridge University Press, (2000).

[109] A. Sóbester, S. J. Leary, and A. J. Keane, "On the design of optimization strategies based on global response surface approximation models," *Journal of Global Optimization*, vol. 33, no. 1, pp. 31–59, 2005.

[110] N. Cressie, "The origins of kriging," *Mathematical Geology*, vol. 22, no. 3, pp. 239–252, 1990.

[111] J. P. Kleijnen, "Kriging metamodeling in simulation: A review," *European Journal of Operational Research*, vol. 192, no. 3, pp. 707–716, 2009.

[112] M. A. Bouhlel, J. T. Hwang, N. Bartoli, R. Lafage, J. Morlier, and J. R. R. A. Martins, "A Python surrogate modeling framework with derivatives," *Advances in Engineering Software*, p. 102662, 2019.

[113] A. Sobester, A. Forrester, and A. Keane, *Engineering design via surrogate modelling: a practical guide*. John Wiley & Sons, (2008).

[114] T. Hastie, R. Tibshirani, J. H. Friedman, and J. H. Friedman, *The elements of statistical learning: data mining, inference, and prediction*, vol. 2. Springer, (2009).

[115] D. R. Jones, "A taxonomy of global optimization methods based on response surfaces," *Journal of Global Optimization*, vol. 21, no. 4, pp. 345–383, 2001.

[116] D. R. Jones, M. Schonlau, and W. J. Welch, "Efficient global optimization of expensive black-box functions," *Journal of Global Optimization*, vol. 13, no. 4, pp. 455–492, 1998.

[117] J. Mockus, V. Tiesis, and A. Zilinskas, "The application of Bayesian methods for seeking the extremum," *Towards Global Optimization*, vol. 2, no. 117–129, p. 2, 1978.

[118] K. Deb, A. Pratap, S. Agarwal, and T. Meyarivan, "A fast and elitist multiobjective genetic algorithm: NSGA-II," *IEEE Transactions on Evolutionary Computation*, vol. 6, no. 2, pp. 182–197, 2002.

[119] X. L D Huang, N. Jain, M. Abkar, R. F Kunz, and X. I A Yang, "Determining a priori a RANS model's applicable range via global epistemic uncertainty quantification," *Computers & Fluids*, vol. 230, p. 105113, 2021.

[120] A. Eidi, N. Zehtabiyan-Rezaie, R. Ghiassi, X. Yang, and M. Abkar, "Data-driven quantification of model-form uncertainty in Reynolds-averaged simulations of wind farms," *Physics of Fluids*, vol. 34, no. 8, p. 085135, 2022.

[121] A. Amarloo, P. Forooghi, and M. Abkar, "Frozen propagation of reynolds force vector from high-fidelity data into Reynolds-averaged simulations of secondary flows," *Physics of Fluids*, vol. 34, no. 11, p. 115102, 2022.

[122] J. R. Martins and A. B. Lambe, "Multidisciplinary design optimization: a survey of architectures," *AIAA Journal*, vol. 51, no. 9, pp. 2049–2075, 2013.

[123] E. M. Papoutsis-Kiachagias and K. C. Giannakoglou, "Continuous adjoint methods for turbulent flows, applied to shape and topology optimization: industrial applications," *Archives of Computational Methods in Engineering*, vol. 23, no. 2, pp. 255–299, 2016.

[124] E. Papoutsis-Kiachagias, N. Magoulas, J. Mueller, C. Othmer, and K. Giannakoglou, "Noise reduction in car aerodynamics using a surrogate objective function and the continuous adjoint method with wall functions," *Computers & Fluids*, vol. 122, pp. 223–232, 2015.

[125] L. Piegl and W. Tiller, *The NURBS book*. Springer Science & Business Media, 1996.

[126] M. Rincón, A. Amarloo, M. Reclari, X. Yang, and M. Abkar, "Progressive augmentation of turbulence models for secondary flow prediction by computational fluid dynamics driven surrogate optimisation," *International Journal of Heat and Fluid Flow*, 2023.

[127] N. Nikitin, N. Popelenskaya, and A. Stroh, "Prandtl's secondary flows of the second kind. Problems of description, prediction, and simulation," *Fluid Dynamics*, vol. 56, no. 4, pp. 513–538, 2021.

[128] M. A. Cruz, R. L. Thompson, L. E. Sampaio, and R. D. Bacchi, "The use of the Reynolds force vector in a physics informed machine learning approach for predictive turbulence modeling," *Computers & Fluids*, vol. 192, p. 104258, 2019.

[129] J. Weatheritt and R. Sandberg, "A novel evolutionary algorithm applied to algebraic modifications of the RANS stress–strain relationship," *Journal of Computational Physics*, vol. 325, pp. 22–37, 2016.

[130] J. Weatheritt and R. Sandberg, "The development of algebraic stress models using a novel evolutionary algorithm," *International Journal of Heat and Fluid Flow*, vol. 68, pp. 298–318, 2017.

[131] A. P. Singh, S. Medida, and K. Duraisamy, "Machine-learning-augmented predictive modeling of turbulent separated flows over airfoils," *AIAA Journal*, vol. 55, no. 7, pp. 2215–2227, 2017.

[132] J. R. Holland, J. D. Baeder, and K. Duraisamy, "Field inversion and machine learning with embedded neural networks: Physics-consistent neural network training," in *AIAA Aviation 2019 Forum*, p. 3200, 2019.

[133] J. Barzilai and J. M. Borwein, "Two-point step size gradient methods," *IMA Journal of Numerical Analysis*, vol. 8, no. 1, pp. 141–148, 1988.

[134] A. Forrester, A. Sobester, and A. Keane, *Engineering design via surrogate modelling: a practical guide*. John Wiley & Sons, 2008.

[135] T.-R. Xiang, X. Yang, and Y.-P. Shi, "Neuroevolution-enabled adaptation of the jacobi method for poisson's equation with density discontinuities," *Theoretical and Applied Mechanics Letters*, vol. 11, no. 3, p. 100252, 2021.

[136] F. Waschkowski, Y. Zhao, R. Sandberg, and J. Klewicki, "Multi-objective CFD-driven development of coupled turbulence closure models," *Journal of Computational Physics*, vol. 452, p. 110922, 2022.

[137] N. V. Queipo, R. T. Haftka, W. Shyy, T. Goel, R. Vaidyanathan, and P. K. Tucker, "Surrogate-based analysis and optimization," *Progress in Aerospace Sciences*, vol. 41, no. 1, pp. 1–28, 2005.

[138] R. D. Sandberg and Y. Zhao, "Machine-learning for turbulence and heat-flux model development: A review of challenges associated with distinct physical phenomena and progress to date," *International Journal of Heat and Fluid Flow*, vol. 95, p. 108983, 2022.

[139] Y. Fang, Y. Zhao, F. Waschkowski, A. S. Ooi, and R. D. Sandberg, "Toward more general turbulence models via multicase computational-fluid-dynamics-driven training," *AIAA Journal*, pp. 1–16, 2023.

[140] Y. Bin, L. Chen, G. Huang, and X. I. Yang, "Progressive, extrapolative machine learning for near-wall turbulence modeling," *Physical Review Fluids*, vol. 7, no. 8, p. 084610, 2022.

[141] S. B. Pope, "A more general effective-viscosity hypothesis," *Journal of Fluid Mechanics.*, vol. 72, no. 2, pp. 331–340, 1975.

[142] P. Forooghi, X. I. Yang, and M. Abkar, "Roughness-induced secondary flows in stably stratified turbulent boundary layers," *Physics of Fluids*, vol. 32, no. 10, p. 105118, 2020.

[143] A. Amarloo, P. Forooghi, and M. Abkar, "Secondary flows in statistically unstable turbulent boundary layers with spanwise heterogeneous roughness," *Theoretical and Applied Mechanics Letters*, vol. 12, no. 2, p. 100317, 2022.

[144] S. Wallin and A. V. Johansson, "An explicit algebraic reynolds stress model for incompressible and compressible turbulent flows," *J. Fluid Mech.*, vol. 403, pp. 89–132, 2000.

[145] S. Kawai and K. Shimoyama, "Kriging-model-based uncertainty quantification in computational fluid dynamics," in *32nd AIAA Applied Aerodynamics Conference*, p. 2737, 2014.

[146] M. A. Bouhlel, J. T. Hwang, N. Bartoli, R. Lafage, J. Morlier, and J. R. Martins, "A python surrogate modeling framework with derivatives," *Advances in Engineering Software*, vol. 135, p. 102662, 2019.

[147] A. Pinelli, M. Uhlmann, A. Sekimoto, and G. Kawahara, "Reynolds number dependence of mean flow structure in square duct turbulence," *Journal of Fluid Mechanics.*, vol. 644, pp. 107–122, 2010.

[148] R. McConkey, E. Yee, and F.-S. Lien, "A curated dataset for data-driven turbulence modelling," *Scientific Data*, vol. 8, no. 1, pp. 1–14, 2021.

[149] R. D. Moser, J. Kim, and N. N. Mansour, "Direct numerical simulation of turbulent channel flow up to re τ= 590," *Physics of Fluids*, vol. 11, no. 4, pp. 943–945, 1999.

[150] M. Lee and R. D. Moser, "Direct numerical simulation of turbulent channel flow up to," *Journal of Fluid Mechanics.*, vol. 774, pp. 395–415, 2015.

[151] R. Vinuesa, P. Schlatter, and H. Nagib, "Secondary flow in turbulent ducts with increasing aspect ratio," *Physical Review Fluids*, vol. 3, no. 5, p. 054606, 2018.

[152] A. Huser and S. Biringen, "Direct numerical simulation of turbulent flow in a square duct," *Journal of Fluid Mechanics*, vol. 257, pp. 65–95, 1993.

[153] M. Emory and G. Iaccarino, "Visualizing turbulence anisotropy in the spatial domain with componentality contours," *Center for Turbulence Research Annual Research Briefs*, pp. 123–138, 2014.

[154] S. D. Hornshøj-Møller, P. D. Nielsen, P. Forooghi, and M. Abkar, "Quantifying structural uncertainties in Reynolds-averaged Navier–Stokes simulations of wind turbine wakes," *Renewable Energy*, vol. 164, pp. 1550–1558, 2021.

[155] A. Parente, C. Gorlé, J. Van Beeck, and C. Benocci, "Improved k–ε model and wall function formulation for the RANS simulation of abl flows," *Journal of Wind Engineering and Industrial Aerodynamics*, vol. 99, no. 4, pp. 267–278, 2011.

[156] F. Menter, A. Garbaruk, and Y. Egorov, "Explicit algebraic reynolds stress models for anisotropic wall-bounded flows," *Progress in flight physics*, vol. 3, pp. 89–104, 2012.

[157] S. Cherroud, X. Merle, P. Cinnella, and X. Gloerfelt, "Space-dependent aggregation of data-driven turbulence models," *arXiv preprint arXiv:2306.16996*, 2023.

[158] A. Amarloo, M. J. Rincón, M. Reclari, and M. Abkar, "Progressive augmentation of turbulence models for flow separation by multi-case computational fluid dynamics driven surrogate optimization," *Physics of Fluids*, vol. 35, p. 125154, 12 2023.

[159] A. Amarloo, P. Cinnella, A. Iosifidis, P. Forooghi, and M. Abkar, "Data-driven Reynolds stress models based on the frozen treatment of Reynolds stress tensor and Reynolds force vector," *Physics of Fluids*, vol. 35, no. 7, p. 075154, 2023.

[160] P. Balakumar and G. I. Park, "Dns/les simulations of separated flows at high Reynolds numbers," in *45th AIAA Fluid Dynamics Conference*, p. 2783, 2015.

[161] Y. Bentaleb, S. Lardeau, and M. A. Leschziner, "Large-eddy simulation of turbulent boundary layer separation from a rounded step," *Journal of Turbulence*, no. 13, p. N4, 2012.

[162] M. Breuer, N. Peller, C. Rapp, and M. Manhart, "Flow over periodic hills–numerical and experimental study in a wide range of Reynolds numbers," *Computers & Fluids*, vol. 38, no. 2, pp. 433–457, 2009.

[163] J.-P. Laval and M. Marquillie, "Direct numerical simulations of converging–diverging channel flow," in *Progress in Wall Turbulence: Understanding and Modeling: Proceedings of the WALLTURB International Workshop held in Lille, France, April 21-23, 2009*, pp. 203–209, Springer, 2011.

[164] L. A. Schiavo, A. B. Jesus, J. L. Azevedo, and W. R. Wolf, "Large eddy simulations of convergent–divergent channel flows at moderate Reynolds numbers," *International Journal of Heat and Fluid Flow*, vol. 56, pp. 137–151, 2015.

[165] R. Matai and P. Durbin, "Large-eddy simulation of turbulent flow over a parametric set of bumps," *Journal of Fluid Mechanics.*, vol. 866, pp. 503–525, 2019.

[166] R. B. Langtry and F. R. Menter, "Correlation-based transition modeling for unstructured parallelized computational fluid dynamics codes," *AIAA journal*, vol. 47, no. 12, pp. 2894–2906, 2009.

[167] F. R. Menter, R. Langtry, and S. Völker, "Transition modelling for general purpose cfd codes," *Flow, turbulence and combustion*, vol. 77, pp. 277–303, 2006.

Aarhus University Press
Aarhus Universitets Fællestrykkeriet
(AU Tryk)
Ole Worms Allé 4
8000 Aarhus, Denmark
October 2023
This document was typeset in LaTeX